Charles University in Prague

Faculty of Science

Study program: Physical Chemistry

Václav Houska

Chemické a fyzikální vlastnosti molekul a jejich souborů adsorbovaných na pevných površích

Chemical and Physical Properties of Molecules and Their Assemblies Adsorbed on Solid Surfaces

Doctoral Thesis

Supervisor: RNDr. Ivo Starý, CSc.

Prague, 2023

Prohlášení:

Prohlašuji, že jsem závěrečnou práci zpracoval samostatně a že jsem uvedl všechny použité informační zdroje a literaturu. Tato práce ani její podstatná část nebyla předložena k získání jiného nebo stejného akademického titulu.

V Praze 16.07.2023

……

Václav Houska

Acknowledgement

Writing these lines signifies that my Ph.D. adventure is coming to an end. It is with great pleasure that I express my gratitude to those who accompanied me on this long journey, never gave up on me, and guided me until its very end.

First and foremost, I would like to thank my family, Rostík, Gustík, Veru—and all my friends for their immense patience and unwavering support. I extend my thanks to Ivo Starý and Irena G. Stará for their assistance in both my professional and personal growth, and for demonstrating the true essence of scientific work. I am deeply grateful to Bohuslav Rezek and Egor Ukraintsev for their instrumental role in saving my doctoral project through our fruitful collaboration.

Naturally, my work would not have been possible without the support and collaboration of my colleagues, to whom I am truly indebted. I want to express my special thanks to Jarda Vacek for his invaluable help with computational chemistry problems and for engaging in inspiring discussions on physics and physical chemistry. I am grateful to my friend and librarian, Isa Gay Sanchez, who never fails to come up with an interesting paper and adds joy to my (not only) office life. I would also like to acknowledge Jirka Rybáček for his support in the lab, as well as all the other lab members whom I had the privilege to meet.

Furthermore, I wish to express my gratitude to all the collaborators and members of the service departments, whose contributions are highlighted in the Author Contribution Statement. I am also thankful to the Department of Physical and Macromolecular Chemistry for their unwavering institutional support.

Lastly, I would like to extend my thanks to the Lidl company for their Lord Nelson Earl Grey tea, which played a crucial role in helping me survive the process of writing this Thesis.

Contents

I. Abstrakt

Interakce organických molekul s pevnými povrchy představuje důležitou oblast fyzikálně-chemického výzkumu. Od heterogenní katalýzy až po OLED displeje, v řadě podobných systémů molekuly interagují na površích a pochopení jejich chování je pro správnou funkci dané aplikace zcela zásadní. V této práci jsem se zaměřil na velké π-konjugované makrocykly složené z dibenzo[5]helicenů a na jejich studium, zejména na povrchu grafitu.

Chemická syntéza studovaných makrocyklů byla zprvu komplikována řadou překážek, zejména pak jejich mimořádně nízkou rozpustností. V rámci této práce se podařilo najít účinnou solubilizační strategii spočívající v modifikaci makrocyklů tritylovými skupinami, které efektivně snižují intenzivní mezimolekulové π-π interakce. Otevřela se tak cesta k následnému studiu vlastností těchto látek. Hlavní pozornost byla věnována zejména trimeru, který se podařilo plně charakterizovat a u něhož bylo možné provést následné experimenty. Jelikož bylo této látky připraveno jen několik desítek miligramů, přičemž některé stereoisomery makrocyklu se podařilo separovat jen v mikroskopických množstvích, bylo nutné u řady experimentů vyvinout vhodnou metodologii. Tato byla s úspěchem aplikována zvláště při měření izomerizační kinetiky, díky čemuž se podařilo zmapovat postupnou inverzi konfigurace jednotlivých helicenových jednotek, určit příslušné rychlostní konstanty a odpovídající inverzní bariéry. Tato studie poskytla cenné údaje o vztahu mezi chováním makrocyklu a jeho jednotlivých helicenových podjednotek.

Další pozornost byla věnována samoskladbě makrocyklu na povrchu pyrolitického grafitu. Pomocí ambientního měření AFM byl pozorován růst vysoce organizovaných 2D krystalů, a to navzdory přítomnosti stericky objemných tritylových skupin. Za použití PeakForce tapping modu se podařilo získat obrázky s molekulárním rozlišením a zobrazit i jednotlivé molekuly zabudované v 2D krystalech. Jak ukázaly následné simulace molekulové dynamiky, tritylové skupiny nejenže samoskladbě nebrání, naopak podstatným způsobem přispívají ke stabilitě vzniklých 2D krystalů a to mechanismem připomínajícím funkci suchého zipu. Vzhledem k tomu, že prováděné MD simulace byly výpočetně značně náročné, pro některé výpočty jsme vyvinuli algoritmus využívající Lennard-Jonesův potenciál, jenž umožnil rychlou evaluaci stability různých geometrických uspořádání molekul na povrchu. I přes značná zjednodušení, která algoritmus zavádí, se s jeho pomocí podařilo vysvětlit řadu jemných strukturních detailů pozorovaných vrstev.

Vzhledem k tomu, že makrocyklus je formálně 4n π-elektronový systém, závěrečná část práce byla věnována studiu jeho možné (anti)aromaticity. Z teoretického hlediska byly provedeny zejména výpočty NICS a ACID, ale získané výsledky byly, překvapivě, značně závislé na řadě výpočetních parametrů. Experimentální měření kruhových proudů s pomocí NMR významnou globální aromaticitu neprokázalo. V samém závěru práce pak byl výpočetně studován přenos náboje mezi molekulou makrocyklu a povrchem grafitu a případné implikace pro aromaticitu makrocyklu. Získané výsledky naznačují, že k významné stabilizaci vlivem aromatizace molekuly nedochází.

Klíčová slova: Heliceny, makrocykly, chiralita, samoskladba, AFM, molekulová dynamika, aromaticita

II. Abstract

Interaction of organic molecules with solid surfaces represents a key area of physical-chemistry research. From heterogenous catalysis to OLED displays, in numerous such systems molecules interact on interfaces, and understanding their behavior is crucial for the correct operation of such applications. In this work, I focused on the study of large π-conjugated macrocycles based on dibenzo[5]helicenes with emphasis on their behavior on graphite surface.

The chemical synthesis of the investigated macrocycles was initially impeded by a number of obstacles, particularly by their extremely low solubility. In this work, an efficient solubilization strategy based on the modification of the macrocycles with trityl groups was discovered, which effectively diminishes the intense intermolecular π-π interactions. This opened a path towards a subsequent study of the compound's properties. The attention was focused mainly on a trimer, which was successfully fully characterized, enabling further experiments. Since only a few tens of milligrams of the trimer was prepared, and some stereoisomers were isolated in only microscopic amounts, it was important to develop a suitable experimental methodology. These methods were successfully employed in the measurement of the isomerization kinetics, which allowed us to map the process of the consecutive helicity inversion, determine the rate constants and the corresponding inversion barriers. This project provided valuable insight into the relationship between the behavior of the macrocycle and its individual helicene subunits.

The attention was subsequently focused on the self-assembly on the surface of pyrolytic graphite. With the help of ambient AFM, macrocycles arranged in highly organized 2D crystals were observed, even despite the presence of the very bulky trityl groups. By using the PeakForce tapping mode, images with molecular resolution were obtained, including even individual molecules within the 2D crystals. As shown by subsequent molecular dynamics (MD) simulations, not only the trityl groups do not prevent the self-assembly, but they even substantially contribute to the stability of the formed 2D crystals, by a mechanism similar to the Velcro. The large computational cost of the MD simulations motivated us to develop an algorithm employing Lennard-Jones potential, with which a fast evaluation of the stability of the various molecular aggregates was possible. Despite its substantial simplifications, the algorithm helped us to explain several fine structural details of the observed adlayers.

Considering the trimer is formally a 4n π-electron system, the last part of the Thesis was dedicated to the study of its possible (anti)aromaticity. On the theoretical level, NICS and ACID calculations were performed, but the obtained results were surprisingly sensitive to the calculation parameters. The experimental investigation of the associated ring currents using NMR did not show evident global aromaticity. On surface calculations on graphite also showed a significant charge transfer from the molecule to graphite and implications on the aromatic state of the molecule were investigated. As in the solution phase, the results suggest that the global aromaticity of the macrocycle on the surface is negligible.

Keywords: Helicenes, macrocycles, chirality, self-assembly, AFM, molecular dynamics, aromaticity

III. Publications related to the Thesis

1. **Houska, V.**; Ukraintsev, E.; Vacek, J.; Rybáček, J.; Bednárová, L.; Pohl, R.; Stará, I. G.; Rezek, B.; Starý, I. Helicene-Based π-Conjugated Macrocycles: Their Synthesis, Properties, Chirality and Self-Assembly into Molecular Stripes on a Graphite Surface. Nanoscale **2023**, *15*, 1542–1553. https://doi.org/10.1039/D2NR04209F.[1]

2. Ukraintsev, E.; **Houska, V.**; Rezek, B. Small Angle Symmetry Splitting of Helicene-Based Molecular Wires on Pyrolytic Graphite. *Carbon* **2022**, *193*, 171–181. https://doi.org/10.1016/j.carbon.2022.03.013.[2]

IV. Author Contribution Statement

The projects discussed in the Thesis would not be realized without a substantial help from other collaborators, contributions of whose are specified below:

Bednárová Lucie – ECD, IR, and UV-Vis service measurements

Fiedler Pavel – IR service measurements and assignment

Houska Václav – Conceptualization, Synthesis, HPLC and SFC, kinetic measurements, NMR measurements and interpretation, MS interpretation, AFM and STM sample preparations and measurements, DFT and MD calculations, data analysis, Publication 1 manuscript preparation, editing and review, Publication 2 manuscript review and editing

Kertisová Kvetoslava – MS service measurements

Nováková Kateřina – MS service measurements

Pohl Radek – NMR measurements and interpretation

Pospíšil Lubomír – CV voltammetry measurements

Rezek Bohuslav – Conceptualization, Publication 2 review, and editing

Rybáček Jiří – Instrumentation support, measurement of racemization barrier of compounds **43** and **45**, Publication 1 manuscript review and editing

Stará Irena, G. – Conceptualization, Publication 1 manuscript preparation, review and editing, Thesis review

Starý Ivo – Doctoral supervisor, conceptualization, Publication 1 manuscript preparation, review and editing, Thesis review

Šaman David – NMR service measurements

Ukraintsev Egor – AFM and STM measurements, conceptualization, Publication 2 manuscript preparation, review, and editing, Thesis review

Vacek Jaroslav – Theoretical support, Thesis review

Doctoral supervisor signature: ……

RNDr. Ivo Starý, CSc.

V. Funding

The project was supported by Czech Science Foundation (Reg. No. 20-23566S), the Charles University Grant Agency (Reg. No. 818319), the European Regional Development Fund (Reg. No. CZ.02.1.01/0.0/0.0/16_019/0000778, CAAS) and the Institute of Organic Chemistry and Biochemistry, Czech Academy of Sciences (RVO: 61388963). The project was conducted with the use of the CzechNanoLab Research Infrastructure, which was supported by the Ministry of Education, Youth and Sports of the Czech Republic (Reg. No. LM2018110).

VI. List of Abbreviations

ACID	*Anisotropy of current induced density*
AEM	*Aryleneethynylene macrocycle*
AFM	*Atomic force microscopy*
APCI	*Atmospheric pressure chemical ionization*
APT	*Attached proton test*
AVM	*Arylenevinylene macrocycle*
CISS	*Chirality-induced spin selectivity*
COSY	*Correlated spectroscopy*
CPP	*Cyclo-p-phenylene*
CSGT	*Continuous set of gauge transformations*
DDQ	*2,3-Dichloro-5,6-dicyano-1,4-benzoquinone*
DFT	*Density functional theory*
DIPA	*Diisopropylamine*
DOSY	*Diffusion ordered spectroscopy*
ECD	*Electronic circular dichroism*
EDDB	*Electron density of delocalized bonds*
EI	*Electron impact*
ESI	*Electrospray ionization*
FT	*Fourier transform*
FFT	*Fast Fourier transform*
GIAO	*Gauge-independent atomic orbital*
GPC	*Gel permeation chromatography*
HMBC	*Heteronuclear multiple bond correlation*
HOMA	*Harmonic oscillator model of aromaticity*
HOMO	*Highest occupied molecular orbital*
HOPG	*Highly oriented pyrolytic graphite*
HPLC	*High-performance liquid chromatography*
HR	*High-resolution*
HSQC	*Heteronuclear single quantum coherence*
IR	*Infra-red*
L-BFGS	*Limited-memory Broyden–Fletcher–Goldfarb–Shanno algorithm*
LCAO	*Linear combination of atomic orbitals*
LUMO	*Lowest unoccupied molecular orbital*
MALDI	*Matrix-assisted laser desorption ionization*
MD	*Molecular dynamics*
MS	*Mass spectroscopy*

NICS	*Nucleus-independent chemical shifts*
NMR	*Nuclear magnetic resonance*
OLED	*Organic light-emitting diode*
PE	*Potential energy*
PEG	*Poly(ethyleneglycol)*
PTFE	*Poly(tetrafluoroethylene)*
QNM	*Quantitative nanomechanical mapping*
ROESY	*Rotating-frame nuclear Overhauser effect correlation spectroscopy*
RRHO	*Rigid rotor/harmonic oscillator*
SFC	*Supercritical fluid chromatography*
SPM	*Scanning probe microcopy*
SPMs	*Shape persistent macrocycles*
STM	*Scanning tunneling microscopy*
TBAF	*Tetra-n-butylammonium fluoride*
TCB	*1,2,4-Trichlorobenzene*
TD-DFT	*Time-dependent density functional theory*
THF	*Tetrahydrofuran*
TIPS	*Triisopropylsilyl*
TIPSA	*(Triisopropylsilyl)acetylene*
TLC	*Thin-layer chromatography*
TOF	*Time-of-flight*
UHV	*Ultra-high vacuum*
UV	*Ultra-violet*
UV-Vis	*Ultra-violet-visible*
VT	*Variable-temperature*

1. Introduction

1.1. Arylenevinylene Macrocycles

Functional organic materials have attracted a considerable attention over the past decades due to their promising applications in various technical or biological fields.[3] The immense power and diversity of organic synthesis have allowed to conceive and prepare highly tailored materials, where the chemical structure is, by design, reflected in their mechanical, electronic, or optical properties. As these properties are often closely related to a precise molecular geometry, one of the important objectives in the field is to achieve high geometrical rigidity of the whole molecule or its relevant functional parts.[4,5]

One of the common answers to the above structural demands is to incorporate the chemical functionality into rigid, well-defined, macrocycles – the so called shape persistent macrocycles (SPMs).[5–9] This class of compounds involves an impressive number of structurally diverse macrocycles which are related on the basis of their structural rather than chemical properties. Their common feature – the persistence of shape – is a reflection of the chemical bonds used to construct them, mostly sp^2 and sp bonds. It is therefore no surprise that SPMs are often based on π-conjugated moieties and most commonly involve a substantial proportion of benzenoid parts. A high degree of rigidity, however, should be understood as the ability to preserve the macrocycle backbone shape. It does not imply that SPMs cannot be flexible, as documented by many recently reported conjugated macrocycles with substantial flexibility.[6,10]

Arylenevinylene macrocycles (AVMs), a subclass of SPMs, are made of arylene building blocks interconnected by vinylene linkers (see Figures 1, 2, 4). Compared to aryleneethynylene macrocycles (AEMs, see examples in Figures 5, 7A , and 9B),[8] their close relatives, AVMs remain relatively underinvestigated, and only a handful of papers covering AVMs have been published to this date. It is perhaps a certain uncertainty in the configuration of the vinylene double bond, their substantially larger conformational freedom,[11,12] and, until recently, a subjectively more challenging synthetic routes to access AVMs, which have discouraged researchers from studying these otherwise interesting compounds.

Probably the first preparation of a macrocycle which could be classified as AVM can be traced back to the works of Staab and co-workers, investigating several areno[n]annulenes.[13,14] A number of years later, Meier *et al.* reported a series of papers dedicated to various areno[n]annulenes **1a-e** (Figure 1). These AVMs were prepared by cyclocondensation from respective imine precursors,[11,15–19] or by McMurry reaction from corresponding aldehydes.[20] The disc-shaped compounds behaved very similarly, regardless of the particular benzenoid building block, and generalization of their properties was thus possible.

Since these compounds can be viewed as annulenes, their aromaticity was investigated.[11] Despite being formally 4n+2 π-electron systems, no global diatropic currents along the macrocycle perimeter were observed in NMR. Instead, local aromaticity was detected within the individual benzenoid rings. This is no surprise, because the NMR, crystal structures and

force field calculations all showed non-planar conformation of **1a-e**. This geometry distortion is a result of steric repulsion of the inner hydrogen atoms which overcomes the aromatic stabilization. The broken conjugation was also apparent from the UV-Vis spectra which feature only a modest red-shift.

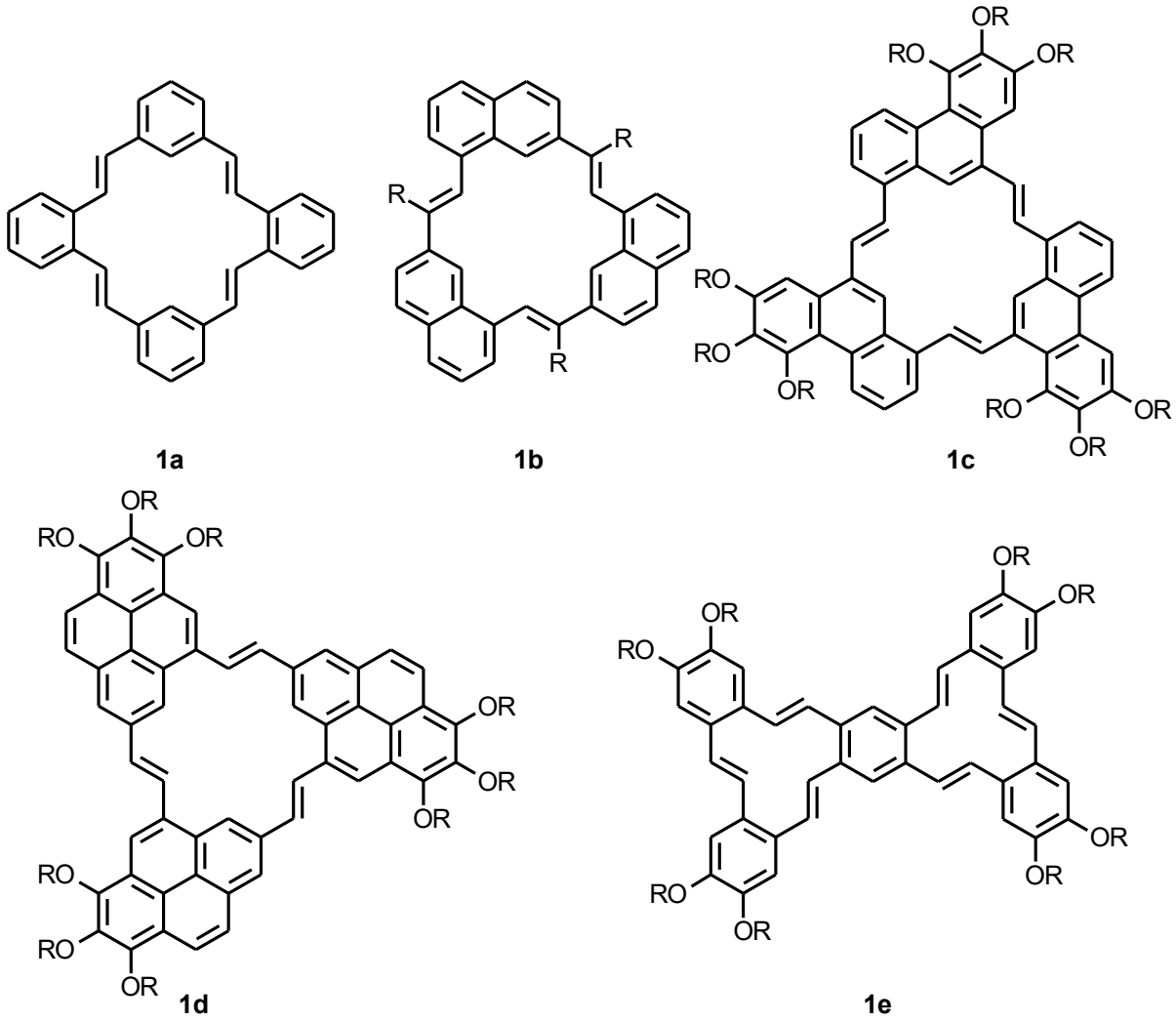

Figure 1. Examples of various annulene AVMs reported by Meier *et al.*[11,15–19]

Molecules **1a-e** were equipped with solubilizing chains of various length to improve their solubility. This turned out to be a necessity because **1a-e** show an unusually strong tendency to aggregate in the solution, resulting in columnar structures.[19] ^{1}H NMR and fluorescence measurements proved that even at concentrations down to 10^{-5} M, **1a-e** exists as a complex mixture of monomers, dimers and higher oligomers. This behavior can be rationalized by a relatively large flexibility of the macrocyclic backbone, which can efficiently adapt to the optimal geometry of the aggregate.[15] The strong tendency for aggregation and the presence of the long solubilizing chains are likely the reason why many AVMs **1a-e** form mesophases in a rather broad temperature range.

When annulene **1c** was irradiated with UV light in a deoxygenated solution, it photodimerized to form cyclophane belts **2** (Figure 2A).[15–19] This photoreaction proceeds at concentrations as low as 10^{-6} M, which again indicates pre-association of the reacting

molecules **1c** even at such extremely low concentrations. When, on the other hand, oxygen was present during the irradiation, oxidative degradation occurred. The same products were also found when the irradiation was performed without solvent, but the reaction required heating to up to 230 °C, to allow the reorganization of the mesophase and the subsequent photodimerization.[15]

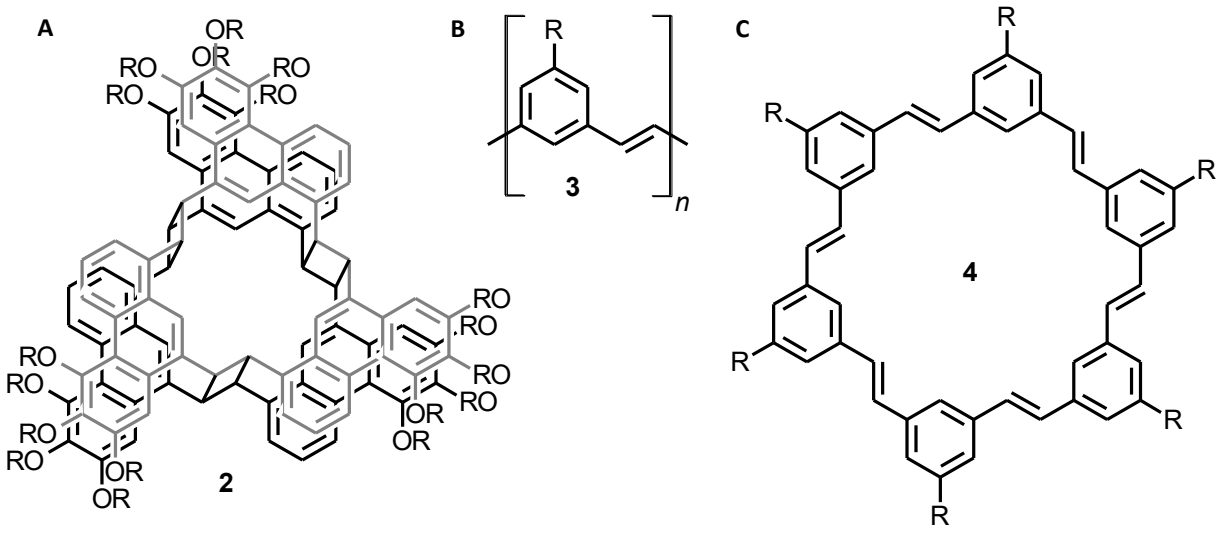

Figure 2. Belt cyclophane **2** reported by Meier *et al.* (A).[15–19] Linear oligomers **3** (B) and AVMs **4** (C) studied by Zhang and co-workers.[21,22]

These extensive studies by Meier and co-workers were first which provided a detailed description of the physico-chemical properties of disc-shaped AVMs. Similar behavior was later found in other AVMs, including macrocycles **31** and **32** discussed in this Thesis (see the Results and Discussion section). Later on, Zhang and co-workers prepared AVMs **4** via olefin metathesis of corresponding divinyl precursors (Figure 2C).[12] Several interesting papers further exploring the various facets of the AVM behavior ensued over the last ten years.

From a synthetic standpoint, the application of the olefin metathesis, adopted in analogy to AEMs (efficiently prepared by alkyne metathesis), significantly simplified the synthesis of AVMs **4** and allowed the application of the principles of dynamic covalent chemistry. Most importantly, as olefin metathesis can be run under thermodynamically controlled conditions, the careful design of the synthetic target can dramatically increase the reaction yield. Although various cyclic and/or linear (**3**, Figure 2B) molecules can be formed during the oligomerization, the final distribution of the products is dictated by their relative thermodynamic stability and, under ideal conditions, the undesired side products are gradually transformed to the desired ones. It should be emphasized, that such progress would not be possible without the tumultuous development in the methodology of olefin metathesis, especially thanks to the contributions of Grubbs and co-workers.[23]

Thus, **4** were prepared in only three steps from commercially available precursors in 45-85% yields, using trivial synthetic techniques.[12,24] The material properties of **4** followed in much the same way the findings already reported by Meier. The molecules had a very strong propensity for aggregation, almost independent of the nature of the substituents R. This is in stark contrast to AEMs where strong aggregation was observed only in molecules bearing

electron deficient functionalities.[24] Similarly to **1**, DFT calculations showed a substantial flexibility of the macrocyclic backbone which could adapt to the optimal geometry of the aggregates.

The prominent aggregation behavior was studied in more detail on **4** decorated with several different substituents and in a range of solvents using various spectroscopic techniques.[24] ^{1}H NMR measurements showed a strong concentration dependence of the proton signals in the aromatic region in **4** decorated with polar groups, such as ester or ether. In contrast, chemical shifts of **4** equipped with nonpolar aliphatic chains were practically independent of concentration. These results were also corroborated by UV-Vis and fluorescence spectroscopy measurements. The authors attributed the above observations to the so-called direct through-space interaction between the polar substituents and the nearby π- system.[24,25]

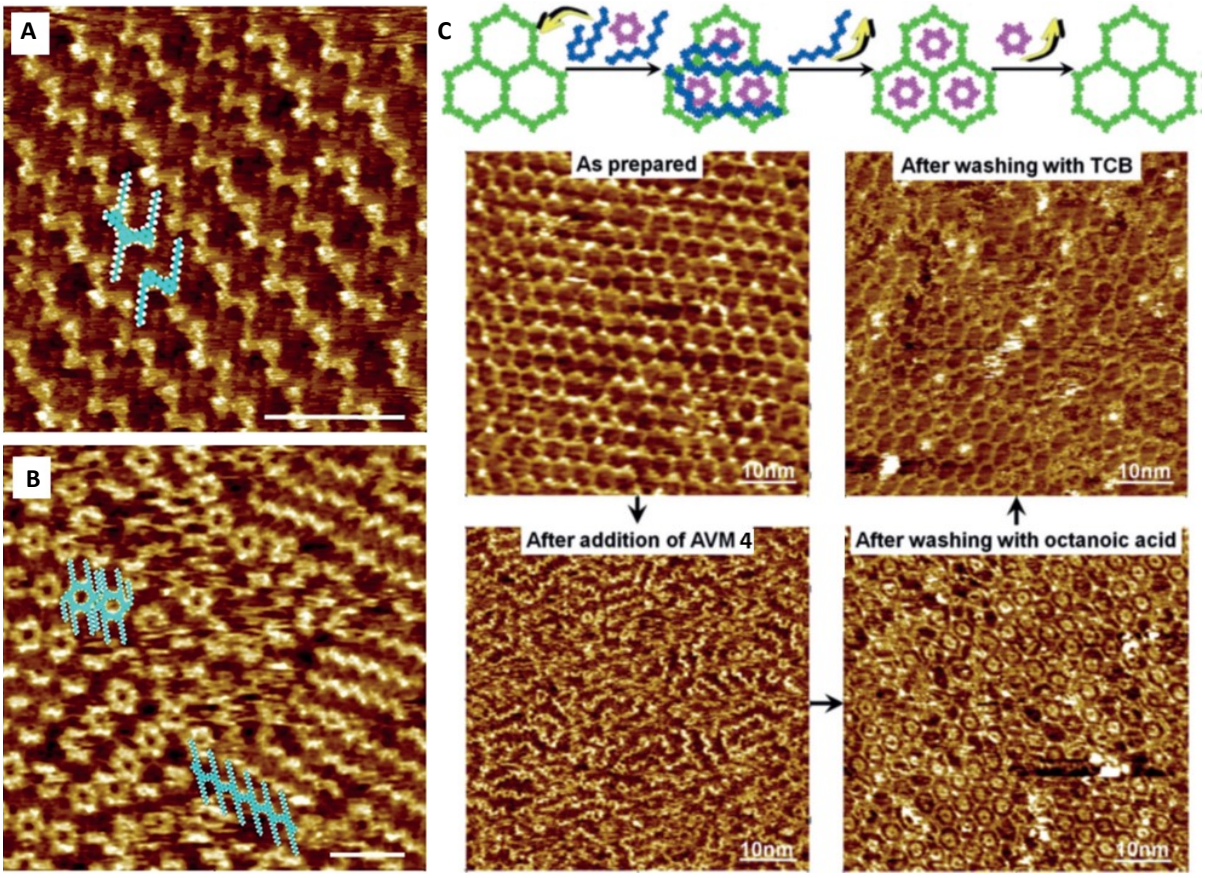

Figure 3. Self-assembly of AVMs **4** on HOPG/*n*-octanoic acid interface imaged by STM. Reaction at 35°C under vacuum, only trimers **3** are present (A). Reaction at 150°C under vacuum, linear dodecamers **3** and cyclic hexamers **4** are present (B).[21] Separation of cyclic **4a** or **4b** from linear oligomers **3** by using imine hexagonal network on HOPG (C).[22] Reproduced and adapted with permission from Wiley-VCH Verlag GmbH & Co. KGaA.

The investigation of the planar AVMs **4** has so far culminated in two on-surface studies. In the first work, Liu *et al.* monitored the macrocyclization process on the interface of highly oriented pyrolytic graphite (HOPG) and *n*-octanoic acid via scanning tunneling microscopy (STM).[21] Interestingly, the product distribution on the surface was substantially different from the analogous reactions in solution. While metathesis in 1,2,4-trichlorobenzene (TCB) under vacuum yielded a relatively high proportions of macrocycle **4**, especially at elevated

temperatures, the reaction performed directly in the thin film of *n*-octanoic acid on the HOPG surface led to the completely different results. In this case, mostly dimers or trimers **3** were found on the surface, in many cases assembled into periodic domains (Figure 3A). With higher temperature, the proportion of the longer oligomers increased, but only at 150 °C a notable portion of the cyclic hexamer **4** was observed (Figure 3B). Authors explain these observations by the preferential adsorption of the short linear oligomers **3** on the surface which hampers the further growth and back biting necessary for the formation of the cyclic product. This reasoning was further supported by an analogous experiment with **3** bearing electron deficient chains, which were expected to have substantially higher affinity to the surface. Indeed, in this case the STM found mainly domains of dimers at 35 °C. The proportion of higher oligomers again increased at higher temperatures, with the cyclic hexamer appearing only at 150 °C with as low as 1% occurrence. Moreover, when the metathesis was repeated under normal pressure in an argon atmosphere, oligomerization was significantly hampered. This is in line with the common necessity to remove the byproduct ethylene gas to shift the reaction equilibrium towards higher, and preferably, cyclic oligomers. This study thus outlined the possibility to alter the product distribution by interaction with the surface.

Building on the above findings, the authors decided to use a hexagonal covalent imine network as a guest for macrocycles **4a** with R = $C_{10}H_{21}$, and **4b** with R = $COOC_{10}H_{21}$, to achieve separation of the cyclic hexamers from the undesired linear oligomers (Figure 4C).[22] Indeed, both **4a** and **4b** easily nested in the network pores. Both the pore size and the nature of the macrocycle-network interactions were important. Macrocycle **4a** substituted with the nonpolar chains had low affinity to the pores, which was reflected in a low resolution of its STM scans. In contrast, the interaction of the ester-substituted **4b** with the imine network was notably stronger, as nicely documented by its high STM contrast. Unlike the cyclic hexamers, the linear oligomers were not strongly bound within the pores and often assembled in the second layer on top of the imine-macrocycle network. This observation was exploited for the efficient separation of **3** from the cyclic products since they could be easily washed off by *n*-octanoic acid, while **4b** remained trapped within the pores. In the subsequent step, **4b** could be released by washing with a stronger solvent such as TCB. Although **4a** was also selectively bound inside the imine pores, the washing with *n*-octanoic acid removed both linear and cyclic oligomers, presumably due to notably weaker interaction of **4a** with the surface. Notably, this procedure could also be scaled up by using powdered graphite to increase the surface area, which led to an impressive separation observable by gel permeation chromatography (GPC).

The macrocycles described above adopt close to planar geometries but several AVMs with inherently 3D shapes were also prepared.[26–28] One such recent example was reported by Kirinda *et al.,* studying *ortho*-phenylenevinylene foldamers locked into trimers **5** and **6** (Figure 4).[29] This work demonstrates the extraordinary versatility of the olefin metathesis which allows preparation of even moderately strained systems such as the above trimers. Although these systems are formally fully π-conjugated, the substantial strain leads to distortion of the foldameric structure and thereby preventing global π-conjugation. This was clearly reflected in UV-Vis spectra which showed absorptions reminiscent of *trans*-stilbene. It is also worth

mentioning that these molecules can exist in several conformational variants, of which the (*M,P,P)*/(*M,M,P)* heterochiral configurations are the most stable ones for both **5** and **6**.

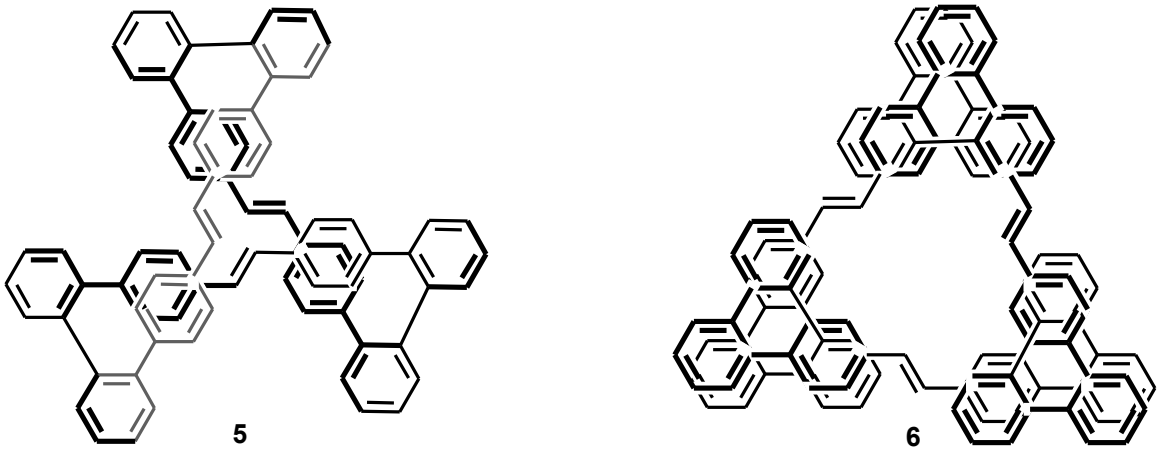

Figure 4. Foldamer-based macrocycles **5** and **6** reported by Kirinda *et al.*[29]

1.2. Chirality and Helicene-Based Macrocycles

Chirality is defined as a geometrical property of an object whose mirror image is non superimposable to the original. Since its first formal definition by Lord Kelvin in the 19th century,[30] this term has penetrated all major fields from mathematics and physics, to chemistry and biology.[31] In chemical sciences, chirality is well-established, albeit many fine details of how chirality influences physicochemical properties of matter remain unclear. From "small" questions, such as, how the chiral geometry determines the chiral compound's crystal packing, to "big" ones about the origin of homochirality in biological systems, the field of chirality still offers many mysteries to unravel.[32] It may seem, at first glance, that the widespread use of "chirality" in different scientific fields is just an etymological coincidence. However, recent discoveries related to chirality induced spin selectivity effect (CISS) by Naaman, Waldeck and co-workers show that chirality (or helicity) of elementary particles[33] and chirality of organic molecules may be closely connected.[34]

A beautiful example of chirality, holding a prominent position among chiral molecules, are helicenes. These inherently chiral, spring-like conjugated hydrocarbons were originally defined as *ortho*-condensed benzene rings arranged in a helical shape. Apart from classical carbohelicenes, a tremendous number of new helicene-like molecules have been synthesized and studied in the past decades.[35] The recent interest in helicenes has been motivated by their unique properties, to name just a few – extraordinary values of optical rotation,[36] circularly polarized luminescence,[37,38] spin filtration,[39,40] or promising applications as chiral ligands.[41,42]

For the reasons above, it is no surprise that helicenes are conceived as interesting building blocks of SPMs, combining their qualities with those of SPMs. Opposed to helicenes, the macrocycles incorporating helicenes still remain quite rare in the literature and only several such works have been published to this date.

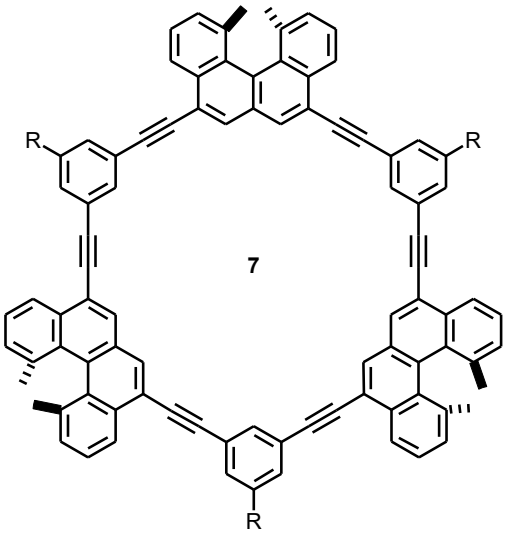

Figure 5. [4]Helicene-based macrocycle **7** reported by Nakamura *et al.*[41]

Probably the first macrocycle based on helical building block was reported by Nakamura *et al.*[43] The authors used a sequential Sonogashira coupling to connect 1,12-dimethylbenzo[c]phenanthrene, a configurationally locked tetrahelicene, with *m*-phenyleneethynylene spacers to form a chiral trimeric macrocycle **7** (Figure 5). Its synthesis started from optically pure starting materials and all four possible stereoisomers, namely (*M*,*M*,*M*)-**7**, (*P*,*P*,*P*)-**7**, (*M*,*M*,*P*)-**7** and (*M*,*P*,*P*)-**7**, were obtained. ^{1}H NMR and ECD spectroscopy clearly indicated a large tendency of molecules **7** to aggregate, with dimers as the main species, as revealed by vapor pressure osmometry. Interestingly, the stability of the aggregates was strongly dependent on their chirality. Thus, the strongest interaction was found for the optically pure homochiral

stereoisomers (*M*,*M*,*M*)-**7** and (*P*,*P*,*P*)-**7**, which was notably stronger compared to the analogous phenyleneethynylene hexamer. On the other hand, a racemic mixture of (*M*,*M*,*P*)/(*M*,*P*,*P*)-**7** showed the weakest aggregation. The authors attributed this behavior to a favorable lock-key interaction based on the performed force field calculations. A follow-up study by Takahira *et al.*,[44] focused on the comparison of **7** with its higher oligomer congeners. These large molecules retained an exceptional backbone rigidity until the octamer, which shower a measurable degree of conformational freedom, as documented by ^{1}H NMR and ECD spectra. However, in contrast to trimer **7**, these molecules did not aggregate.

More than a decade later, Robert *et al.* published the synthesis and characterization of helicene dimer **8** (Figure 6).[45] Its synthesis is based on the Perkin reaction to build a flexible macrocyclic precursor before the final oxidative photocyclization affording **8**. The same strategy was used by Naulet *et al.* to deliver a highly strained trimer **9** having Möbius topology (Figure 6).[46] Both enantiomeric pairs (*M*,*M*,*P*)/(*M*,*P*,*P*)-**9a** and (*M*,*M*,*M*)/(*P*,*P*,*P*)-**9b** were found in almost equal proportions, as documented by NMR, and were isolated by crystallization. The X-ray analysis showed that the neighboring helicene terminal benzene rings between each two helicenes are coplanar, indicating their π-conjugation, as also corroborated by a noticeable red shift in their UV-Vis spectra. A topological analysis revealed **9a** is twisted once, while **9b** is twisted three times. Even though all conjugated pathways within the backbones of **9** involve 4n π-electrons, a stable arrangement is possible due to the Möbius topology of these macrocycles. The seemingly large twist, which would otherwise be associated with enormous strain, is transferred into writhe – a favorable folding of the structures. The aromaticity of **9** was further studied by several computational methods. Although π-diatropic current inside the ring, and σ-paratropic current outside the ring were found by ACID[47,48] along the whole macrocycle backbone in both **9a** and **9b**, these currents almost cancel. As a result, no global aromaticity is observed which was also confirmed by NICS[49,50] and HOMA[51,52] calculations.

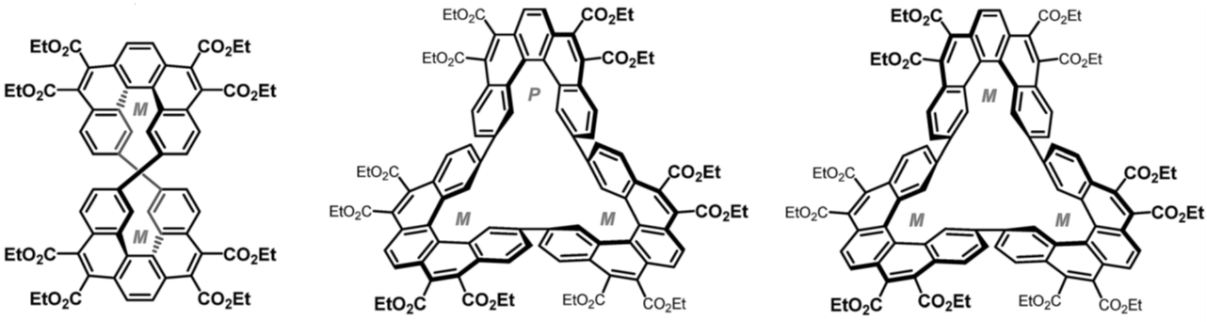

Figure 6. Dimer **8** and Möbius trimers (*M*,*P*,*P*)-**9a** and (*M*,*M*,*M*)-**9b** reported by Robert *et al.*[45] and Naulet *et al.*[46] Reproduced and adapted with permission from the Royal Society of Chemistry.

A similar Möbius helicene trimer was reported by Jiang *et al.*, who used the alkyne metathesis to connect propynyl helicenes into macrocycle **10** (Figure 7A).[53] The reaction proceeded towards the desired product only at elevated temperature of 60 °C in 84% yield. Strikingly, only (*M*,*M*,*P*)/(*M*,*P*,*P*)-**10** stereoisomer was identified in the reaction mixture, although the DFT calculations found the (*M*,*M*,*M*)/(*P*,*P*,*P*)-**10** stereoisomer to be 1-2 kcal·mol^{-1} more stable. To explain this unexpected observation, the authors calculated the reaction path

from the corresponding acyclic trimers to their cyclic counterparts (*M,P,P)*-**10** and (*P,P,P)*-**10**. The calculations showed that the energy barrier towards the metallacyclobutadiene intermediate, the rate determining step, is by 21.6 kcal·mol^{-1} lower for (*M,P,P)*-**10** than (*P,P,P)*-**10**. The barrier of the reverse process, taking into account the energy difference between the reactants and products, was even higher – 38.2 kcal·mol^{-1}, which nicely explained the kinetic stability of the product **10**. Additional investigation of **10** focused again on its aromaticity. Only a slight red shift in the UV-VIS spectra was observed, indicating the electronic conjugation of the helicene fragment with one side of the alkyne π-orbitals. This was also in line with the cyclic voltammetry measurement indicating an independent reduction of each helicene unit, again pointing at the fragmented conjugation. These results were finally confirmed by ACID and EDDB calculations which showed no global aromaticity, as in the case of **9**.

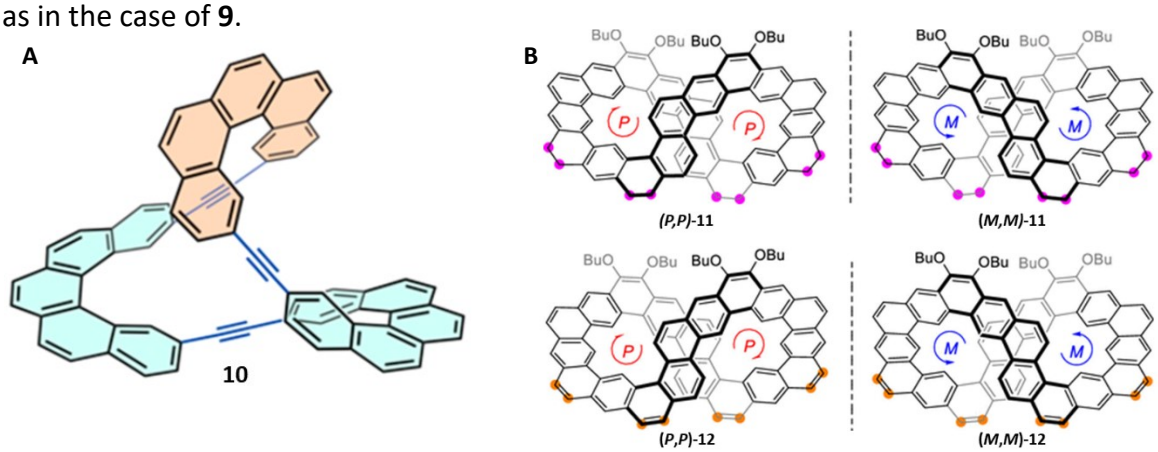

Figure 7. Möbius helicene trimer **10** reported by Jiang *et al.*[53] (A). Stereoisomers of saturated precursor macrocycle **11** and conjugated macrocycle **12** studied by Fan *et al.* (B).[54] Reproduced and adapted with permission from American Chemical Society, Copyright 2023.

Free helical structures often show enantiomerization barriers too low for practical applications. Unlike in the previous examples, embedding helix into a carefully designed figure-eight macrocycle can significantly increase the configuration stability of such a system. This approach was exemplified in the work of Fan *et al.*, where authors reported a homochiral figure-eight (*M*,*M*)/(*P*,*P*)-**12** (Figure 7B).[54] The synthetic strategy for this compound is based on a stepwise incorporation of strain into this highly twisted macrocycle. The twist was introduced by a careful choice of starting building blocks with conveniently placed substituents. These were connected via Suzuki-Miyaura macrocyclization in 23% yield, followed by benzannulation to give highly saturated macrocycle **11** in 77% yield. The ring closure was enabled by high flexibility of the saturated periphery of macrocycle **11**, despite its relatively high strain energy of 22.0 kcal·mol^{-1}. The target nanobelt **12**, with strain energy of 32.4 kcal·mol^{-1}, was then obtained by quantitative oxidative dehydrogenation with DDQ. Molecule **12** formed as homochiral (*M*,*M*)/(*P*,*P*)-**12** enantiomers which were readily resolved via chiral HPLC and their absolute configuration was assigned by comparison of the experimental and calculated ECD spectra. Although the authors did not measure the enantiomerization barrier, it was estimated by calculation to be above 83 kcal·mol^{-1}. Interestingly, the ACID and NICS calculations showed that the electronic structure of the belt resembles kekulene with ten localized Clar's sextets, instead of a structure with global

delocalization across the whole belt. These results are also in line with the UV-Vis and fluorescence spectra corresponding to a high degree of local aromaticity.

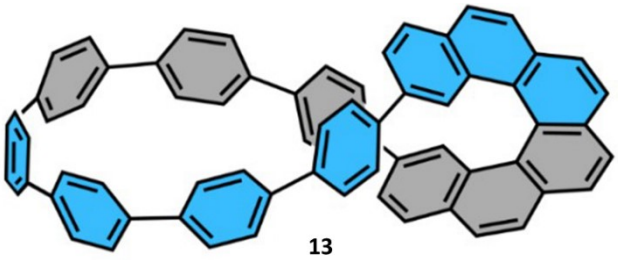

Figure 8. Helicene-CPP nanohoop **13** reported by Malinčík *et al.*[1] Reproduced and adapted with permission from Wiley-VCH Verlag GmbH & Co. KGaA.

Another figure-eight nanohoop structure **13**, combining hexahelicene and cycloparaphenylene (CPP), has recently been published by Malinčík *et al.* (Figure 8).[55] The objective of this study was to use the configurational stability and chiroptical properties of hexahelicene to alter the optoelectronic behavior of cycloparaphenylene (CPP). The target molecule **13** was prepared by a simple Suzuki-Miyaura coupling of 2,2'-dibromo[6]helicene with a CPP precursor synthesized by methodology developed by Jasti and co-workers.[56] Interestingly, **13** adopts Möbius topology both in solid state and in solution, as proved by X-ray analysis and variable temperature ^{1}H NMR. The accompanying DFT data revealed that the corresponding Hückel conformation is by 5 kcal·mol^{-1} higher in energy and, therefore, should not be populated in a considerable amount. Given the number of π-bonds in its structure, **13** cannot be fully conjugated due to the 2,2'-connections of the helicene to CPP resulting in cross-conjugated pathways. Thus, **13** is only locally aromatic. As desired, calculations found **13** has 55.4 kcal·mol^{-1} of strain energy, close to 57.7 kcal·mol^{-1} for [10]CPP, and enantiomerization barrier of 38-44 kcal·mol^{-1}, which is in line with its conformational rigidity. The presence of the CPP moiety results in the UV-Vis and fluorescence spectra being substantially different from the parent helicene, both showing a substantial red shift compared to 2,2'-ditolyl[6]helicene. In contrast, its ECD spectra are dominated by a chiroptical structure originating from the helicene fragment. Additionally, the molecule is a strong emitter of circularly polarized light with the g_{lum} factor 2.2·10^{-3}. This, in combination with a high quantum yield of fluorescence and a high value of CPL brightness of 63, makes **13** a very promising material with potential applications in CPL light sources.

While the previous works involved a classical helicene backbone as the macrocycle building blocks, others have focused on expanded helicene structures. For example, Kiel *et al.* prepared a large expanded helicene **14** via Ir-catalyzed [2+2+2] cyclotrimerization of the corresponding precursors in 80% isolated yield (Figure 9A).[57] Surprisingly, the procedure left the terminal alkyne groups intact, even under forcing conditions. This could be conveniently utilized in the subsequent ring closure leading to three different macrocycles. When **14** was submitted to alkyne metathesis conditions using a molybdenum-based catalyst, a figure-eight dimer **15** formed in excellent 98% yield (Figure 9B). In a different synthetic pathway, **14** was transformed to a zirconocene intermediate **16** (Figure 9D) which was finally transformed to either selenium macrocycle **17** (71%) or to a phenylene macrocycle **18** (65%) (Figure 9C). The synthesis of **15** and **18** was also realized in a one pot setup to deliver the same products in gram quantities, albeit in slightly smaller yields of 77% and 51%, respectively. Unlike **18**, which showed appreciable aggregation in $CDCl_3$, compounds **14**, **15**, and **17** did not show any

appreciable concentration dependence of their chemical shifts in ^{1}H NMR. The X-ray analysis showed crystals of **15** consist of homochiral (*M*,*M*) or (*P*,*P*) molecules, which was also supported by gas-phase DFT calculations. Crystals of **15** have an interesting packing where the molecules are arranged in helices along two adjacent helical axes. As far as the photophysical behavior is concerned, macrocycles **15**, **17**, and **18** have only a small red shift in UV-Vis compared to the parent helicene **14**. Likewise, the λ_{max} in their emission spectra are almost identical. Finally, the authors also studied the enantiomerization of the macrocycles. Both variable temperature ^{1}H NMR and HPLC-ECD measurements determined only small enantiomerization barriers. The figure-eight macrocycle **15** is only slightly more stable than the parent helicene **14** (12.5 vs 11.9 kcal·mol^{-1}), while the selenium and phenylene macrocycles **17** and **18** had higher barriers of 16.6 and 22.1 kcal·mol^{-1}, respectively.

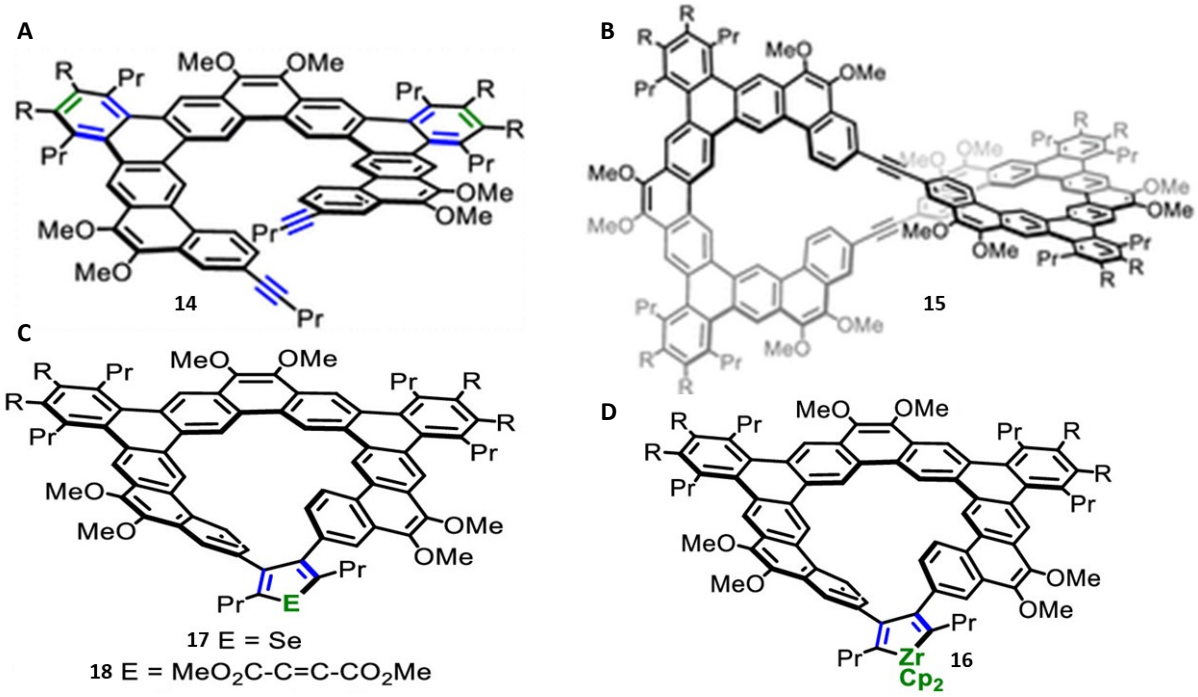

Figure 9. Expanded helicene **14** substituted with two alkyne groups (A), later used to construct figure-eight macrocycle **15** (B), or macrocycles **17** and **18** (C) through a zirconocene intermediate **16** (D), as reported by Kiel *et al.*[57] Reproduced and adapted with permission from the American Chemical Society, copyright 2023.

1.3.Self-Assembly of Macrocycles on Solid Surfaces

1.3.1. Basics

The molecular self-assembly is a spontaneous aggregation of individual molecules into a highly organized supramolecular architecture. The process is governed by the arrangement of the binding centers in the molecules which determines how they interact with each other or with their environment such as solvent or surface. The very specific nature of such interactions results in a high degree of order, which typically exceeds the molecular size by many folds.

The self-assembly process on the solid-liquid interface can be pictured in the following way: A surface is exposed to a liquid containing the solute molecules. As the molecules approach the surface by a simple diffusion, they adsorb if their adsorption enthalpy is larger than their kinetic energy. Once adsorbed, the adsorbates move on the surface, i.e. diffuse, the rate of which depends on factors such as the binding of the adsorbate to the specific surface sites or the system's temperature. The movement of the individual adsorbates is thus restricted from three to only two dimensions. The surface diffusion goes on until the adsorbates either desorb or encounter a site with substantially higher binding energy. This can be a surface defect or another adsorbate. If the intermolecular interaction between the two adsorbates is favorable, an aggregate is formed which serves as a first nucleation center, a predecessor of a 2D adlayer. The aggregation process then repeats until a whole molecular assembly is born. It must be remembered that this process is, in general, a dynamic equilibrium. At any moment, new molecules adsorb, some already present desorb. The assemblies can transform in time, but under constant conditions, the system is headed towards a thermodynamic equilibrium. How fast this equilibrium is established is then limited by the height of the corresponding energy barriers between the individual thermodynamic states.

As self-assembly of organic molecules, and particularly macrocycles, is often studied on surfaces, STM[58] and atomic force microscopy (AFM)[59] seem to be ideal tools to monitor such phenomena. These microscopic techniques image the sample surface by moving a special probe in its close proximity while simultaneously recording a signal which is then used to reconstruct the surface properties. Technically, a common denominator for both STM and AFM is the use of piezoceramic elements to move the measuring probe, which provides an extreme precision necessary for achieving very high, sometimes up to subatomic, resolution.[60,61] The difference between STM and AFM lies in the nature of the feedback signal used for the image construction.

From the experimental point of view, perhaps the most controlled environment for the study of self-assembly can be achieved under ultra-high vacuum (UHV) conditions, wherein the system of a pristine solid surface can be prepared, upon which molecules can be carefully deposited.[62] Such experimental setups are ideal for investigating the very basic laws of intermolecular and molecule-surface interactions behind the self-assembly processes. Unfortunately, experiments in UHV are instrumentationally very demanding and a single

study may take many hours or even days. The biggest drawback of the UHV techniques, however, is that the vast majority of self-assembly we encounter in nature or industrial applications proceeds under ambient conditions, i.e. surfaces and molecular assemblies are exposed to liquids or air at room temperature. On one hand, the ambient environment dramatically increases the number of factors involved and makes the precise quantification of ambient self-assembly a challenging endeavor. On the other, however, it makes the UHV experiments unrealistic for many real-world problems. Even though the general principles of STM or AFM are the same in both vacuum and ambient environment, the corresponding technical implementations are obviously substantially different. Further discussion will therefore be limited only to the ambient STM and AFM.

The following chapters will focus on elucidation of the essential principles behind the self-assembly on the solid/liquid interface, its kinetics, thermodynamics, and epitaxy. The introduction is then closed off by a brief outline of the basics of STM, AFM and their use in the study of macrocycle self-assembly.

1.3.2. Thermodynamics of Self-Assembly on Solid-Liquid Interface

In general, molecules self-assembled on surfaces can adopt many different structural variants, i.e. polymorphs. The polymorphs differ in the way their constituent molecules are geometrically arranged with respect to each other, to the underlying surface and the solvent above. Such different arrangements, naturally, must be associated with different interaction enthalpies, as well as various entropic contributions, in other words by their thermodynamic states. Unfortunately, the thermodynamic stability of the polymorphs in ambient conditions is influenced by a multitude of various external and internal factors, which are very difficult to quantify. Nevertheless, the paragraphs below present at least the most elemental view of the thermodynamics of ambient self-assembly.

From a practical point of view, the free energy ΔG of an assembly in equilibrium is conveniently defined by the sum of the individual chemical potentials μ_i in the phase i:

$$\Delta G = \sum_i \mu_i \, \Delta N_i \qquad (1)$$

where N_i is the number of molecules within a particular phase. Palma *et al.* expanded equation (1) to the sum of three contributions corresponding to solvated molecules, surface with adsorbed molecules, and surface in contact with solvent.[63]

$$G = \sum_i \mu_i N_{i,solv} + \sum_i \gamma_i A_i + \gamma_{surf/solv} \left(A_{tot} - \sum_i A_i\right) \qquad (2)$$

The first component of equation (2) is quantified by the chemical potential of solvated molecules μ_i and their number in solution N_i. The second component is made of the area of surface covered with the adlayer A_i and its corresponding surface free energy γ_i. The last component is the surface free energy of the surface in contact with solvent, $\gamma_{surf/sol}$.

When the number of solute molecules is significantly larger than the number adsorbed on the surface, the monolayer eventually covers the whole surface and the last term in (2) vanishes. The surface free energy can be then lowered by maximizing the number of

molecules adsorbed on the surface and creating a dense crystal packing which increases the intermolecular interactions.

In the opposite extreme case, when the number of molecules in the solution is very low, all the molecules transfer from the solution onto the surface and the first term in (2) goes to zero. The equilibrium is than controlled by a balance between the free energy of the adlayer and the free energy of the bare surface in contact with the solvent.

The equilibrium on the solid/liquid interface can be influenced by many factors. The temperature, concentration and solvent effects were studied by Lei *et al.* for assemblies of alkoxy substituted dehydrobenzo[12]annulenes **19** on HOPG surface (Figure 10).[64] While a high concentration led to the formation of densely packed monolayers with linear structure, porous honeycomb polymorph formed when the concentration was low. The authors used equation (3) to describe the relative coverages corresponding to the two observed polymorphs as a function of the concentration of **19** *c*, temperature *T*, the type of solvent (represented by the chemical potentials μ_0), and the number of molecules per unit area for linear, *l*, and for honeycomb, *h*, polymorph.

$$\frac{Y_h}{Y_l^{\left(\frac{l}{h}\right)}} = e^{\left(\frac{\left(\mu_{0,sol}-\mu_{0,h}\right)-\left(\frac{l}{h}\right)\left(\mu_{0,sol}-\mu_{0,l}\right)}{k_b T}\right) c^{\left(1-\frac{l}{h}\right)}} \qquad (3)$$

It follows from the equation, that when the concentration of **19** is low, the relative coverage of the honeycomb polymorph Y_h is large compared to the relative coverage of the linear dense polymorph Y_l. When the concentration is increased, Y_l increases accordingly.

Besides changing the concentration, the proportion of the two polymorphs can be influenced by the change in temperature. As seen from the denominator of the exponent in (3), increasing the temperature promotes the formation of the densely packed linear polymorph.

The role of solvent in equation (3) is captured by the differences in chemical potentials between **19** in solution, $\mu_{0,sol}$ and the honeycomb polymorph on the surface, $\mu_{0,h}$, or between **19** in solution, $\mu_{0,sol}$ and the linear polymorph on the surface, $\mu_{0,l}$. These differences can be attributed to the differences between the solvation enthalpy of **19** and the adsorption enthalpy of its respective polymorphs on the surface.

Although (3) is applicable to all two-component systems where the adsorbate forms two polymorphs, irrespective of the concrete solute, solvent, and surface, its weakness is that it neglects the adsorbate specific intermolecular interactions. These are, however, critical in the structural control of the adlayers and a more elaborate thermodynamic model is required in such cases. In contrast to the above case described by (3), the proportion of different polymorphs may not always change gradually with the solution concentration. Bellec *et al.* observed a sharp phase transition between two polymorphs of **20** on HOPG grown from 1-phenyloctane depending on the concentration (Figure 10).[65] Starting at low concentration, a porous polymorph formed until the critical value of concentration, when **20** abruptly begins to assemble into dense linear polymorph. To describe such behavior, the authors came up

with equation (4). Instead of considering single molecules in different environments as the basis for the definition of the chemical potentials, the authors defined the chemical potential of whole domains by introducing the aggregation number *N*. In this model, *N* = 1 corresponds to non-interacting adsorbates and the equation transforms to the equation (3).

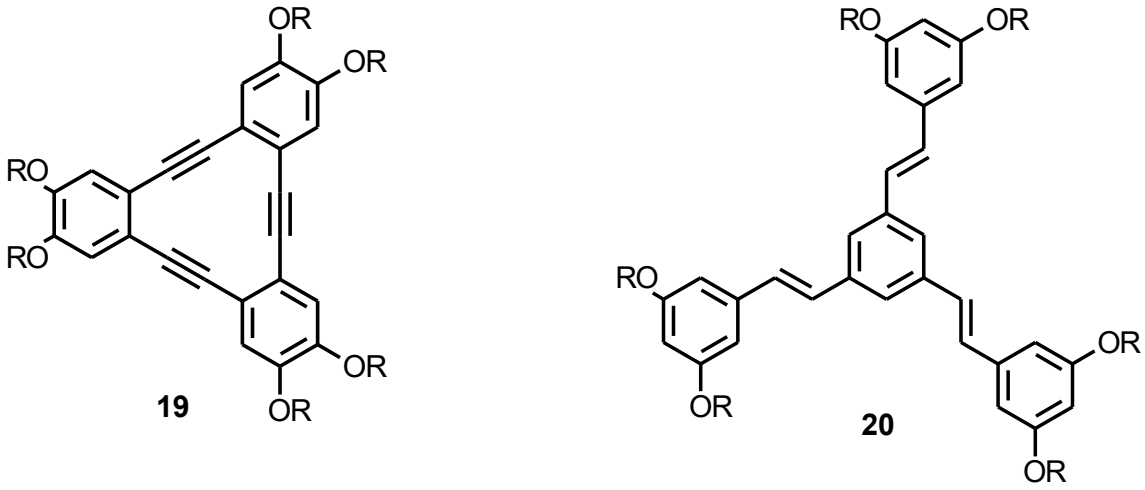

Figure 10. Structures of dehydrobenzo[12]annulenes **19** studied by Lei *et al.*[64] and alkoxy substituted 1,3,5-tristyrylbenzene **20** studied by Bellec *et al.*[65]

$$\left(\frac{Y_h}{Y_l^{\left(\frac{l}{h}\right)}}\right)^{\frac{1}{N}} = e^{\left(\frac{\left(\mu_{o,sol}-\frac{1}{N}\mu_{o,h}\right)-\left(\frac{l}{h}\right)\left(\mu_{o,sol}-\frac{1}{N}\mu_{o,l}\right)}{k_bT}\right)c^{\left(1-\frac{l}{h}\right)}} \qquad (4)$$

The transfer of a molecule from a solution onto a surface is entropically a very costly event. The translation degrees of freedom are reduced from three to two dimensions, the rotations and vibrations are also reduced to a large degree. With regard to the equation (5), the inevitable drop in entropy, accompanying the adsorption process, goes against the effort to minimize the value of *G*, and a spontaneous growth of the adlayer must therefore be an exothermic process. The negative enthalpy is then a sum of a number of contributions such as adsorption enthalpy, intermolecular interactions within the adlayer and in the solvent.

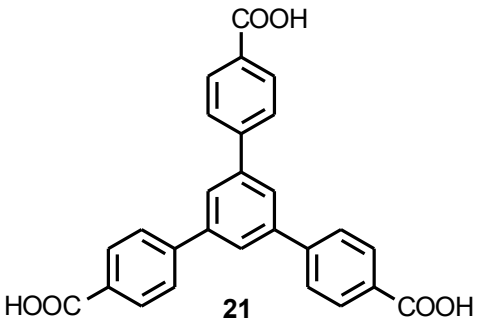

Figure 11. Tricarboxylic acid **21** studied by Gutzler *et al.*[64]

In a study reported by Gutzler *et al.,* the authors investigated thermodynamic equilibrium of different polymorphs of compound **21** deposited onto HOPG as a solution in either *n*-octanoic or *n*-nonanoic acid (Figure 11).[66] At low temperature, the compound assembled into a porous honeycomb structure, which, when heated to a critical temperature, transformed into a densely packed row structure. The reversibility of this process upon cooling signifies that the transition occurs between two thermodynamically stable, rather than kinetically trapped, polymorphs. When the monolayers were grown from the *n*-nonanoic solution, the transition occurred at somewhat higher temperature, but the behavior was otherwise analogical to the *n*-octanoic case.

To describe the above findings, instead of using chemical potentials as in equation (2), the authors used the traditional phenomenological Gibbs free energy:

$$\Delta G = \Delta H - T\Delta S \qquad (5)$$

The enthalpic component of (5) was obtained by molecular mechanics calculations, while to cover the entropic changes, Sackur-Tetrode equation was employed. Although the model provides only qualitative picture, it allows to conveniently separate the individual energetic and entropic contributions and attribute them to specific features of the system. Thus, as the temperature is increased, the weight of the positive entropic contributions increases, and the enthalpy must drop accordingly. This is achieved by the exchange of the solvent adsorbed on the surface for the additional molecules of **21** to form the densely packed adlayer. The driving force for this transformation is the adsorption enthalpy and interactions between molecules **21**.

1.3.3. Kinetics of Self-assembly on Solid-Liquid Interface

Kinetics in self-assembly processes has a profound effect on the growth of the adlayers, since the initially observed adlayer is often not a thermodynamic minimum. This is a result of the Ostwald's rule of stages, where a kinetically most accessible crystal structure is formed first. This metastable state is then gradually transformed, possibly through other metastable intermediates, into the thermodynamic minimum. Sometimes, the global minimum cannot be achieved because it is isolated by too high energy barriers. In this case of a so-called kinetic trapping, the most stable local minimum is formed.

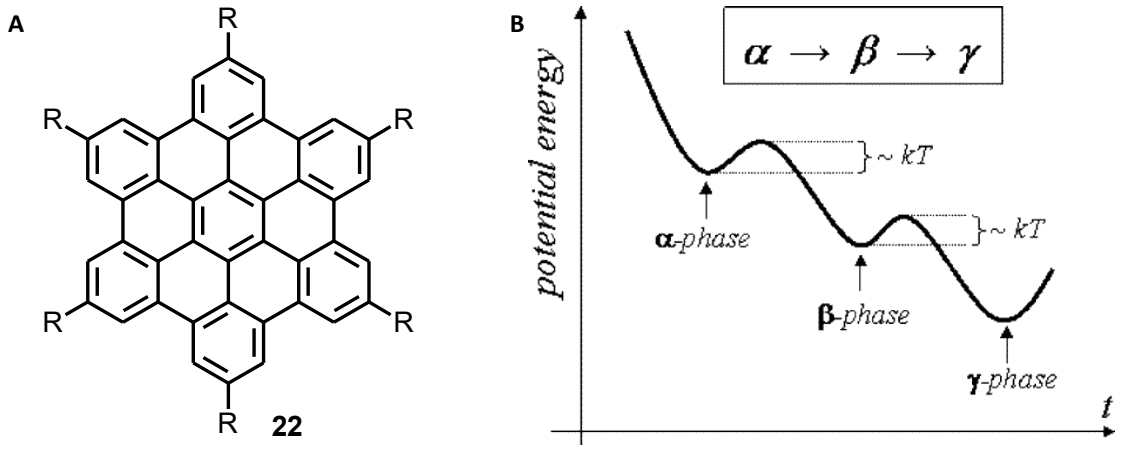

Figure 12. Substituted hexa-*peri*-benzocoronene **22** studied by Piot *et al.* (A). Potential energy diagram showing the time evolution of system of **22** self-assembled on HOPG/*n*-pentacontane/*n*-tetradecane interface. The initially formed *α*-phase spontaneously transforms to the metastable *β*-phase, which after several hours eventually transforms to the thermodynamically stable *γ*-phase. The barrier heights are similar to the system's thermal energy *kT* (B).[67] Reproduced and adapted with permission from the American Chemical Society, copyright 2023.

A nice demonstration of the above principles is a work reported by Piot *et al.*[67] A hexa-*peri*-benzocoronene **22** adsorbed from *n*-tetradecane on the surface of *n*-pentacontane-modified HOPG (Figure 12A). Starting from the initial loosely packed *α*-phase, the system goes through a metastable *β*-phase before it arrives at the densely packed *γ*-phase after several

hours (Figure 12B). As discussed in the previous chapter, the polymorph with the enthalpically most preferred dense packing, maximizing the intermolecular interactions, is formed.

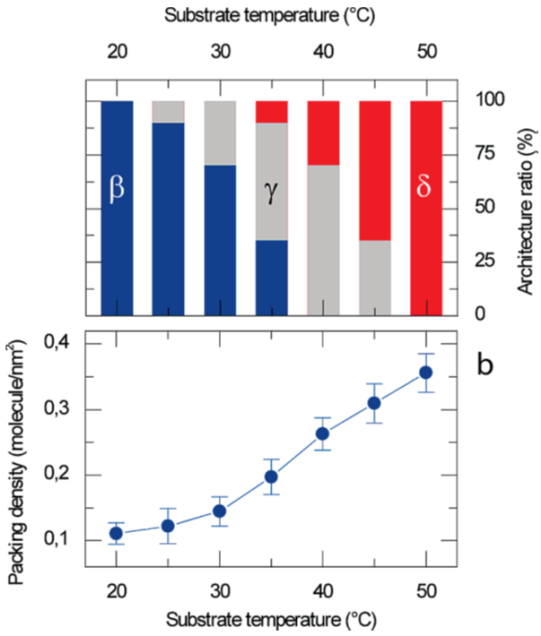

Figure 13. Proportion of different polymorphs of **22** self-assembled on Au(111) as a function of temperature.[66] Reproduced and adapted with permission from the American Chemical Society, copyright 2023.

The progress towards the thermodynamic minimum can be, typically, accelerated by increasing the temperature. Marie *et al*. studied such temperature effects on the same molecule **22**, but this time adsorbed on Au(111) surface, where a higher adsorption enthalpy can be anticipated.[68] The initially observed polymorph spontaneously transformed to a second one at room temperature. When the temperature was subsequently raised, the system transitioned to a third polymorph, before finally arriving at the fourth one at the highest temperature (Figure 13). As the phase transitions were unidirectional, the authors concluded the observed structural evolution is a kinetic effect.

Sometimes, certain polymorph can appear only at a specific concentration as a kinetic form, which is subsequently transformed to more thermodynamically stable structures, as demonstrated by Ahn *et al.* on the case of an amide amphiphile adsorbed on HOPG.[69]

On the microscopic level, the structure of molecular adlayers is strongly influenced by the interplay between the rate of formation of small crystal seeds, defined by the nucleation rate, and the rate of growth from these seeds to larger domains, the growth rate. These parameters are connected to the rate of adsorption of the molecules on the surface, which affects the nucleation rate, and by the rate of their on-surface diffusion which then controls the rate of the monolayer growth. Nucleation rates larger than growth rates typically result in the formation of a large number of small domains. In the opposite case, a small number of large domains are formed.

The situation is even more complex when multicomponent systems are concerned. Sometimes, the growth of mixed domains is preferred,[70] while in other cases single-component domains form. The latter case was demonstrated by Baker *et al.* on a system comprising *n*-tetracontane and 4'-alkyl-4-cyanobiphenyl **23** on HOPG.[71] *n*-Tetracontane, having a large nucleation rate, initially forms vast monolayers which are only occasionally interrupted by domains of **23**. However, since the domains of **23** have a larger growth rate and are thermodynamically more stable, the surface is almost entirely covered by **23** after the period of two days.

Another interesting phenomenon worth mentioning, associated with the domain growth, is the Ostwald's ripening.[72,73] During this process, numerous small domains on a surface

gradually coalesce into the largest possible single domain. This reorganization is driven by the system's tendency to minimize the free energy of the domain boundaries. Molecules at the domain edges are not fully bound, compared to the molecules inside, resulting in their substantially higher adsorption enthalpy. The reduction in the polycrystallinity of the adlayer thus minimizes these energy contributions.

1.3.4. Key Lessons from Molecular Epitaxy

So far, we have treated the molecule-surface interactions without specifically considering the substrate structure. In most cases, molecular self-assembly is studied on periodic lattices, such as HOPG or Au(111). Since the structure of the interface between the organic adlayers and the underlying crystalline surfaces has a large impact on its properties and potential industrial applications, it is important to understand the impact of the substrate structure on the formation of the adsorbate. The relationship between the lattice structure of the substrate and the overlayer (term commonly used for crystalline adlayers in epitaxy related literature) is described by their mode of epitaxy. A very informative review of this subject was provided by Hooks *et al.*,[74] and a few fundamental concepts useful for the further discussion are outlined in the following paragraphs.

The modes of epitaxy are best understood from a geometrical representation of the two interfacing lattices. The mathematical relationship between the crystal lattices of the substrate and the overlayer is described by a linear transformation of the substrate lattice vectors,[†]

$$\begin{pmatrix} \boldsymbol{b}_1 \\ \boldsymbol{b}_2 \end{pmatrix} = \begin{pmatrix} \alpha & \beta \\ \gamma & \delta \end{pmatrix} \begin{pmatrix} \boldsymbol{a}_1 \\ \boldsymbol{a}_2 \end{pmatrix} \qquad (6)$$

where $\boldsymbol{a}_1$, $\boldsymbol{a}_2$, and $\boldsymbol{b}_1$, $\boldsymbol{b}_2$, are the substrate and overlayer lattice vectors, respectively, and the transformation matrix is characteristic of the epitaxial relationship between the two latices. Note that the overlayer lattice vectors $\boldsymbol{b}_i$ are just a linear combination expressed in the basis of the substrate lattice vectors $\boldsymbol{a}_i$. The particular values of the transformation coefficients α, β, γ, and δ then determine the commensurability of the two lattices.

Figure 14A shows *commensurate* registry of the two lattices, which is also often denoted as *point-on-point* (POP) coincidence because every symmetry equivalent point of the overlayer coincides with a symmetry equivalent point of the substrate. The overlayer lattice points lay at the same time on two primitive substrate lattice lines. As a geometrical consequence, the smallest coincident supercell of the overlayer is also coincident with its primitive unit cell. Mathematically, all coefficients in the transformation matrix are small integers.

[†]The relationship between the substrate and the overlayer can also be expressed by Wood's notation. However, it is less general and insufficient for the description of most molecular assemblies.

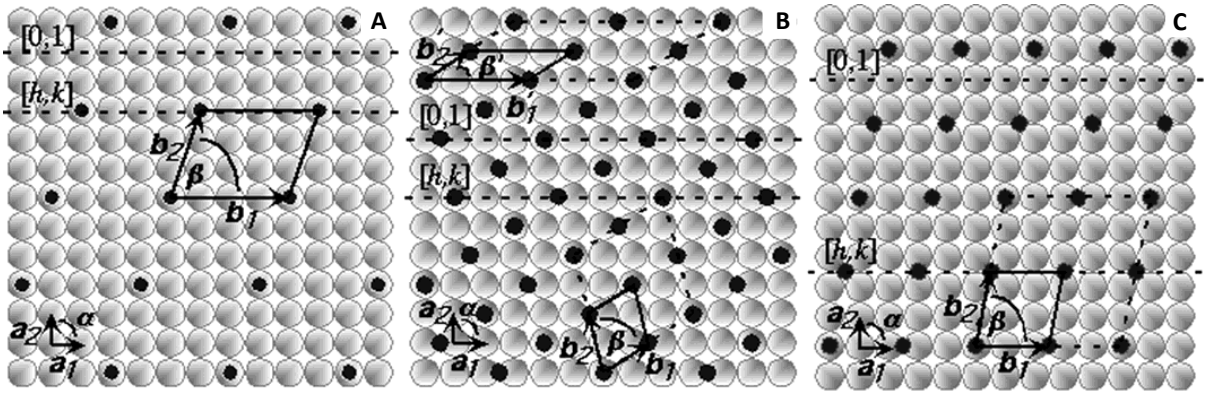

Figure 14. Different epitaxial modes of molecular overlayers on substrate lattice: Commensurism (POP) (A), POL coincidence (B), geometrical coincidence (C). Incommensurism is not shown. Grey balls represent symmetry equivalent points of the substrate, black dots represent symmetry equivalent points of the overlayer. Solid-line rhomboid represents the overlayer primitive cell, the dashed-line rhomboid represents the supercell coinciding with the substrate lattice. Reproduced and adapted with permission from Wiley-VCH Verlag GmbH & Co. KGaA.[74]

For *point-on-line coincidence* (POL), the match between the two lattices can be realized in several ways, each differing in the appearance of the transformation matrix. The overlayer lattice points always lie on one set of primitive substrate lines. In one version, the transformation matrix contains at least two integers confined into one column, all coefficients being rational numbers. Consequently, the overlayer supercell coincident with the substrate lattice is always larger than the overlayer primitive unit cell (Figure 14B). In the second version, the coincident match is realized only along one primitive lattice vector, in the other direction, the overlayer lattice points cannot be matched with the substrate. This is expressed by the transformation matrix containing one column of integers and at least one of the remaining coefficients being irrational. The result of these relations is that the supercell cannot be established because it is infinitely large.

In the case of *geometrical coincidence*, although not all overlayer lattice points lie on the substrate lattice lines, registry between the two lattices can still be achieved. The transformation matrix contains only rational numbers (Figure 14C).

The last case, where epitaxial relationship between the substrate and the overlayer is not present, is described as *incommensurism*. Although both lattices are periodic, there is no possible linear transformation of the substrate lattice vectors, which would define a coincident relationship between the two lattices. This situation can be pictured as a special case of coincidence, with an infinite supercell in both lattice directions.

From an energetic perspective, it is useful to view the resulting structure as a fine balance between the intralayer (intermolecular), E_{intra}, and interlayer (overlayer-surface), E_{inter}, interactions. These interactions and corresponding energies are described by periodic surface and overlayer potentials, whose geometrical registry determines the optimal arrangement of the overlayer on the surface.

Relative proportions of E_{intra} vs E_{inter} can be used as a measure of epitaxy. In the case of commensurism, where E_{inter} is much larger than E_{intra}, the interactions of the adsorbates with the substrate are so strong in comparison with their mutual interactions that the overlayer

geometry is fully controlled by the substrate lattice. Such epitaxial arrangements are often encountered in atomic, or small molecule overlayers, where their small size and relatively strong adsorption allow achieving the optimum arrangement on the surface. Commensurism is consequently usually the energetically most favorable epitaxial mode.

Most organic molecules, however, cannot satisfy the above conditions for commensurism, because of moderate values of E_{inter}, and large size of their overlayer unit cells. In the case, where E_{inter} is about the same as E_{intra}, coincident epitaxy is observed, where the molecules often adjust to the optimal binding positions of the substrate while still mostly retaining the native overlayer structure. When the E_{inter} is lower than E_{intra}, the geometry of the native overlayer lattice is formed, where the coincidence is achieved by optimal position of the whole overlayer without distorting its internal geometry.

Lastly, in the extreme case, where E_{inter} is substantially lower than E_{intra}, the geometry of the overlayer lattice is fully dictated by intermolecular interactions regardless of the substrate and incommensurate overlayer is formed.

It is worth noting that even large molecules are often found to assemble epitaxially on the substrate, because achieving the lattice registry is a large energetic benefit and the elasticity of organic overlayers allows certain adjustment to the optimal adsorption geometry. In experiment, the epitaxial arrangement can be recognized by orientation of the adsorbates to the substrate. Moreover, an indicator, that the registry of the overlayer lattice with the substrate cannot be realized on small scale, are Moiré patterns, often observed on domains of large molecules of low symmetry.[74]

1.3.5. Scanning Tunneling Microscopy

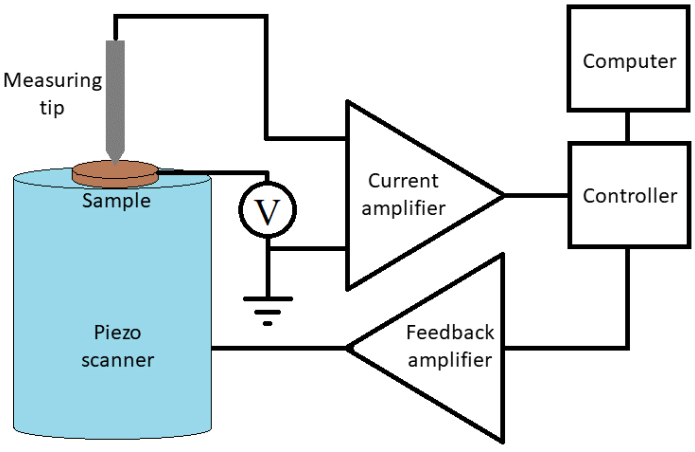

Figure 15. A schematic representation of STM. One of numerous possible technical implementations is shown. The tunneling current flows between the tip (gray) and a biased sample (brown).

In STM, the measuring feedback is realized by introducing a bias voltage between a conductive sample and, ideally, an atomically sharp conductive tip (Figure 15). By placing the tip very close to the sample, usually not more than a few nanometers, a minuscule tunneling current starts to flow between the tip and the sample surface, which is amplified and further processed. The exact description of the tunneling current as a function of the measuring parameters is very challenging, and in practice, only rather simplified models are used. But generally, the magnitude of the tunneling current depends on two parameters κ and x in equation (7).[75] κ is related to the tunneling energy barrier comprising of the average work functions of the tip and sample surfaces, x is a distance between the tip apex and the surface, and V is the tip-

sample bias voltage. The exponential decay of the tunneling current with *x* is the main reason for the extraordinary spatial resolution of STM.

$$I \sim \frac{kV}{x} e^{-2\kappa x} \quad (7)$$

An important factor influencing the STM image resolution is the condition of the tip. While electrochemical etching can produce very sharp tips with excellent aspect ratios, the production method is somewhat laborious.[76] It is therefore more common to use tips mechanically cut from $Pt_{0.8}Ir_{0.2}$ alloy.[77] Although such procedure is less reproducible, it does not require any special equipment besides a pair of sharp scissors. One of five thus prepared tips usually gives acceptable resolution. Additionally, a blunt tip can be reconditioned during the measurement by applying short voltage pulses at ca 2 - 8 V, which can provide additional improvement in the resolution.[78,79]

Naturally, the values of the tunneling parameters have a large impact on the image quality. With electrically conducting solid surfaces, currents up to several nA are allowed, but for imaging weakly adsorbed molecular assemblies, much lower currents, down to a few pA, must be used to prevent a destruction of the adsorbates. Similarly, the voltage bias has a large effect on the material contrast. Again, good conductors can be imaged by using voltages as low as a few mV, when the tip is brought very close to the surface. Poorly conducting adsorbates, on the other hand, require voltages sometimes over 1 V. This is not only necessary to drive a sufficient current through a high resistance material but also to increase the tip-sample distance and preserve the delicate surface structures. However, the upper voltage limit in the ambient conditions is around 1.5 – 2 V, where the tip and the surface can be damaged by ionization caused by strong electric fields or electrochemical reactions.[80] The polarity of the bias can also influence the contrast and often the negative pole is connected to the sample.[81]

A method particularly suitable for the study of self-assembly is to cover the imaged surface with a suitable liquid, which can partially counteract the negative effects of the ambient atmosphere. The imaging is then performed on the surface/liquid interface, instead of the air/surface interface. The success of this method is documented by countless publications, some of which are cited throughout this Thesis, often showing adlayers with submolecular resolution. One of the important benefits of the added liquid is probably its ability to damp mechanical and acoustic vibrations of the tip which otherwise substantially lower the attainable resolution. The liquid also limits diffusion of contaminants towards the surface and, consequently, helps to keep the surface clean for a limited period. Moreover, the liquid serves as a reservoir of the adsorbing material and plays an important role in the dynamic equilibrium between the adsorbed and dissolved molecules. The typical liquids used for such measurements are weakly adsorbing organic molecules with low volatility such as *n*-octanoic acid (or other long chain alkanoic acids),[82] 1-phenyloctane, TCB, or even simple long chain alkanes.[83]

Certain limitations of the ambient STM are related to the interaction of the sample and tip with the surroundings and difficulty to perform the measurement at low temperatures. As

a result, only chemically stable materials with high adhesion to the surface can be successfully imaged. Thus, the imaging is typically performed on surfaces such as HOPG,[84] graphene,[85] Au,[68] Ag,[86] which are not prone to oxidation in air. Even these low-interacting surfaces, however, can weakly adsorb undesired contaminants and usually must be freshly prepared.

In this context, Tahara *et al.* investigated the effects of substrate material and the decoration of the periphery of macrocycle **24** with various alkyl ester chains on the ordering in self-assembled monolayers (Figure 16).[78] On HOPG, where a good registry between the long alkyl chains and substrate can be achieved, the packing of the alkyl chains was oriented along the HOPG crystal axes. The different length of the alkyl chains resulted in different packings, and, in the case of butyl ester, the molecules were stabilized even by intermolecular hydrogen bonds. As expected, molecule **24c** without any substitution did not form stable monolayers. In contrast, on Au(111) surfaces the alkyl chains adsorbed only weakly due to the mismatch between the gold lattice and the geometry of the alkyl chains but the ordering of the macrocyclic core was clearly incident with the gold lattice, due to the strong interaction of the π-conjugated macrocycle core and the gold surface.

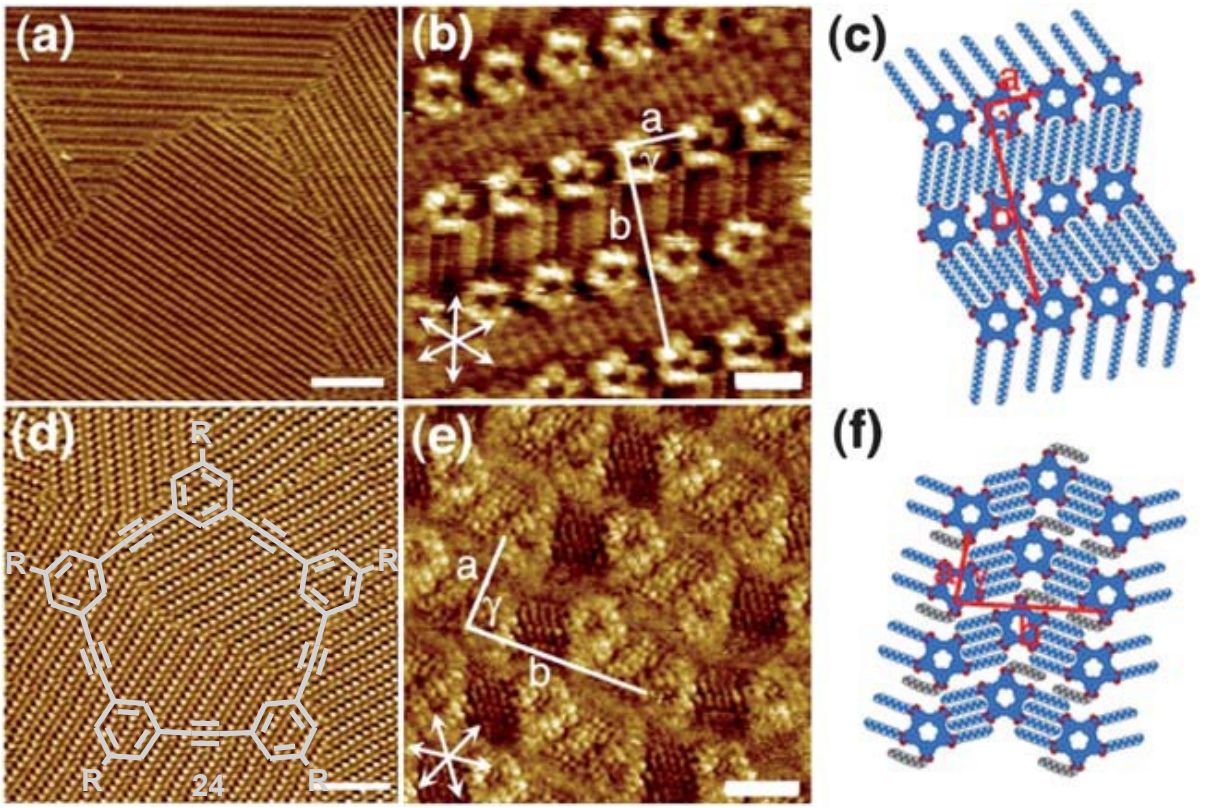

Figure 16. Self-assembly of macrocycle **24** on HOPG/TCB interface imaged by STM. **24a** with R = $COOC_6H_{33}$, large scale image (A), high-resolution image with details of the macrocycle and alkyl chains (B), proposed pacing model (C); **24b** with R = $COOC_{10}H_{21}$, large scale image (D), high-resolution image with details of the macrocycle and alkyl chains (E), proposed pacing model (F).[78] HOPG main axes are represented by white asterisk. Reproduced and adapted with permission from Royal Society of Chemistry.

It should be noted that for successful imaging, the molecules must be efficiently immobilized on the surface. The most common approach to accomplish this is to decorate the molecule with long alkyl chains that stabilize the molecules by Van der Waals interactions with the substrate lattice as well as by mutual interdigitation of the chains.[84] Sometimes,

covalent bonding to the surface can be used, for instance, in the case of thiol substituted molecules on gold surfaces.[87] An elegant approach is also to use an already present porous adlayer as a host for the guest molecules to be imaged.[88] It must be borne in mind, however, that the presence of the alkyl chains or other external functionalities does not only improve the adsorption, but it can have a profound effect on the molecular packing.[89,90] The chain substituents thus represent an integral part of the adsorbing molecule.

The STM imaging on the solid/liquid interface brings a unique opportunity to follow sufficiently slow dynamical processes. For example, Shen *et al.* showed that photoisomerization of macrocycles **25** containing photosensitive azobenzene units leads to extensive changes in the adlayer structure (Figure 17).[91] When UV light was shone on the surface, the macrocycles, embedded within a 1,3,5-tris(10-carboxydecyloxy)benzene **26** matrix, adopted many different configurations which could be resolved by STM. Figure 17 shows an example of a partially disordered domain, consisting of rectangular (*t*,*t*,*t*,*t*)-**25** and triangular (*t*,*t*,*t*,*c*)-**25** embedded in a matrix of **26**.

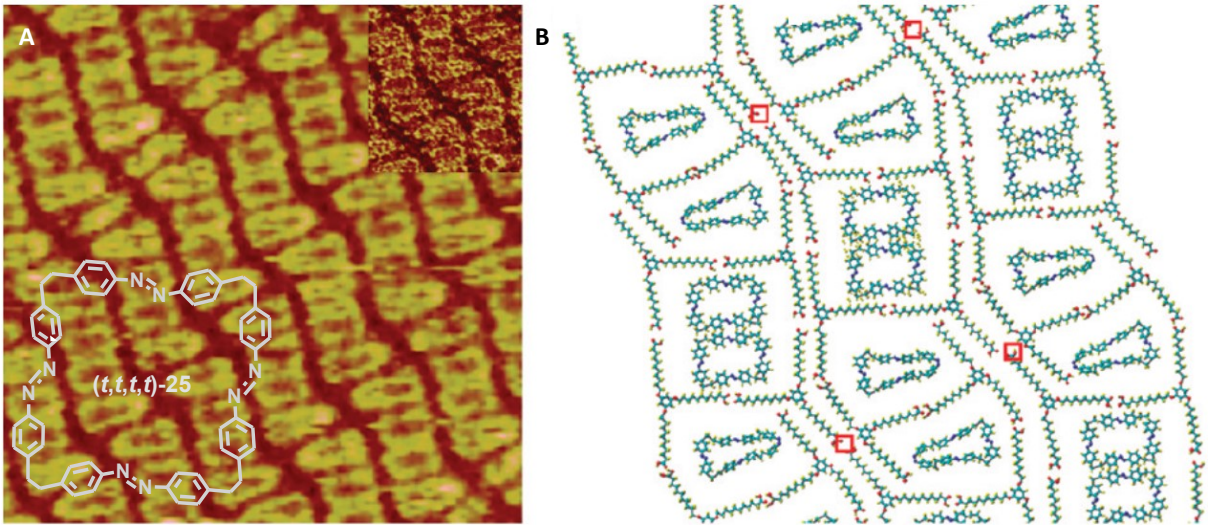

Figure 17. Self-assembly of photosensitive macrocycle **25** entrapped within a porous matrix of **26** imaged by STM on HOPG/*n*-heptanoic acid interface. Domain of rectangular cycles (*t*,*t*,*t*,*t*)-**25** and triangular cycles (*t*,*t*,*t*,*c*)-**25** in matrix of **26**. STM image (A) and a corresponding packing model (B).[91] Reproduced and adapted with permission from the American Chemical Society.

STM can be used not only as a mere "magnifying glass", but it can be efficiently employed for structural elucidation of large molecules. One of the challenges associated with the investigation of these molecules is their structural analysis. Often, crystals for X-ray analysis cannot be obtained due to the presence of numerous solubilizing groups. Likewise, NMR spectra are commonly complicated by overlapping signals due to many similar structural units and a high conformational freedom. May *et al.* showed how STM can help to overcome such characterization issues.[92] Self-assembled layers of a giant spoked wheel **27** were imaged on HOPG/*n*-octanoic acid interface in high resolution (Figure 18). The STM image clearly shows the molecular perimeter, including its internal parts. The measurement was also able to

distinguish between the cyclized product **27** and its open precursor **28** (Figures 18A and B vs 18C), highlighting the analytical power of STM.

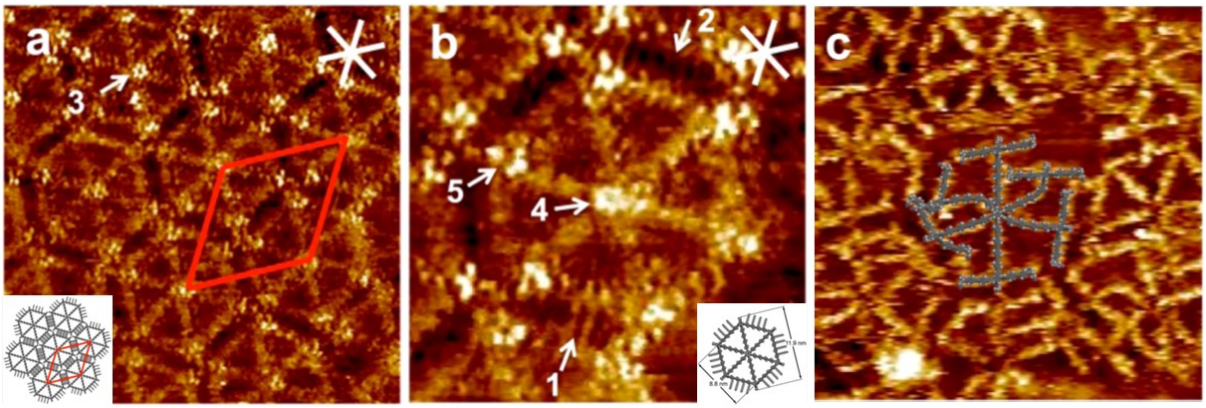

Figure 18. STM image of the giant spoked wheels **27** assembled on HOPG/*n*-octanoic acid interface. Inset shows packing model (A), High resolution STM image of **27** and a corresponding model (B), STM image of uncyclized precursor **28** overlayed with a molecular model (C). HOPG main axes are represented by white asterisk. Reproduced and adapted with permission from the American Chemical Society.[92]

Lastly, STM on solid/liquid interface can be used not only to analyze products of classical synthesis, as in the previous examples, but it can follow macrocycles formed directly on the surface. Apart from the two examples presented in Chapter 1.1. (Figure 3), investigations concerning the on-surface synthesis of extensive networks of imine polymers was reported by Yu *et al.*[93,94] By choice of different reaction conditions such as molar ratios, concentration, and temperature, various structures were obtained. At low concentration and favorable molar ratio, porous honeycomb networks formed while at high concentrations, densely packed linear chains prevailed. By a careful choice of suitable building blocks, the size of the macrocyclic pores could be controlled, with pore sizes up to 5.2 nm. Moreover, the dynamic equilibrium between the surface and solution phase was highlighted by a facile reconstruction of the networks when an amine building block with a higher adsorption enthalpy was applied to the preexisting networks built of diamines with lower surface affinity.

1.3.6. Atomic Force Microscopy

The control feedback of AFM is based on measuring tip-sample force instead of tunneling current (Figure 19). Although the relationship between the force, the parameters of the tip, and the measured surface is even more complex than in the case of STM, AFM is substantially more universal analytical tool because there is no need for a conductive sample. The technical implementation of AFM is realized in the following way: The probing tip is placed at the end of a pliable cantilever which is scanned above the surface by the same type of piezoceramic scanner as in other scanning probe microscopy instruments. The attractive or repulsive force between the tip and the surface is projected into a mechanical deformation of the cantilever, whose top side is equipped with a reflective coating. A laser beam is reflected from the coating and aimed at a quadrant photodiode which sends the feedback electrical signal into

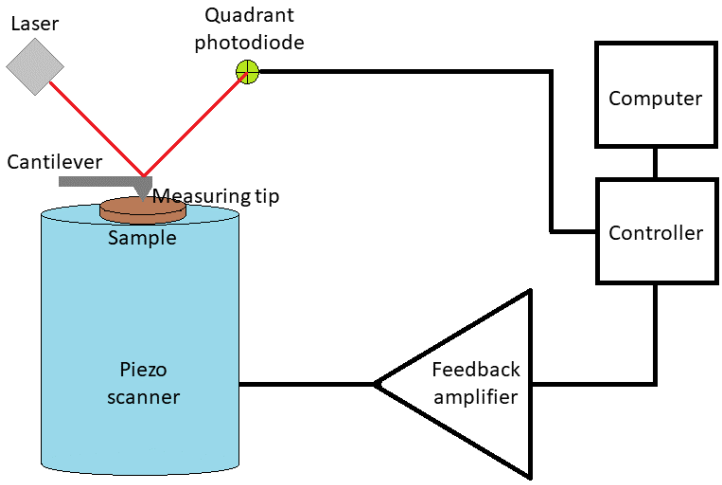

Figure 19. A schematic representation of AFM. Red line shows a laser beam produced by a laser diode, reflected from a cantilever, and arriving at a quadrant photodiode producing the feedback signal.

the processing electronics. This technical realization ensures a high resistance to electrical and mechanical noise and experimental simplicity of the method. Even if ambient AFM has a substantially lower resolution than STM,[‡] the above qualities has earned it a prominent place among currently used ambient SPM techniques.

AFM offers many different measuring modes with applications in a wide range of technical fields. To name just a few, the initially developed contact mode[59] was soon complemented by tapping mode, characteristic of only an intermittent tip-sample contacts,[95] PeakForce QNM allowing a simultaneous measurement of different mechanical properties of the surface,[96] or electric[97,98] and magnetic[99] force modes allowing the measurement of the surface potential or local magnetization.

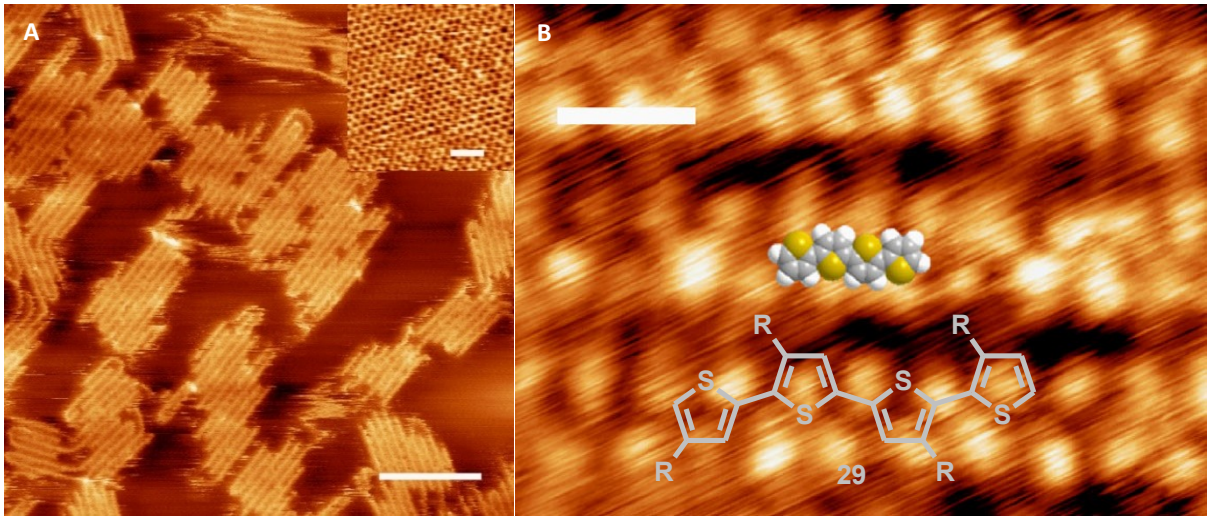

Figure 20. Thiophene oligomers **29** self-assembled on hexagonal boron nitride, imaged by high-resolution tapping mode AFM in air (A). Submolecular resolution showing individual thiophene units (B). Reproduced and adapted with permission from Springer-Nature.[101]

Despite its many strengths, a lower resolution and difficulty to scan surfaces covered with liquids, make ambient AFM less convenient for investigation of molecules and their assemblies. Scanning on the surface/liquid interface cannot be realized in the same way as in STM, because the instrument usually misidentifies the liquid surface for a solid. Moreover,

[‡]Interestingly, the situation is opposite in UHV where AFM tips modified with molecules of Xe or molecule of CO routinely provide impressive submolecular resolution.[62]

the solvent rises along the cantilever and contaminates the holder due to capillary forces. Although liquid cells specially designed for such measurements do exist, they are usually not very resistant to aggressive solvents and a large amount of liquid must be used. In practice, AFM is therefore more suitable for scanning dry films. The studied molecules must be rather large and preferably be a part of stable surface assemblies.

One of the first works demonstrating the use of ambient AFM to obtain molecular resolution was reported by Klinov *et al.*,[100] where the authors used the tapping mode and an ultra-sharp Si probe modified with carbon spikes for imaging of 2D crystals based on 2,4-hexadienylenebis(*p*-fluorobenzenesulfonate).

Substantial progress was later made by Korolkov *et al.*, who developed a tapping mode AFM methodology based on excitation of low-amplitude higher eigenmodes of the cantilever which allowed imaging of various polymeric structures **29** with submolecular resolution, as recently presented in several papers (Figure 20).[101]

A nice example of using a repulsive tapping AC mode AFM with molecular resolution was given by Summerfield *et al.* showing large porphyrin nanorings **30** assembled on HOPG (Figure a21).[10] The nanorings formed hexagonal lattices with varying degree of deformation (frustration) and appeared as bright spots without any internal structure, as opposed by the highly resolved images provided by STM.

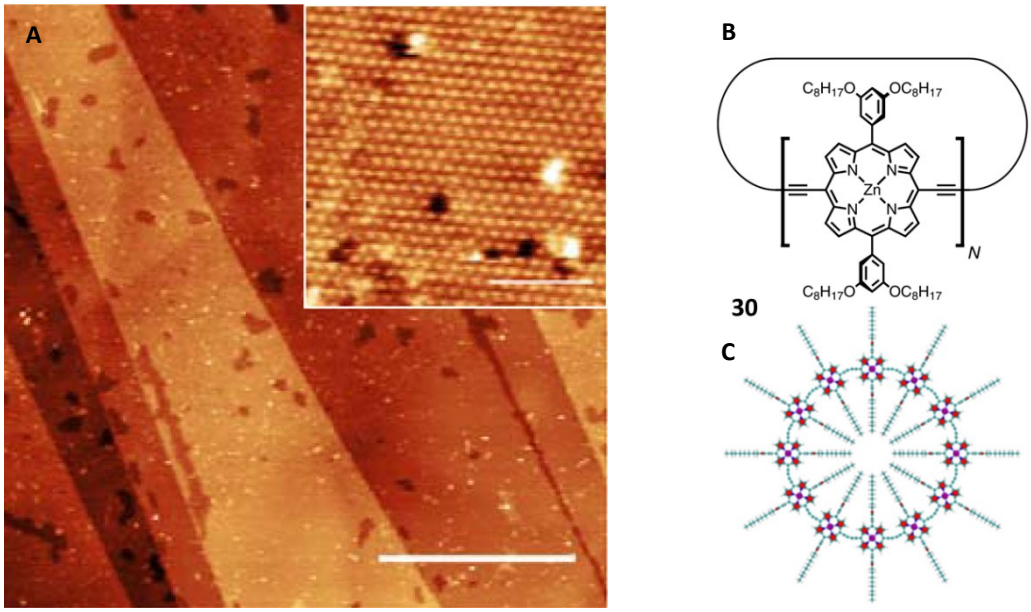

Figure 21. Dodecamer porphyrin nanorings **30** assembled on HOPG in air, imaged with molecular resolution by repulsive tapping AC mode AFM. Inset shows individual molecules in high resolution (A). General formula of porphyrin nanorings **30** (B). Molecular model of dodecamer **30** (C). Reproduced and adapted with permission from Springer-Nature.[10]

Finally, as shown in this Thesis (see Chapter 3.7.1.), we have successfully used the PeakForce AFM mode to image delicate assemblies of helicene-based macrocycles with molecular, and in some cases, submolecular resolution.[1]

2. Motivation and Aims of the Project

Since the research in our laboratory revolves around helicenes and related π-conjugated compounds, it was only natural to incorporate these screw-shaped molecules into a macrocyclic structure. Combining different chiral and π-conjugated elements in a single molecule opens a way to tune its overall 3D shape, symmetry and bring together the unusual qualities of both conjugated macrocycles and helicenes. It was presumed that such a combination could potentially deliver materials with unusual chiroptical, electronic, and even spintronic properties.

With respect to the ideas above, the project summarized in this Thesis builds upon the author's previous synthetic attempts to prepare helicene-based AVMs **31** and **32** (Figures 22 and 23).[102,103] What was initially viewed as a routine synthetic task to provide the desired study material, soon turned into a laborious endeavor. Although it has been previously known that AVMs show a high degree of aggregation (see Chapter 1.1.), earlier analogs of **31**/**32** turned out to be exceptionally insoluble. The possibility to solubilize **31**/**32** was crucial for its successful structural characterization and further experiments and it was therefore necessary to develop robust solubilization strategy. Since the standard approach to decorate the molecular scaffold with solubilizing groups based on long chains failed, an alternative strategy had to be developed. Using trityl group, eventually discovered within this work, turned out not only to provide excellent solubility, but also gave macrocycles **31**/**32** a unique self-assembly behavior.

Thus, with the soluble compounds **31**/**32** in hands, the following questions could be addressed:

- *How does the chirality of their constituent building blocks influence the chirality of the entire macrocycles **31/32**?*
- *Can molecules **31/32** be studied with SPM on surfaces despite its anticipated 3D shape?*
- *How do **31/32** interact with surfaces? Can it assemble into stable surface aggregates?*
- *Does the chirality of **31/32** influence their self-assembly on surfaces?*
- *What is the "aromaticity" status of the molecules and how does it influence their properties?*
- *Can surfaces influence the "aromaticity" state of the adsorbates?*

3. Results and Discussion

3.1.Structure of the Target Macrocycles

The target macrocycles **31** and **32** consist of dibenzo[5]helicene units connected by conformationally flexible stilbene linkers. Additionally, the central cycle is decorated with bulky trityl groups which were primarily introduced to increase its solubility. Macrocycles with three or four helicene units were studied in this work, with the main focus on the relatively easily isolable trimer (Figures 22 and 23).

Regarding stereochemistry, trimer **31** contains three helical chiral elements which, in principle, give four possible stereoisomers, namely (*M*,*M*,*M*)-**31**/(*P*,*P*,*P*)-**31** enantiomeric pair, and (*M*,*M*,*P*)-**31**/(*M*,*P*,*P*)-**31** enantiomeric pair (Figure 24). The trityl propeller is also chiral, adding six more chiral elements, but the inversion barrier between the possible propeller configurations is so low that they can be safely regarded as low barrier conformers.[104]

In the following text, (*M**,*M**,*M**)-**31** will be used for denoting (+)-(*M*,*M*,*M*)-**31**/(-)-(*P*,*P*,*P*)-**31**, when a particular enantiomeric pair is discussed but chirality is not relevant. Similarly, (*M**,*M**,*P**)-**31** will be used to denote the (+)-(*M*,*M*,*P*)-**31**/(-)-(*M*,*P*,*P*)-**31** enantiomeric pair. When absolute configuration is discussed, full assignment will be used namely, (+)-(*M*,*M*,*M*)-**31**, (-)-(*P*,*P*,*P*)-**31,** (+)-(*M*,*M*,*P*)-**31**, and (-)-(*M*,*P*,*P*)-**31**. When stereochemistry is totally irrelevant, only number **31** will be used.

The stereochemistry of tetramer **32** is even more complex, as the four helical chiral elements give rise to two chiral (*M*,*M*,*M*,*M*)/(*P*,*P*,*P*,*P*)-**32** (denoted as (*M**,*M**,*M**,*M**)-**32**) and (*M*,*M*,*M*,*P*)/(*M*,*P*,*P*,*P*)-**32** (denoted as (*M**,*M**,*M**,*P**)-**32**) enantiomeric pairs, and (*M*,*M*,*P*,*P*)-**32** and (*M*,*P*,*M*,*P*)-**32** achiral stereoisomers.

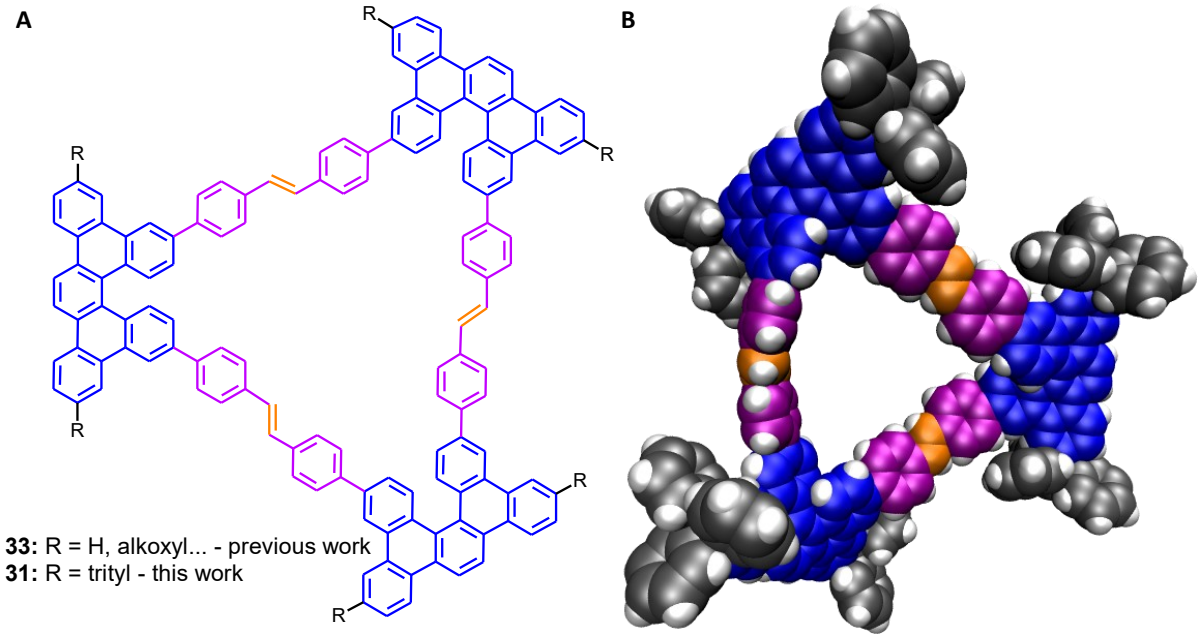

Figure 22. Rigid dibenzo[5]helicene units (blue) connected with flexible stilbene linkers (purple-orange) to form trimer **31**. The molecule is decorated with bulky trityl groups (black) for better solubility (A). 3D model of trimer **31** (B). (*P*,*P*,*P*)-**31** stereoisomers are shown.

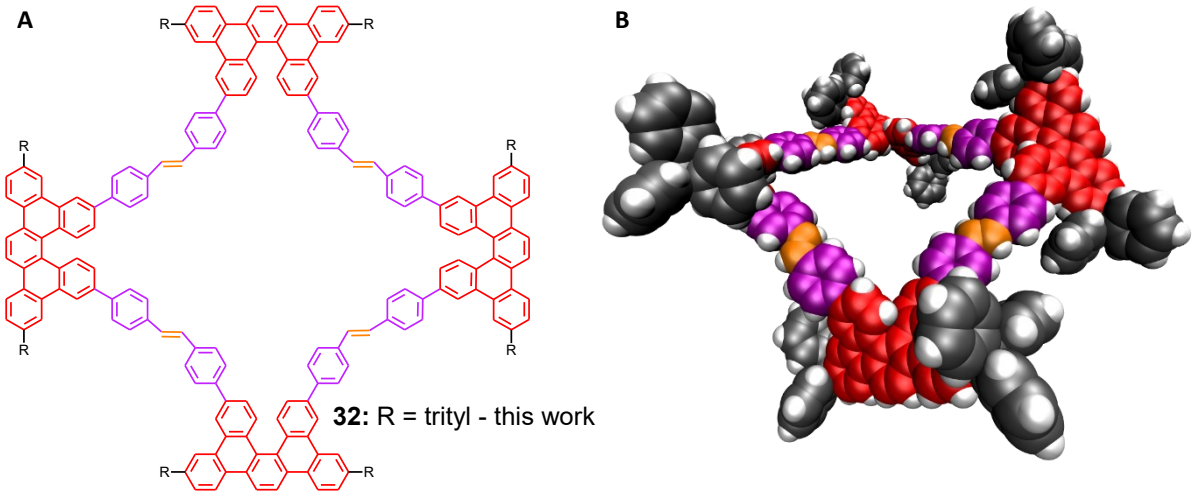

Figure 23. Tetramer **32** (A) and its corresponding 3D model (B). (*M*,*M*,*M*,*M*)-**32** stereoisomers are shown.

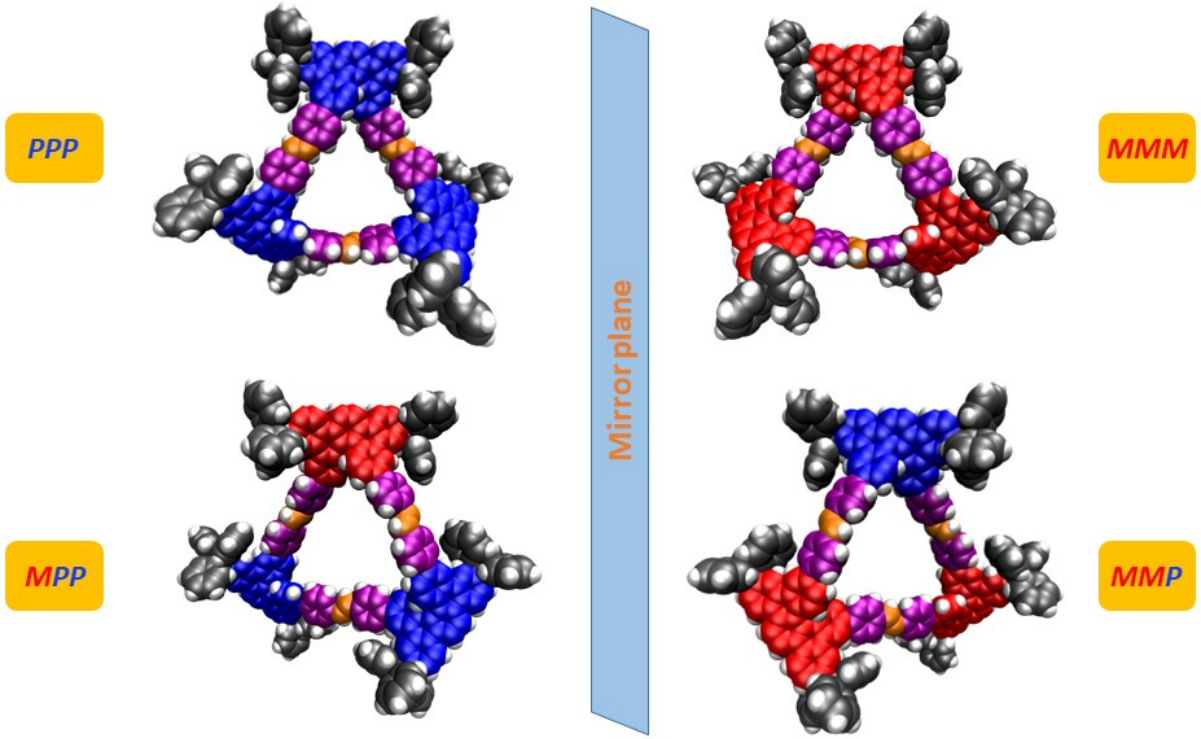

Figure 24. 3D models of the four possible stereoisomers of trimer **31**.

3.2.Synthesis of the Target Macrocycles

Although the synthesis of macrocycles **31** and **32** mostly followed in the footsteps of the previous experiments, it was no less challenging. The former solubilization strategies are not discussed herein because they were not studied as part of this Ph.D. project and do not provide conceptually important findings beyond technical details. Thus, the synthesis and the related discussion focus on the trityl solubilized molecules. Other synthetic strategies explored in parallel to those presented in this work, which turned out to be blind alleys, are not discussed either to limit the discussion to a reasonable length.

3.2.1. Precursors

Following a methodology for the synthesis of dibenzohelicenes developed by Jančařík *et al.*,[105] the preparation of monomer **43** (see Scheme 3) started with the Friedel-Craft tritylation of **34** to afford tritylated aniline **35** in almost quantitative yield (Scheme 1). Aniline **35** was subsequently converted to iodide **36** by diazotization, followed by Sonogashira coupling to provide alkyne **37**, both in good yields. Unlike the previous steps, the final lithiation-borylation of **37** was challenging due to its low reactivity, most likely caused by the electronic and, especially, steric effects of the trityl group. However, the use of *t*-BuLi and a high concentration, followed by the reaction with triisopropyl borate, afforded the desired boronic acid **38** in 84% yield.

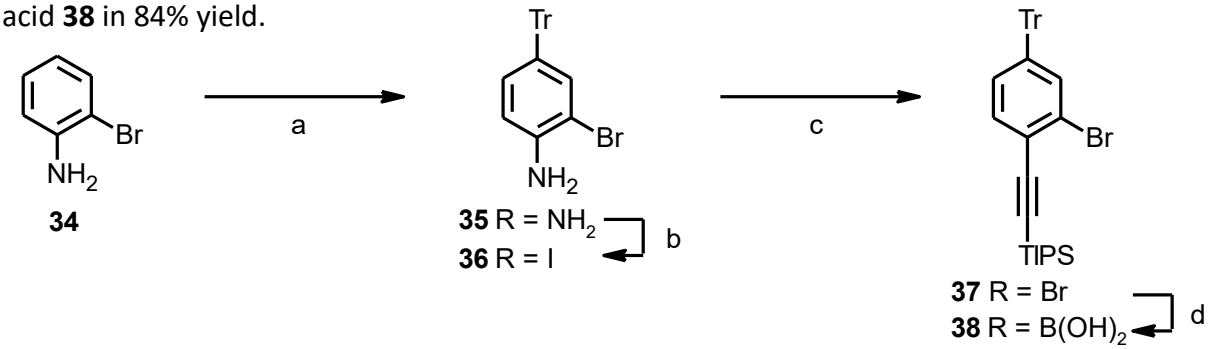

Scheme 1. Preparation of boronic acid **38**. a) 1. TrOH (0.71 equiv.), HCl (1.1 equiv.), AcOH, reflux, 16 h; 2. KOH (9.0 equiv.), EtOH-H_2O (3:1), reflux, 1.5 h, 98%; b) 1. $NaNO_2$ (1.5 equiv.), HCl (aq.), acetone, 0 °C, 1 h; 2. KI (2.0 equiv.), 0 °C to rt, then reflux for 2h, 93%; c) TIPSA (1.1 equiv.), $Pd(PPh_3)_2Cl_2$ (5 mol%), CuI (10 mol%), DIPA-toluene (1:1.4), 0 °C to rt, overnight, 80%; d) 1. *t*-BuLi (2.0 equiv.), THF, -78 °C, 1 h; 2. B(O-*i*-Pr)$_3$ (2.0 equiv.), 0 °C to rt, 16 h, 3. HCl (aq.), 84%.

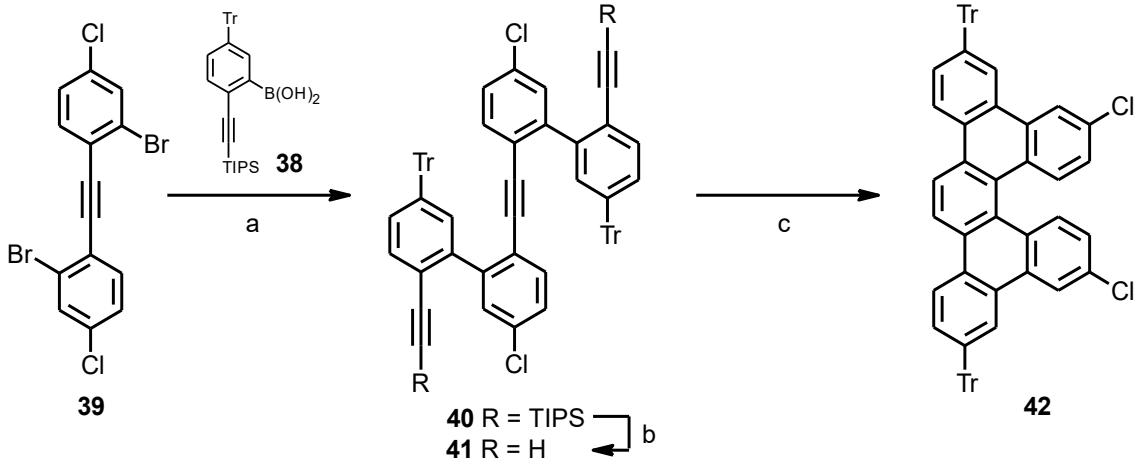

Scheme 2. Preparation of helicene **42**. a) **38** (3.0 equiv.), K_2CO_3 (4.0 equiv.), $Pd(PPh_3)_2Cl_2$ (10 mol%), toluene-*n*-PrOH-H_2O (4.2:4.2:1), reflux, 3 h, 98%; b) TBAF·$3H_2O$ (4.0 equiv.), MeOH (2.0 equiv.), THF, rt, 1 h, 83%; c) $CpCo(CO)_2$ (1.0 equiv.), THF-toluene (3.2:1), 250 °C, 8 min, 85%.

The obtained boronic acid **38** was coupled with a previously prepared diarylacetylene **39**[106] in a Suzuki-Miyaura reaction. Triyne **40**, obtained in 98% yield, was then, after a routine removal of the TIPS groups affording **41**, submitted to the cobalt catalyzed cycloisomerization in a flow reactor to afford dichlorodibenzo[5]helicene **42** in 85% yield (Scheme 2).

To complete the synthesis of monomer **43**, helicene **42** was finally arylated in the Suzuki-Myiaura reaction using a commercially available boronic acid (Scheme 3). The reaction was accompanied by an extensive styrene-type polymerization which substantially decreased the reaction yield. Contrary to expectation, the addition of a small amount of 4-*t*-Bu-catechol as a polymerization inhibitor did not appreciably suppress the unwanted polymerization. Moreover, a marked decrease in solubility with the introduction of the styrene moiety was observed, which complicated the isolation of **43** using standard chromatography. Therefore, the reaction mixture was purified by filtration through a short column of silica gel column followed by gel permeation chromatography in dichloromethane.

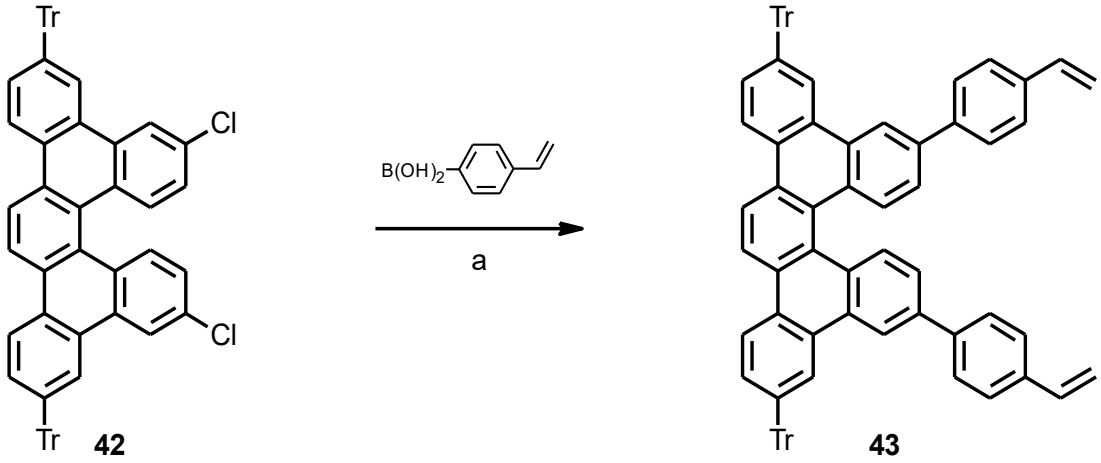

Scheme 3. Preparation of vinyl-substituted helicene **43**. a) 4-vinylphenylboronic acid (4.0 equiv.), XPhos Pd G2 (10 mol%), K_3PO_4 (0.5M aq., 4.0 equiv.), THF, 100 °C, 3 h, 77%.

3.2.2. Final Macrocyclization

The synthesis of **31** and **32** relies on creating the stilbene linkers which connect the helicene moieties (Figure 22). From many synthetic options, olefin metathesis based macrocyclization was chosen for its robustness and reversibility, allowing the formation of even moderately strained molecules.[107] Zhang *et al.* showed that reversibility of alkyne metathesis can be harnessed to prepare macrocycles of a desired size.[12,108] When energetically disfavored macrocycles are formed during the course of such macrocyclization, they are later transformed to the thermodynamically preferred products.[109,110] Similar results were found in the case of AVMs as reported by Liu *et al.,* showing a highly reversible nature of olefin metathesis in the formation of these molecules.[21]

Inspired by the aforementioned works, olefin **43** was submitted to the metathesis catalyzed by Grubbs 2nd generation catalyst in high-boiling TCB under reduced pressure. This approach, commonly employed in the field, facilitates the removal of the formed ethylene

gas, and thus supports the oligomerization reaction pathway. Moreover, high-dilution conditions were used to favor the formation of small macrocycles over linear oligomers.

Shortly after the start of the metathesis, the color of the reaction mixture darkened, and the fluorescence of the solution shifted from faint purple to intense blue (assessed by a naked eye and a UV lamp). This change in visual appearance served as a convenient indication of the formation of larger π-conjugated oligomers.

Moreover, no precipitate was observed during the reaction which was in stark contrast to the metathesis of previously studied molecules decorated with solubilizing groups based on long alkyl or alkoxy chains. This demonstrates a substantial solubilization capacity of the trityl groups, efficiently limiting the π-π stacking between molecules **31** or other oligomers.

The reaction progress was monitored by using analytical gel permeation chromatography (GPC) and MALDI mass spectrometry. Despite the successful solubilization, using the 2nd generation Grubbs catalyst led to only a moderate conversion of monomer **43**. Similar results were obtained with the 2nd generation Hoveyda-Grubbs catalyst. It was anticipated that the catalyst would be deactivated before a significant conversion could be achieved. To tackle this problem, an exceptionally active Piers 2nd generation catalyst **44** was used (Scheme 4).[111] The high activity of **44** can be rationalized by the fact that, unlike its predecessors, **44** is a true catalyst (in contrast to a pre-catalyst such as the Grubbs catalysts) without a stabilizing phosphine ligand, which can immediately enter the catalytic cycle even at a very low temperature.[112]

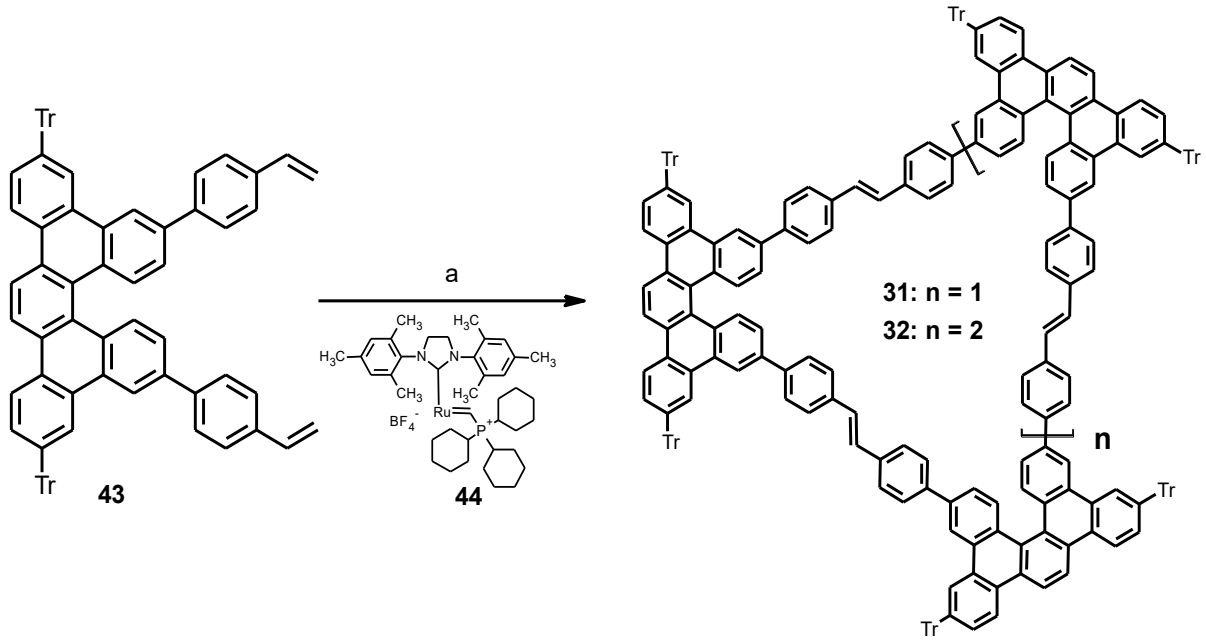

Scheme 4. Final macrocyclization providing **31** and **32**: a) Piers 2nd gen. catalyst (20 mol%), 1,2,4-trichlorobenzene, vacuum, 50 °C, overnight, 33% of trimer **31**, 22% of tetramer **32**.

Indeed, when **43** was submitted to the metathesis using 20 mol% of the Piers 2nd generation catalyst at 50 °C in TCB and reduced pressure, the observed conversion of **43** was notably higher. Nonetheless, a further increase in the catalyst loading or reaction temperature did not change the conversion anymore. However, when the reaction mixture

was, by accident, left to slowly evaporate to dryness, the subsequent GPC and MALDI MS analysis showed a practically total absence of the starting monomer **43**, along with several new peaks which were later attributed to the cyclic trimer **31**, tetramer **32**, and higher oligomers (Figure 25).

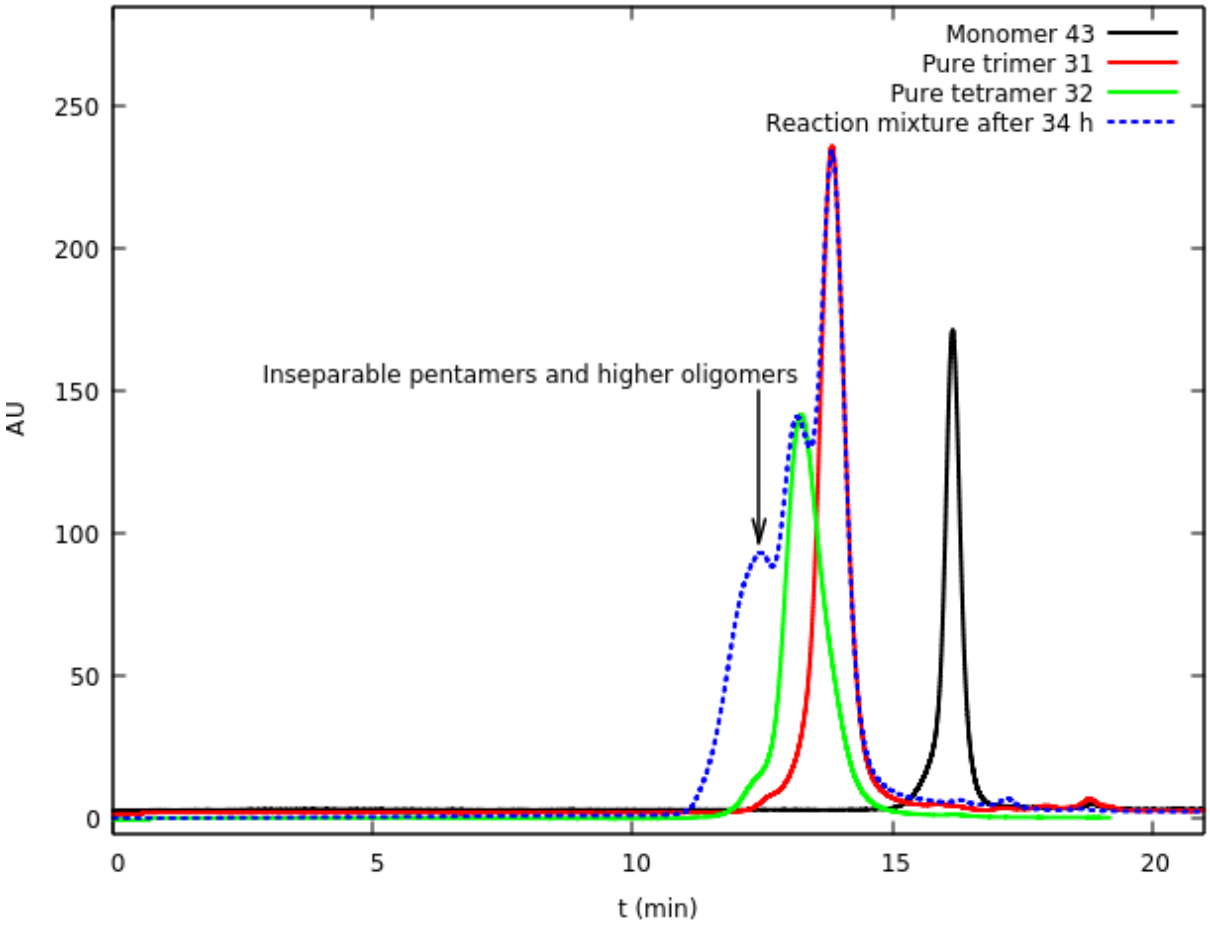

Figure 25. Gel permeation chromatogram of the reaction mixture after macrocyclization of racemic **43** compared with chromatograms of pure **31**, **32**, and **43**. The separation was performed on TSK GEL G2000HHR (7.8 mm ID × 300 mm, 5 µm) and Eurogel SEC 100, HF352 (7.8 mm ID × 300 mm, 5 µm) analytical GPC columns connected in series, dichloromethane as eluent (flow rate of 1 mL·min^{-1}).

This result can be interpreted in the following way: When the solvent volume is constant, the conversion of monomer **43** to a corresponding dimer leads to a two-fold drop in the molar concentration of the reacting molecules, markedly suppressing the reaction rate. Conversion of the dimer to a trimer decreases the reaction rate even further. If a low activity catalyst is used, it is deactivated before a substantial conversion can be achieved. With the Piers 2nd generation catalyst, the reaction can proceed at a low concentration with a sufficient rate. Additionally, when the reaction solvent is slowly removed during the course of the reaction, it can compensate for the decrease in concentration caused by the oligomerization process and thus keep the reaction rate reasonably high.

This explanation was further supported by performing the reaction at initially low concentration of **43**, leading to a very low conversion. On the contrary, when the initial concentration was high, most of the starting material was converted to undesired higher oligomers. Moreover, the ethylene removal by the action of the reduced pressure and the

high-dilution conditions both promote the formation of the cyclic products, which was confirmed by the absence of the corresponding peaks in MALDI MS spectra.

Apart from the metathesis-type oligomerization, the reaction was also extensively accompanied by, presumably, styrene-type polymerization which was likely a major cause of only a moderate yield of the macrocyclization. Unfortunately, attempts to suppress the polymerization by addition of a small amount of 4-*tert*-butylcatechol as a radical scavenger failed.

The preparative separation of **31** and **32** was achieved in a multistep procedure. First, the remaining ruthenium catalyst and its decomposition products were removed by an amine functionalized silica gel, followed by filtration through a short pad of silica gel. The obtained mixture of various oligomers was then separated by a repeated preparative GPC on a cross-linked polystyrene gel, giving pure **31** and **32** as a mixture of stereoisomers. The separation of the individual stereoisomers could be achieved using supercritical fluid chromatography (SFC) or repeated preparative HPLC (see Chapter 3.3.). Under the optimized reaction and separation conditions, pure **31** and **32** were obtained in multi-milligram quantities with yields of up to 33% and 22%, respectively.

For the purpose of the chirality assignment (see also Chapters 3.6.3. and 3.6.4.), the synthesis of **31** was also repeated starting from optically pure (+)-(*P*)-**43** and (-)-(*M*)-**43**. Unlike in the previous case, the reaction was performed at room temperature to prevent an excessive racemization of the starting helicene monomers. Up to three days of reaction time was necessary to push the reaction to completion. Despite all the effort, a substantial loss of optical purity was observed, as evidenced by SFC analysis (Figures 73 and 74). From these chromatograms, and with the known configuration of the starting **43**, it was easy to assign the absolute configuration of the isolated homochiral trimers (*M**,*M**,*M**)-**31**.

As stated above, macrocyclizations based on olefin metathesis are generally reversible. Whether reversibility plays a role in a particular case is, however, determined by the specific reaction conditions. To explore the metathesis reversibility in the case of **31**, an equilibration experiment was performed. Tetramer **32** was subjected to identical reaction conditions (Piers 2nd gen. cat., 50 °C, TCB, reduced pressure) and the composition of the reaction mixture was analyzed using analytical GPC and MALDI MS. Only a trace amount of trimer **31** was detected after 18 hours. When the reaction temperature was raised to 70 °C for an additional 14 hours, the formation of **31** was observed both in GPC and MALDI MS. However, a concomitant formation of a large amount of insoluble material was noticed. Based on these observations, it can be concluded that at 50 °C and the used reaction concentration, **31** is a kinetic product. The reversible nature of olefin metathesis is exposed only at higher temperatures when it is also disrupted by a kinetically preferred oligomerization-precipitation.

3.3.Separation of Stereoisomers of **31**

For further studies, the individual stereoisomers of **31** had to be separated. As the macrocycle structure is based on a dibenzo[5]helicene building block which has an inversion barrier of only 26 kJ.mol^{-1} (see Chapter 5.6.), a primary question was, whether the individual stereoisomers would be even separable.

Indeed, the separation was achieved by HPLC or SFC using chiral stationary phase columns. A range of different stationary phases was tested, with Chiral Art Amylose-SA giving the best results in both HPLC and SFC.

The analytical HPLC (*n*-heptane : toluene : THF : *i*-PrOH = 60 : 30 : 5 : 0.3, Chiral ART Amylose-SA column) could separate the stereoisomers but the peak widths were too large. Obviously, **31** adsorbs on the stationary phase and is difficult to elute completely. Figure 26 shows a representative chromatogram along with a signal from a polarimetric detector. Interestingly, only three peaks can be observed although four stereoisomers are expected in the mixture. The peaks are already assigned to avoid confusion but the full stereochemical assignment will be discussed later in Chapter 3.6.4.

Reflecting the above problems, attention was turned to SFC (CO_2 : chloroform = 53 : 47, chloroform modified with 0.1% of *i*-PrOH, Chiral ART Amylose-SA column). Indeed, the superior separation power of this technique was confirmed as demonstrated by a chromatogram in Figure 27. The elution of the compounds was almost perfect, allowing quantitative measurements important for subsequent kinetic measurements. Again, only three peaks were present, suggesting that one of the peaks contains two stereoisomers.

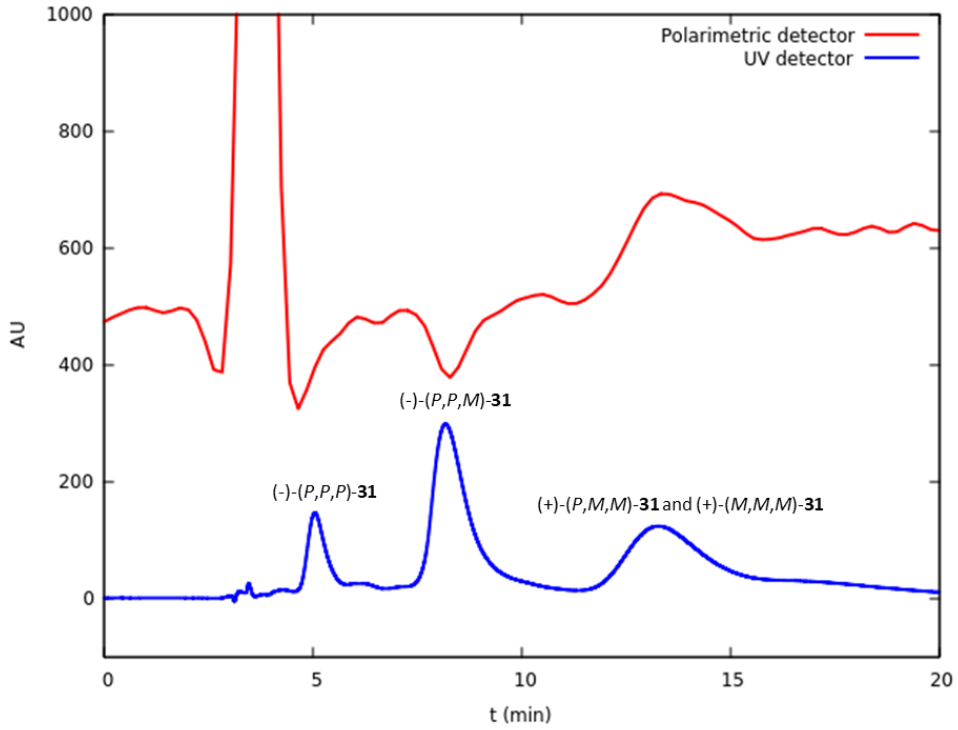

Figure 26. HPLC chromatogram of **31** as a mixture of stereoisomers. UV absorption signal (blue) is accompanied by a signal from polarimetric detector (red) for optical rotation assignment.

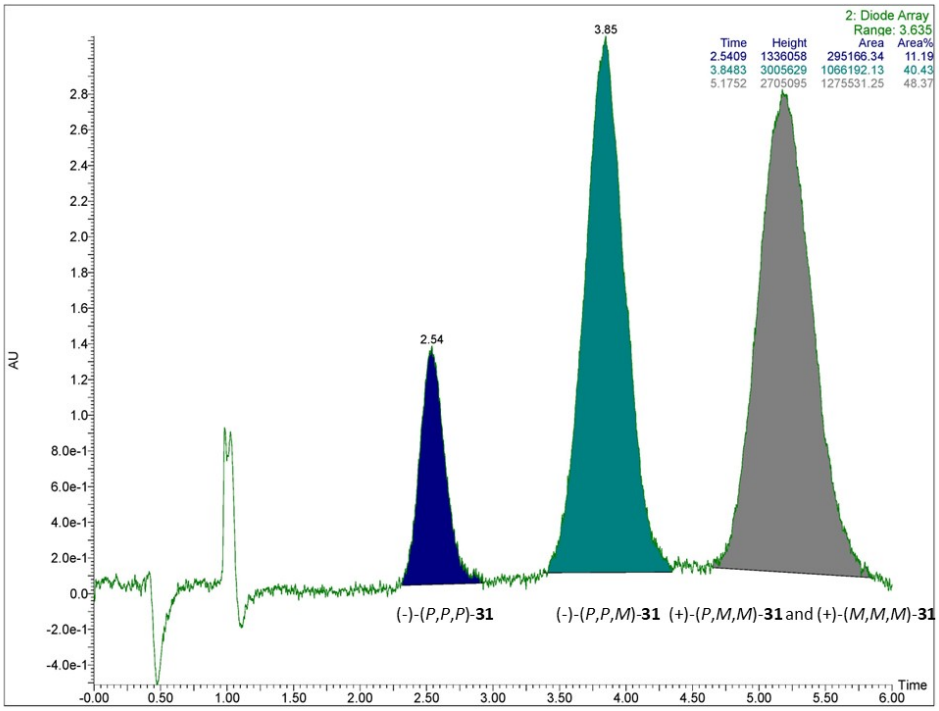

Figure 27. SFC chromatogram of **31** as a mixture of stereoisomers. The separation was performed on Chiral ART Amylose-SA column (4.6 mm ID × 250 mm, 5 µm particle size) using CO_2 – chloroform (53:47) mixture as eluent, chloroform was modified by addition of 0.1% of *i*-PrOH (flow rate of 3 mL·min^{-1}, 35 °C column temperature, 1500 psi ABPR pressure).

The semi-preparative isolation of stereoisomers was performed by both SFC and HPLC. For later AFM measurements, where just a minuscule amount of material is required, the samples were collected directly from a single analytical SFC separation. To obtain a larger amount of a pure material, up to 0.2 mg of (-)-(*P*,*P*,*P*)-**31** was obtained after about a hundred repeated analytical separations. This approach was, however, soon abandoned in order to preserve the analytical column and, above all, the author's mental health.

Larger amounts of material were isolated by a semipreparative HPLC using eluent system identical to the analytical measurements (Chiral ART Amylose-SA column). Approximately 0.2 mg of (-)-(*P*,*P*,*P*)-**31** was obtained in a reasonably high ca 95% *ee*, *de*. Unfortunately, the (-)-(*M*,*P*,*P*)-**31** stereoisomer could only be obtained in a substantially lower optical purity due to a strong adsorption of **31** on the stationary phase and resulting cross-contamination of the chromatographic peaks. (+)-(*M*,*M*,*P*)-**31** and (+)-(*M*,*M*,*M*)-**31** could not be separated at all as they were combined in a single peak.

3.4. Isomerization of Stereoisomers of **31**

Configuration inversion of helicenes has been studied in a number of works.[113–116] In the case of classical [5]helicenes, the inversion proceeds through a typical saddle-shaped transition state.[116] To see how the helicity inversion would proceed when helicenes are restrained within the macrocycle molecule **31**, isomerization kinetics complemented by DFT calculations was studied.

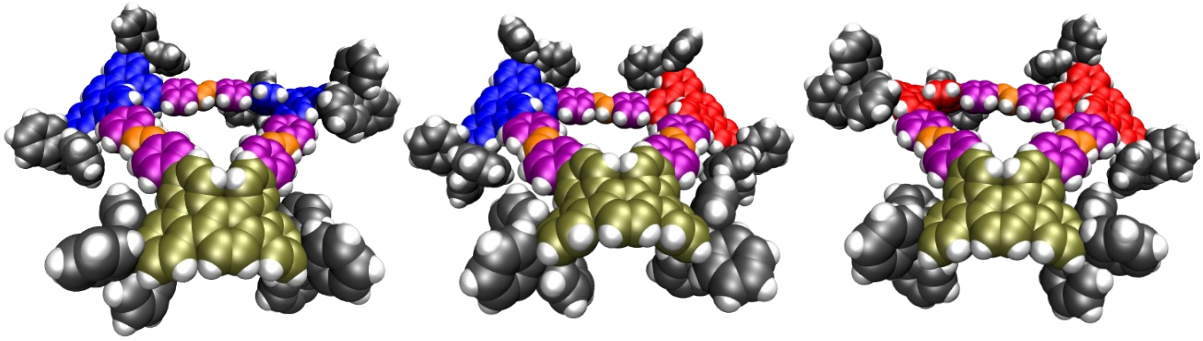

Figure 28. 3D models of three conceived transition states of helicity inversion in **31** obtained by DFT calculations. (*P*,*P*,*saddle*)-**31** (A), *exo*-(*M*,*P*,*saddle*)-**31** (B), and *endo*-(*M*,*P*,*saddle*)-**31** (C).

The simplest scenario of the isomerization was considered, where a consecutive change of helicity of one helicene unit at a time generates all possible stereoisomers of **31**. The model assumes the inverting helicene adopts the saddle transition state, similarly as in the case of the enantiomerization of free [5]helicene (Figure 28). If the process is reversible, all stereoisomers will be in equilibrium as described by Scheme 5.

$$(P,P,P)\text{-}\mathbf{31} \underset{k_{-1}}{\overset{k_1}{\rightleftharpoons}} (M,P,P)\text{-}\mathbf{31} \underset{k_2}{\overset{k_2}{\rightleftharpoons}} (M,M,P)\text{-}\mathbf{31} \underset{k_1}{\overset{k_{-1}}{\rightleftharpoons}} (M,M,M)\text{-}\mathbf{31}$$

Scheme 5. Kinetic scheme describing the equilibrium between individual stereoisomers of **31**.

Note the conspicuous symmetry of the kinetic scheme reflecting the presence of the enantiomeric pairs in the mixture. As shown in the following discussion, this symmetry allowed considerable simplification of the whole problem.

The isomerization equilibrium can be quantified with a kinetic model described by the following set of differential equations

$$\frac{d[PPP]}{dt} = -k_1[PPP] + k_{-1}[MPP] \quad (8)$$

$$\frac{d[MPP]}{dt} = k_1[PPP] - k_{-1}[MPP] - k_2[MPP] + k_2[MMP] \quad (9)$$

$$\frac{d[MMP]}{dt} = k_2[MPP] - k_2[MMP] - k_{-1}[MMP] + k_1[MMM] \quad (10)$$

$$\frac{d[MMM]}{dt} = k_{-1}[MMP] - k_1[MMM] \quad (11)$$

where the left side denotes the rate of the concentration change for individual stereoisomers and the right sides contain the immediate concentrations multiplied by corresponding rate constants as described by Scheme 5. The nature of the transition states involved in the isomerization can be subsequently deduced from the height of the barrier of helicity

inversion, which can be calculated from the corresponding rate constant by the well-known Eyring-Polanyi equation

$$\Delta G_i^{\ddagger} = -RT \ln \frac{k_i h}{\kappa k_B T} \quad (12)$$

where R is the universal gas constant, k_i are the rate constants, h is the Planck constant, κ is the transmission coefficient, k_b is the Boltzmann constant, and T is the thermodynamic temperature. In the case of a simple configuration inversion, κ can be taken to be 1.

However simple this model seems to be, its experimental implementation required many additional measurements and non-standard techniques. The main complication was that only a microscopic amount of pure (-)-(*P*,*P*,*P*)-**31** was available. (-)-(*M*,*P*,*P*)-**31** could not be used for the measurements because it was contaminated by a substantial quantity of other isomers. (+)-(*M*,*M*,*P*)-**31** and (+)-(*M*,*M*,*M*)-**31** could not be used either, as they were completely inseparable.

Considering the very small amount of (-)-(*P*,*P*,*P*)-**31**, the process was studied in chloroform by using SFC equipped with a diode array UV detector. To be able to estimate the concentration changes of individual isomers during the measurements, it was first necessary to evaluate their extinction coefficients. A trivial measurement by a classical UV-Vis absorption spectroscopy was impossible because the tiny amounts of samples could not be weighted accurately. An alternative route was therefore chosen. First, concentration ratio (equilibrium constant) between the stereoisomers in equilibrium was estimated. This was achieved either by a simple integration of the ^{1}H NMR spectrum (see Chapter 3.6.2.) or by an equilibration measurement described below. With the equilibrium constant in hand, a modified Lambert-Beer law was used to estimate the UV absorption extinction coefficients. The obtained coefficients then allowed the processing of the kinetic measurement data and the subsequent calculations.

The thermodynamic assessment of the equilibrium constant took advantage of the special stoichiometric and energetic relationships between the stereoisomers of **31**. The strength of this strategy is that it is independent of the value of the extinction coefficients of a particular stereoisomer. The principle of the method can be understood as follows: Consider we thermally equilibrate n_{10} moles of a pure (-)-(*P*,*P*,*P*)-**31**. The equilibration results in a mixture of n_1 remaining moles of (-)-(*P*,*P*,*P*)-**31**, n_2 moles of (-)-(*M*,*P*,*P*)-**31**, n_3 moles of (+)-(*M*,*M*,*P*)-**31**, and n_4 moles of (+)-(*M*,*M*,*M*)-**31**. Because the stoichiometry of the isomerization must be 1 : 1 between each pair of stereoisomers, the molar distribution of the stereoisomers after equilibration is determined by the following equation:

$$n_{10} - n_1 = n_2 + n_3 + n_4 \quad (13)$$

Since in equilibrium the amount of enantiomeric pairs n_1 and n_4, or n_2 and n_3, must be equal, the equation (13) can be simplified to involve only the (-)-(*P*,*P*,*P*)-**31** and (-)-(*M*,*P*,*P*)-**31** stereoisomers:

$$\frac{n_{10} - 2n_1}{2} = n_2 \quad (14)$$

Because the equilibration process takes place in a constant volume, the ratio of (-)-(*M*,*P*,*P*)-**31** and (-)-(*P*,*P*,*P*)-**31** stereoisomers in the equilibrium mixture is therefore:

$$K = \frac{n_2}{n_1} = \frac{n_{10}-2n_1}{2n_1} = \frac{c_{10}-2c_1}{2c_1} = \frac{c_2}{c_1} = \frac{[PMM]}{[MMM]} = \frac{[PPM]}{[MMM]} = \frac{[PMM]}{[PPP]} = \frac{[PPM]}{[PPP]} \qquad (15)$$

The value *K* = 2.92, corresponding to ca 75% of (-)-(*M*,*P*,*P*)-**31** and 25% of (-)-(*P*,*P*,*P*)-**31**, from the equilibration experiment was identical to the value obtained by the integration of the ^{1}H NMR spectrum. It is worth noting that the equilibration was performed at 92 °C, but the value is valid practically for the whole range of temperatures between 22 and 140° C, as the equilibrium is practically independent of temperature (see Chapters 3.6.2. and 5.4.).

The estimation of the UV absorption extinction coefficients was performed using a relative measurement and was based on the linearity and additivity of the Lambert-Beer law. A chromatographic peak area A_i of a compound *i* in a mixture is proportional to its extinction coefficient ε_i, optical path *l*, and a product of its relative concentration c_r and reference concentration c_i (unknown value corresponding to the compound *i* in the mixture):

$$A_i = \varepsilon_i l c_i c_r \qquad (16)$$

Of course, we suppose that the concentrations in the optical detector are related to the concentrations in the input sample. This assumption should be valid unless the compound is irreversibly adsorbed on the stationary phase. Another important assumption is that the molecules in the mixture do not aggregate, which should be valid at low concentrations.

If we perform a series of SFC measurements of an equilibrium stereoisomeric mixture of **31** with various reference concentrations c_i and construct corresponding calibration lines as a function of the relative concentration c_r, we can use the line slopes to estimate relative extinction coefficients. Considering the equation (16), the slope S_i of each calibration line *i* can be expressed as:

$$S_i = \varepsilon_i l c_i \qquad (17)$$

By taking a ratio of any two calibration line slopes, we obtain the following expression:

$$\frac{Si}{Sj} = \frac{\varepsilon_i l c_i}{\varepsilon_j l c_j} = \frac{\varepsilon_i c_i}{\varepsilon_j c_j} \qquad (18)$$

Therefore, the equation (18) allows us to evaluate the ratio of extinction coefficients of diastereomers (*M**,*M**,*M**)-**31** and (*M**,*P**,*P**)-**31** in a mixture, provided we know their concentration ratio c_i/c_j, which in this case corresponds to the equilibrium constant between compounds *i* and *j*.[§]

Figure 29 shows the measured calibration lines as a function of the relative concentration c_r, multiples of the unknown concentration c_i. The measurement was performed on an equilibrium mixture of **31** using combined wavelength signal for greater sensitivity. For the evaluation of the specific extinction coefficient, a single 350 nm (absorption maximum) wavelength was chosen. The individual calibration lines correspond to the peaks in the

[§] Due to generally low values of c_i, we assume the concentrations to be equal to activities.

chromatograms shown in Figure 27. It is clear the individual line slopes of (-)-(*P*,*P*,*P*)-**31** and (-)-(*M*,*P*,*P*)-**31** are markedly different, indicating their substantially different extinction coefficients (Figure 29A and B). If the second and third chromatographic peaks (suppose (-)-(*M*,*P*,*P*)-**31** and (+)-(*M*,*M*,*P*)-**31**) contained solely these two enantiomers, the calibration lines would have to be identical. This is, however, contradicted by the comparison shown in Figure 29C. The calibration lines corresponding to the second and third peaks are clearly different. Moreover, when we compare the calibration lines of the third peak and a sum of the first and the second peaks, we see they almost coincide, as shown in Figure 29D. These observations therefore suggest that the third peak actually might contain both (+)-(*M*,*M*,*P*)-**31** and (+)-(*M*,*M*,*M*)-**31** which was corroborated by subsequent experiments.

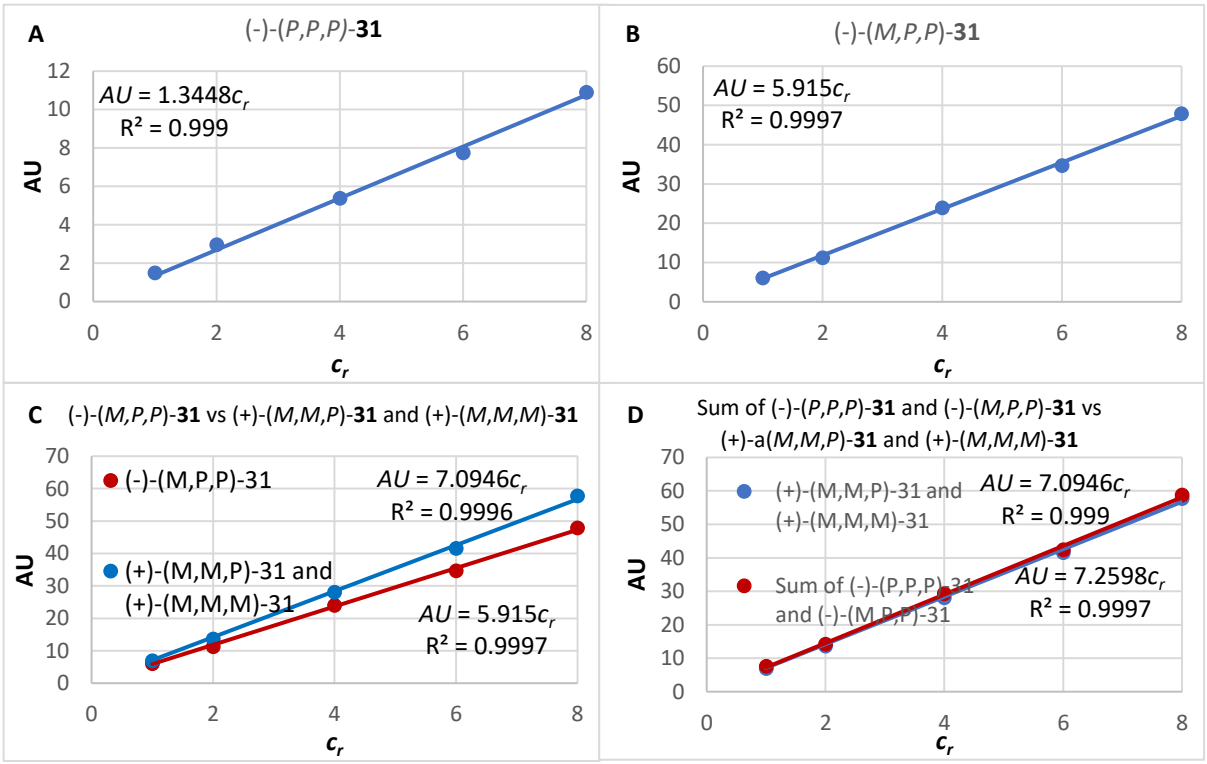

Figure 29. Calibration lines for individual chromatographic peaks from Figure 76 constructed as linear fit of absorbance *versus* relative concentration c_r. The first peak - (-)-(*P*,*P*,*P*)-**31** (A), the second peak - (-)-(*M*,*P*,*P*)-**31** (B), the third peak - mixture of (+)-(*M*,*M*,*P*)-**31** and (+)-(*M*,*M*,*M*)-**31**. Comparison with the second peak shows the third peak contains (+)-(*M*,*M*,*P*)-**31** and (-)-(*M*,*M*,*M*)-**31** (C). Comparison of sum of the first peak of (-)-(*P*,*P*,*P*)-**31** and the second peak of (-)-(*M*,*P*,*P*)-**31** vs the third peak indicates the third peak might be a mixture of (+)-(*M*,*M*,*P*)-**31** and (+)-(*M*,*M*,*M*)-**31.**

Weighing the individual stereoisomers was certainly unfeasible but the equilibrium mixture could be weighed without any difficulty since it was available in a multi-milligram amount. Since both absorbance and concentration are in this present case additive quantities, the UV absorption of the equilibrium mixture at 350 nm could be partitioned to the contributions corresponding to the individual stereoisomers by a simple algebraic exercise below:

$$\varepsilon = \frac{\varepsilon_2}{\varepsilon_1} \tag{19}$$

$$K = \frac{c_2}{c_1} \tag{20}$$

$$c = c_1 + c_2 = c_1 + Kc_1 = (1 + K)c_1 \tag{21}$$

$$A = \varepsilon_1 c_1 l + \varepsilon_2 c_2 l = \varepsilon_1 c_1 l + \varepsilon\varepsilon_1 K c_1 l = (1 + \varepsilon K)\varepsilon_1 c_1 l = (1 + \varepsilon K)\varepsilon_1 \frac{c}{1+K} l \quad (22)$$

$$\varepsilon_1 = \frac{A(1+K)}{(1+\varepsilon K)lc} \quad (23)$$

$$\varepsilon_2 = \frac{\varepsilon A(1+K)}{(1+\varepsilon K)lc} \quad (24)$$

where ε is the ratio between the extinction coefficients of (*M*,M*,M**)-**31** and (*M*,M*,P**)-**31**, ε_1 is the molar extinction coefficient of (*M*,M*,M**)-**31**, ε_2 is the molar extinction coefficient of (*M*,M*,P**)-**31**, *l* is the optical path, *K* is the ratio between the concentrations of the individual diastereomers, c_1 and c_2 are molar concentrations of the two diastereomers, *c* is the total molar concentration of all stereoisomers of **31**, and *A* is the total absorbance of the measured solution which was taken from the corresponding UV spectrum (Table 1).

c (mol·L^{-1})	*l* (cm)	*ε (350 nm)*	*A (350 nm)*	*K*	ε_1 (L·mol^{-1}·cm^{-1})	ε_2 (L·mol^{-1}·cm^{-1})
$1.0 \cdot 10^{-4}$	0.1	1.23	2.50	2.92	$2.1 \cdot 10^{5}$	$2.6 \cdot 10^{5}$

Table 1. Calculation input data and molar absorption coefficients of (*M*,M*,M**)-**31** and (*M*,M*,P**)-**31**.

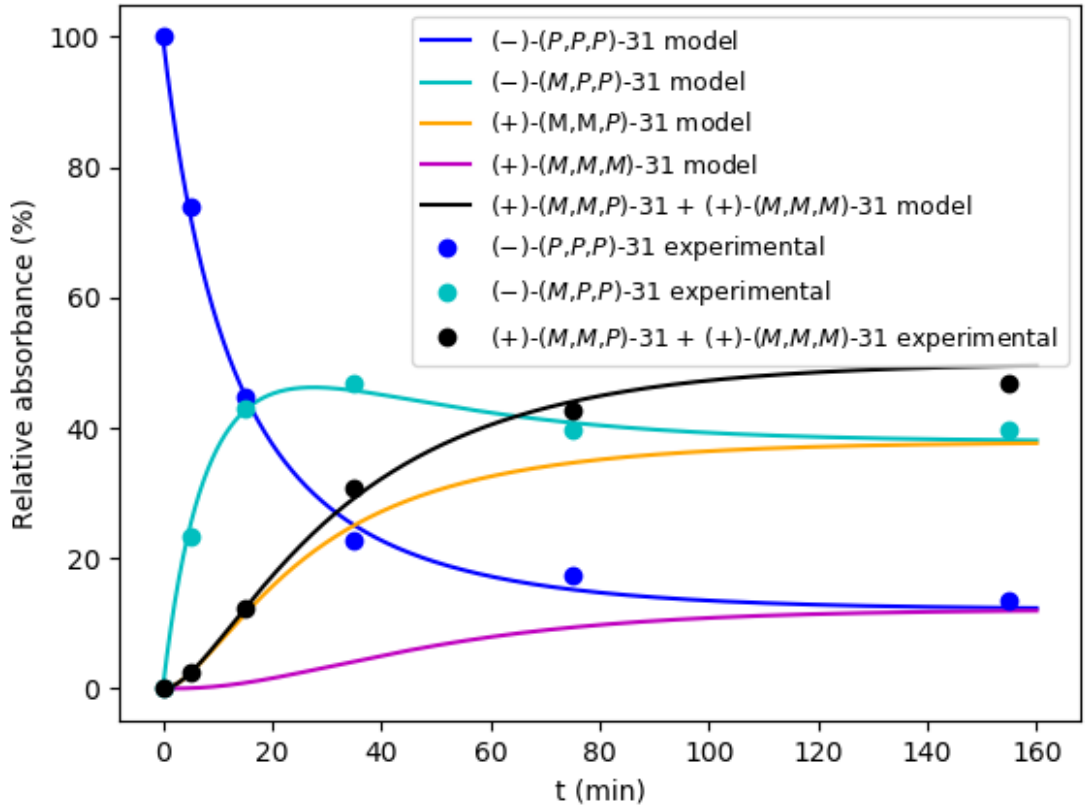

Figure 30. Kinetics of interconversion of stereoisomers of **31** at 76 °C in $CHCl_3$ (dots) fitted with simulated curves (lines), starting from (-)-(*P,P,P*)-**31**. Relative absorbance is used instead of relative concentration.

With the extinction coefficients in hand, the isomerization kinetics of (-)-(*P,P,P*)-**31** could be measured. A solution of (-)-(*P,P,P*)-**31** dissolved in chloroform was heated to 76 °C (temperature optimized for this particular system) and the composition of the mixture was monitored by SFC in suitable time intervals. The progress of the isomerization is shown in

Figure 30. The graph shows the evolution of the three measurable values – relative absorbances of the starting (-)-(*P*,*P*,*P*)-**31,** and the formed (-)-(*M*,*P*,*P*)-**31**, and (+)-(*M*,*M*,*P*)-**31** and (+)-(*M*,*M*,*M*)-**31** in one peak (shown by dots).

The experimental data was processed with a custom-made Python script (smooth curves, see Appendix 1). This was, however, not without obstacles, because (+)-(*M*,*M*,*P*)-**31** and (+)-(*M*,*M*,*M*)-**31** stereoisomers were inseparable by SFC and eluted as a single peak. There was no straightforward way to partition their contributions to the overall relative absorbance within that peak (they are not in equilibrium during the analysis), a reverse approach was therefore taken. Again, as the relationship between the relative absorbance and concentration is linear and the isomerization is described by a system of first order differential equations, it is possible to use the relative absorbance directly (the solution multiplied by a factor must also satisfy the equations). The values of the rate constants are unaffected by this approach. When the absorbance was used instead of concentrations, it was possible to separate the time evolution of the concentrations and thus treat each stereoisomer separately. The calculated relative absorbances were then fitted to the experimental data and the rate constants were obtained as the fitting parameters. In the case of (+)-(*M*,*M*,*P*)-**31** and (+)-(*M*,*M*,*M*)-**31**, their calculated absorbances were simply summed and used in the fitting. This is the reason why a relative absorbance was used in the plot in Figure 30.

Note how the evolution diagram shows the gradual approaching of the cyan and orange, or the blue and pink curves, indicating the racemization of the mixture as it reaches the equilibrium.

Inversion	*PPP → MPP*	*PPP ← MPP*	*MPP → MMP*	*MPP ← MMP*	*MMP → MMM*	*MMP ← MMM*
k_i (s^{-1})	0.0008	0.0004	0.0006	0.0006	0.0004	0.0008
$\Delta G_i^{\ddagger}$ (kcal·mol^{-1})	25.6	26.1	25.6	25.6	26.1	25.6
ΔG_{DFT} (kcal·mol^{-1})	26.5	26.6	26.3	26.3	26.6	26.5

Table 2. Measured rate constants and corresponding experimental and DFT inversion barriers between stereoisomers of **31** at 76 °C in $CHCl_3$. The symmetry of the kinetic scheme was highlighted by using black *vs* grey color.

The obtained rate constants were subsequently converted to the corresponding Gibbs free energies of the barriers of the helicity inversion and compared with the values calculated by DFT (Table 2, see Chapter 3.5.). Both sets of values are in excellent agreement and support the initial choice of the kinetic model of the consecutive configuration inversion. The overall isomerization process is summarized in Figure 31. All barriers of the helicity inversion have practically equal value and are also very close to the enantiomerization barrier of monomer **43** (26.1 kcal.mol^{-1}) It suggests that the helicity inversion proceeds rather independently of the rest of the molecule. This is interesting because similar π-conjugated macrocycles are often very rigid and therefore denoted as “shape-persistent”. This term, however, is misleading because these molecules are in many cases very flexible, considering the above results and as also nicely demonstrated by Summerfield *et al.*[10]

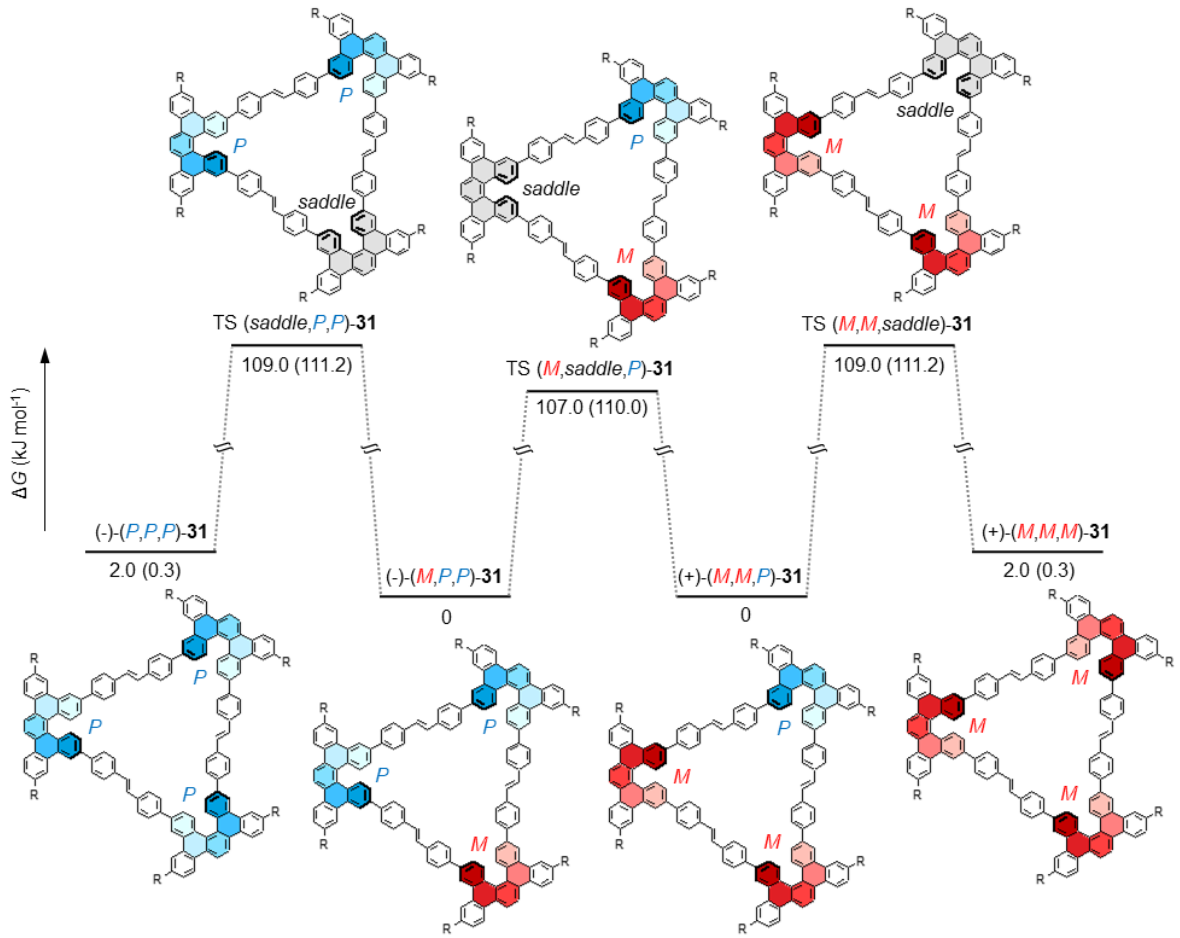

Figure 31. Energy profile of the interconversion of stereoisomers of **31** in chloroform at 76 °C compiled from the experimental and DFT-calculated barriers of the helicity inversion and based on the proposed kinetic model. DFT values are in parentheses.

3.5. DFT Calculations of Barriers of Helicity Inversion

To gain more insight into the mechanism of the helicity inversion discussed in the previous chapter, the experimental results were also corroborated by theoretical calculations. The computational details are described in Chapter 5.11. The Gibbs free energies and a corresponding proportion of stereoisomers in the equilibrium mixture (considering only conformational, not configurational, changes) were calculated for conformers of (-)-(*P*,*P*,*P*)-**31** and (-)-(*M*,*P*,*P*)-**31** (the values for (+)-(*M*,*M*,*M*)-**31** and (+)-(*M*,*M*,*P*)-**31** are naturally identical) selected from a short MD run. The found energy differences between individual conformers were only a few kcal.mol^{-1}, within the expected error of the applied calculation method.[117] Therefore, the calculations must be interpreted with caution, especially in the case of partitioning the energy to enthalpic and entropic contributions. Still, the results confirm that the stereoisomers of **31** are energetically very close and exist as a rich mixture of conformers, mainly due to the presence of the rotationally loose trityl groups.

The most stable conformers were chosen for the subsequent calculation of the energy barriers. From a stereochemical viewpoint, the transition between (-)-(*P*,*P*,*P*)-**31** and (-)-(*M*,*P*,*P*)-**31** (and similarly (+)-(*M*,*M*,*M*)-**31** and (+)-(*M*,*M*,*P*)-**31**) can proceed only through a single transition state (*P*,*P*,*saddle*)-**31**, with the calculated barrier of 26.6 kcal.mol^{-1}. On the contrary, the transition state between (-)-(*M*,*P*,*P*)-**31** and (+)-(*M*,*M*,*P*)-**31** can be realized via two stereochemically distinct structures. In the case of *exo*-(*M*,*P*,*saddle*)-**31**, the concave surfaces of the saddle helicene and the opposing stilbene linker point in the opposite directions, while in the case of *endo*-(*M*,*P*,*saddle*)-**31** the concave surfaces point in the same direction (Figure 32). The corresponding energy barriers for these structures are 26.3 and 27.1 kcal.mol^{-1}, respectively.

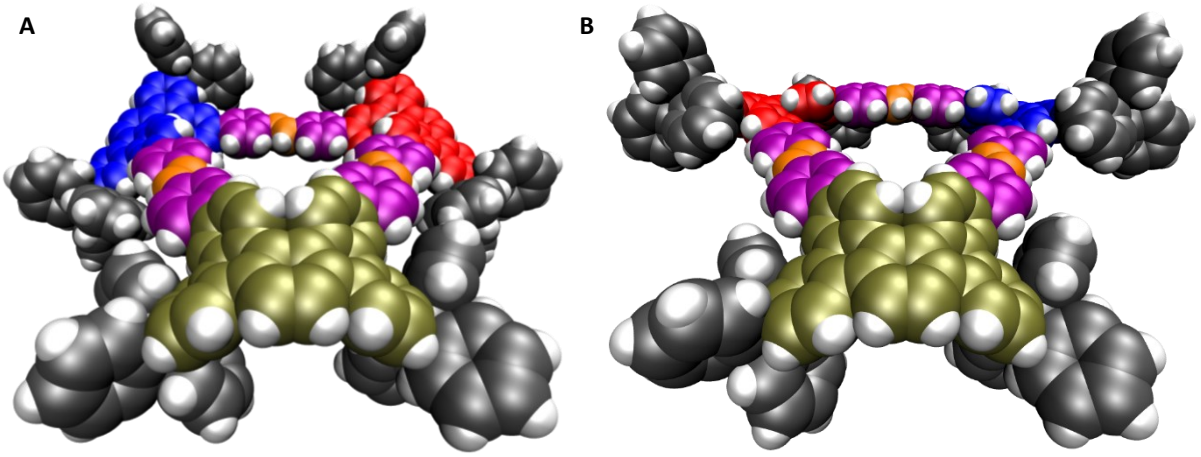

Figure 32. Two possible transition states corresponding to the helicity inversion of (+)-(*M*,*M*,*P*)-**31** ↔ (-)-(*M*,*P*,*P*)-**31**. The transition state *exo*-(*M*,*P*,*saddle*)-**31** (A) is more stable than *endo*-(*M*,*P*,*saddle*)-**31** (B).

Overall, the calculation results are in a very convincing agreement with the corresponding experimental values, confirming the correct choice of the kinetic model (Tables 3 and 4). The overall results are also summarized in the graphical energy diagram in Figure 31.

Structure	ΔH (kcal·mol^{-1})	$-T\Delta S$ (kcal·mol^{-1})	ΔG (kcal·mol^{-1})
(-)-(*M*,*P*,*P*)-31	0	0	0
(+)-(*P*,*P*,*P*)-31	0.382	-0.311	0.072
(*P*,*P*,*saddle*)-31	23.8	2.75	26.6
***exo*-(*M*,*P*,*saddle*)-31**	24.2	2.10	26.3
***endo*-(*M*,*saddle*)-31**	24.3	2.80	27.1

Table 3. Relative Gibbs free energies and its enthalpic and entropic components between the most stable minima and inversion transition states of **31** calculated at 349 K. The lower transition state *exo*-(*M*,*P*,*Saddle*)-**31** was used in further calculations.

Inversion	*PPP → PPM*	*PPP ← PPM*	*PPM → PMM*	*PPM ← PMM*	*PMM → MMM*	*PMM ← MMM*
ΔG_{DFT} (kcal·mol^{-1})	26.5	26.6	26.3	26.3	26.6	26.5
ΔG_{EXPER} (kcal·mol^{-1})	25.6	26.1	25.6	25.6	26.1	25.6

Table 4. Summary of the Gibbs free energy barriers for individual inversions between stereoisomers of **31**, calculated at 349 K. Values obtained from the measurement of isomerization kinetics are shown for comparison.

To compare the barriers of the helicity inversion between stereoisomers of **31** with those of individual helicenes **43** and **45** (3,3'-dichlorodibenzo[5]helicene, for structure see Figure 46), an analogous computational study was adopted.

Calculations regarding helicene **45** did not involve the conformer search as this molecule has very little conformational freedom. On the contrary, **43** bearing the trityl groups was screened by the conformer search using OpenBabel.[118] Eight energetically lowest conformers were then optimized using DFT. The conformation of the trityl groups in the most stable structure was used as the starting geometry for the corresponding transition state.

Again, the obtained values were in excellent agreement with the experimental values (Tables 5 and 6). Surprisingly, helicenes **43** and **45** had similar enantiomerization barriers, showing only a very small contribution of the trityl groups.

Structure	ΔH (kcal·mol^{-1})	$-T\Delta S$ (kcal·mol^{-1})	ΔG (kcal·mol^{-1})
(-)-(*M*)-45	0	0	0
45-TS	25.5	0.813	26.3

Table 5. Gibbs free energy and its enthalpic and entropic components of the enantiomerization transition state **45**-TS relative to the corresponding energy minimum of **45** calculated at 325 K.

Structure	ΔH (kcal·mol^{-1})	$-T\Delta S$ (kcal·mol^{-1})	ΔG (kcal·mol^{-1})
(-)-(*M*)-43	0	0	0
43-TS	24.9	1.96	26.8

Table 6. Gibbs free energy and its enthalpic and entropic components of the inversion transition state **43**-TS relative to the most stable energy minimum of **43** calculated at 325 K.

3.6.Structural Elucidation

Trimer **31** and tetramer **32** were characterized by multiple spectroscopic methods but MALDI MS, and especially NMR measurements provided the most valuable data worth of further discussion. Figure 33 shows structural formulas of (*M**,*M**,*P**)-**31** and (*M**,*M**,*M**)-**31** diastereomers along with atom numberings which will be used in the subsequent text. As discussed in more detail in the NMR section, (*M**,*P**,*P**)-**31** has two structural units, the (*M**,*P**) unit being numbered 1-25, and the (*M**,*M**) unit numbered 1†-25†. The same numbering can also be used in the case of the structural units of tetramer **32**, although in this case the structural assignment was not complete due to the limited amount of data.

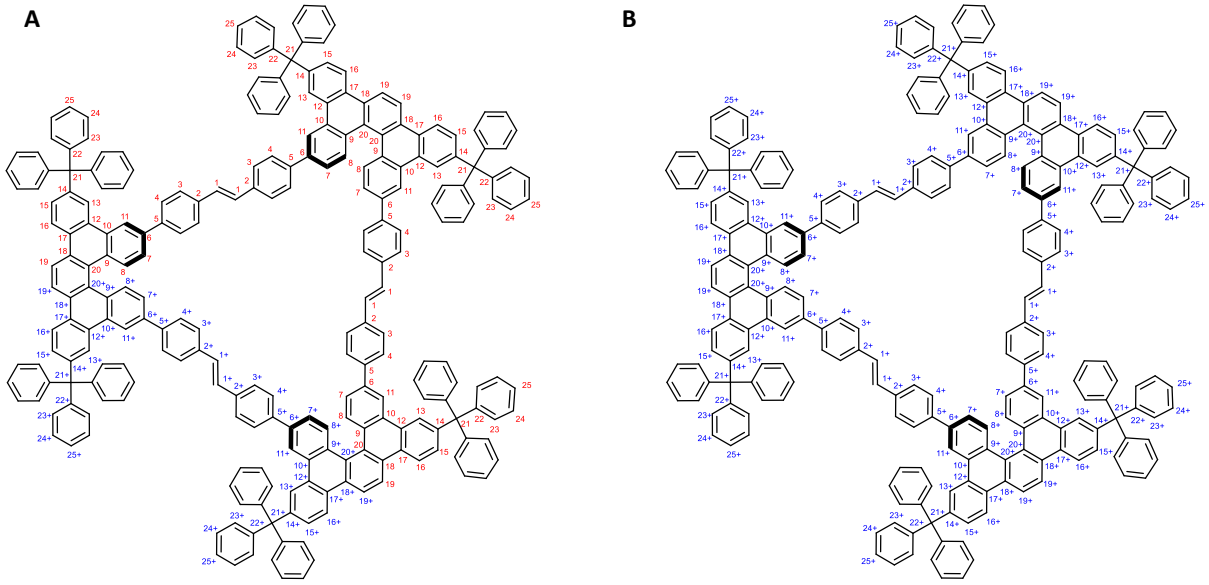

Figure 33. Numbering of atoms in (*M**,*M**,*P**)-**31** (A) and (*M**,*M**,*M**)-**31** (B) stereoisomers as used in the MS and NMR assignment.

3.6.1. MS Characterization of Trimer **31** and Tetramer **32**

*Trimer **31***

The large molecules of trimer **31** and tetramer **32** do not have any polar functional groups and it is therefore not surprising that EI or ESI MS could not be used for their analysis. Conversely, the MALDI MS turned out to be a reliable analytical tool as demonstrated by a spectrum of trimer **31** shown in Figure 34.

Despite using the soft MALDI ionization, molecule **31** exhibits a complex fragmentation pattern. It was possible to assign many of the peaks as indicated in the spectrum. For clarity, the lost fragments are represented by abbreviations. Their specific atomic compositions are written out in the synthetic part within the MS characterization of each compound (Chapter 5.2.). The most populated fragments were formed by the loss of phenyl groups (from the trityl or loss of the whole trityl group, forming stable carbocations). As only singly charged ions were detected, all but one fragmentation sites were apparently terminated by hydrogen, likely by abstraction from the matrix. Moreover, each isotopic cluster corresponding to these

fragments overlaps with the species formed by abstraction of molecular hydrogen. Since in some instances a maximum of three hydrogen molecules were observed to fall off, it is likely the dehydrogenation occurs in positions 8 and 8† of the helicene moiety (Figure 33). We observed such dehydrogenation in a number of helicene derivatives in our research group, while other examples were shown by Ernst and co-workers,[119] or Scott and co-workers.[120] Figure 35 shows a high resolution MALDI spectrum of [**31**+H]$^+$ overlapping with patterns of the aforementioned dehydrogenated species.

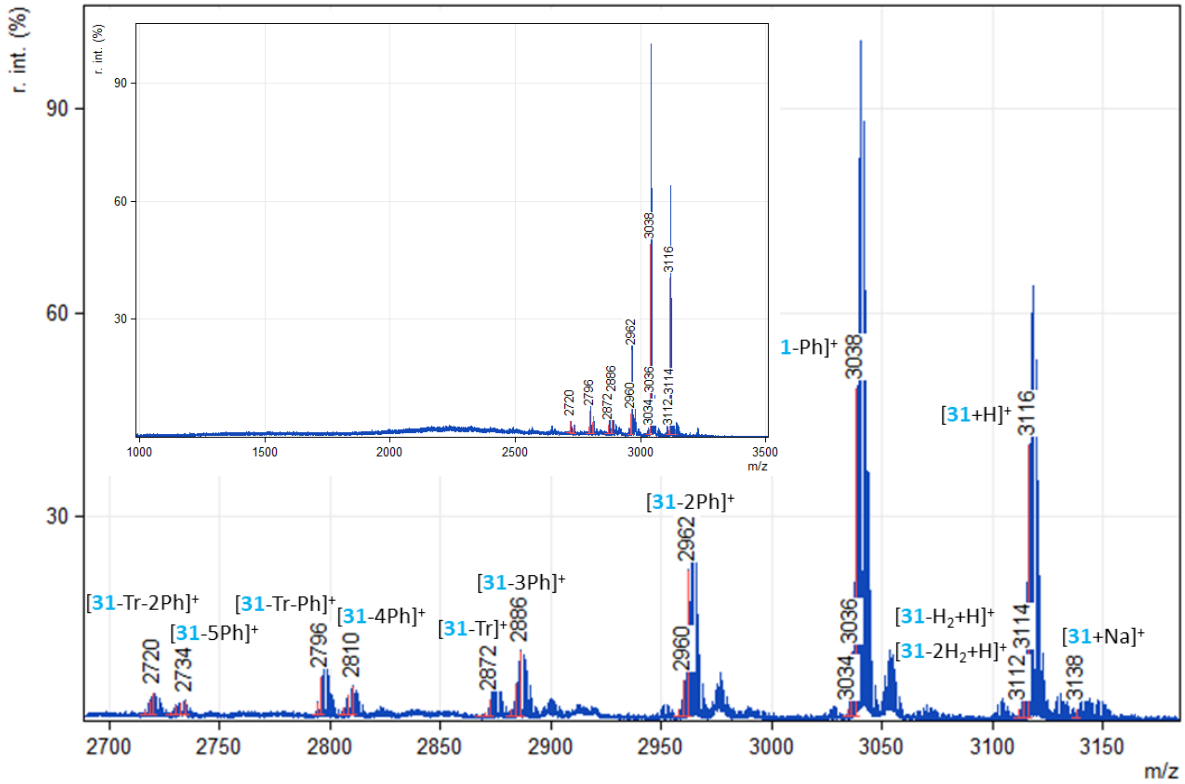

Figure 34. Expanded region of MALDI mass spectrum of trimer **31** showing the assigned ions. H_2 indicates hydrogen molecule, Ph = phenyl, Tr = triphenylmethyl. The inset shows the full spectrum.

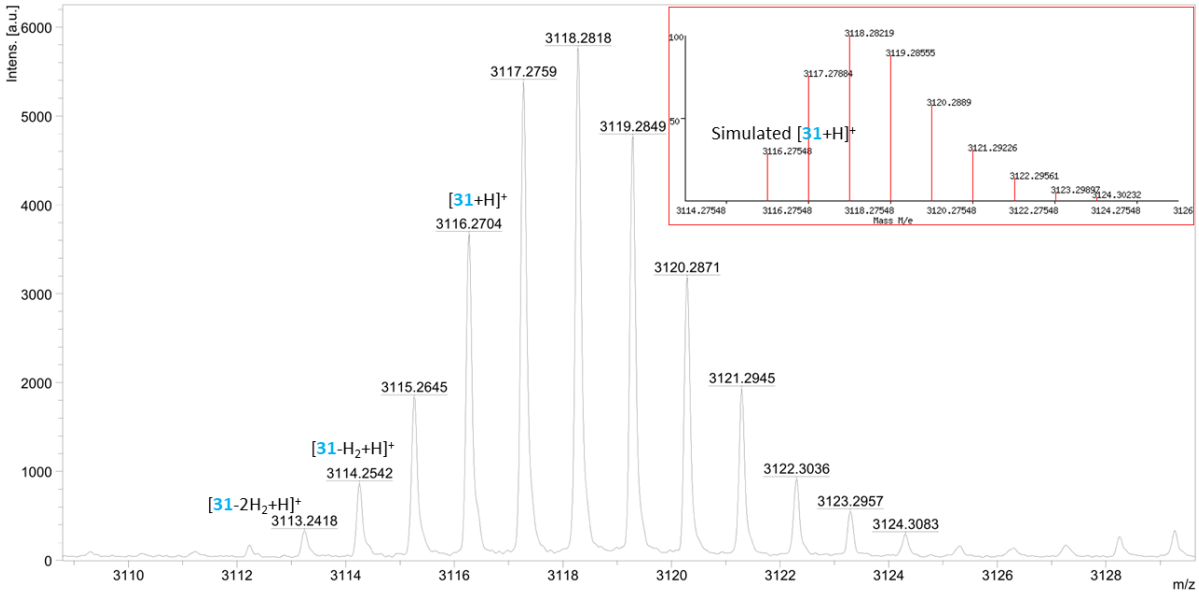

Figure 35. High resolution MALDI mass spectrum of trimer **31**. The isotopic pattern of [**31**+H]$^+$ overlaps with patterns of dehydrogenated **31**. Inset shows a corresponding simulated isotopic pattern of [**31**+H]$^+$.

*Tetramer **32***

Figure 36 shows the MALDI spectrum of tetramer **32**. Compared to trimer **31**, tetramer **32** was substantially more prone to form a sodium complex. Interestingly, this complex did not undergo dehydrogenation which allowed a straightforward comparison of its high-resolution spectrum with the simulated isotopic pattern (Figure 37). Otherwise, the fragmentation behavior of tetramer **32** was practically identical to trimer **31**.

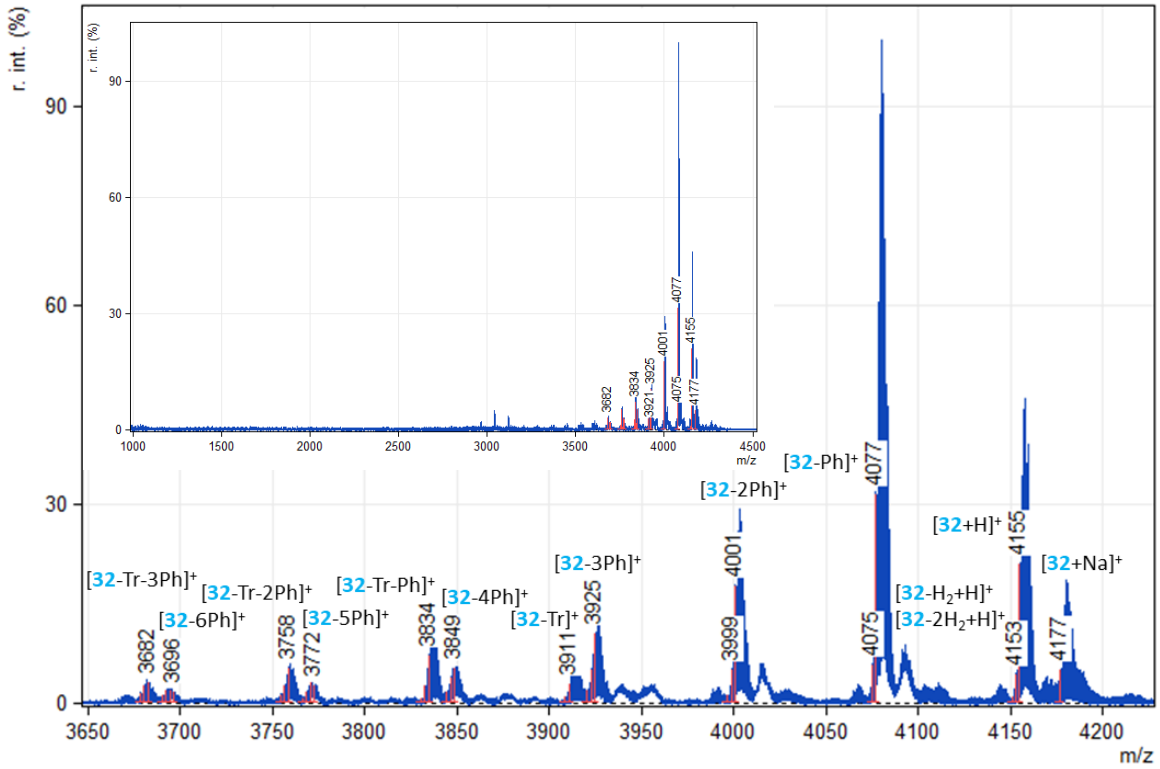

Figure 36. Expanded region of MALDI mass spectrum of tetramer **32** showing the assigned ions. H_2 indicates hydrogen molecule, Ph = phenyl, Tr = triphenylmethyl. Inset shows the full spectrum.

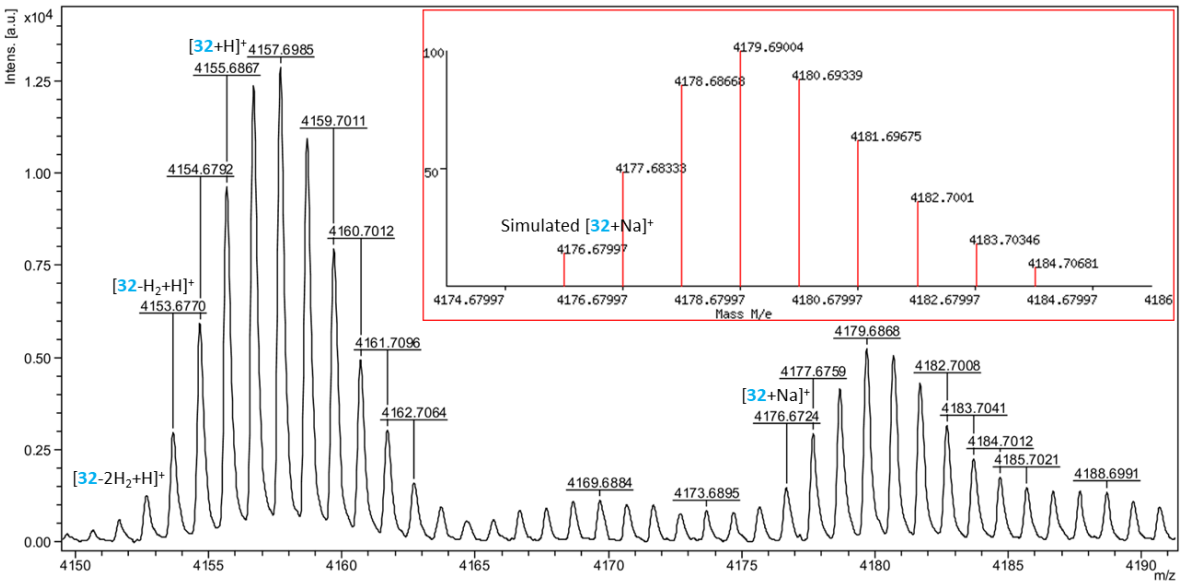

Figure 37. High resolution MALDI mass spectrum of tetramer **32**. The isotopic pattern of [**32**+H]+ overlaps with patterns of dehydrogenated **32** but the sodium complex [**32**+Na]+ allowed a direct comparison with the simulated isotopic pattern (inset).

3.6.2. NMR Characterisation of Trimer **31** and Tetramer **32**

*Trimer **31***

The discussion in this section will be focused on the qualitative findings, rather than on the detailed reasoning behind the signal assignment which is covered in the experimental section. While in achiral environment enantiomers must have identical spectra, the spectra of stereoisomers (*M**,*M**,*P**)-**31** and (*M**,*M**,*M**)-**31** should be different. Therefore, in ideal case, NMR spectra of each stereoisomer should be treated separately. Unfortunately, the isolation of pure stereoisomers in amounts sufficient for NMR measurement was rather challenging and the analysis had to be performed on mixtures only enriched in (*M**,*M**,*P**)-**31** or (*M**,*M**,*M**)-**31**. Nevertheless, even spectra of these mixtures showed trends which proved very valuable for the correct structural assignment.

Regarding (*M**,*M**,*M**)-**31**, it has D_3 symmetry, therefore only one third of the molecule as a single structural unit needs to be considered. Conversely, the C_2 symmetrical (*M**,*M**,*P**)-**31** stereoisomer is expected to feature two distinct structural units. The actual challenge resided in the correct identification of these units. In the case of the highly symmetrical (*M**,*M**,*M**)-**31**, the situation is simple and only one type of (*M**,*M**) structural unit is present (Figure-33B). In the case of (*M**,*M**,*P**)-**31**, however, two alternative assignments are possible. Initially, (*M)*- or (*P)*-helicene with the adjacent phenylene vinylene units (analogous to monomer **43**) was considered as the structural unit, but the measurement of the stereoisomerically enriched mixtures ruled this possibility out. The second option is depicted in Figure 33A. (*M**,*M**,*P**)-**31** contains two units where one includes halves of helicenes of the same chirality (*M**,*M**) (note the blue numbering) while the other incorporates halves of helicenes of the opposite chirality (*M**,*P**) (note the red numbering).

Figure 38 shows a ^{1}H NMR spectrum of the equilibrium stereoisomeric mixture of (*M**,*M**,*M**)-**31** and (*M**,*M**,*P**)-**31**. The spectra of the individual stereoisomers are obviously rather similar, a slight difference in chemical shifts originating from the whole (*M**,*M**,*M**)-**31** and (*M**,*M**,*P**)-**31** molecules can be noticed in signals of atoms 16, 16† and 19, 19†. Besides that, the spectrum mainly consists of the superposition of the peaks of the (*M**,*M**) and (*M**,*P**) structural units regardless of their origin from a particular stereoisomer. As a result, the (*M**,*M**) unit belonging to the (*M**,*M**,*P**)-**31** is practically indistinguishable from that of (*M**,*M**,*M**)-**31**. This is a clear advantage, since the attention can be focused on the individual structural units and the signal assignment is not complicated by a cluttered forest of peaks.

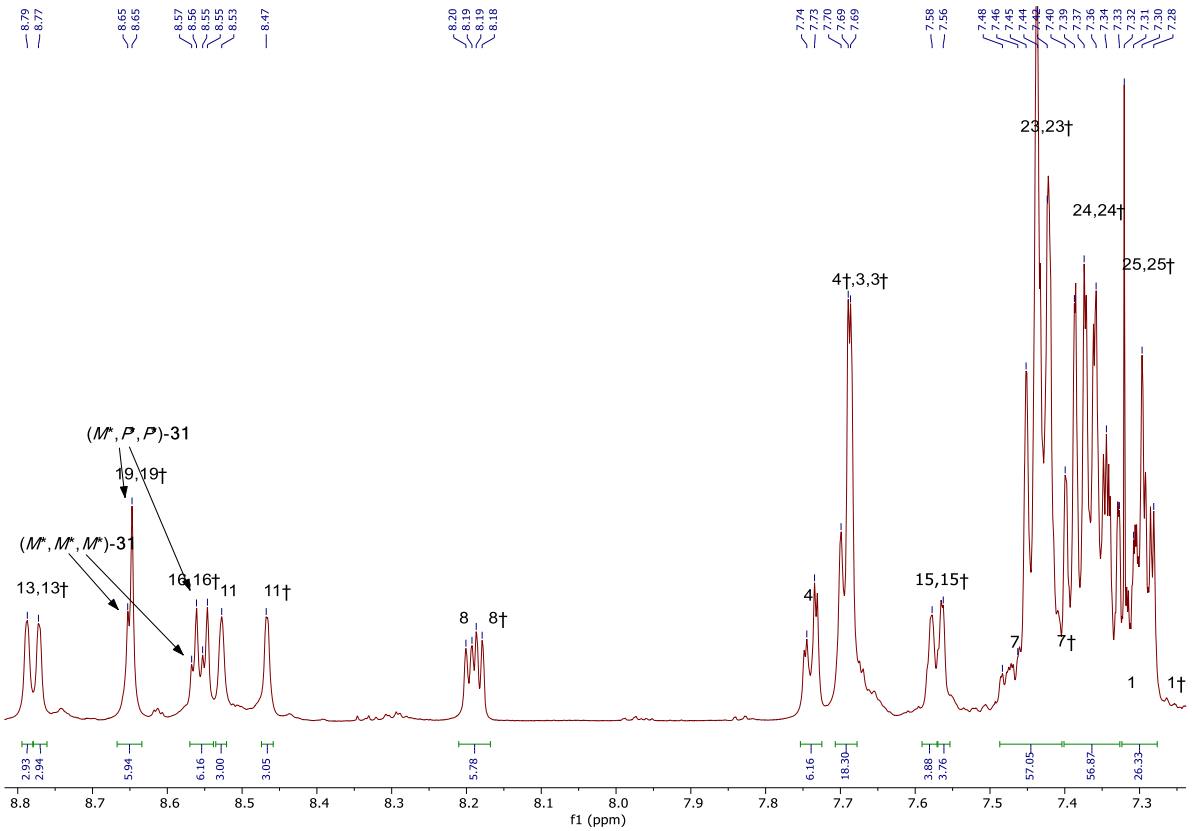

Figure 38. ^{1}H NMR spectrum of the stereoisomeric mixture of **31** with a signal assignment. In the case of protons 16, 16† and 19, 19† arrows show peaks corresponding to specific diastereomers.

The difference between the structural units is most pronounced in the case of atoms 11 (*M*,P**) and 11† (*M*,M**). Figure 39 shows a comparison of ^{1}H spectra of the equilibrium mixture of **31** and mixtures enriched in either (*M*,M*,M**)-**31** or (*M*,M*,P**)-**31**. The spectra show how the signal intensity of nuclei 11 and 11† is related to the composition of the mixture. In the case of the equilibrium mixture, the intensity ratio is almost exactly 1 : 1. The spectrum of the mixture with excess (*M*,M*,M**)-**31** shows a weaker signal of 11 and stronger signal of 11†, while in the case of the mixture with excess of (*M*,M*,P**)-**31**, the trend is opposite and the signal of 11 is stronger than that of 11†.

By integrating the proton signals of 11 and 11† it was possible to measure the molar ratio of (*M*,M*,M**)-**31** and (*M*,M*,P**)-**31**. Based on simple stoichiometric relations, it is easy to evaluate the signal intensity as a function of the stereoisomeric composition. Figure 40 shows that the intensity of 11 and 11† should be equal at 75% content of (*M*,M*,P**)-**31** which is the same value as that observed in the spectrum of the equilibrium mixture.

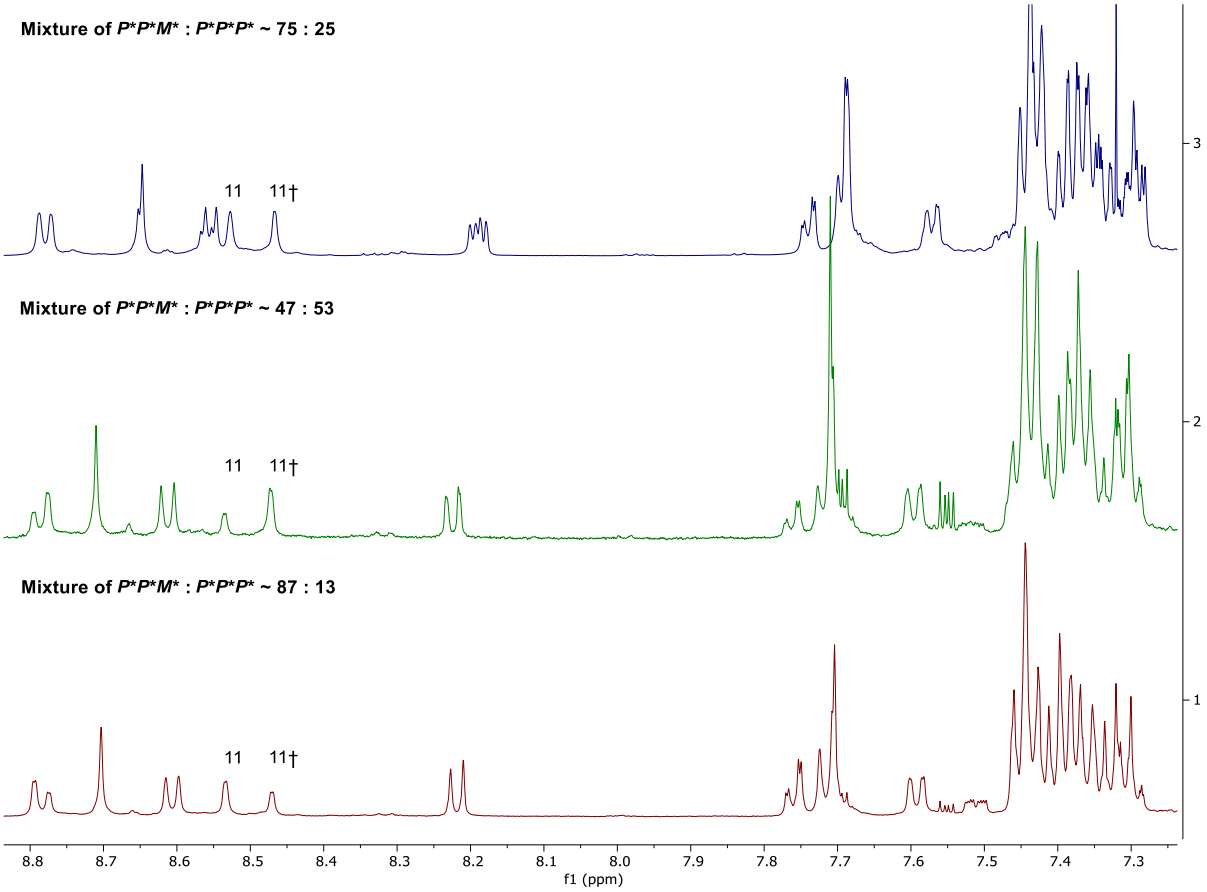

Figure 39. Comparison between the ^{1}H NMR spectra of the stereoisomeric mixture of **31** and the samples enriched in either (-)-(*M*,*P*,*P*)-**31** or (-)-(*P*,*P*,*P*)-**31** stereoisomers.

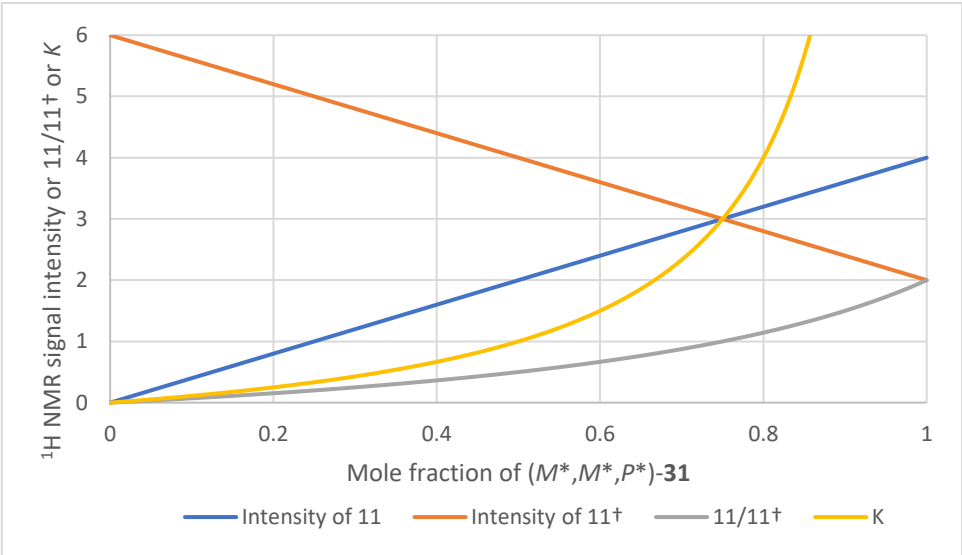

Figure 40. Diagram showing relationship between ^{1}H NMR signal intensity of protons 11, 11† and the mole fraction of (*M**,*M**,*P**)-**31** in the stereoisomeric mixture. Likewise, the diagram also shows the relationship between the mole fraction and the signal intensity ratio of 11/11† or the equilibrium constant *K = [*(*M**,*M**,*P**)-**31***]/[* (*M**,*M**,*M**)-**31***].* The number of protons 11 and 11† is related to the whole molecule, where in *(M*,M*,M*)-**31***, 11 and 11† have intensities of 0 and 6, respectively. Similarly, in *(M*,M*,P*)-**31**,* 11 and 11† have intensities of 4 and 2, respectively.

As seen from Figure 40, the equal intensity of proton signals 11 and 11† in the equilibrium stereoisomeric mixture is not a coincidence. To understand this, consider formation of the

macrocycle trimer **31** during the metathesis. Suppose the (*M*)- or (*P*)-helicene building blocks **43** of a specific helicity are incorporated into the macrocycle with a 50% probability. In other words, the helicity of the newly added helicene is independent of the helicity of the already present helicene units. When a trimer is formed under such conditions, the statistical distribution of the stereoisomers must be (-)-(*P*,*P*,*P*)-**31** : (-)-(*M*,*P*,*P*)-**31** : (+)-(*M*,*M*,*P*)-**31** : (+)-(*M*,*M*,*M*)-**31** = 1 : 3 : 3 : 1, which corresponds to (*M**,*M**,*P**)-**31** content in the equilibrium mixture of 75% - the same as experimentally obtained value. This finding means that the helicene building blocks in trimer **31** behave rather independently.

To further reinforce the above findings, variable temperature NMR of the equilibrium mixture was measured in the 22-140 °C range. Figure 41 shows that the stereoisomeric composition (measured by the ratio of 11 and 11† signal intensity) is practically independent of temperature, the same behavior as observed in the SFC analyses. Unfortunately, the precise measurement of the intensities was difficult due to a low quality of the measured spectra, so only qualitative conclusion can be drawn. Nevertheless, from a simple consideration of the enthalpic and entropic contributions to the Gibbs free energy based on the van't Hoff analysis, it follows that entropy plays a major role in determining the stereoisomeric composition of **31**.

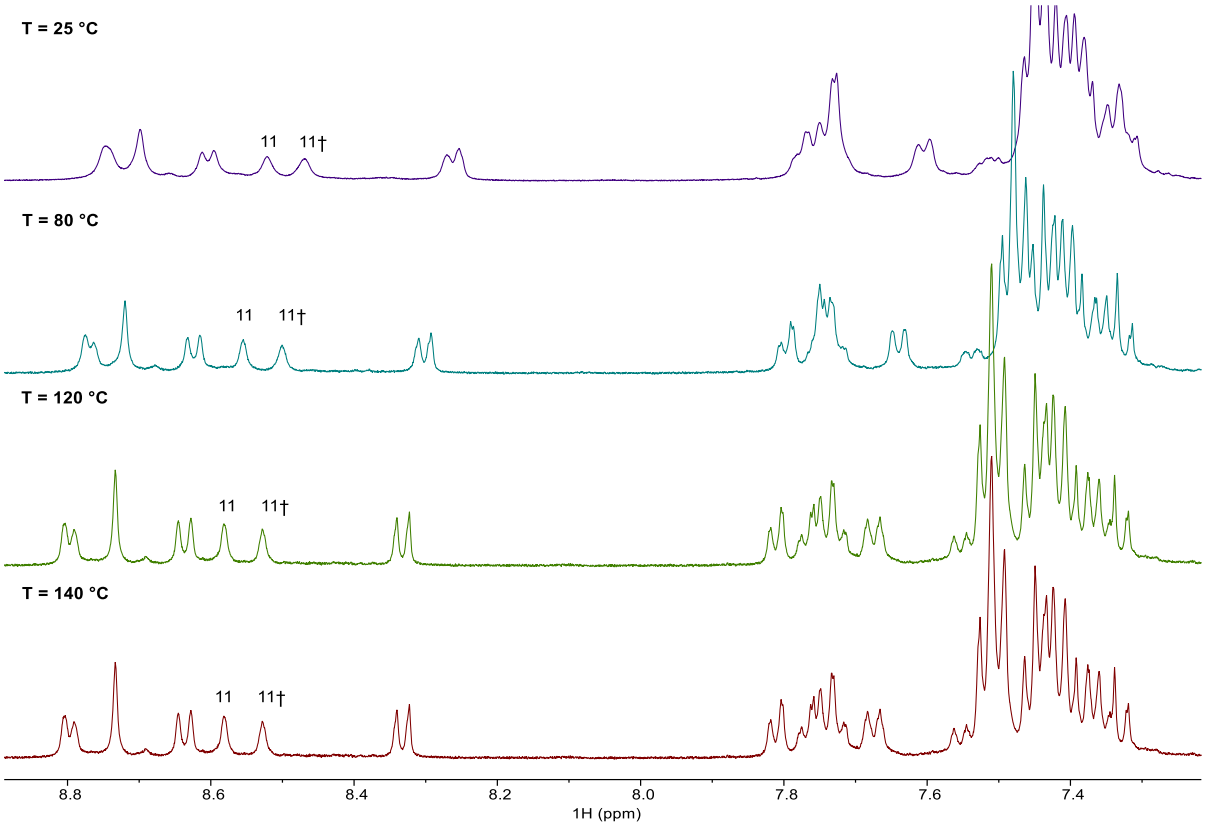

Figure 41. ^{1}H NMR spectra of the stereoisomeric mixture of **31** in $CDCl_2CDCl_2$ at various temperatures. The ratio between intensity of protons 11 and 11† is 1 and is practically independent of temperature.

It is noteworthy to mention that the statistical arguments presented in the preceding paragraph are simply a different formulation of the very same thing – the composition of the stereoisomeric mixture is dictated by the configuration entropy of the chiral elements within

the molecule **31**. In this context, the finding is just an extension of the well-known fact that racemization of chiral compounds is a purely entropy driven process.

*Tetramer **32***

Tetramer **32** was obtained as a complex mixture of stereoisomers, so only basic structural information was obtained from NMR measurements. The compound was poorly soluble in CD_2Cl_2 which led to a strong aggregation and very broad spectral lines (Figures 110 and 111). A better solubility was achieved by using $CDCl_2CDCl_2$ as a solvent which provided spectra with an apparent helicene structural pattern, especially at high temperature (Figures 42 and 116). Figure 42 shows a comparison between spectra of **31** and **32** at 140 °C. It can be noted that helicene, stilbene, and trityl signals, common to both **31** and **32**, are present in the spectrum of **32**. Although the integration in the region 7.30-7.60 ppm is obviously inaccurate, the integrals in the rest of the spectrum are in accordance with the expected stoichiometry of **32**. It is interesting that the signals at 8.47 ppm and 8.53 ppm from the (*M**,*M**) and (*M**,*P**) structural units in the spectrum of **31** collapse to one broad peak at 8.53 ppm in the spectrum of **32**. This could suggest that a symmetrical or even (*M**,*M**,*M**,*M**)-**32** stereoisomer forms the bulk of the mixture.

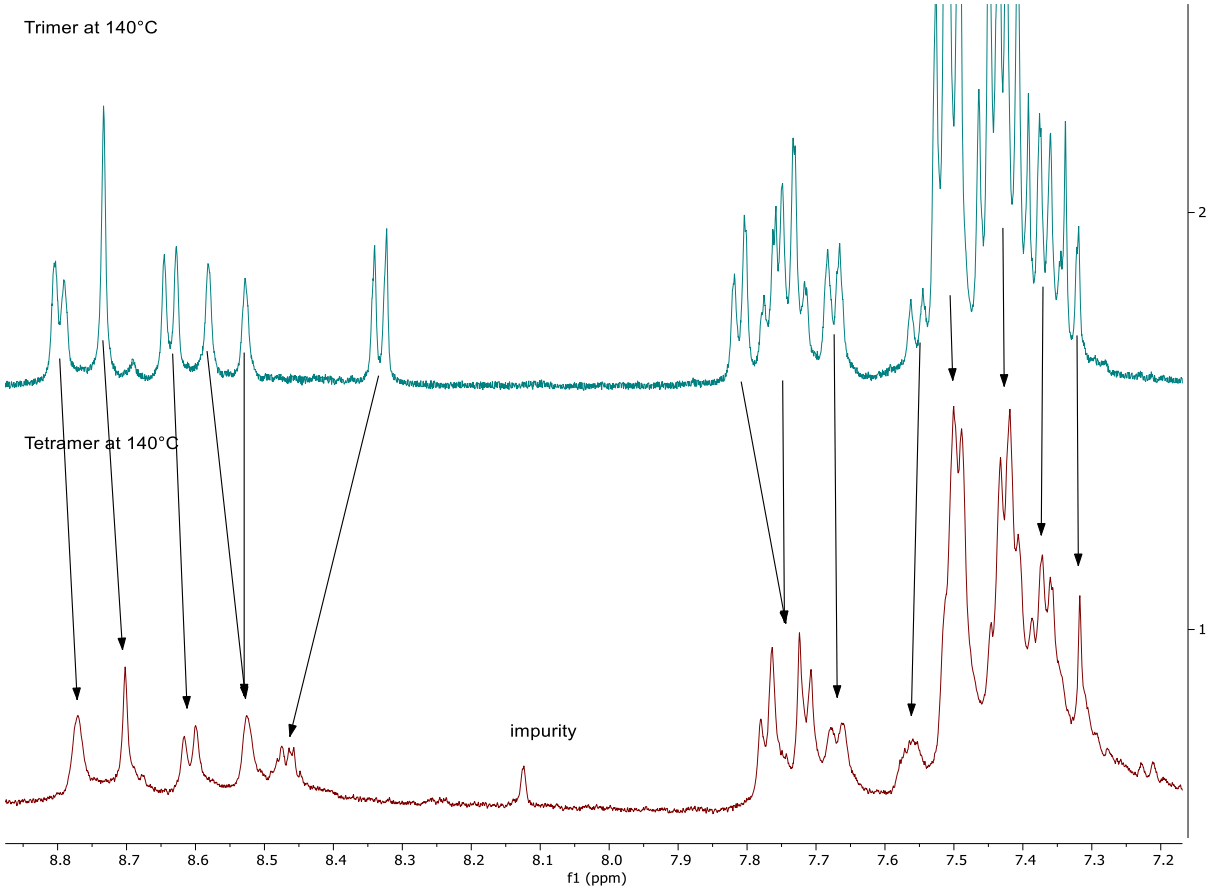

Figure 42. Comparison between ^{1}H NMR spectra of stereoisomeric mixtures of **31** and **32**, measured in $CDCl_2CDCl_2$ at 140 °C and 500 MHz.

To further show that the proton spectrum of **32** originates from molecules of a comparable size (and therefore similar diffusion coefficients), DOSY measurement of

a mixture of **31** and **32** was performed. **31** was added to the sample as a reference. However, while the signals of the obvious impurities at 6.99 or 8.12 ppm are separated, the cross peaks of **31** and **32** seem to have practically identical diffusion coefficients, as shown by the spectrum in Figure 43. This could also be the result of extensive aggregation of **31** and **32** into clusters which have similar diffusion behavior.

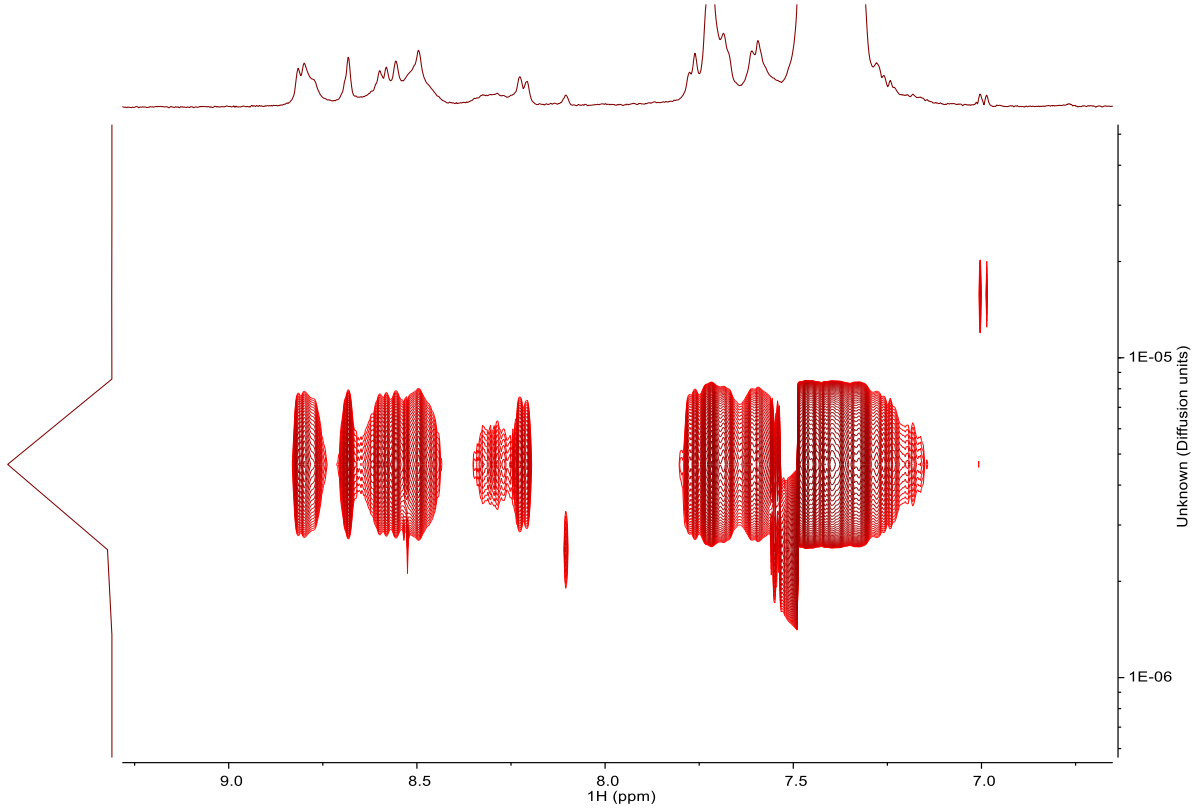

Figure 43. DOSY NMR spectrum of a combined mixture of **31** and **32**, measured in $CDCl_2CDCl_2$ at 500 MHz.

3.6.3. Optical Spectra of Trimer **31** and Tetramer **32**

*UV-Vis and Fluorescence Spectra of **31**, **32**, and **43***

Both trimer **31** and tetramer **32** are bright yellow resins exhibiting conspicuous blue fluorescence. The UV-Vis and fluorescence spectra of isomers of **31** and even that of **32** (studied as a stereoisomeric mixture) are all very similar (Figure 44). (-)-(*M*,*P*,*P*)-**31** has a UV-Vis absorption maximum at 349 nm (with the onset of the longest wavelength band at ca 450 nm) and an emission maximum in the fluorescence spectrum at 444 nm. (-)-(*P*,*P*,*P*)-**31** shows practically identical absorption bands in the UV-Vis spectrum but with notably lower intensity, while in the case of tetramer **32** the absorption intensity is even lower. The optical HOMO-LUMO gap of (-)-(*M*,*P*,*P*)-**31** calculated from the UV-Vis or fluorescence spectra is ca 2.8 eV. In comparison with the parent monomer **43** (UV-Vis maximum at 291 nm, absorption onset at ca 426 nm and emission maximum at 429 nm) (-)-(*M*,*P*,*P*)-**31** shows only a small red shift.

The above observations suggest that the electronic conjugation within the macrocycles is disrupted and connecting more helicene units has only marginal impact on the spectral

features. Similar results follow from TD-DFT calculations (see details in Chapter 5.11.), as the HOMO and LUMO orbitals are not delocalized over the whole cycle but, instead, reside on two helicene units.

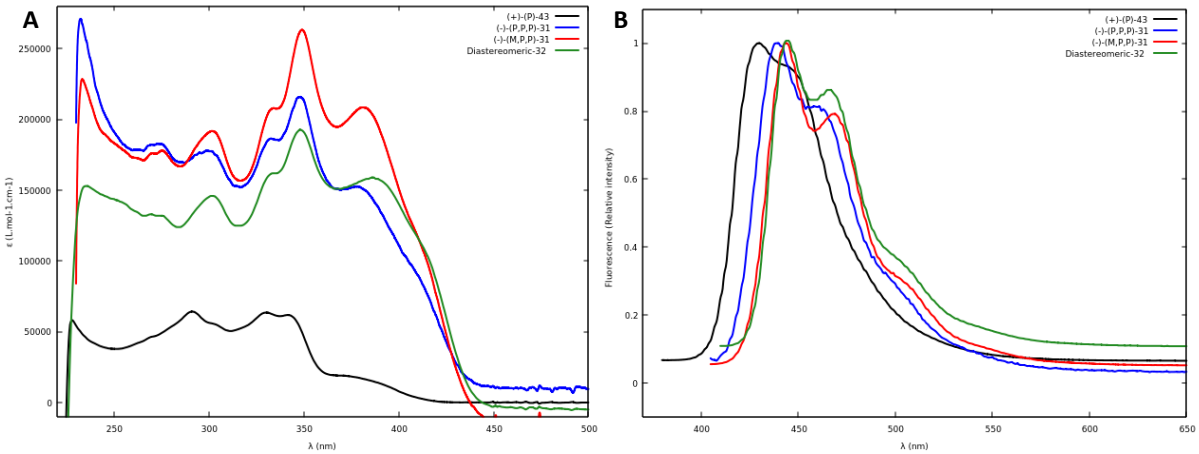

Figure 44. UV-VIS (A) and fluorescence (B) spectra of (+)-(*P*)-**43** (10^{-4} mol·L^{-1}), (-)-(*P,P,P*)-**31** (10^{-5} mol·L^{-1}), (-)-(*M,P,P*)-**31** (10^{-6} mol·L^{-1}), and a stereoisomeric mixture of **32** (10^{-4} mol·L^{-1}). Spectra were measured in $CHCl_3$. Fluorescence excitation parameters: **43** – λ_{ex} = 370 nm; **31** and stereoisomeric mixture of **32** – λ_{ex} = 400 nm, the fluorescence spectra were normalized to the highest intensity band.

*ECD Spectra of **31**, **43**, and **45***

The ECD spectra followed trends observed also in other measurements – the rather independent behavior of the helicene units within the macrocycle. Figure 45 shows only modest differences between (-)-(*P,P,P*)-**31** and (-)-(*M,P,P*)-**31**. The spectrum of the heterochiral (-)-(*M,P,P*)-**31** has a lower intensity, likely reflecting the smaller proportion of the (*M**,*M**) structural units. Surprisingly, while the sign of optical rotation is the same for (-)-(*P,P,P*)-**31** and (-)-(*M,P,P*)-**31**, in the case of monomer building block (+)-(*P*)-**43** the sense of optical rotation is reversed. This finding demonstrates that, aside from the chirality of the individual building blocks, the influence of the macrocycle overall shape on its chiroptical properties should not be underestimated. Although individual (+)-(*M,M,M*)-**31** and (+)-(*M,M,P*)-**31** could not be measured, the mirror-symmetric ECD spectrum of their mixture shows the same, but reflected features, as in the case of (-)-(*P,P,P*)-**31** and (-)-(*M,P,P*)-**31** (Figure 45A).

By comparing the ECD spectra with their TD-DFT calculated counterparts, it was possible to assign the absolute configuration of the studied molecules (Figure 46). Unfortunately, **31** and **43** exist as a mixture of a large number of conformers, mainly due to the present trityl groups. The calculations revealed significant spectral differences between the individual conformers and, therefore, the modeled spectra had to be formed by a Boltzmann averaging of the spectra of the most populated conformers. The conformer input geometries were taken from the calculations discussed in Chapter 3.5. The monomer building block **43** showed a satisfactory agreement allowing the assignment of its absolute configuration. In the case of trimer **31**, the agreement between the calculated and experimental results was less convincing, but still showed the most prominent features as their experimental counterparts. For additional comparison, experimental and calculated ECD spectra of dibenzohelicene **44**

were also compared. Here, Figure 46D shows a very convincing agreement of the predicted and measured spectra. It was shown that for helicenes, the sign of the longest wavelength band in the ECD spectrum is characteristic of their helicity. The configuration assignment of (-)-(*M*)-**43** was therefore also confirmed by comparison with the spectrum of (-)-(*M*)-**45.**

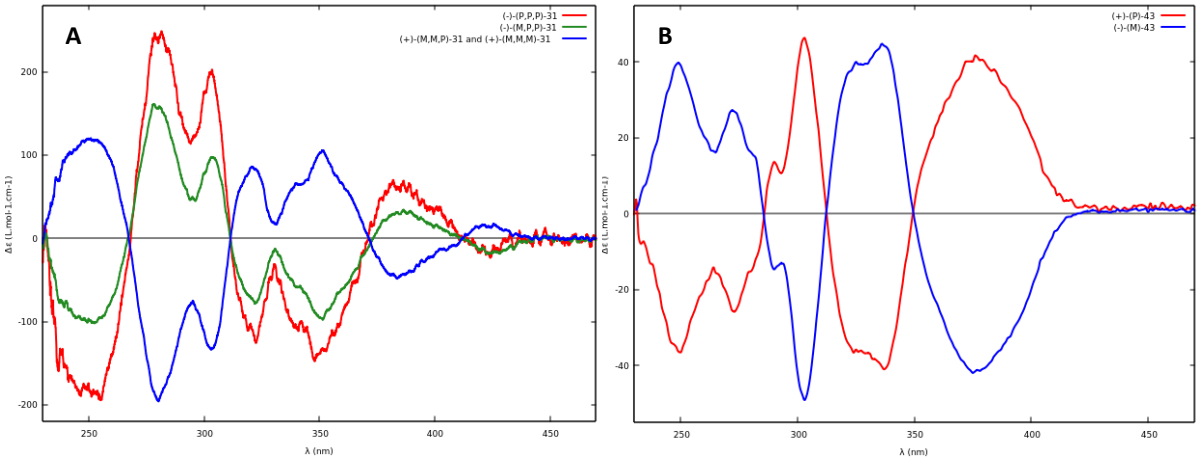

Figure 45. ECD spectra of (-)-(*P*,*P*,*P*)-**31** (10^{-6} mol·L^{-1}), (-)-(*M*,*P*,*P*)-**31** (10^{-5} mol·L^{-1}), and mixture of (+)-(*M*,*M*,*P*)-**31** and (+)-(*M*,*M*,*M*)-**31** (10^{-5} mol·L^{-1}) (A); and of (-)-(*M*)-**43** and (+)-(*P*)-**43** (10^{-4} mol·L^{-1}) (B).

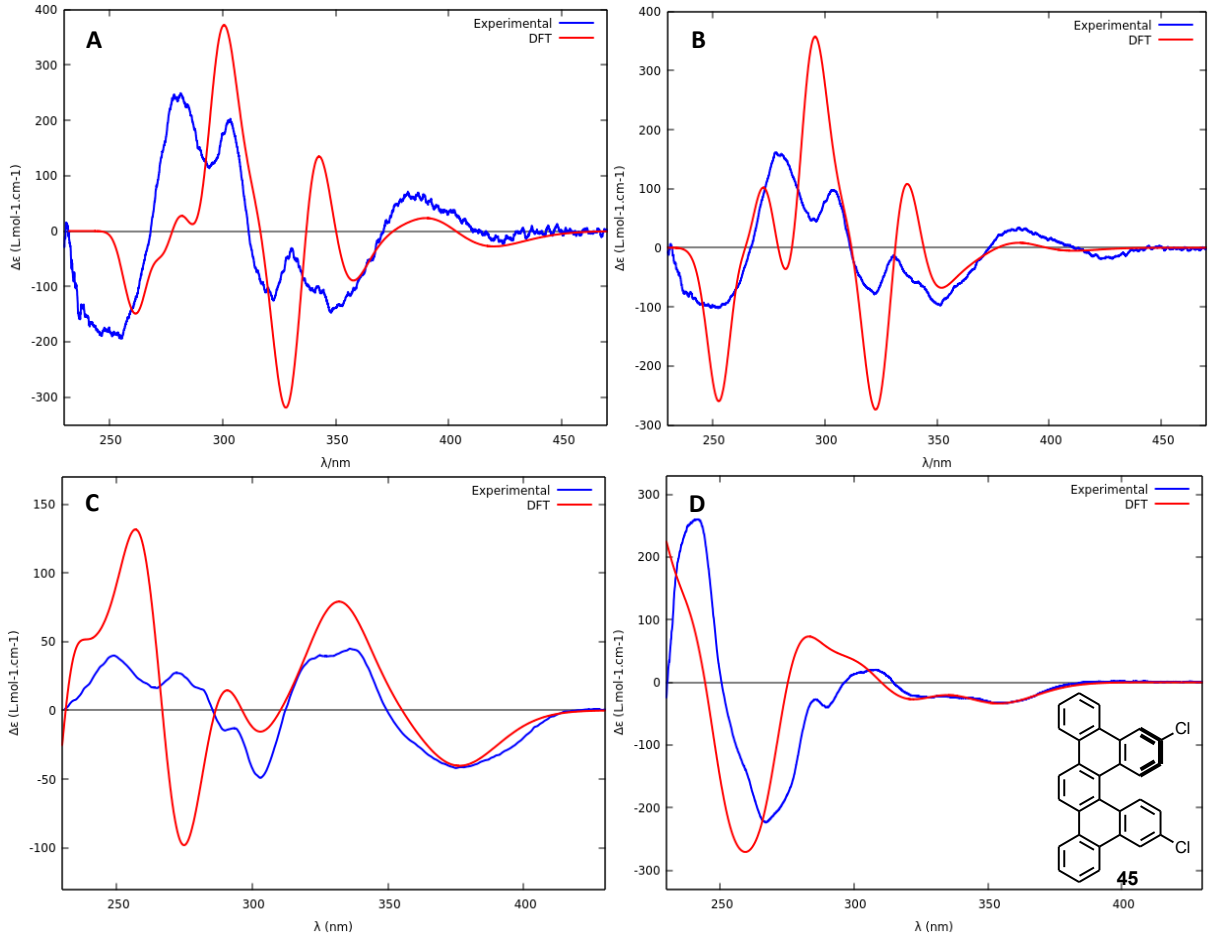

Figure 46. Comparison of measured and TD-DFT calculated ECD spectra of (-)-(*P*,*P*,*P*)-**31** (10^{-6} mol·L^{-1}), 120 singlet states (A); (-)-(*M*,*P*,*P*)-**31** (10^{-5} mol·L^{-1}), 120 singlet states (B); (-)-(*M*)-**43** (10^{-4} mol·L^{-1}), 120 singlet states (C); (+)-(*M*)-**45** (10^{-5} mol·L^{-1}), 200 singlet states (D). The spectra were measured and calculated in $CHCl_3$ and expressed in differential molar extinction Δε, σ = 0.3 eV.

3.6.4. Final Chirality Assignment to Stereoisomers of **31**

Although stereoisomers of **31** have been so far discussed throughout the text with their configuration assigned, mainly to avoid confusion, from the research perspective, only with all the information compiled from the synthesis and separation of **31**, the kinetic measurements, and finally the ECD spectra of **31**, **43** and **45**, it was possible to make final conclusions regarding the stereochemistry of **31**. Chirality assignment of **31** is a nice example where such information can be obtained only through an interdisciplinary approach.

3.7.Self-Assembly of Trimer **31** and Tetramer **32** on Solid Surfaces

*Measurement of Trimer **31***

As outlined in the Theoretical Part, the self-assembly of conjugated macrocycles have been intensely studied by SPM techniques, both in ambient environment and under UHV conditions. Although the superior environmental control of the UHV techniques provides unmatched resolution, such experiments are at the same time jeopardized by their methodological complexity. Moreover, in most experimental setups, the studied molecules can only be deposited by thermal evaporation within the UHV system which limits the experiment to molecules with small molecular weight. Although this substantial weakness of the thermal deposition has been overcome by using techniques such as electro spray ionization deposition[121–125] or its more advanced cousin electrospray ion beam deposition,[126–128] these promising methods are still available only to a very limited number of experimentalists.

In contrast, the ambient SPM provides a cost-effective and methodologically facile alternative at the expense of the resolution and a range of compounds which can be studied. While the UHV experiments are particularly suited for small molecules whose surface mobility can be easily tuned by the choice of the measuring temperature or the underlying substrate, under ambient conditions, the thermal motion of the studied molecules is so prominent that additional stabilization groups must be introduced to the molecule structure. These functionalities serve to increase the intermolecular as well as molecule-surface interactions. Most frequently, long alkyl chains[129–131] are used for this purpose for their extensive Van der Waals interactions with each other and, particularly in the case of HOPG, with the surface. Similarly, other strongly interacting groups, such as carboxyl capable of relatively strong hydrogen bonding, can be employed to stabilize the surface assemblies.[66,132–134]

In the light of the preceding discussion, trimer **31** with its six trityl groups (18 phenyls) represents an interesting system in terms of its on-surface behavior. Since the non-planar molecules **31** do not contain any strongly interacting groups, it was anticipated that their surface assemblies would be rather unstable. Indeed, the preliminary standard STM and AFM measurements did not show stable aggregates of **31** deposited on HOPG(001) or Au(111) surfaces, indicating the fragile nature of the formed assemblies. Therefore, different approaches to the AFM measurements had to be taken to successfully image assemblies of **31** on solid surfaces.

3.7.1. AFM Measurements on HOPG

A stereoisomeric mixture of **31** was drop-cast as a dichloromethane solution on HOPG surface and left to evaporate. The samples were then scanned by AFM in air at room temperature.

Only very low-quality images were obtained when the standard tapping AFM mode was used. However, when the PeakForce measuring mode[96] was employed, images with submolecular resolution could be obtained. The success of this choice stems from superior

control of the tip-substrate interactions attained by the PeakForce mode, limiting the disruption of the surface assemblies by the tip. Apart from the PeakForce, standard tapping, and contact AFM modes, a technique developed by Korolkov *et al*[101] was also tried. In this case, the scanning was performed using the tapping mode at the higher cantilever eigenmode frequency. Indeed, this imaging mode initially produced promising results, but the tip was quickly contaminated, with a consequent loss of resolution.

Pertaining to the choice of the AFM probes, cantilevers with an ultra-sharp (nominal tip radius down to 2 nm) and soft (spring constant less than 0.4 N/m, such as SNL-A or SNL-B cantilevers from Bruker), proved to deliver reliable and reproducible results. Other probes, such as Multi75Al (BudgetSensors), were also tested, occasionally giving acceptable resolution, especially after treatment with CF_4 plasma.[135]

With the optimal imaging conditions, the AFM measurements revealed that **31** forms various assemblies on the HOPG surface. At low surface coverage, individual small islands of molecular aggregates were found (Figure 47). With the increasing surface coverage, gradually larger 2D-crystalline domains were found (Figure 48). The small island shown in Figure 47A shows that the 2D crystals are formed by molecules arranged in long stripes. In the lower right part of the aggregate even individual molecules can be noticed (note the inner hole in the macrocycle, highlighted by a white arrow). However, on most AFM scans, the individual molecules were not resolved and, instead, the molecular stripes showed internal structure with faint regular depressions in the middle of the stripe (see the second and third stripes from the bottom in Figure 47A).

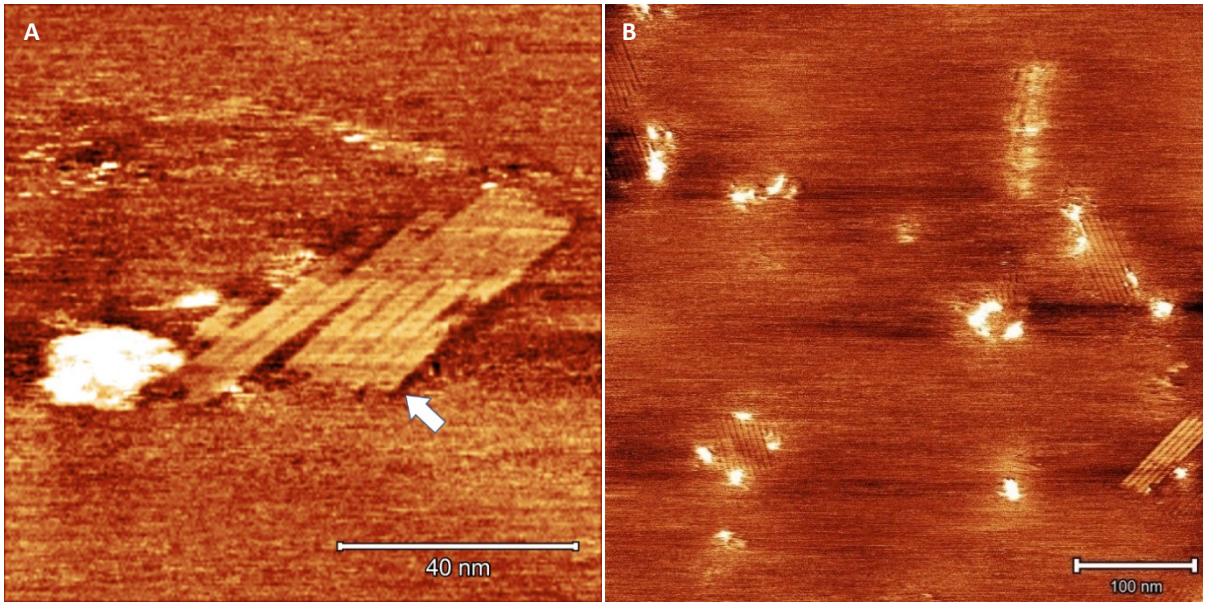

Figure 47. AFM images of samples prepared from ca 12.5% of (-)-(*P,P,P*)-**31**, 12.5% of (+)-(*M,M,M*)-**31**, 37.5% of (-)-(*M,P,P*)-**31**, and 37.5% of (+)-(*M,M,P*)-**31**. A small island of molecules arranged into stripes where two adsorption isomers are apparent. White arrow indicates individual molecules (A); Isolated islands of molecular assemblies aligned with the graphite lattice (B).

Depending on the mode of sample preparation and a particular region on the sample, the structure of the observed layers varied slightly. When the sample was prepared by a simple drop-casting at room temperature, a large proportion of disordered mass was present on the surface. Conversely, when the solution was applied onto a sample held at 30 °C in a chamber

filled with the solvent vapor to suppress evaporation, the degree of ordering increased significantly.

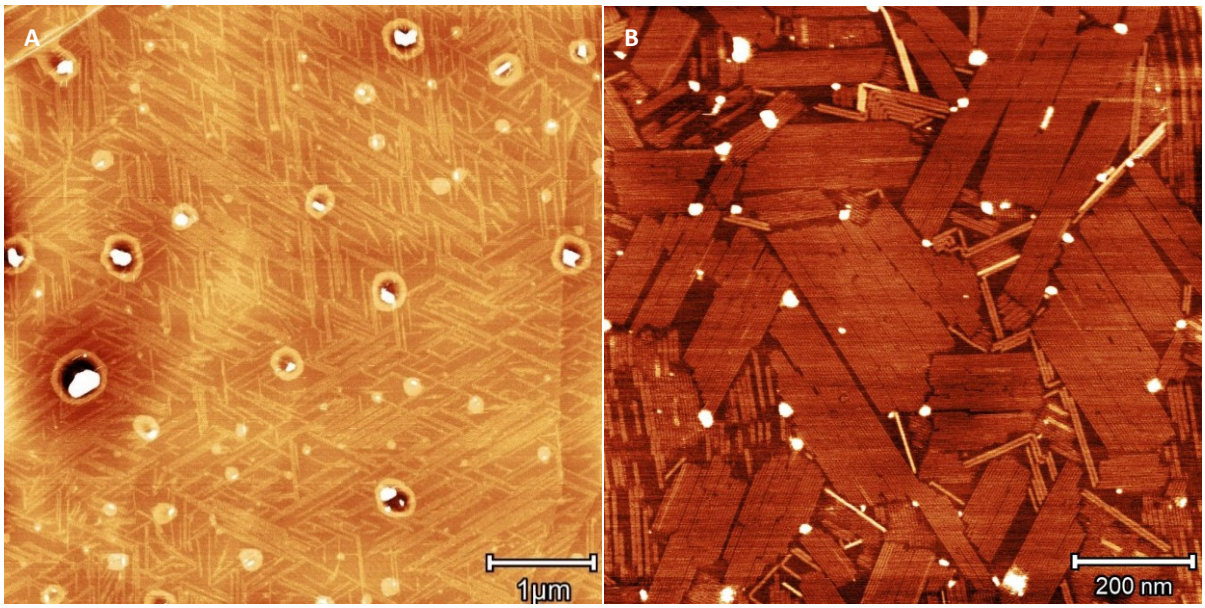

Figure 48. AFM images of samples prepared from ca 12.5% of (-)-(*P,P,P*)-**31**, 12.5% of (+)-(*M,M,M*)-**31**, 37.5% of (-)-(*M,P,P*)-**31**, and 37.5% of (+)-(*M,M,P*)-**31**. Surface covered with narrow stripes of vastly unified orientation on the surface. The layer is occasionally broken by much taller nanocrystals (A). Image showing a rich variety of structural forms adopted by **31** (B).

A closer inspection of the molecular adlayers showed stripes 4.6-4.8 nm wide and up to several hundred nanometers long. The fact, that majority of the observed 2D crystals are longer and with smooth edges (except occasional defects) along the direction of the molecular stripes suggests a greater stability of the molecules within the stripes compared to the inter-stripe stability. This preference reveals directional interactions between the molecules within the individual stripes. Although the perimeter of free molecules **31** with its six trityl groups forms an almost ideal hexagon, the molecule itself has roughly trigonal symmetry which is broken upon aggregation into the stripes. The possible explanation was provided by the MD simulations and is discussed in Chapter 3.7.2.

As far as the height of the adlayers is concerned, it was often substantially lower than expected from the molecular geometry. This might be caused by a large elasticity of the molecules which are compressed under the tip.

It is apparent from the AFM images that the molecules in the assemblies are ordered, but the AFM did not have a sufficient resolution to image the detailed periodic structures on the molecular level. Therefore, besides the inter-stripe distance, other lattice parameters of the adlayers could not be reliably obtained only from the AFM images. The same limitation also applies to the resolution of the underlying graphite lattice, preventing the estimation of the azimuthal tilt of the adlayers with respect to the HOPG lattice. Nonetheless, the unified orientation of the isolated 2D-crystals suggests that their mutual orientation of ca 120° is controlled by the substrate lattice. This is commonly interpreted as a sign of an epitaxial growth of the adlayers (see Chapter 1.3.4.). Considering the dense packing and a large size of **31** in the adlayers, it is likely that the molecules assemble in coincidence with the substrate lattice.

The above observations were further expanded by a statistical analysis of exact measurements of the mutual orientation, which revealed a 5.4 ± 0.1° deviation between the expected 120° directions (Figures 48A, 86A and B). Apart from the different tilt the domains appear to be identical, but since their detailed internal structure was not resolved, it was difficult to make any conclusions about their enantiomorphism.

Although the hexagonal orientation of the adlayers was the most frequent adsorption mode observed but occasionally, structures with other geometries were also observed. Examples are shown in Figures 48B and 50 where assemblies of various sizes and geometries can be found. Many domains indeed follow the predominant hexagonal pattern, but there are also many structures having almost orthogonal mutual orientation. Such a rich variety of the observed structural patterns suggests that the self-assembly process is influenced by many variables. Although these were not studied systematically in this Thesis, the most important factors are briefly discussed in the following paragraphs.

The role of the concentration of the drop-cast solution is not straightforward in this case. It is important to remind the reader that AFM is a local analytical method, revealing the topography of a very small part of the sample. Therefore, to make any general conclusions, a large number of samples must be studied. In this view, the impact of different concentrations is rather difficult to study under the conditions used in the discussed experiments. During the drop-casting process, the solvent applied to the HOPG surface gradually evaporates and the solute concentration increases. At a certain point, the uniform liquid layer breaks into numerous isolated zones separated by a dry surface. As the liquid zones get smaller, the solute concentration further increases, accompanied by its crystallization. The regions where the solvent evaporated first usually have only small surface coverage with the solute, while the highest surface coverage is found on regions where the solvent evaporated last. The initial solute concentration is therefore of only limited importance, determining is the surface concentration on a particular spot of the sample. Moreover, since the evaporation process was rather fast, many observed aggregates might have been kinetically frozen far from the thermodynamic optimum.[68] This is in stark contrast to the STM studies of various molecules performed on the solid/liquid interface where the concentration usually changes only slowly, giving the system more time to find thermodynamically more favored structures.[67]

To find sample regions with a desired concentration, optical camera images of the surface could be conveniently used. Molecular layers of up to several hundred nm thick were often revealed by prominent interference patterns on the HOPG surface (see example in Figure 88 in Chapter 5.8.). These patterns were particularly useful for identifying places with a desired surface coverage. The visible structures were generally very difficult to measure, as the adsorbed molecules did not have high degree of ordering and the large molecular concentration rapidly contaminated the AFM tip, leading to the loss of resolution. Moving away from the visible layers gradually led to a decreased surface coverage. Spots several μm from the visible layers were often covered with only isolated islands of small molecular assemblies or were even totally free of molecules.

The influence of the underlying substrate on the structure of the assemblies is demonstrated by Figure 50. Molecules adsorbed on large graphite terraces assembled into regular, well ordered 2D crystals. In contrast, unusual orthogonal molecular stripes could be often seen on small graphite terraces. Apparently, the growth of aggregates requires unhindered surface diffusion of the free molecules. As the graphite step edges represent a significant diffusion barrier, densely packed aggregates cannot form on small terraces due to a limited amount of material present within the terrace.

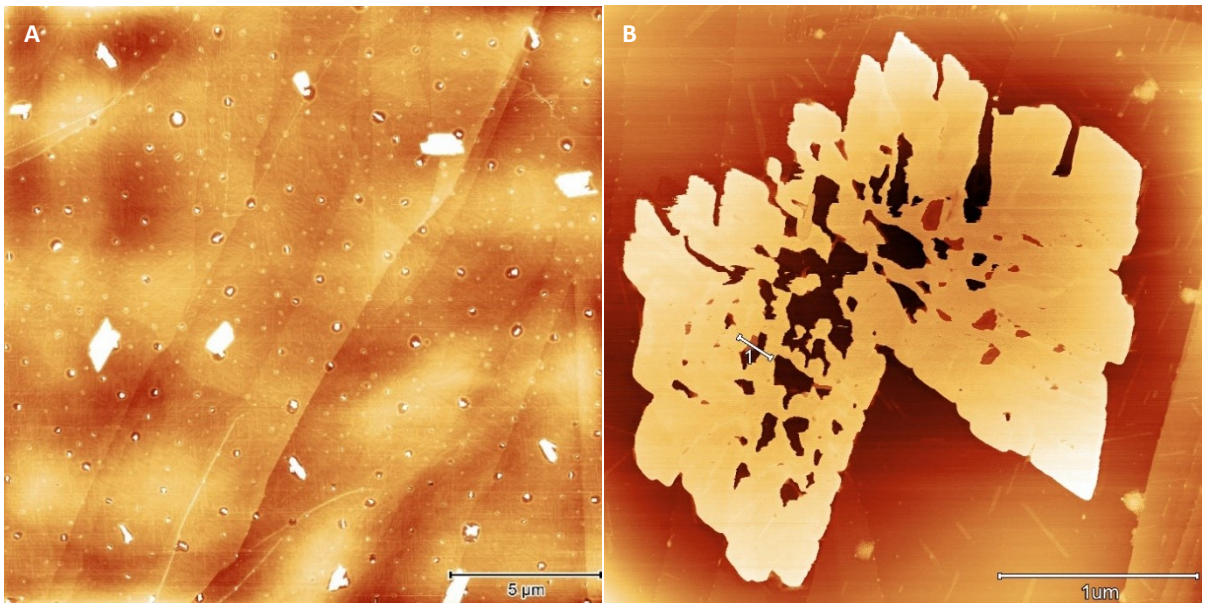

Figure 49. AFM image of a larger area on the same sample as shown in Figure 48A showing numerous large nanocrystals (A). AFM image of a large nanocrystal prepared from 5% of (-)-(*M,P,P*)-**31**, 67% of (+)-(*M,M,P*)-**31**, and 28% of (+)-(*M,M,M*)-**31** mixture (B). Line 1 indicates the direction of a profile shown in Figure 87, Chapter 5.8.

The limiting role of the surface diffusion can also be noted in Figure 49A. The surface is covered with dense layers of **31** along with numerous 3D-nanocrystals. Many nanocrystals are visibly surrounded by a circular zone of depleted material used in the process of crystal growth. The size of the crystals is, therefore, likely limited by a diffusion-controlled mass transport over large surface distance before the solvent evaporates. The lateral size of these crystals reached up to several micrometers with height of several nanometers, as exemplified by Figure 49A. Figure 49B then shows an example of such a large crystal in detail. The crystal structure features ca 4 nm vertical steps along the measured line profiles. Based on this value, the molecules in the crystals likely favor a vertical orientation with respect to the graphite surface as opposed to the horizontal orientation observed in the 2D assemblies.

As mentioned above, many assemblies of **31** were likely kinetically frozen due to the fast evaporation during the sample preparation. This is demonstrated on a 1×1 µm^2 region shown in Figures 50A and B which shows a dynamic nature of even the dry self-assembled layers. A smaller section of the region (333×333, later 500×500 nm^2) was selected and scanned repeatedly. Figure 50B shows the same 1×1 µm^2 area shown in Figure 50A after 9 such scans. Figures 50C and 50D, respectively, show the same scans but in the deformation QNM channel which emphasizes the compression and expansion of the adsorbed molecules during the mechanical interaction with the AFM tip. Here, the bright contrast highlights the adlayers

more easily deformed by the tip. Substantial structural changes can be noticed in many places, of which the most obvious is a large surface reconstruction in the middle of the scan. While the central part of Figures 50A and C shows many structurally diverse domains, a large single domain formed after the repeated scans of the region (Figures 50B and 50D). Admittedly, as scanning such a large region took several hours, the regions are partially spatially shifted due to the thermal drift (mostly in the downward direction), but the corresponding structures before and after the repeated scans can still be easily identified.

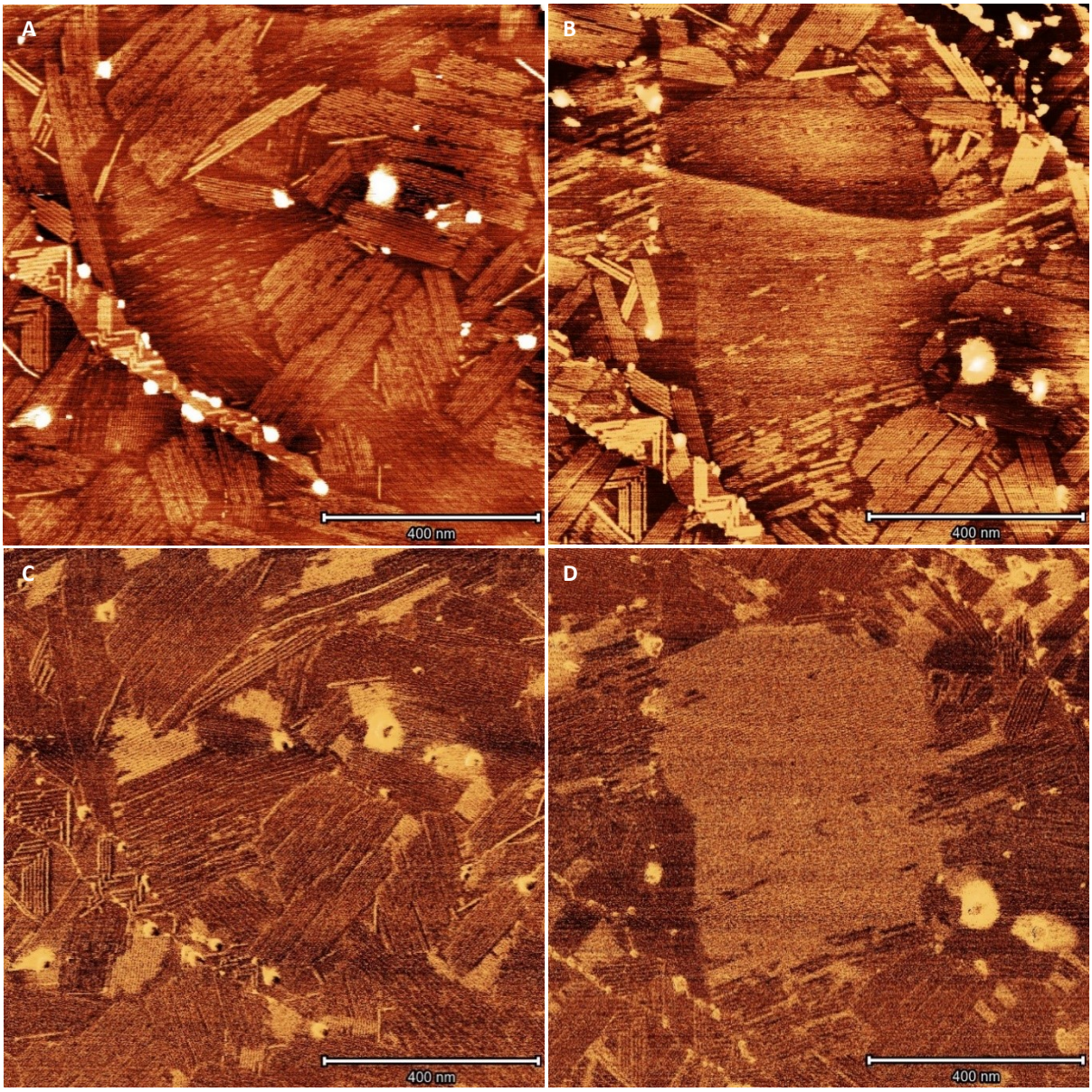

Figure 50. AFM images of samples prepared from ca 12.5% of (-)-(*P,P,P*)-**31**, 12.5% of (+)-(*M,M,M*)-**31**, 37.5% of (-)-(*M,P,P*)-**31**, and 37.5% of (+)-(*M,M,P*)-**31** Topography channel showing many different domains on several graphite terraces (A); The same area after 9 additional scans showing a reconstruction into a large uniform domain (B); respective images in the deformation channel (C and D).

Even though the reconstruction proceeded irreversibly towards a uniform domain with a higher deformability, the explanation on the molecular level remains elusive. The change in the deformation can reflect simple changes in the molecular packing or the mode of

interaction with the surface. But it could also signify the tip-induced change of stereochemistry of the adsorbates. Nevertheless, even with experiments on the stereoisomerically pure samples, the insufficient data renders the precise interpretation of these results inconclusive.

Besides the surface reconstruction, subtle structural changes can be noticed on many aggregates. These observations indicate that the molecules are adsorbed only weekly to the surface which allows a facile molecular movement and reassembly of the adlayers upon even a gentle stimulus. It cannot be excluded that such changes occur spontaneously during the long scanning period. In the case of the large surface reconstruction, however, it can be safely stated that it would not have occurred without the repeated interaction with the AFM tip because such event was never observed on samples studied during the course of even several months.

Measurement of Non-Racemic Mixtures

Unfortunately, a systematic study of the influence of the stereoisomeric composition on the structure of the self-assembled adlayers was limited, as only (-)-(*P*,*P*,*P*)-**31** was available in a sufficiently pure form and other isomers were obtained only in mixtures of varying composition. The first noticeable difference from the racemic samples was the lower stability of the non-racemic adlayers during the AFM measurement, resulting in a substantially lower resolution and severe tip contamination. Imaging areas smaller than 100×100 nm^2 with a good resolution was practically impossible as the molecules were easily moved by the tip. Although no direct proof was obtained, it might indicate that in the samples prepared form racemic **31** the molecules prefer to assemble into racemic rather than conglomerate domains.

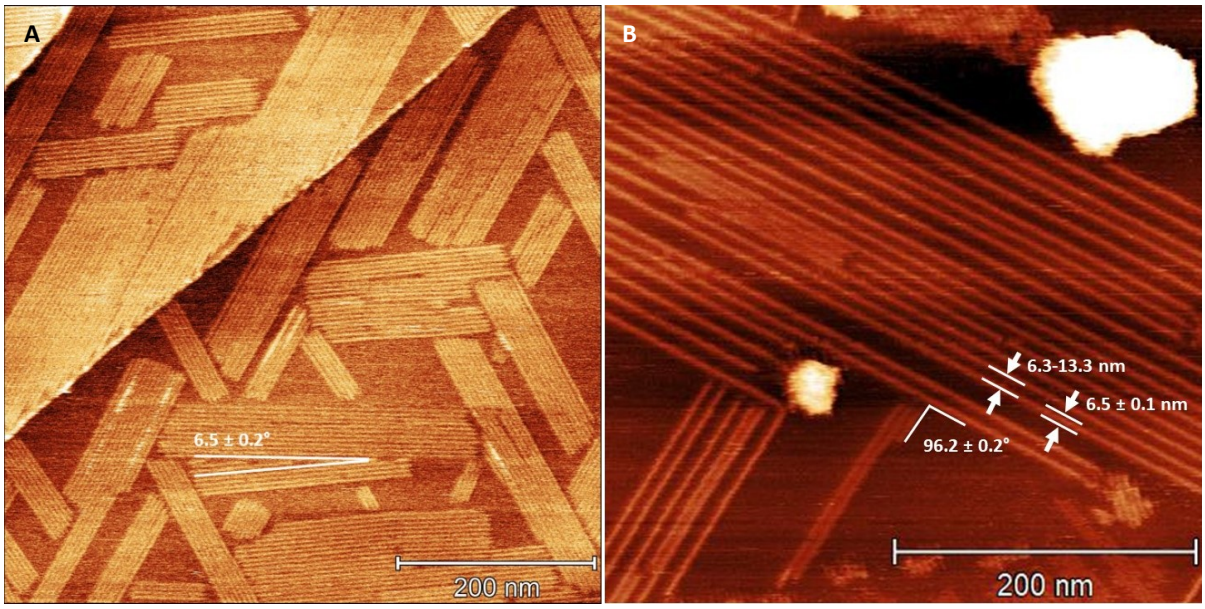

Figure 51. AFM image of (-)-(*P*,*P*,*P*)-**31** (ca 95% *de*). The stereoisomer forms large, highly ordered domains of a single type with the angle between different adsorption isomers of 6.5 ± 0.2° (A). AFM image of samples prepared from a mixture of 75% of (-)-(*M*,*P*,*P*)-**31**, 17% of (+)-(*M*,*M*,*P*)-**31**, and 8% of (+)-(*M*,*M*,*M*)-**31**. High proportion of domains with almost rectangular symmetry were found. Lines with large separation and a low tendency to form close packed structures. Image also shows angles between different line directions as well as the line separations (B).

Apart from the factors discussed above, the stereoisomeric composition of the deposited mixtures had a profound effect on the structure of the adlayers. Figure 51A shows an AFM image of a sample prepared from (-)-(*P*,*P*,*P*)-**31** on HOPG showing large domains, very similar to those of stereoisomeric **31**. The molecules are arranged in long stripes over 500 nm in length. The distance between the centers of the individual stripes was ca 4.8 nm with the mutual orientation of the domains 120°, the same values which were observed in the racemic mixtures. The deviation from the expected 120° directions between the domains was again statistically significant and slightly higher to be 6.5 ± 0.2°.

When samples prepared from a mixture containing an excess of (-)-(*M*,*P*,*P*)-**31** were scanned, apart from the usual hexagonal domains with the inter-stripe separation of ca 4.8 nm, numerous aggregates of a very diverse structure were found on the surface (Figure 51B). The most interesting example concerns several hundred nanometers long and 6.5 ± 0.1 nm wide stripes, with a separation of 6.3 -13.3 nm, with the mutual angle between the stripes 96.2 ± 0.2°. As the diameter of molecule **31** is ca 3.5 - 4 nm, the packing in the stripes must be substantially different from that in the hexagonal domains. It is also interesting that such 1D crystals are stable considering the lateral intermolecular stabilization is available only in one dimension. In this case the deviation from the average directions was not investigated because of the small number of suitable areas.

Changing the composition of the mixture to 5% of (-)-(*M,P,P*)-**31**, 67% of (+)-(*M*,*M*,*P*)-**31**, and 28% of (+)-(*M*,*M*,*M*)-**31**, the AFM images showed mostly adlayers with a hexagonal arrangement, occasionally interrupted by domains of notably different packing and symmetry (Figure 52A).

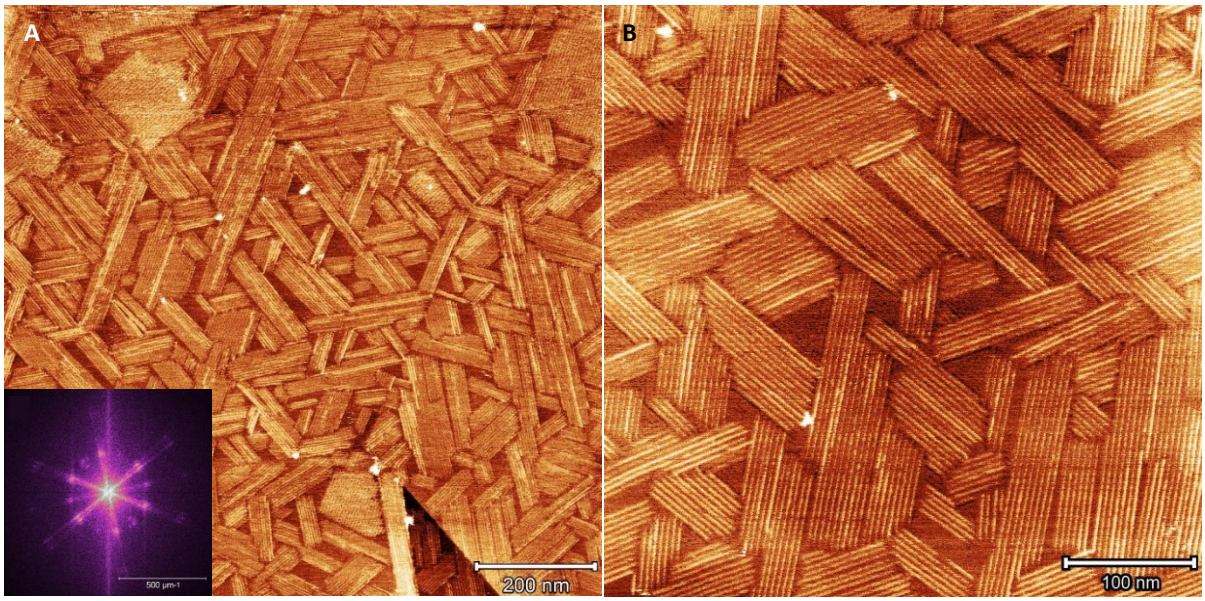

Figure 52. AFM images of samples prepared from 5% of (-)-(*M,P,P*)-**31**, 67% of (+)-(*M*,*M*,*P*)-**31**, and 28% of (+)-(*M*,*M*,*M*)-**31** Large scan showing different domain types (A) and a crop of a small region showing the hexagonal assemblies in detail (B). Inset shows 2D FFT of image (A), featuring twelve-fold orientation of the adsorbates.

The above findings demonstrate that adlayers formed from racemic mixtures and from pure (-)-(*P*,*P*,*P*)-**31** enantiomer are rather similar. The dimensions and orientation of the domains, as well as their internal structure, share common features, although the exact

values vary slightly. Interestingly, for samples prepared from non-racemic mixtures, structural patterns with less dense packing and of non-hexagonal symmetry emerged. Although more data would be necessary to confirm the observed trends, the influence of the stereoisomeric composition on the adsorbate structure was clear. Similar results were observed by Fasel *et al*. in the case of helicenes on Cu(111) surface.[136] A small change in enantiomeric composition caused a substantial change in the structure of the studied adsorbates.

*Measurement of Tetramer **32***

The samples made of tetramer **32** prepared in an identical fashion as those of **31** were studied by AFM (Figure 53). In this case, however, the molecules did not form well-ordered assemblies. Most often, only clusters of molecules of varying height without a resolved internal structure were found. Most of the adsorbed material could be found along the graphite step edges. Additionally, small clusters lying on the graphite terraces were easily moved by the tip which manifested as parallel stripe shaped artefacts.

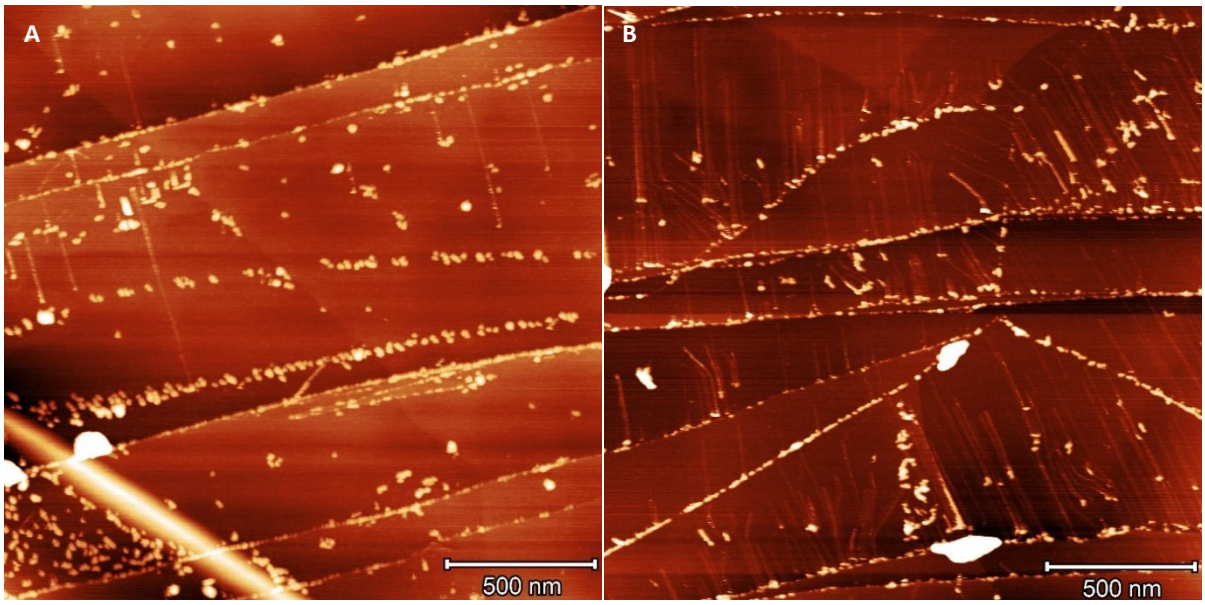

Figure 53. AFM images of stereoisomeric mixture of tetramer **32**. Only weakly adsorbing aggregates were found, and the molecules were apparently moved by the AFM tip, resulting in an artefact of parallel lines (A). Close-up region showing non-ordered aggregates (B).

A possible explanation of the surprising absence of the stable assemblies of **32** might lie in its geometry. Similarly, as in the case of **31**, it was shown that molecules of tetramer **32** planarize upon adsorption on graphite. The octagonal outer perimeter of the molecule might be less suitable for the formation of the linear aggregates in which a close intertwining of the trityl groups can be achieved, while for **31**, its hexagonal geometry can be easily arranged into compact stripes. Still, the MD simulations showed that **32** can form linear and cyclic aggregates (see Chapter 3.7.2.), there must be, therefore, other subtle factors influencing the on-surface behavior of **32**.

3.7.2. Molecular Dynamics Simulations and Potential Energy Calculations

To better understand the process leading to the observed assemblies of **31**, AFM measurements were supported by molecular dynamics simulations (MD). The attention was focused mainly on stereoisomers of trimer **31**, behavior of tetramer **32** was investigated only briefly. The purpose of the simulations was to investigate the preferred geometrical mode of interaction between molecules placed on graphite surface as well as studying the role of interactions between the different stereoisomers.

In the subsequent study, orientation of **31** on the graphite lattice was investigated by MD and potential energy (PE) methods.

*MD of Trimer **31***

The simulation system consisted of a double-layer graphite slab with 36 molecules **31** (Figure 54A). Various combinations of stereoisomers were studied, namely, 18 (+)-(*M*,*M*,*P*)-**31** and 18 (-)-(*M*,*P*,*P*)-**31** molecules, 18 (+)-(*M*,*M*,*M*)-**31** and 18-(-)-(*P*,*P*,*P*)-**31** molecules, 18 (+)-(*M*,*M*,*M*)-**31** and 18 (+)-(*M*,*M*,*P*)-**31** molecules, 18 (+)-(*M*,*M*,*M*)-**31** and 18 (-)-(*M*,*P*,*P*)-**31**, 36 (+)-(*M*,*M*,*M*)-**31** molecules. For simplicity, the systems will be denoted by shortcuts *MMP-MPP*, *MMM-PPP* and so on. Additionally, 36 (*M*,*M*,*M*)-**31** molecules without trityl groups denoted as *MMM*noTr. The simulations were performed at 303 K, using ReaxFF potential parametrized for graphene and hydrocarbon molecules.[137] A detailed description of the simulation protocol and data processing can be found in Chapter 5.13.1, The full MD trajectories are available upon request from the author or, more conveniently, as YouTube videos.[138]

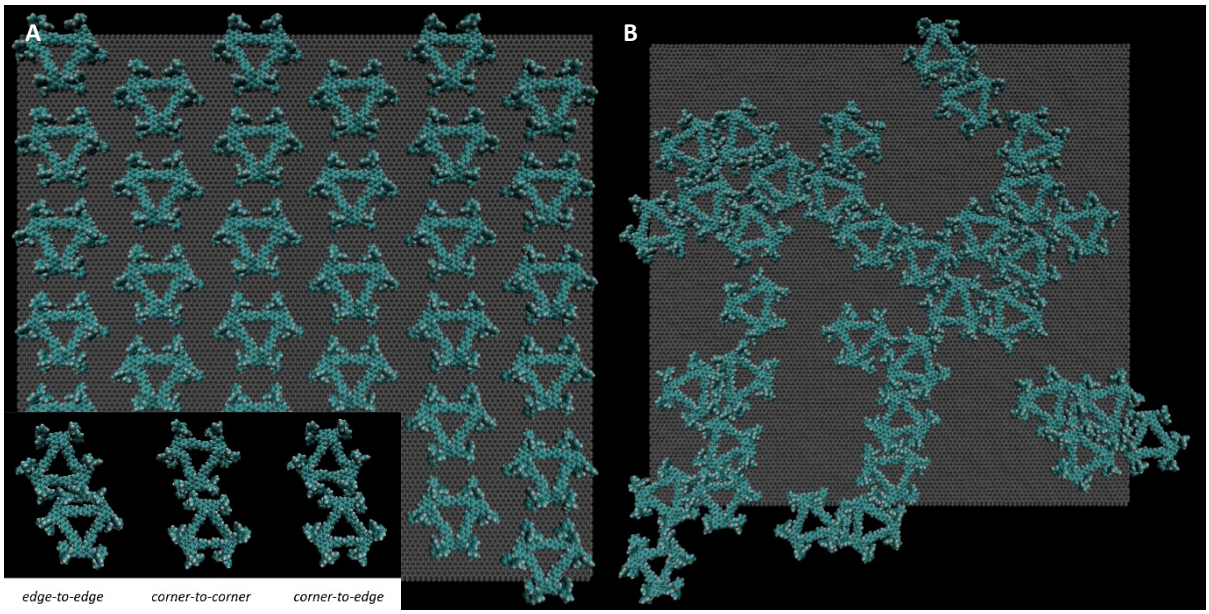

Figure 54. Initial configuration of the *MMP-PPM* system (A) and the same system after 4.63 ns (B). Intermolecular contact types - *edge-to-edge*, *corner-to-corner*, and *corner-to-edge* as described in the text (A inset).

Each system was first prepared by a simulated annealing protocol, to remove the excess energy and approximate a global energy minimum. Without this procedure, the system had a tendency to explode. During the procedure, the initial 3D geometry of the molecule

underwent a radical conformation change resulting in its planarization (Figure 55). The relatively symmetrical trityl propellers reoriented one phenyl ring coplanar with the graphite surface, leaving the other two phenyls almost perpendicular to the surface. As the measured heights of the adlayers were, depending on the particular image, ca 0.5 nm, it is likely such planarization occurs also in the real experiments. Moreover, the AFM topography showing two parallel sub-stripes within the main stripe seems to be a result of the tip interaction with the vertical phenyl rings, while the macrocycle core lies hidden below.

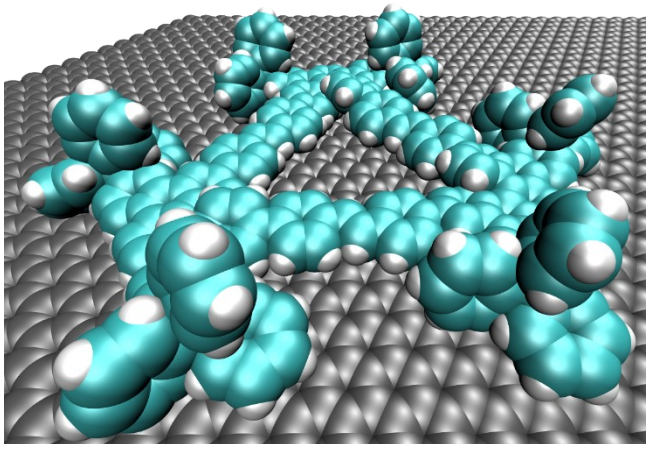

Figure 55. Geometry of **31** after simulated annelaing protocol. A large degree of planarization is apparent.

Following the simulated annealing, the systems were left to evolve at a specified temperature. Generally, the molecules had a high surface mobility at 303 K which was in line with the surface reconstruction and the tip-induced self-healing observed during the AFM measurements. Shortly after the simulation began, the molecules started to aggregate. The molecules gradually assembled into short segments of linear aggregates which often followed the hexagonal lattice directions. Apart from the linear structures, the molecules also intermittently adopted cyclic arrangement. In the case of **31**, however, the geometry of the molecule and the character of the trityl-trityl interaction seem to enforce the linear arrangement. It can be noted in the MD trajectories that the trityl groups within the stripes are strongly interlocked but the trityls on the sides of the stripe have markedly less durable contacts. This might explain the dense molecular packing within the stripes in contrast with the notably weaker interactions between the stripes in the 2D crystals. The same reason likely stands behind the stability of even the self-standing stripes found in some of the AFM images. It has been shown in the previous chapters, that low molecular concentration usually favors the formation of porous, low-density structures. This is in line with the results of the MD simulations where dense aggregates did not form.

Due to the large size of the systems, the simulation times were limited to ca 3-5 ns. With such short trajectories, it is likely the systems did not achieve thermodynamic equilibrium. Consequently, there was no ambition to predict the spontaneous formation of the experimentally observed large 2D crystals. Instead, the individual intermolecular contacts were analyzed statistically using a self-made Python script. The three most common orientations of macrocycles were identified and denoted as *edge-to-edge*, *corner-to-edge*, and *corner-to-corner* (Figure 54, inset).

Despite the initial orientation of the molecules resembled the *corner-to-edge* type (albeit over a long distance), the molecules quickly reoriented to engage mostly in the *edge-to-edge* contacts which dominated throughout the rest of the simulation. A careful examination of the *edge-to-edge* contacts showed an important role of the interlocking trityl groups which

apparently maximize the attractive Van der Waals forces. Such molecular "Velcro" clearly could not be efficiently realized in the case of the far less abundant *corner-to-edge* and *corner-to-corner* contacts. The formed linear assemblies remained stable for up to 2 ns and transformed its geometry only slowly. The tendency of **31** to assemble in the *edge-to-edge* fashion was further underlined by the time-evolution of the contact types, exemplified by the *MMM-PPP* system (Figure 56A). A similar *edge-to-edge* packing was observed also in the case of other triangular macrocycles such as those studied by Xu *et al.,* where the stabilizing function was facilitated by long alkyl chains.[139]

As far as stereochemistry is concerned, all systems showed the preference for the *edge-to-edge* contacts, regardless of their stereoisomeric composition. This supports the experimental results, where samples prepared from pure (-)-(*P*,*P*,*P*)-**31** and from the stereoisomeric mixtures showed a very similar morphology. On the other hand, Fasel *et al.* showed that even minor deviation from enantiomeric composition can have a dramatic impact on the structure of the adsorbates.[136] Here, the situation is more complex because **31** forms two different enantiomeric pairs but it was apparent that the richest structural diversity was found in non-racemic mixtures such as that shown in Figure 51B. Unfortunately, the simple MD simulations and the small size of the studied systems are short of capturing such complex on-surface behavior.

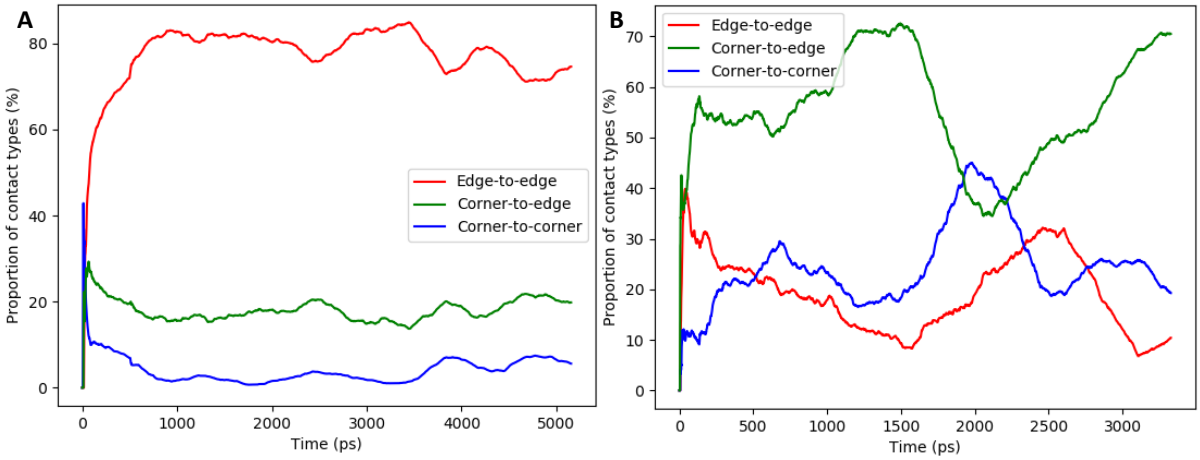

Figure 56. Time evolution of molecular contact types for *MMM-PPP* (A), and *MMM*noTr (B) system.

To shine more light on the role of the trityl groups in the self-assembly process, a system consisting of non-tritylated trimer *MMM*noTr was also studied. At 303 K, the molecules had similar surface mobility like **31** but they did not form stable aggregates. Only when temperature was gradually lowered to around 50 K, the molecules started to aggregate and eventually froze in their equilibrium positions. Furthermore, there was no preferred contact type stable in time and the preferences changed significantly during the whole MD trajectory as shown by the evolution diagram in Figure 56B.

Here, it is worth mentioning that the co-planar macrocycles *MMM*noTr floating on the graphite surface have only little opportunity to form intermolecular π – π interactions unless multilayers are formed. In contrast, close inspection of the MD trajectories involving **31** showed trityl phenyl rings interacting in the typical π – π or CH - π[140] fashion. However, it must

be admitted that no direct comparison with the non-tritylated trimer **31** beyond this simulation was possible as it was not synthesized.

*Orientation of **31** on Graphite Lattice*

Apart from focusing on the intermolecular contacts, the orientation of molecules **31** with respect to the underlying graphite lattice was also investigated. It was noted in many MD trajectories that the formed stripes form approximately 120° angle, and the stripes follow similar directions (Figure 54), as seen in the AFM images. This behavior might plainly stem from the hexagonal geometry of **31** imprinted on the structure of the aggregates as a-consequence of the intermolecular interactions. However, since the isolated islands of **31** on HOPG assembled in a unified direction, a more specific incidence between **31** and HOPG lattices should be anticipated.

A number of methods have been devised to model the adsorption of molecules on periodic lattices. Although the DFT calculations, implemented as linear combination of atomic orbitals or plane-waves, have a potential for a high precision, they become prohibitive for large molecules like **31**. Computationally cheap alternatives are PE methods utilizing various empirical potentials such as Morse[141] or Lennard-Jones[142,143] (L-J). Its "dynamical" version – MD can also be used, particularly when the evolution of the assembly process needs to be studied.

In line with the previous MD simulations, a similar approach was adopted herein to study the orientation of **31** on graphite surface. The simulation was set up using a single molecule (-)-(*M*,*P*,*P*)-**31** on a sufficiently large double layer graphite slab to avoid intermolecular contacts with itself over the periodic boundaries (Figure 57A). The molecule was left to move on the surface and its orientation to an arbitrarily chosen graphite lattice vector was monitored. At 298 K, the thermal motion was so intense that no preferred orientation could be discerned among the many random positions. But when the simulation temperature was lowered to 35 K, just above the freezing point of the system, the molecule moved slowly and resided in the energy minima for a sufficient time.

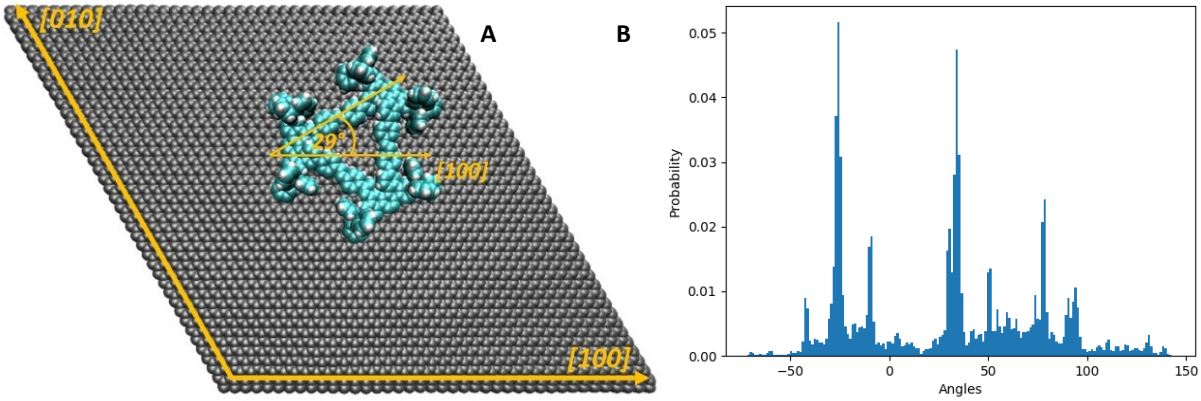

Figure 57. Orientation of the (-)-(*M*,*P*,*P*)-**31** molecule with respect to the [100] direction (A). Corresponding histogram showing the most frequent orientations (B).

Figure 57B shows a histogram of orientations of **31** constructed from 1 ps snapshots of a 42 ns MD trajectory. The most prominent peaks, corresponding to the most frequent

azimuthal orientations of **31**, are located at 29° and -29°. The difference of 60° is in good agreement with the expected hexagonal orientations observed experimentally. Additionally, the peaks around 29°, 73°, and 89° also have their smaller siblings 4° apart. This is again close to the experimentally observed small angle deviations of 5-6° between the 2D domains of **31**.

The principal advantage behind using MD for this study lies in the fact that such simulations inherently involve the entropic contributions resulting from many different, but energetically very close, positions of **31** on the surface which are not always included in the static energy calculations. Conversely, despite the predictive ability of this trivial model, it also has evident flaws. Most importantly, the results depend on the stochastic behavior of the thermal motion of the studied molecule and therefore the molecule does not necessarily adopt all possible configurations within a finite time. In fact, after 42 ns of the simulations the molecule did not even rotate a full 360°. Moreover, since there was no straightforward way to define an aggregate of several molecules within this approach, only a single molecule could be studied. This is a major flaw of the method because the adlayers of **31** are not commensurate with the graphite lattice and the energy minimum of an individual molecule may be significantly different from that of a molecule in a vast 2D crystal. Still, the results show that the interaction of **31** with graphite is not insignificant and that various adsorption isomers are indeed possible.

To address the aforementioned issues, a L-J potential based PE method was developed by Ukraintsev *et al.*[2] Therein, rigid, and fully planarized molecules **31** were placed sequentially on the surface and potential energy (in arbitrary units) was evaluated after each such addition. By optimizing the position and rotation of the macrocycle with respect to the lattice and the other molecules, potential energy minima could be found. To simplify the calculation, a set of geometrical constraints on the position and rotation of the macrocycles was introduced which significantly lowered the computational cost and allowed the calculation of a large ensemble of molecules.

The azimuthal tilt of **31** on the graphite lattice was, within a few degrees, identical to that obtained from the MD calculation. The corresponding 7.3° difference between the orientation of the two isomers was slightly higher, and close to the experimental values of 5 – 6°.

The most interesting results, however, were obtained when assemblies of several molecules were studied. The algorithm employing ten molecules **31** found either long stripes shown in Figure 58A or denser aggregates shown in Figure 58B. When only molecules (-)-(*M*,*P*,*P*)-**31** were used as a component of these assemblies, the resulting aggregates were somewhat unstable and a uniform structure did not form. However, when both enantiomers (-)-(*M*,*P*,*P*)-**31** and (+)-(*M*,*M*,*P*)-**31** were alternately distributed within the aggregate, a stable and uniform structure formed. This shows that racemic adlayers are likely favored based on simple geometric arguments when a racemate is used for the sample preparation. This behavior is also nicely corroborated with slightly different geometry and lower stability of the experimentally observed enantiomeric adlayers.

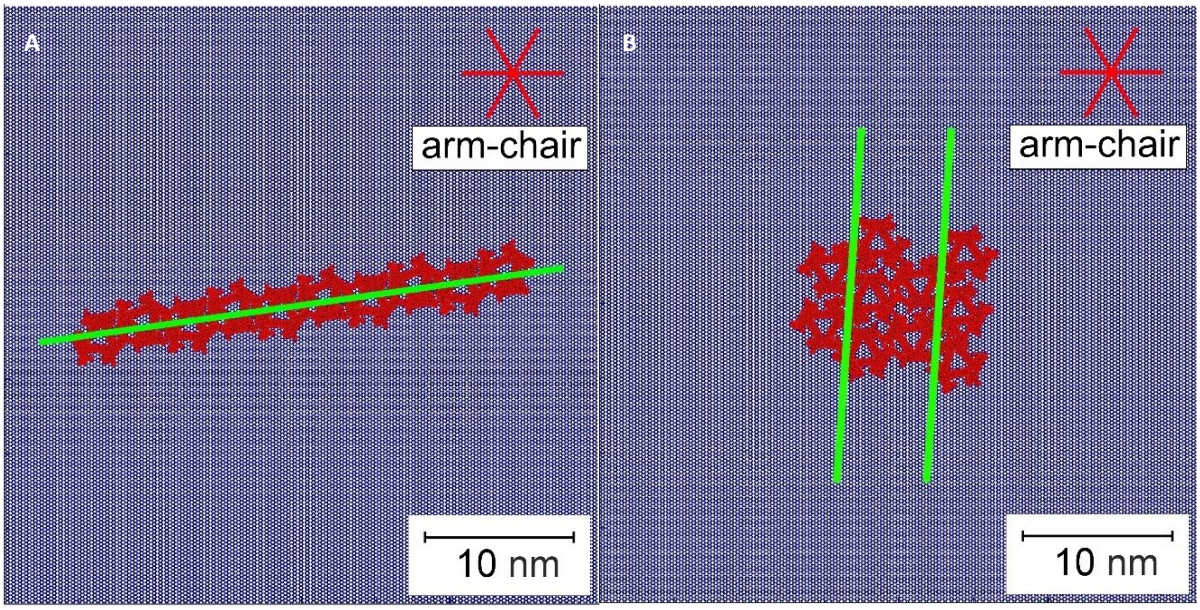

Figure 58. Linear assembly of 10 planarized molecules (-)-(*M*,*P*,*P*)-**31** (A). Closed-packed assembly of 10 planarized molecules (-)-(*M*,*P*,*P*)-**31** (B). Green lines indicate the direction of the molecular stripes.

4The stripes presented in Figure 58A were found to orient in directions separated by 8.5°. Although the experimental splitting of the angles varied with a particular AFM scan, the simulated value of 8.5° is still reasonably close to the experimental values between 5 – 6°. Moreover, the method was also able to correctly predict the total number of possible adsorption polymorphs reflected in the total number of beams in the 2D FFT of the AFM images. Thus, the simulated decameric stripes adsorbed in 12 different directions, which was observed in several 2D FFT filtered AFM images (see example in Figure 52A inset).

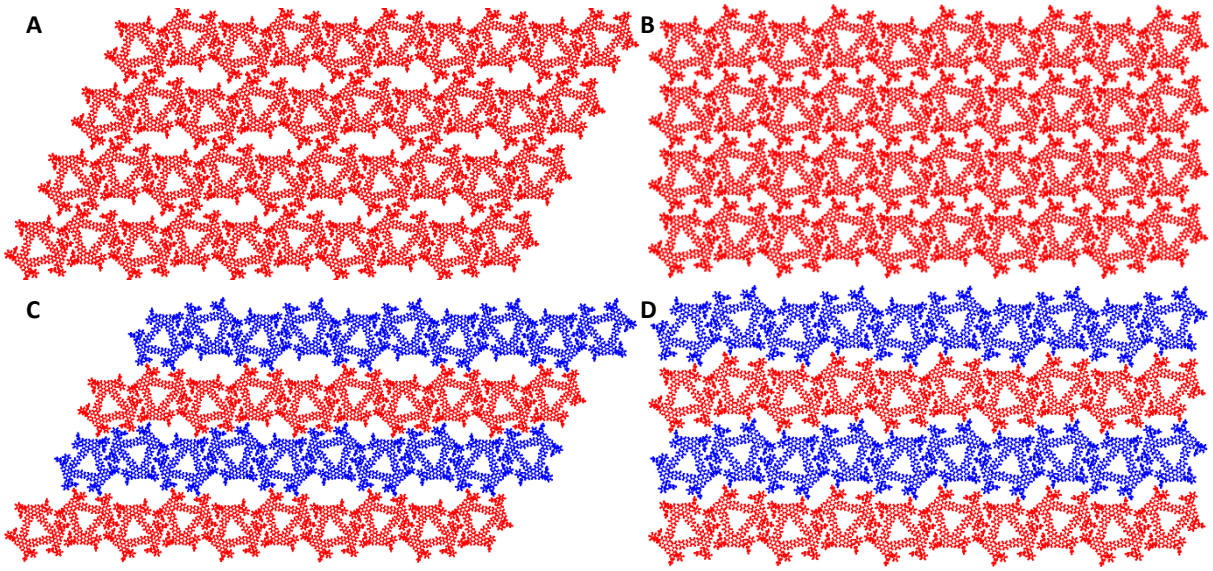

Figure 59. 2D domains with the lowest potential showing a possible mutual position of the molecular stripes. Domain with 63° between domain edges and the *edge-to-edge* orientation between different stripes (A). Domain with 90° between domain edges and the *corner-to-edge* orientation between different stripes (B). Domain with 59° between domain edges, an alternating rotation of stripes, and *edge-to-edge* orientation between different stripes (C). Domain with 90° between domain edges, an alternating rotation of stripes, and *edge-to-edge* orientation between different stripes (C). Stripes rotated by 180 °C are marked blue.

Besides studying individual stripes or small aggregates, the mutual interaction of the stripes was also studied. As discussed earlier, it was apparent from the AFM images that the intermolecular interactions within the observed stripes were substantially stronger than the interactions between the stripes. This manifests in a notably wider separation of the stripes as opposed to the separation of the molecules within the stripes, which is in fact almost indiscernible. To implement these observations using the PE method, many possible mutual positions of the stripes in a larger 2D assembly were probed. It was possible to find several 2D domains with a distinctly low potential (Figure 59). In one example of a possible arrangement, the relative shift of the stripes involved the *edge-to-edge* interactions, resulting in a domain with 63° angle between the domain edges (Figure 59A). When the relative shift was such that the macrocycles adopted the *corner-to-edge* interaction, the angle between the domain edges changed to 90° (Figure 59B). The potential further decreased when every other stripe was rotated by 180°, giving slightly different geometries of the domains (Figure 59C and D). It is evident from the structures, that only limited number of trityl-trityl interactions is geometrically possible between the stripes which might explain the morphology of the experimentally observed adlayers and a surprisingly high stability of even the standalone stripes. Note that both hexagonal and rectangular domains were identified in AFM as shown in Figure 52A demonstrating a good predictive power of the model.

It should be emphasized that there was no opportunity to compare the obtained absolute azimuthal tilts to the experiment, as such data was not accessible. The differences between the MD and PE methods obviously reflect the distinct methodological specifics discussed above. In the MD simulations, molecules **31** can adapt to the small nuances in the geometry of the graphite surface and thus optimize the geometry of the whole molecule even on the level of individual atoms. This simulation also involves double layer graphite and 3D molecule **31**. Furthermore, the used ReaxFF forcefield is likely to provide a more realistic picture of the interatomic interactions and thus may contribute to the accuracy of the method on the single-molecule level.

On the other hand, despite the crude simplifications employed in the PE method which uses only atoms close to the surface as a planar model of **31** and a very primitive L-J potential, it becomes a very powerful tool to handle large aggregates, capable of predicting many experimentally observed geometries. To justify the utilized simplifications, it has been shown, for example, that even simple models of the electrostatic imprint, simulated as ellipsoidal potentials for the whole molecule, can provide convincing agreement with the experimental measurements.[144]

*MD of Tetramer **32***

Since tetramer **32** did not form stable structures on HOPG, there was hope that MD could provide explanation for this unexpected behavior. The simulation, involving 10 molecules (*M*,*M*,*M*,*M*)-**32** and 10 molecules (*P*,*P*,*P*,*P*)-**32** on a doble layer graphite slab, was performed analogously to the simulations with trimers **31** (Figure 60).

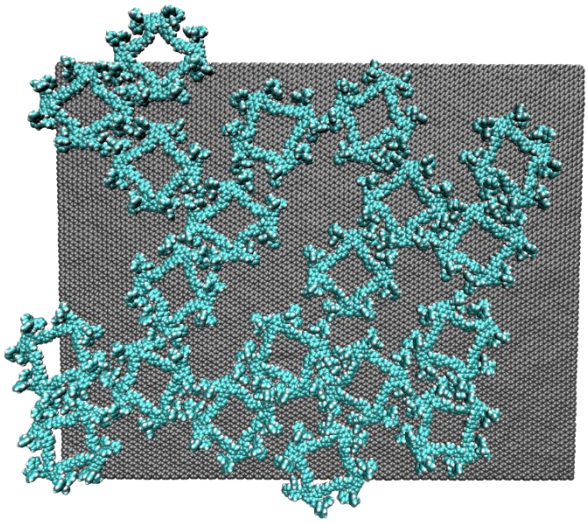

Figure 60. Snapshot of a MD trajectory of the PPPP/MMMM system after 0.76 ns. *Edge-to-edge* interactions, similar to those observed in the trimer-based systems are apparent.

As in the case of trimer **31**, tetramer **32** planarized on the surface and moved with ease on the surface. The molecules assembled into aggregates, in the similar *edge-to-edge* fashion like **31** (analyzed only visually). Apart from linear aggregates, tetramers had also a clear tendency to form cyclic arrangements. The above results are in a stark contrast to the experimental observations, where the molecules did not show a tendency to form stable adsorbate structures.

3.7.3. AFM measurements on Gold

In analogy to the experiments on HOPG, self-assembly was also studied on Au(111) surfaces. Muscovite sheets with a resistively evaporated 40 nm gold layer which was thermally annealed by a Bunsen burner immediately after evaporation to form (111) terraces were used as substrates. Molecules **31** were then applied in the same way as in the case of deposition on HOPG.

Figure 61 shows a representative AFM image of mostly disordered three dimensional layers of **31** on the surface. Although a certain degree of organization is apparent in the image, **31** has obviously much higher affinity to gold surfaces compared to HOPG, leading to the growth of less ordered structures.

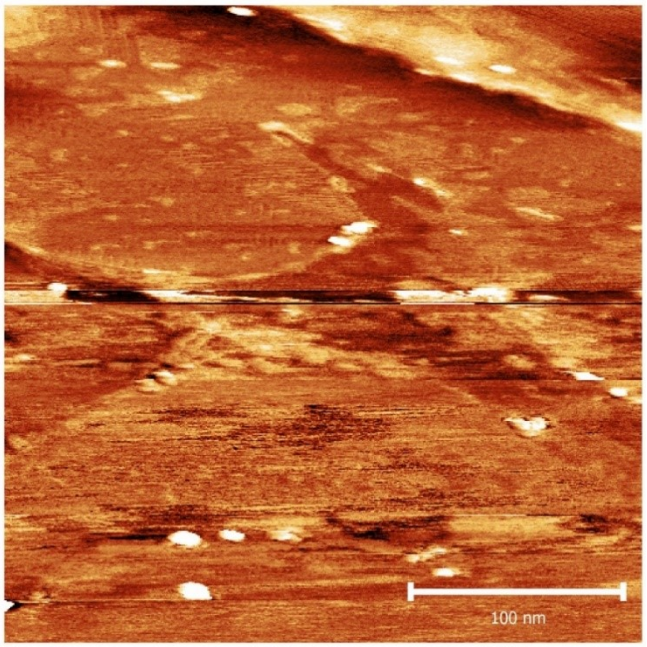

Figure 61. AFM image of ca 12.5% of (-)-(*P,P,P*)-**31**, 12.5% of (+)-(*M,M,M*)-**31**, 37.5% of (-)-(*M,P,P*)-**31**, and 37.5% of (+)-(*M,M,P*)-**31** deposited on Au(111) surface. Partially organized layers are apparent in the upper part of the image.

3.7.4. STM Measurements

To study self-assembly of **31** on solid-liquid interface using STM, a solution of **31** in *n*-octanoic acid was applied to the HOPG surface and subsequently scanned. In contrast with the methodology used for the AFM measurements, here the molecules were found almost exclusively on the graphite step edges (Figure 62A). This finding reflects the low adhesion of the molecules to the surface and only a limited stability of their assemblies. While the PeakForce AFM offers a very delicate control of the tip-sample interaction, the electric forces in the vicinity of the STM tip can have a rather destructive effect on the adlayers. As a result, the molecules are easily moved by the STM tip and remain in stable positions only on the graphite step edges where the molecule-surface interaction is significantly higher. Figure 62B shows a stripe of molecules **31** ordered along the graphite step edge. The stripe is fragmented and its double-stripe internal structure, similar to that observed by AFM, is clearly visible.

Interestingly, when **31** was deposited either as a solution in *n*-octanoic acid, TCB or 1-phenyloctane solution on Au(111) surface, no assemblies were found by STM.

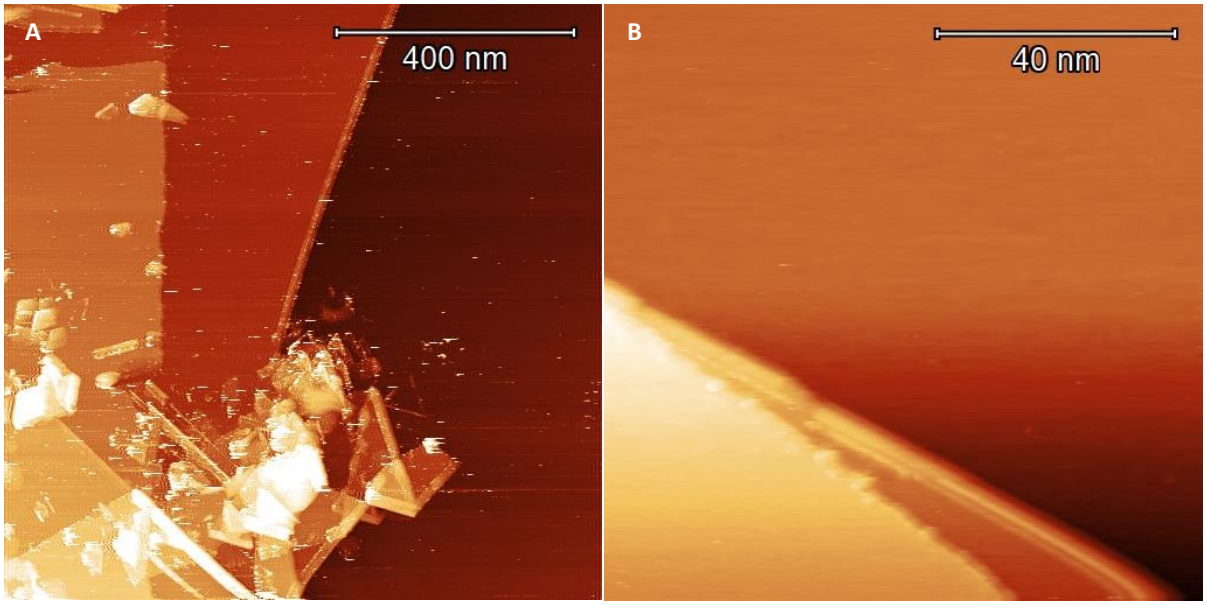

Figure 62. STM images of ca 12.5% of (-)-(*P,P,P*)-**31**, 12.5% of (+)-(*M,M,M*)-**31**, 37.5% of (-)-(*M,P,P*)-**31**, and 37.5% of (+)-(*M,M,P*)-**31** mixture on the HOPG/*n*-octanoic acid interface. Molecules reside mostly on the graphite step edges (A). A close-up view of the graphite step edge showing a row of molecules **31** (B).

3.8.(Anti)aromaticity of Trimer **31**

The concept of (anti)aromaticity, as found in the current literature, has been discussed mainly in the context of electronic structure and molecular geometry.[52,145] However, the environment of the molecule, such as a surrounding solvent or an underlying solid surface, may well have a decisive impact on its (anti)aromaticity state. In this project, there was no ambition to address the still controversial foundations of the (anti)aromaticity concept. The attention was rather focused on the influence of molecular adsorption on aromatic character of the studied molecules **31**. For simplicity, the NICS and ACID calculations were performed on macrocycle **31noTr** where the trityl groups were replaced with hydrogen atoms.

Figure 63A shows a molecular formula of trimer **31noTr** with highlighted Clar's sextets. While the helicene and phenylene units always contribute 4n+2 π-electrons, the vinylene moieties introduce two additional electrons per helicene unit, turning the macrocycle into a 4n π-electron system. Counting along the shortest conjugated path in **31noTr** then gives 60 π-electrons (Figure 63B). Naturally, the π-electron count is only one of several criteria of (anti)aromaticity. The molecular geometry and topology translated to the spatial distribution of electron density must also fulfill specific criteria to render the molecule (anti)aromatic.[146]

It is important to emphasize that truly antiaromatic molecules are rare. The reason is clear – if the molecule can avoid antiaromatic states, for example, by distorting its geometry, it will happen. 1,3,5,7-Cyclooctatetraen is a typical textbook example of a non-aromatic 4n π-electron molecule having a non-planar geometry. In certain cases, molecules can even adopt a conformation that allows achieving the electronic states with Möbius topology.[46,53] Especially in the case of large polycyclic systems, only local aromaticity is often formed and the global antiaromatic state is thus easily avoided.[147] In many cases, the molecule has to be oxidized or reduced to become globally (anti)aromatic.[148]

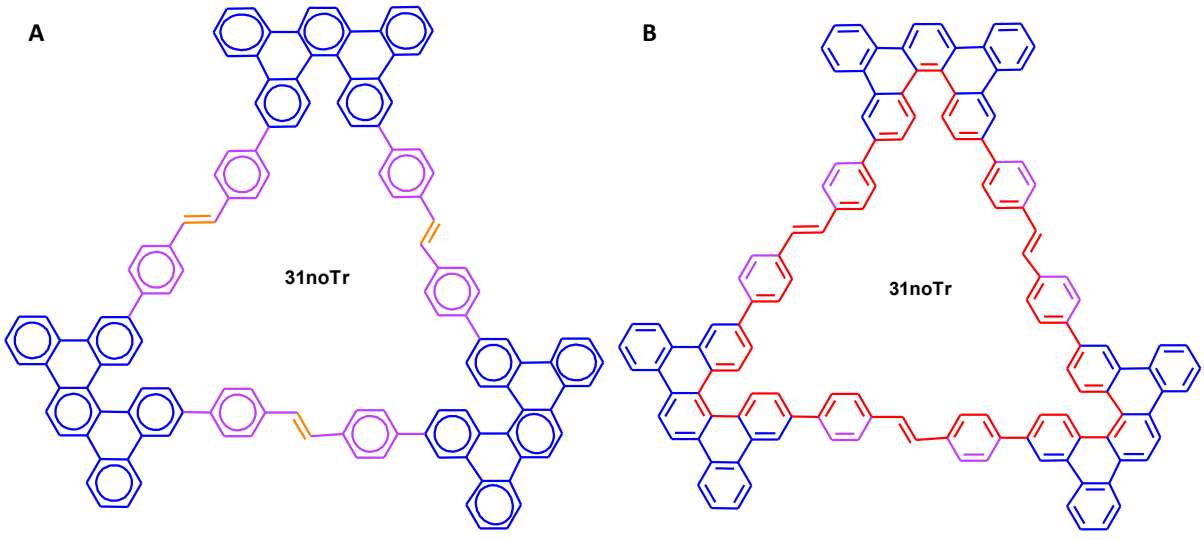

Figure 63. Structures of truncated molecule **31noTr** without trityl groups. Clar's sextets show how the additional vinylene groups (orange) contribute to the 4n π-electron count of **31noTr** (A). Red color highlighting the 60 π-electron (4n) conjugated path (B).

Here, it is worth mentioning that the case of **31noTr** is different from the situation in small (anti)aromatic cycles. The requirement for a strict planarity of the molecule to achieve the

aromatic state, as first envisioned by Hückel,[149–151] can be somewhat weakened, as long as the overlap of the p orbitals remains sufficient. This is indeed the case for many large macrocycles with a surprisingly high curvature.[152] Thus, it is anticipated that a perfect planarity of **31noTr** is not crucial to achieve the global (anti)aromatic state.

Below follows a discussion of the computational and experimental investigation of the (anti)aromatic nature of **31**.

3.8.1. (Anti)aromaticity in Solution

Computational results

As a prelude to the on-surface study, the (anti)aromaticity of stereoisomers of **31noTr** was briefly studied in solution using computational methods, as well as electrochemical and ^{1}H NMR measurements.

To obtain a qualitative picture, standard implementation of nucleus independent chemical shift - NICS(0)$_{ZZ}$, and anisotropy of current induced density – ACID, methods were used (see Chapter 5.11. for more details).

First, calculations at B3LYP/cc-pVDZ/GD3/PCM($CHCl_3$)//B3LYP/cc-pVDZ/PCM($CHCl_3$)/NICS or ACID (geometry optimization//NICS or ACID) level were performed. The neutral [(*M*,*P*,*P*)-**31noTr**]^0 did not show global aromaticity. In both NICS(0)$_{ZZ}$ and ACID plots, only local aromatic currents were found. When the molecule was oxidized to [(*M*,*P*,*P*)-**31noTr**]$^{2+}$, global diatropic ring currents could be observed (Figure 64A and C), as expected from its 4n+2 π-electron count. Interestingly, when two more electrons were removed to form [(*M*,*P*,*P*)-**31noTr**]$^{4+}$, ACID plots still showed diatropic current, in conflict with its 4n π-electron count, while NICS(0)$_{ZZ}$ indicated the expected paratropicity (Figure 64B and D). Another peculiar feature of the [(*M*,*P*,*P*)-**31noTr**]$^{4+}$ species were substantially higher values of the induced currents compared to other forms of [**31noTr**]$^{x+}$.

Similarly, [(*P*,*P*,*P*)-**31noTr**]^0 did not exhibit global aromaticity, but oxidation to [(*P*,*P*,*P*)-**31noTr**]$^{2+}$ showed the expected diatropic currents in both ACID and NICS(0)$_{ZZ}$ plots. The higher oxidation state, [(*P*,*P*,*P*)-**31noTr**]$^{4+}$, again, retained the diatropic current, but this time in both the NICS(0)$_{ZZ}$ and ACID calculations.

With the hope of resolving the above inconsistencies and contradictions, another functional was tried for the calculations. It was nicely shown by Rickhaus *et al.* that for a reliable prediction of (anti)aromaticity, it is important to employ long-range corrected functionals such as LC-ωhPBE.[148,153] With that in mind, the above calculations were repeated at the level of LC-ωhPBE/cc-pVDZ/PCM($CHCl_3$)//LC-ωhPBE/cc-pVDZ/PCM($CHCl_3$)/ACID or NICS. Surprisingly, no global paratropic or diatropic currents were found in this case.

An important difference between both methods is that the LC-ωhPBE functional does not include any dispersion terms, unlike the B3LYP functional, which can be complemented with the Grimme dispersion correction. It has been shown by Grimme and co-workers that the inclusion of dispersion is critical for obtaining accurate geometries and energies of aromatic

molecules, particularly when electrically charged.[115,154] Indeed, the geometries obtained by the above two methods were markedly different, but when the NICS calculation of the [(*M*,*P*,*P*)-**31noTr**]$^{2+}$ system was repeated at the B3LYP/cc-pVDZ/PCM($CHCl_3$)//B3LYP/cc-pVDZ/B3LYP/PCM($CHCl_3$)/NICS level, omitting the dispersion correction in the optimization step, no qualitative change in the NICS plot was observed, showing that the dispersion alone seems not to be the main issue. However, when the geometry of [(*M*,*P*,*P*)-**31noTr**]$^{2+}$ obtained with the LC-ωhPBE functional was used for the NICS calculation using the B3LYP functional (LC-ωhPBE/cc-pVDZ/PCM($CHCl_3$)//B3LYP/cc-pVDZ/PCM($CHCl_3$)/NICS), the calculation showed diatropic ring current. This shows that the applied functional is indeed the main factor influencing the calculation results.

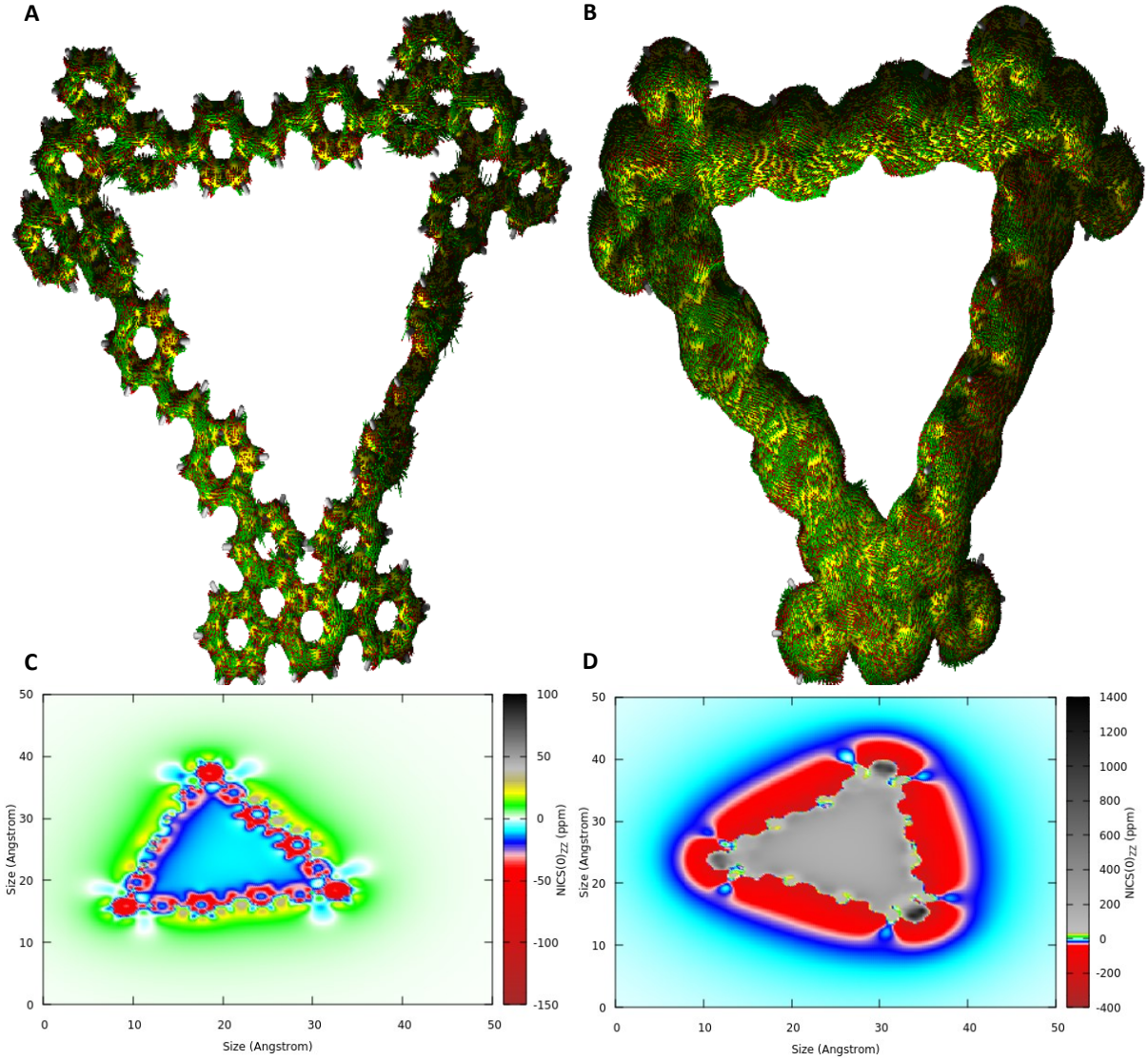

Figure 64. ACID plot showing a global diatropic current on the periphery of [(*M*,*P*,*P*)-**31noTr**]$^{2+}$ (A). ACID plot showing a global diatropic current of [(*M*,*P*,*P*)-**31noTr**]$^{4+}$ (B). NICS(0)$_{ZZ}$ plot showing strongly negative chemical shifts in the center of macrocycle [(*M*,*P*,*P*)-**31noTr**]$^{2+}$ (C). NICS(0)$_{ZZ}$ plot showing strongly positive chemical shifts in the center of macrocycle [(*M*,*P*,*P*)-**31noTr**]$^{4+}$ (D). NICS(0)$_{ZZ}$ was calculated at B3LYP/cc-pVDZ/B3LYP/PCM($CHCl_3$)/NICS(0)$_{ZZ}$ level. ACID was calculated at B3LYP/cc-pVDZ/B3LYP/PCM($CHCl_3$)/ACID level and plot with anisotropy of the current density isovalue of 0.07.

Another important aspect to consider when discussing the above results is the topology of the molecules and their respective electron densities. When dealing with large cyclic

systems, the Möbius topology of the electron density can lead to the reversal of the (anti)aromaticity states relative to the molecules with the Hückel topology. The different calculation methods clearly showed various distributions of the electron density for [**31noTr**]$^{x+}$, where some conformers seemed to possess Möbius arrangement of the ACID surface. However, such visual assessment of topology can be misleading for molecules like [**31noTr**]$^{x+}$ and computational topological analysis is needed. This unfortunately goes beyond the scope of this project, as an appropriate program was not available in our group. The overall results of the NICS and ACID calculations are summarized in Tables 7 and 8.

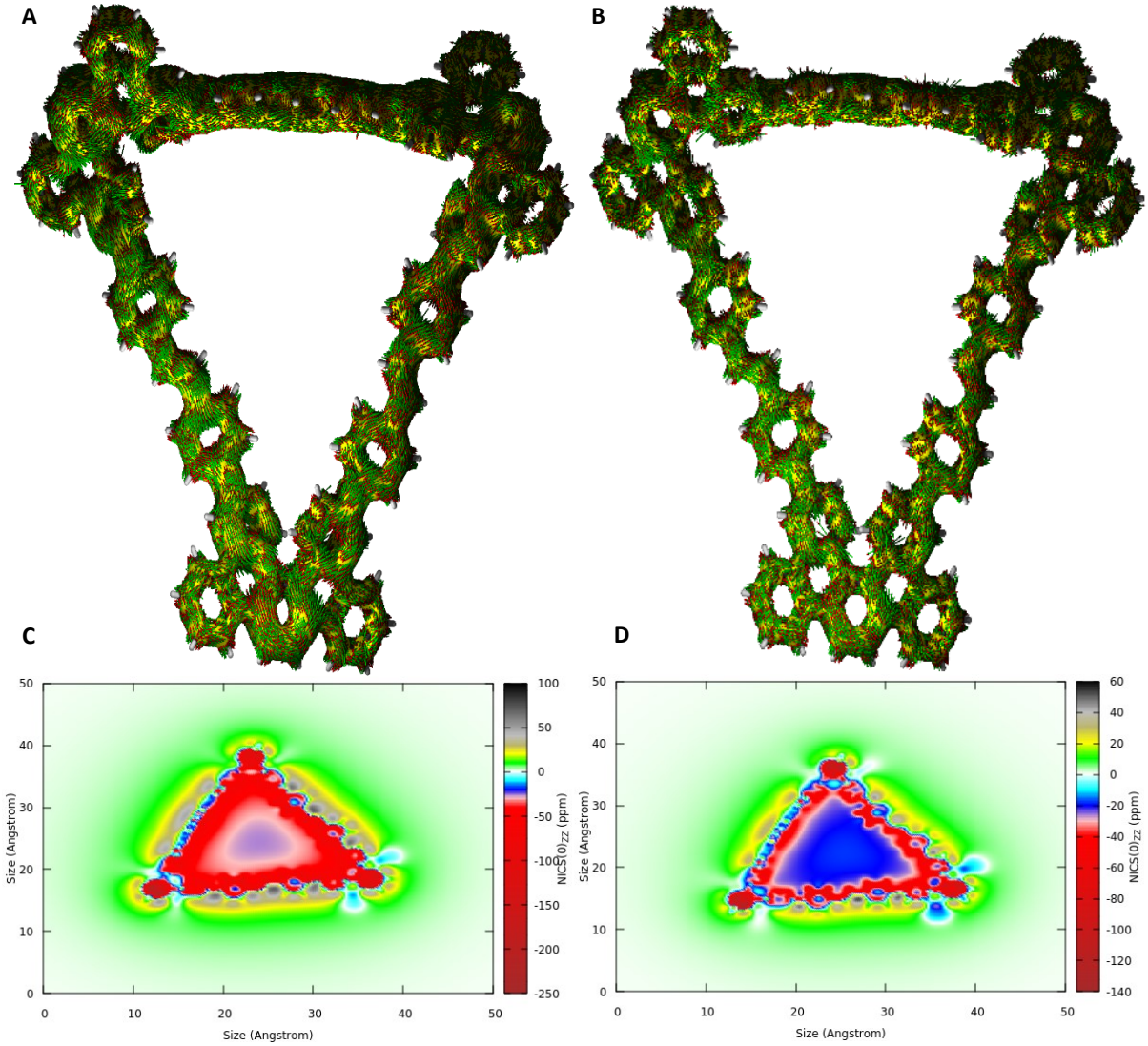

Figure 65. ACID plot showing a global diatropic current in [(*P*,*P*,*P*)-**31noTr**]$^{2+}$ (A). ACID plot showing a global diatropic current in [(*P*,*P*,*P*)-**31noTr**]$^{4+}$ (B). NICS(0)$_{ZZ}$ plot showing strongly negative chemical shifts in the center of macrocycle [(*P*,*P*,*P*)-**31noTr**]$^{2+}$ (C). NICS(0)$_{ZZ}$ plot showing strongly negative chemical shifts in the center of macrocycle [(*P*,*P*,*P*)-**31noTr**]$^{4+}$ (D). NICS(0)$_{ZZ}$ was calculated at B3LYP/cc-pVDZ/B3LYP/PCM($CHCl_3$)/NICS(0)$_{ZZ}$ level. ACID was calculated at B3LYP/cc-pVDZ/B3LYP/PCM($CHCl_3$)/ACID level and plot with anisotropy of current density isovalue of 0.07.

Molecule	Calculation method - ACID	
	B3LYP/cc-pVDZ/GD3/PCM($CHCl_3$)// B3LYP/cc-pVDZ/PCM($CHCl_3$)/ACID	LC-ωhPBE/cc-pVDZ/PCM($CHCl_3$)// LC-ωhPBE/cc-pVDZ/PCM($CHCl_3$)/ACID
[(*M*,*P*,*P*)-**31noTr**]^{0}	No global ring current	No global ring current
[(*M*,*P*,*P*)-**31noTr**]$^{2+}$	Diatropic ring current	No global ring current
[(*M*,*P*,*P*)-**31noTr**]$^{4+}$	Diatropic ring current	No global ring current
[(*P*,*P*,*P*)-**31noTr**]^{0}	No global ring current	No global ring current
[(*P*,*P*,*P*)-**31noTr**]$^{2+}$	Diatropic ring current	No global ring current
[(*P*,*P*,*P*)-**31noTr**]$^{4+}$	Diatropic ring current	No global ring current

Table 7. Summary of results of ACID calculations for individual stereoisomers of **31noTr** and different calculation methods.

Molecule	Calculation method - NICS	
	B3LYP/cc-pVDZ/GD3/PCM($CHCl_3$)// B3LYP/cc-pVDZ/PCM($CHCl_3$)/NICS(0)$_{ZZ}$	LC-ωhPBE/cc-pVDZ/PCM($CHCl_3$)// LC-ωhPBE/cc-pVDZ/PCM($CHCl_3$)/NICS(0)$_{ZZ}$
[(*M*,*P*,*P*)-**31noTr**]^{0}	No global ring current	No global ring current
[(*M*,*P*,*P*)-**31noTr**]$^{2+}$	Diatropic ring current	No global ring current
[(*M*,*P*,*P*)-**31noTr**]$^{4+}$	Paratropic ring current	No global ring current
[(*P*,*P*,*P*)-**31noTr**]^{0}	No global ring current	No global ring current
[(*P*,*P*,*P*)-**31noTr**]$^{2+}$	Diatropic ring current	No global ring current
[(*P*,*P*,*P*)-**31noTr**]$^{4+}$	Diatropic ring current	No global ring current

Table 8. Summary of results of NICS(0)$_{ZZ}$ calculations for individual stereoisomers of **31noTr** and different calculation methods.

Experimental measurements

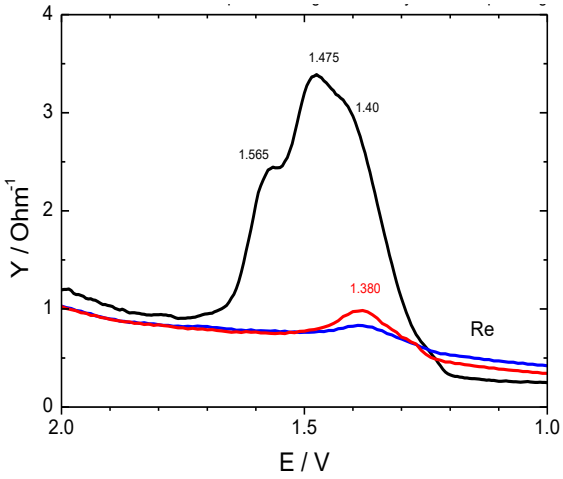

Figure 66. AC voltammogram of **31** in 1,2-dichloroethane showing three oxidation steps. Real part of admittance is shown. Red and blue curves show the second and third scan. Measurement was performed on polished platinum working electrode, using Ag/AgCl/LiCl reference electrode. Concentration of **31** 0.28 mg/mL, frequency 16 Hz.

To bring more light to the inconclusive computational results presented in the previous section, the (anti)aromaticity status of **31** was also investigated experimentally. The study commenced by investigating its redox behavior using cyclic voltammetry (CV). The classical CV showed only very weak and irreversible signals, likely due to strong adsorption of **31** on the electrodes. To overcome this complication, a solution of **31** in 1,2-dichloroethane was submitted to phase sensitive AC voltammetry (ps-ACV) on platinum electrode. As documented by a voltammogram in Figure 66, **31** undergoes three oxidation steps at 1.40, 1.48, and 1.57 V vs Ag/AgCl reference electrode, but again, repeated scanning led to a gradual inhibition of the electrode. No reduction processes were observed, indicating that the oxidation is irreversible. Clearly, whether the strong adsorption of the oxidation products is promoted by their aromatization is difficult to conclude. But interestingly, the obtained values are in stark contrast to the redox behavior of dibenzo[5]helicene, which undergoes three irreversible reductions at -2.59, -2.84,

and -3.12 V.[155] It is likely that such large difference in redox behavior is a result of the electronic coupling of the helicene units and might reflect the tendency of **31** to avoid the formation of the globally conjugated 4n π-electron system.

It is also important to point out that without additional investigation, it is not clear whether the three oxidation steps correspond to three single-electron or three double-electron oxidations. It can be assumed that after the first electron transfer, the formed radical cation species might be easily oxidized by immediate removal of the second electron, resulting in the net double-electron oxidation. Under such an assumption, each oxidation step in the AC voltammogram would then correspond to double-electron transfer.

The (anti)aromaticity status of **31** in neutral and oxidized form was also probed by variable temperature ^{1}H NMR. It was apparent from previous measurements that neutral **31** does not show any unusual chemical shifts typical for (anti)aromatic species. To check whether an oxidized forms of **31** would have a different (anti)aromaticity status, its solution in CD_2Cl_2 was mixed with a solution of $I_2/AgSbF_6$ reagent (1.14 V vs Fc/Fc^+)[156] and ^{1}H NMR of the resulting deep-purple solution was measured at temperatures ranging from -50 to 25 °C. The measurements showed a significant broadening of the signals compared to pure **31** (Figure 67). Although part of this effect can be attributed to aggregation and viscosity effects due to the low temperatures, the comparison with the spectrum of pure **31** suggests that other sources of broadening are likely. As the electrochemical measurements revealed that **31** can be oxidized to odd-electron species, it is also reasonable that the broadening might originate from such paramagnetic oxidized forms of **31**. Similarly to neutral **31**, the spectra did not show any significant changes in the chemical shifts that would indicate the presence of globally aromatic or antiaromatic molecules. The chemical shifts of the inner protons 3, 4, 7, 8, where the effects should be most noticeable, remained practically unchanged. Also, the outer protons 13, 15, and 16 remained intact. In contrast, a relatively large change was observed in protons 11 and 19 but reflecting the absence of the chemical shift changes in other protons, this likely reflects a localized chemical change in the structure of **31**.

Although more experimental effort is needed to clarify the observations, the above experimental results seem to support the computational predictions from $NICS(0)_{ZZ}$ and ACID employing the LC-ωhPBE functional, where no global (anti)aromaticity was observed.

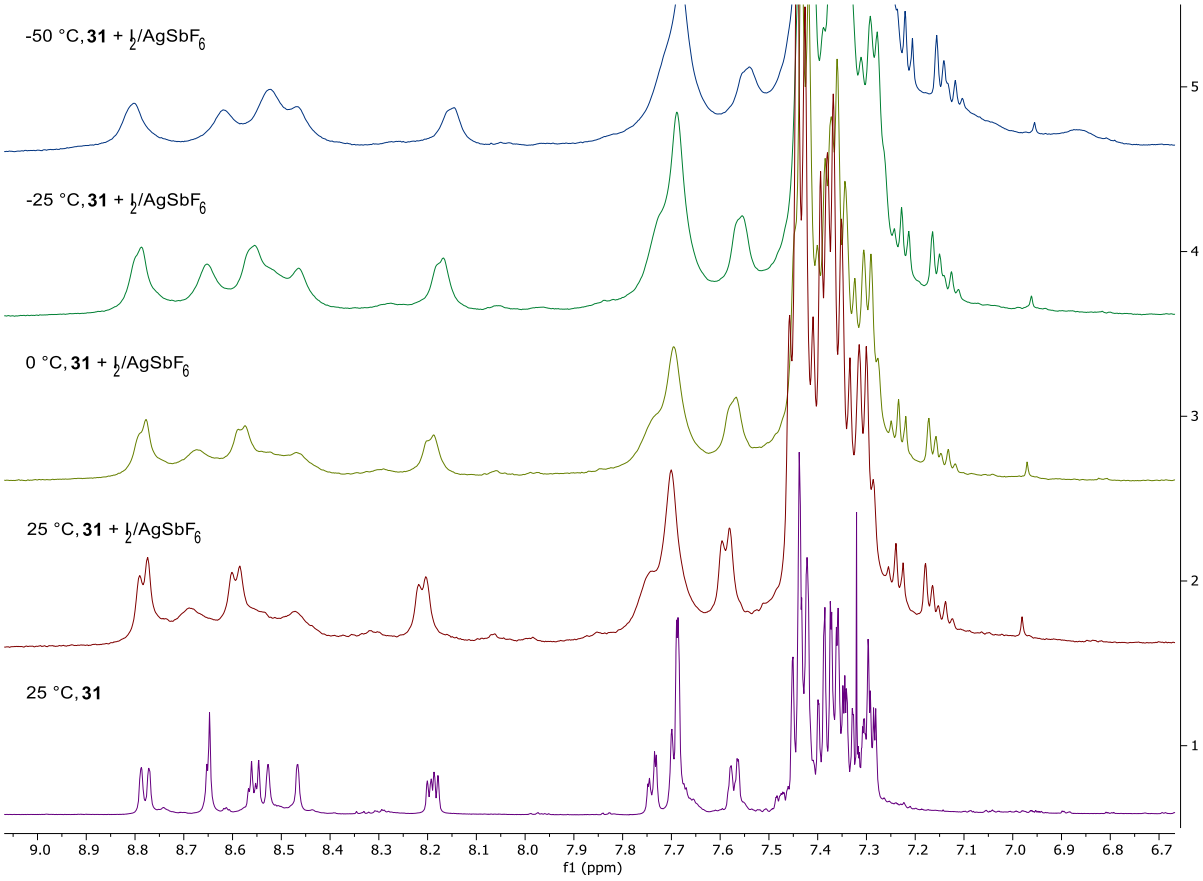

Figure 67. ^{1}H NMR spectra of mixture of **31** and $I_2/AgSbF_6$ reagent at various temperatures. The lowest spectrum shows pure stereoisomeric **31** for comparison. Spectra were measured in CD_2Cl_2 at 500 MHz, the lowest spectrum at 600 MHz.

3.8.2. (Anti)aromaticity on Surfaces

Following the study of (anti)aromaticity in solutions, the more interesting question of how the (anti)aromaticity state is influenced by the adsorption of **31** on the surface could be studied. The concept of aromaticity of isolated molecules in vacuum or in solution has been a subject of a rich debate for decades, but aromaticity studied on surfaces has been substantially less explored. Herein, the discussion is focused solely on the question, whether a molecule **31** could become (anti)aromatic by binding to an electrically conductive surface without any concomitant chemical change. Hence, for example, a molecule of cyclohexane can surely become aromatic by dehydrogenation to benzene on a platinum surface,[157] but this is a chemical process which is not the subject of this study.

The unexpected propensity of nonplanar molecules **31** to form stable assemblies on graphite surfaces raised a question whether their (anti)aromatic character could contribute to this behavior. Since molecules can be forced to large conformation changes to avoid antiaromaticity, it was hypothesized that the neutral 60 π-electron molecule **31** might be stabilized on the surface by a charge transfer of up to two electrons accompanied by a substantial planarization of the otherwise very bulky molecule. Such an oxidation would transform **31** to a more stable 58 π-electron $[\mathbf{31}]^{2+}$. Note that the enormous graphite bulk could easily drain the electrons provided by the monolayers of **31** on its surface.

Electron transfer between an adsorbate and a conductive surface is not a new concept. It has been observed on many organic molecules adsorbed on metals, graphite, graphene, or other (semi)conductive materials.[158,159] It has also been shown that the charge transfer is accompanied by the formation of an electrostatic interface dipole, oriented perpendicularly to the surface. This dipole is associated with an interesting charge and spin redistribution between the molecule and the surface, a so-called cushion effect, resulting from the Pauli repulsion.[160] Together, these effects may have profound implications for the electronic properties of the surface. In contrast to the well documented charge transfer, it is noteworthy that on-surface aromatization, as the consequence of the on-surface charge transfer, has been reported only by Zugermeier *et al.* who showed an aromaticity driven aromatization of a corrole radical cation.[161]

Theoretical and experimental investigation of the validity of the proposed hypothesis should be divided into three parts. First, theoretical calculation of the charge transfer, second, computational aromaticity assessment of the resulting charged species, and third, experimental measurement of the charge transfer. Herein, the first part, the charge transfer, is discussed as the other two topics are still under investigation. The last logical step, "the measurement of aromaticity" is clearly not an option because aromaticity is not an observable quantity. The experimental evidence of aromaticity would therefore have to rely on indirect measures, such as geometry, charge distribution, IR and Raman spectra, or magnetic properties.

Charge Transfer Calculation

To see whether **31** adsorbed on graphite would be spontaneously oxidized by the charge transfer, a series of LCAO DFT calculations with boundary conditions were performed (see Chapter 5.12. for more details). A single molecule (-)-(*M*,*P*,*P*)-**31** was placed onto a rectangular slab of a double layer graphite. The system was equilibrated using a simulated annealing sequence with ReaxFF forcefield[137] and the obtained geometry was subsequently submitted to the LCAO single point calculation. The degree of charge transfer was then quantified by summing the Mulliken charges on **31** and on graphite, and by subtracting the electron density of the free molecule and the free graphite slab from the original system (Figure 68). As preliminary results with a four-layer graphite showed only a marginal difference in the charge transfer, all subsequent calculations were performed with the double layer graphite. The choice of a large basis set was necessary to achieve convincing results.

The calculations showed a significant transfer of electron density from the molecule to graphite as documented by the electron density differences shown in Figures 68A and B. A large cushion of negative charge can be noted between the molecule and the surface (Figure 69A). This result is rather similar to previous works studying organic molecules on metals.[160] The Mulliken analysis revealed that the electron density redistribution corresponds to the transfer of almost two electrons from the molecule to the surface, resulting in the positive charge on the molecule.

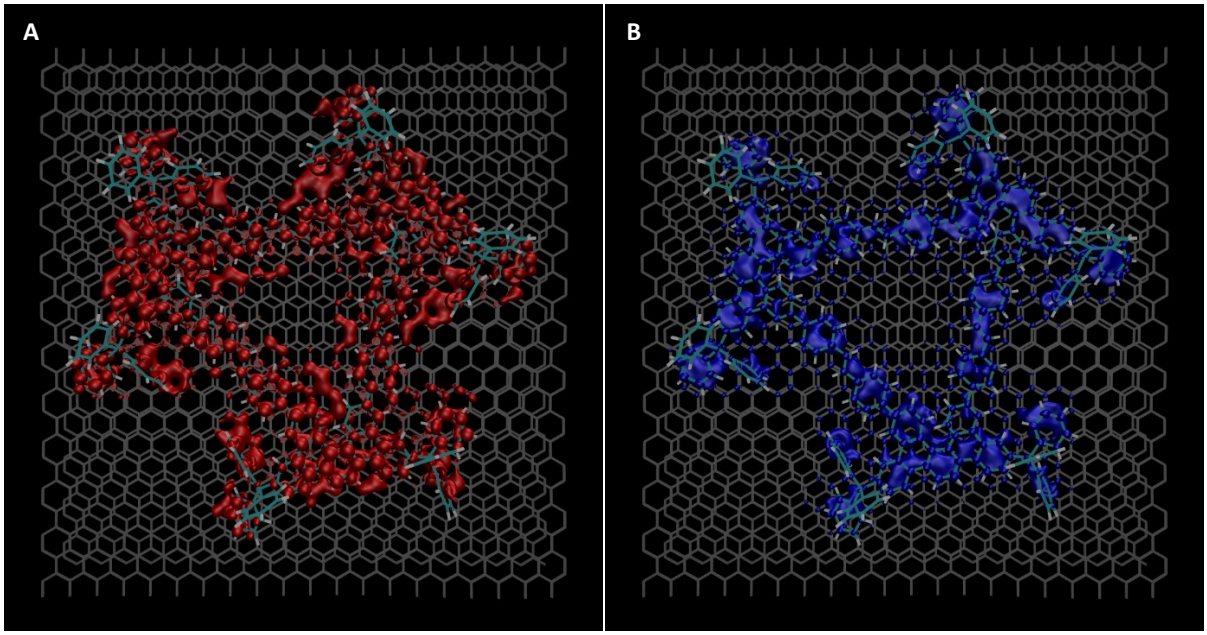

Figure 68. Calculation of charge transfer between (-)-(*M*,*P*,*P*)-**31** and graphite. Regions with depleted electron density after adsorption (positive charge, A). Regions with increased electron density after adsorption (negative charge, B), Iso = ±0.0003.

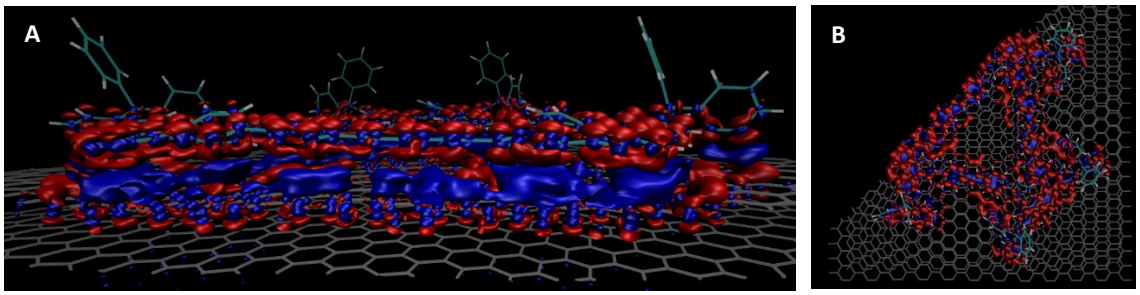

Figure 69. Calculation of charge transfer between (-)-(*M*,*P*,*P*)-**31** and graphite (A). Side cut through the system along one of the (-)-(*M*,*P*,*P*)-**31** triangle's sides (B). Cushion of negative charge between the molecule and the surface due to the Cushion effect (A). Top view of the cut (B), Iso = ±0.0003.

To further distinguish between the contribution of the individual helicene units and the influence of the electronic conjugation over the whole macrocycle, three modified molecules **46a**, **46b**, and **46c** were also investigated. These analogues are derived from **31** by replacing one, two, or three vinylidenes by ethylenes to break the conjugation (Figure 70, highlighted by red color). Interestingly, the calculations showed practically the same degree of charge transfer, around 2 electrons. It is therefore clear, that the formal interruption of the electronic conjugation has a negligible effect on the electron transfer. This can either mean that the isolated units can still communicate with each other by hyperconjugation or even through coupling with the surface. The more trivial explanation, however, is that the charge transfer stems from the contributions corresponding to the individual helicene units, regardless of the global conjugation.

To address this issue, a (*P*)- fragment corresponding to the molecule of monomer **43** was created from the (-)-(*M*,*P*,*P*)-**31**/double graphite system used in the previous calculations and the charge transfer was calculated by analogous methodology. The Mulliken analysis showed the charge transfer of ca 0.6 electron from the molecule to the surface. As this is one third of the charge observed for the whole trimer **31**, it clearly shows that the total transferred charge

is a sum of the contributions of the individual helicene units and global aromatization is not the driving force behind the charge transfer and strong adsorption of **31** on the surface.

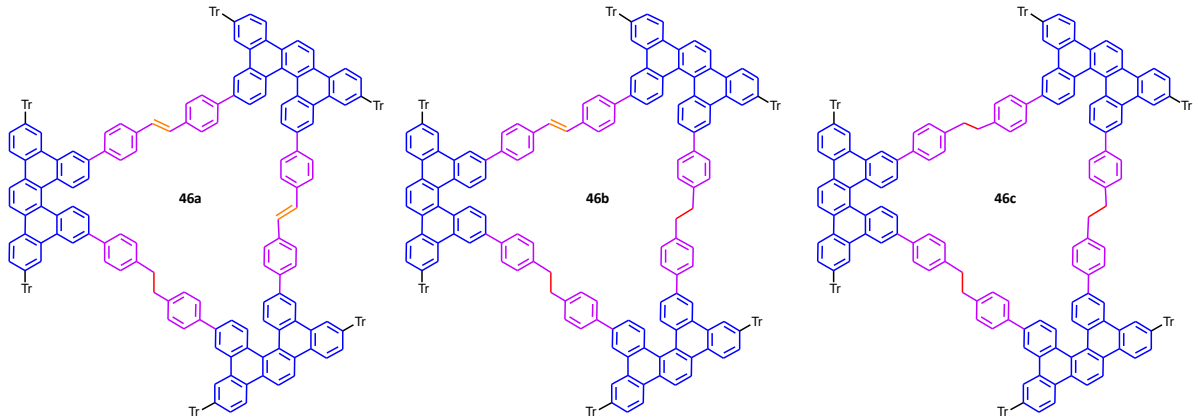

Figure 70. Analogues of **31** with conjugation interruption introduced by hydrogenation of the vinylene moieties.

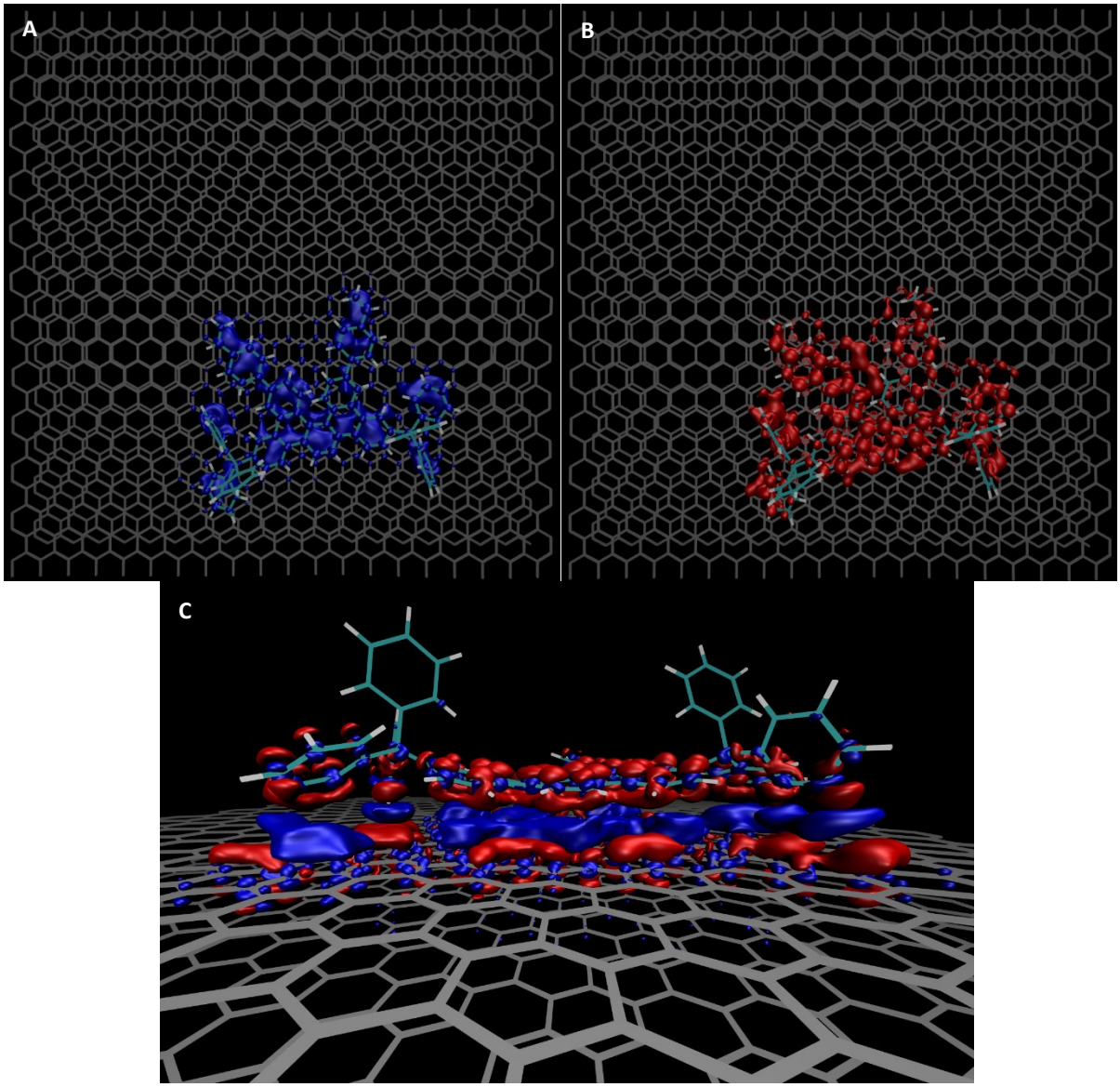

Figure 71. Charge transfer between a fragment analogous to monomer **43** and graphite. Spatial distribution of positive charge (A), negative charge (B), and both viewed from the side (C), Iso = ±0.0003. Ca 0.6 electron is transferred.

4. Summary and Outlook

The presented Thesis was built upon a successful synthesis of a large helicene-based macrocycle **31**. The synthetic part of the work mostly followed standard procedures developed either in our laboratory or elsewhere and was, therefore, described only briefly even despite an overall large number of performed experiments. The final oligomerization, based on olefin metathesis, provided more room for invention, as the reaction conditions had to be finely tuned to allow the formation of **31** in appreciable quantities and challenging separation techniques were necessary to obtain a sufficiently chemically and stereochemically pure product.

In previous studies, many chain-like solubilizing groups were tested with disappointing results. Only when very bulky and comparably rigid trityls were incorporated into the macrocycle structure, the goal of the successful solubilization was finally achieved. This opened a possibility to study **31** in a great detail from many different angles which forms the main body of this Thesis.

Although most material for the structural elucidation was available only as the mixture of stereoisomers, it was possible to perform detailed analytical measurements. Particularly NMR techniques, despite many challenges, assured the final proof of the macrocycle structure. Most NMR signals were assigned to a specific nucleus and differentiation between chiral elements was even possible in many cases.

Separation of (-)-(*P*,*P*,*P*)-**31** stereoisomer allowed a detailed investigation of its conversion to the remaining stereoisomers, providing an entire energy profile of the process. The comparison of the experimental and calculated ECD spectra was successfully utilized to assign the absolute configuration of (-)-(*M*)-**43** and consequently of (*M**,*M**,*M**)-**31** stereoisomers, while the obtained kinetic data was advantageously utilized for the assignment of (*M**,*M**,*P**)-**31** stereoisomers. These studies showed that the core dibenzo[5]helicenes were only minimally restrained within the macrocycle core. This was also reflected in the composition of both the equilibrium and kinetic stereoisomeric mixtures, which was almost entirely governed by statistical, not energetic, factors.

Further studies focused on the self-assembly of **31** on surfaces. Despite initial doubts whether the very bulky molecules **31** would even adsorb on surfaces, AFM measurements showed the molecules form vast mono- and multi-layers on HOPG/air interface. Due to a fine control of the used PeakForce imaging mode, it was possible to obtain many detailed images of structurally diverse assemblies, at times with submolecular resolution. The AFM measurements were also performed with practically enantiomerically pure (-)-(*P*,*P*,*P*)-**31** or various non-equilibrium mixtures. It turned out that assemblies formed from pure (-)-(*P*,*P*,*P*)-**31** behave similarly as those made from racemic **31**. Conversely, more complex, yet non-racemic, mixtures were prone to form unusual structures. Despite the lower stability of the enantiomerically pure aggregates during the AFM imaging, even isolated stripes of molecules were observed in some cases. Self-assembly of **31** was also briefly studied on Au(111) surface. The measurement was, however, hampered by the formation of multilayers with a consequent AFM tip contamination.

To gain more insight into the structure of the assemblies, AFM was accompanied by MD simulations which suggested the possible mode of intermolecular interactions in the assemblies of **31**. It was demonstrated that Van der Waals interactions between the present trityl groups, originally intended only to increase solubility, played a crucial role in stabilizing the assemblies. Additionally, PE simulations, in line with the results of the MD simulations, also showed possible packings of **31** in the 2D domains.

Besides AFM, STM on the HOPG/*n*-octanoic acid interface was also used to study the self-assembly of **31**, but with only limited success. In this case, it is likely the strong electric field along with the presence of the solvent had detrimental effect on the stability of the adlayers.

Since **31** has a 4n π-electron count, its global anti/aromaticity was investigated both in solution and on surfaces. DFT calculations in solution were inconclusive, as the results were strongly dependent on the used functional. The AC voltammetry measurement showed irreversible three-fold oxidation of **31** but the exact implications for its (anti)aromaticity were unclear. Finally, VT-NMR measurements on **31** mixed with $I_2/AgSbF_6$ reagent showed clear peak broadening but no changes in chemical shifts that could be attributed to the change of the (anti)aromaticity status.

The DFT calculations of charge transfer between **31** and HOPG showed that almost two electrons are transferred from the molecule to the surface which initially suggested a possible on-surface oxidation and a consequent aromatization. However, calculation with a fragment analogous to monomer **43** showed that the charge transfer is a sum of the contributions of the individual helicene subunits and likely not a result of the global aromatization.

Finally, although **31** was investigated from many different perspectives, it still offers a number of areas which should be studied. The process of on-surface aromatization still needs to be better understood. Currently, on-surface NICS and ACID calculations are being developed to map the ring currents and experimental measurements such as the graphene enhanced Raman spectrometry and the Kelvin probe AFM are planned to challenge the preliminary computational conclusions. Of particular interest is also investigation of the relationship between the chirality of **31** and spin polarization resulting from the CISS effect. It is envisioned that an intense electrostatic communication of **31** with the surface coupled with its chirality might show a remarkable degree of spin polarization. Currently, experiments employing the spin polarized STM are underway to investigate this interesting area.

5. Experimental Part and Computational Details

5.1. General Synthetic and Analytical Methods

^{1}H NMR spectra were measured at 400.13 MHz, 499.88 MHz, or 600.13 MHz, the ^{13}C NMR spectra at 100.61 MHz, 125.71, or 150.90 MHz in $CDCl_3$, CD_2Cl_2, or $CDCl_2CDCl_2$, as indicated. All chemical shifts are quoted on the δ scale in ppm and referenced using residual ^{1}H solvent signal in ^{1}H NMR spectra ($\delta(CHCl_3)$ = 7.26 ppm; $\delta(CHDCl_2)$ = 5.32 ppm) and ^{13}C solvent signal in ^{13}C NMR spectra ($\delta(CDCl_3)$ = 77.0 ppm; $\delta(CD_2Cl_2)$ = 54.0 ppm). Coupling constants (J) are reported in Hz with the following splitting abbreviations: s = singlet, d= doublet, t = triplet, q = quartet. Where necessary, ^{1}H and ^{13}C resonances were fully assigned using H,H-COSY, H,H-ROESY, H,C-HSQC, and H,C-HMBC techniques. The EI mass spectra were determined at an ionizing voltage of 70 eV, the *m/z* values are given along with their relative intensities (%). The standard 70 eV spectra were recorded in the positive ion mode. ESI mass spectra were recorded using ZQ Micromass mass spectrometer (Waters) equipped with an ESCi multi-mode ion source. Alternatively, the low-resolution ESI mass spectra were recorded using a quadrupole orthogonal acceleration time-of-flight tandem mass spectrometer (Q-Tof micro, Waters) and high-resolution ESI mass spectra using a hybrid FT mass spectrometer combining a linear ion trap MS and the Orbitrap mass analyzer (LTQ Orbitrap XL, Thermo Fisher Scientific). The APCI mass spectra were recorded using an LTQ Orbitrap XL (Thermo Fisher Scientific) hybrid mass spectrometer equipped with an APCI ion source. The MALDI-TOF spectra were measured on UltrafleXtremeTM MALDI-TOF/TOF mass spectrometer (Bruker Daltonics, Germany) with 1 kHz Smartbeam II laser using Dried Droplet technique with 2,5-DHB as matrix. The measurements were done in a positive reflectron mode technique. The accelerating voltage was set at 20kV. IR spectra were measured in $CHCl_3$ on FT-IR Nicolet 6700 spectrometer (Thermo Fisher Scientific, USA) equipped with a standard mid-IR source, a KBr beam-splitter and a DTGS detector and with a cell compartment purged by dry nitrogen. The ECD, absorption, and fluorescence spectra were measured on a Jasco 1500 spectropolarimeter equipped with a fluorescence emission monochromator (FMO522) and separate fluorescence emission detector (FDT-538). The ECD and absorption spectra were measured over a spectral range of 230 nm to 500 nm in chloroform. Measurements were made in a quartz cell with a 0.1 cm path length using a scanning speed of 10 nm/min, a response time of 8 seconds, a standard instrument sensitivity. After a baseline correction, spectra were expressed in terms of differential molar extinction (Δε). Fluorescence spectra were measured with constant emission slit (10 nm) and excitation slit (5 nm) with excitation wavelength indicated in the spectra. The SFC separations were performed on Waters Acquity UPC^2 system using chiral stationary phase column. The HPLC analyses were performed on KNAUER HPLC system equipped with a UV detector and a downstream IBZ Messtechnik Chiralyser polarimetric detector. The semi-preparative HPLC separations were performed on Interchim puriFlash HPLC system. The commercial reagents were used as received unless otherwise noted. Diisopropylamine was distilled from calcium hydride under nitrogen before use; THF, dioxane, and toluene were distilled from sodium/benzophenone under nitrogen. TLC was performed on silica gel 60 or silica gel RP-18 F_{254}-coated aluminum sheets (Merck) and spots were detected by the solution of $Ce(SO_4)_2 \cdot 4\ H_2O$ (1%) and $H_3P(Mo_3O_{10})_4$ (2%) in

sulfuric acid (10%). The flash chromatography was performed on silica gel 60 (0.040-0.063 mm, Merck), or reversed phase silica gel C18, 120 A, 50 um, YMC. Gel permeation chromatography was performed on BIO-RAD BioBeads SX1 gel in dichloromethane. $Pd(OAc)_2$, $Pd(PPh_3)_2Cl_2$, XPhos Pd G2, $CpCo(CO)_2$, Grubbs 2nd gen. catalyst, Piers 2nd gen. catalyst, and XPhos were purchased. The starting materials 4-vinylphenylboronic acid, triphenylmethanol, and **34** were purchased, and **45**[105] was synthesized according to the literature procedures.

5.2.Synthesis of Precursors **35**, **36**, **37**, **38**, **40**, **41**, **42**, and **43**

2-Bromo-4-tritylaniline 35

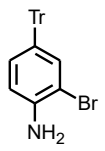

A flask equipped with a reflux condenser and a magnetic stirring bar was charged with triphenylmethanol (50.0 g, 192 mmol, 0.71 equiv.), 2-bromoaniline **34** (46.3 g, 269 mmol), glacial acetic acid (99%, 210 mL), and concentrated HCl (35% aq., 18 mL, 211 mmol, 1.1 equiv.). The resulting white suspension was stirred to reflux (150 °C bath) for 16 h until the solid gradually dissolved and a red solution formed. After cooling down, the mixture was diluted with toluene (150 mL) and the solvents were removed *in vacuo*. To rid the reaction mixture of the remaining acetic acid, toluene (50 mL) was added, and the mixture was evaporated *in vacuo*. To the residue, ethanol (96%, 300 mL) was added, followed by an aqueous solution of KOH (97.0 g, 1.73 mol, 9.0 equiv., dissolved in 100 mL of H_2O). The mixture was then heated under reflux for 1.5 h. The resulting white solid was filtered off and rinsed with hot water (3 x 200 mL), ethanol (3 x 50 mL), and ether (1 x 50 mL). Then it was dried *in vacuo* to yield compound **35** (78.2 g, 98%) as a white powder.

^{1}H NMR (400 MHz, CD_2Cl_2): 4.03 (s, 2H), 6.65 (d, *J* = 8.5 Hz, 1H), 6.91 (dd, *J* = 8.5, 2.2 Hz, 1H), 7.17 – 7.28 (m, 16H).

^{13}C NMR (101 MHz, $CDCl_3$): 64.04, 108.46, 114.74, 125.94, 127.48, 131.00, 131.64, 134.39, 138.29, 141.84, 146.66.

IR ($CHCl_3$): 3489 w, 3396 w, 3087 w, 3061 w, 1672 w, 1618 s, 1596 w, 1572 vw, sh, 1559 vw, 1498 s, 1493 s, 1447 w, 1444 w, 1410 w, 1402 w, 1186 vw, 1167 w, 1142 vw, 1036 w, 1002 vw, 916 vvw, 818 w, 703 vs, 643 m, 619 vvw, 602 w, 438 vw cm^{-1}.

ESI MS: 414 ($[M+H]^+$).

HR ESI MS: calcd. for $C_{25}H_{21}N^{79}Br$ 414.0852, found 414.0854.

2-Bromo-1-iodo-4-tritylbenzene 36

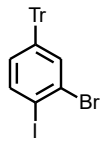

A flask equipped with a magnetic stirring bar was charged with **35** (2.00 g, 4.83 mmol), and acetone (48 mL). To the resulting suspension HCl (35% aq., 4.3 mL) was added. The mixture was further cooled to 0 °C in an ice bath and a cold aqueous $NaNO_2$ solution (500 mg, 7.24 mmol, 1.5 equiv. in 3.2 mL of H_2O) was added dropwise, gradually forming a precipitate. The mixture was stirred at 0 °C for 1 h, after which time a cold aqueous KI solution (1.60 g, 9.65 mmol, 2.0 equiv. in 4.3 mL of H_2O) was added dropwise. The mixture was subsequently stirred at 0 °C for 1 h, then for 1 h at room temperature, and under reflux for 2 h. The suspension was diluted with chloroform (10 mL) and washed with an aqueous solution of $Na_2S_2O_3$ (30 mL). The organic phase was separated and the aqueous one was extracted with chloroform (4 x 30 mL). The combined extracts were dried over anhydrous $MgSO_4$, and the solvents were removed *in vacuo*. The crude material was purified by a flash chromatography on silica gel (hexane-chloroform 95:5 to hexane-dichloromethane 1:1) to provide product **36** (2.36 g, 93%) as a white solid.

^{1}H NMR (400 MHz, CD_2Cl_2): 6.90 (dd, *J* = 8.4, 2.3 Hz, 1H), 7.20 – 7.24 (m, 9H), 7.26 – 7.30 (m, 6H), 7.54 (d, *J* = 2.3 Hz, 1H), 7.74 (d, *J* = 8.4 Hz, 1H).

^{13}C NMR (101 MHz, CD_2Cl_2): 65.20, 98.69, 126.83, 128.36, 129.58, 131.34, 132.27, 135.34, 139.80, 146.40, 150.00.

IR ($CHCl_3$): 3088 w, 3061 w, 3032 w, 1598 w, 1575 vw, 1561 vw, 1540 vw, 1493 m, 1458 w, 1447 m, 1405 vw, 1303 vvw, 1263 vw, 1188 vw, 1157 vvw, 1142 vvw, 1085 w, 1035 w, 1106 vw, 997 vw, 945 vw, 880 vw, 844 vvw, 821 w, 704 vs, 638 w, 633 w, 619 vw, 441 vw cm^{-1}.

EI MS: 524 ($M^{+\bullet}$, 64), 447 (100), 239 (94), 165 (89).

HR EI MS: calcd. for $C_{25}H_{18}{}^{79}BrI$ 523.9637, found 523.9636.

(2-Bromo-4-tritylphenyl)ethynyl][tris(1-methylethyl)]silane 37

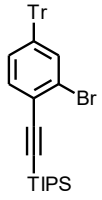

A flask equipped with a magnetic stirring bar and a Schlenk adaptor was charged with **36** (26.7 g, 50.9 mmol), $Pd(PPh_3)_2Cl_2$ (1.79 g, 2.55 mmol, 5 mol%), CuI (0.97 g, 5.1 mmol, 10 mol%), diisopropylamine (260 mL), and toluene (360 mL) under argon. The resulting yellow suspension was degassed by three freeze-pump-thaw cycles, immersed in a 0 °C cold ethanol bath, and (triisopropyl)silyl acetylene (11.6 mL, 51.9 mmol, 1.1 equiv.) was added *via* syringe. The solution was left stirring while the temperature was gradually brought to a room temperature overnight (by using a thermostat). The solvents were removed *in vacuo*, the residue was dissolved in chloroform (100 mL) and washed with a saturated NH_4Cl solution (100 mL). The solvent was removed *in vacuo* and the residue was re-dissolved in a small amount of toluene (10 mL) and filtered through a short pad of silica gel (toluene – chloroform 10:0 to 8:2) to remove most impurities. The compound was subsequently recrystallized from *n*-heptane to provide product **37** (23.6 g, 80%) as a white powder.

^{1}H NMR (400 MHz, CD_2Cl_2): 1.13 – 1.16 (m, 21H), 7.15 (dd, *J* = 8.3, 1.9 Hz, 1H), 7.18 – 7.24 (m, 9H), 7.25 – 7.30 (m, 6H), 7.40 (d, *J* = 8.3 Hz, 1H), 7.50 (d, *J* = 1.9 Hz, 1H).

^{13}C NMR (101 MHz, CD_2Cl_2): 11.86, 18.98, 65.40, 96.72, 105.23, 123.55, 125.47, 126.79, 128.33, 130.65, 131.39, 133.25, 134.85, 146.50, 149.76.

IR ($CHCl_3$): 3061 w, 3027 w, 2959 m, sh, 2945 m, 2866 m, 2159 w, 1593 w, 1560 w, 1493 m, 1470 m, 1448 m, 1405 w, 1382 w, 1367 w, 1048 w, 997 w, 883 m, 675 m cm^{-1}.

ESI MS: 579 ($[M+H]^+$), 601 ($[M+Na]^+$), 617 ($[M+K]^+$).

HR ESI MS: calcd. for $C_{36}H_{40}{}^{79}BrSi$ 579.2077, found 579.2079.

2-{[Tris(1-methylethyl)silyl]ethynyl}-5-tritylphenyl)boronic acid 38

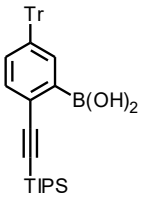

A flask equipped with a magnetic stirring bar and a Schlenk adaptor was charged with **37** (3.23 g, 5.57 mmol), and THF (32 mL) was added under argon. The solution was cooled to -78 °C before a solution of *t*-BuLi (1.7 M in pentane, 6.56 mL, 11.1 mmol, 2.0 equiv.) was added dropwise. The whole mixture gradually solidified. After stirring for 1 h, B(O-*i*-Pr)$_3$ (2.56 mL, 11.1 mmol, 2.0 equiv.) was added dropwise and the mixture was allowed to slowly reach room temperature overnight. The reaction was quenched with aqueous HCl (1 M, 20 mL), the organic phase was separated, and the aqueous phase extracted with chloroform (3 x 20 mL). The combined extracts were dried over anhydrous $MgSO_4$, solvents removed *in vacuo*, and the residue was chromatographed on silica gel (hexane – chloroform 1:1 to chloroform – ethyl acetate 7:3) to afford product **38** (2.56 g, 84%) as a pale yellow amorphous solid.

^{1}H NMR (400 MHz, CD_2Cl_2): 1.12-1.17 (m, 21H), 5.89 (s, 2H), 7.18 – 7.30 (m, 15H), 7.33 (dd, *J* = 8.2, 2.2 Hz, 1H), 7.45 (d, *J* = 8.3 Hz, 1H), 7.88 (d, *J* = 1.9 Hz, 1H).

^{13}C NMR (101 MHz, CD_2Cl_2): 11.83, 18.91, 65.61, 96.39, 108.83, 124.92, 126.58, 128.23, 131.44, 132.95, 133.99, 138.06, 146.99, 147.86. The quaternary carbon with the boron group was not found.

IR ($CHCl_3$): 3622 w, 3513 w, 3087 w, 3061 w, 3031 w, 2946 m, 2142 w, 1596 w, 1547 w, 1492 m, 1463 m, 1447 m, 1406 m, 1367 m, 1061 w 1048 w, 1035 m, 997 m, 883 m, 680 m, 607 w cm^{-1}.

ESI MS: 543 ([M-H]$^-$), 589 ([M+C_2H_5O]$^-$).

HR ESI MS: calcd. for $C_{36}H_{40}O_2BSi$ 543.2896, found 543.2893.

Ethyne-1,2-diylbis[(5-chloro-6'-tritylbiphenyl-2,3'-diyl)ethyne-2,1-diyl]}bis[tris(1-methylethyl)silane] 40

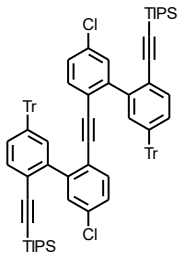

A Schlenk flask equipped with a reflux condenser was charged with **39**[106] (100 mg, 0.247 mmol), boronic acid **38** (404 mg, 0.741 mmol, 3.0 equiv.), K_2CO_3 (137 mg, 0.988 mmol, 4.0 equiv.), and $Pd(PPh_3)_2Cl_2$ (17 mg, 0.025 mmol, 10 mol%). Toluene (2.5 mL), *n*-PrOH (2.5 mL), and water (0.6 mL) were added, and the mixture was purged with a stream of argon for 10 min after which time the flask was sealed and stirred under reflux at 110 °C for 3 h. The mixture was then diluted with chloroform (5 mL), water (5 mL), the aqueous phase was extracted with chloroform (3 x 10 mL), the combined extracts were dried over anhydrous $MgSO_4$, and the solvents were removed *in vacuo*. The solid residue was purified by flash chromatography on silica gel (hexane – toluene 9:1 to 0:1) to provide product **40** (301 mg, 98%) as a yellow resin.

^{1}H NMR (400 MHz, CD_2Cl_2): 0.93 – 0.94 (m, 42H), 6.77 (d, *J* = 8.3 Hz, 2H), 6.96 (dd, *J* = 8.3, 2.2 Hz, 2H), 7.05 – 7.15 (m, 18H), 7.16 – 7.22 (m, 12H), 7.24 (m, 2H), 7.39 -7.40 (m, 4H), 7.54 (d, *J* = 8.3 Hz, 2H).

^{13}C NMR (101 MHz, CD_2Cl_2): 11.71, 18.85, 65.62, 92.47, 95.33, 105.81, 120.91, 121.41, 126.64, 127.99, 128.13, 130.99, 131.41, 131.48, 132.05, 132.49, 133.94, 134.20, 141.87, 144.82, 146.89, 147.28.

IR ($CHCl_3$): 3087 w, 3060 w, 2959 w, 2944 m, 2891 w, 2154 w, 1596 w, 1588 w, 1492 m, 1476 m, 1464 w, 1448 w, 1444 w, 1383 w, 1140 vw, 1037 w, 997 w, 884 w, 834 w, 652 w, 644 w, 634 m cm^{-1}.

MALDI MS: 1265 ($[M+Na]^+$), 1281($[M+K]^+$).

HR MALDI MS: calcd. for $C_{86}H_{84}{}^{35}Cl_2NaSi_2$ 1265.5381, found 1265.5353.

2,2'-Ethyne-1,2-diylbis(5-chloro-5'-ethynyl-2'-tritylbiphenyl) 41

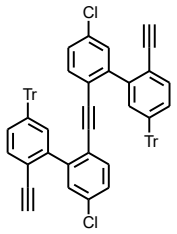

To a solution of **40** (280 mg, 0.225 mmol) dissolved in THF (2.3 mL), methanol (18 µL, 0.45 mmol, 2.0 equiv.) and TBAF · $3H_2O$ (1M solution in THF, 0.9 mL, 0.9 mmol, 4.0 equiv.) were added under argon. The resulting solution was stirred at room temperature for 1 h after which time it was quenched with MeOH (5 mL) and a saturated solution of NH_4Cl (5 mL). The aqueous phase was extracted with chloroform (3 x 10 mL), the combined extracts were dried over anhydrous $MgSO_4$, and the solvents were removed *in vacuo*. The obtained oil was filtered through a short pad of silica gel (dichloromethane). The solution was evaporated and the oily residue **41** (175 mg, 83%) was used directly in the next step because the compound was unstable and difficult to purify.

^{1}H NMR (400 MHz, $CDCl_3$): 2.98 (s, 2H), 6.77 (d, *J* = 8.3 Hz, 2H), 7.05 (dd, *J* = 8.3, 2.2 Hz, 2H), 7.08 – 7.18 (m, 18H), 7.18 – 7.24 (m, 12H), 7.26 (dd, *J* = 8.3, 2.1 Hz, 2H), 7.33 – 7.34 (m, 4H), 7.55 (d, *J* = 8.3 Hz, 2H).

^{13}C NMR (151 MHz, CD2Cl2): 65.61, 81.06, 82.52, 92.39, 119.56, 121.53, 126.67, 128.18, 128.20, 130.53, 131.49, 132.09, 132.34, 132.67, 133.93, 134.01, 142.13, 144.82, 146.81, 147.99.

IR ($CHCl_3$): 3302 w, 2107 vw, 1598 w, sh, 1563 vw, 1492 m, 1460 w, sh, 1448 w, 1363 w, 1309 vw, 1082 w, 1036 w, 703 vs, 620 w cm^{-1}.

MALDI MS: 931 ($[M+H]^+$), 953 ($[M+Na]^+$).

HR MALDI MS: calcd. for $C_{68}H_{45}{}^{35}Cl_2$ 931.2893, found 931.2865.

6,11-Dichloro-3,14-ditrityldibenzo[*f,l*]pentahelicene 42

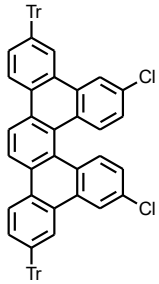

To a solution of **41** (147 mg, 0.158 mmol) in THF (19 mL) and toluene (6 mL), $CpCo(CO)_2$ (21 µL, 0.16 mmol, 1.0 equiv.) was added under argon, and the resulting solution was submitted to cyclotrimerization in a flow reactor (250 °C, 8 min). The solvent was removed *in vacuo* and the residue was purified by flash chromatography on silica gel (hexane – toluene 7:1 to 0:1) to provide product **42** (125 mg, 85%) as a pale-yellow powder.

^{1}H NMR (600 MHz, CD_2Cl_2): 7.10 (dd, *J* = 8.9, 2.2 Hz, 2H), 7.24 – 7.29 (m, 6H), 7.34 (m, 12H), 7.41 (m, 12H), 7.63 (dd, *J* = 8.7, 2.0 Hz, 2H), 8.08 (d, *J* = 8.9 Hz, 2H), 8.11 (d, *J* = 2.2 Hz, 2H), 8.53 (d, *J* = 8.8 Hz, 2H), 8.56 (d, *J* = 1.9 Hz, 2H), 8.62 (s, 2H).

^{13}C NMR (151 MHz, CD_2Cl_2): 65.92, 122.79, 123.50, 123.61, 125.41, 126.15, 126.74, 127.37, 128.17, 128.35, 129.09, 129.79, 130.67, 131.64, 132.16, 132.54 (2C), 133.33, 147.18, 147.22.

IR ($CHCl_3$): 3087 w, 3061 w, 1598 w, 1493 m, 1447 w, 1185 w, sh, 1085 vw, 1036 w, 1001 vw, 709 vs, 630 w cm^{-1}.

MALDI MS: ($[M\text{-}C_6H_5]^+$) 853, ($[M\text{-}^{35}Cl]^+$) 895, ($[M]^+$) 930.

HR MALDI MS: calcd. for $C_{68}H_{44}{}^{35}Cl_2$ 930.2815, found 930.2815.

6,11-Bis(4-ethenylphenyl)-3,14-ditrityldibenzo[f,l]pentahelicene 43

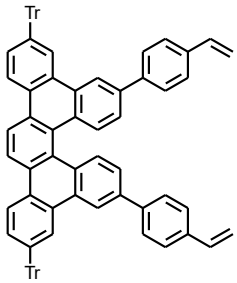

A pressure Schlenk flask was charged with **42** (35 mg, 38 µmol), 4-vinylphenylboronic acid (22 mg, 0.15 mmol, 4.0 equiv.), and XPhos Pd G2 (3.0 mg, 4 µmol, 10 mol%). THF (1.1 mL) was added *via* syringe, followed by the addition of an aqueous solution of K_3PO_4 (0.5M, 300 µL, 0.15 mmol, 4.0 equiv.). The mixture was purged with argon for 5 min and the flask was sealed. The mixture was heated to 100 °C for 3 h while being vigorously stirred after which time it was diluted with chloroform (5 mL), brine (5 mL), the mixture was extracted with chloroform (3 x 5 mL), and the combined extracts were dried over anhydrous $MgSO_4$. The solvents were removed *in vacuo* and the solid residue was purified by flash chromatography on a fine particle silica gel 60 (15 – 40 µm, hexane – toluene 8:2 to 0:1) to provide product **43** (31 mg, 77%) as a yellow resin. In some instances, when separation on silica gel did not give a sufficiently pure product, separation via GPC in dichloromethane was used.

^{1}H NMR (600 MHz, CD_2Cl_2): 5.31 (dd, *J* = 10.9, 0.9 Hz, 2H), 5.85 (dd, *J* = 17.6, 0.9 Hz, 2H), 6.80 (dd, *J* = 17.6, 10.9 Hz, 2H), 7.28 – 7.31 (m, 6H), 7.34 – 7.38 (m, 12H), 7.41 – 7.44 (m, 12H), 7.46 (dd, *J* = 8.7, 1.9 Hz, 2H), 7.52 – 7.56 (m, 4H), 7.58 (dd, *J* = 8.6, 2.0 Hz, 2H), 7.62 – 7.67 (m, 4H), 8.31 (d, *J* = 8.6 Hz, 2H), 8.44 (d, *J* = 2.0 Hz, 2H), 8.55 (d, *J* = 8.7 Hz, 2H), 8.65 (s, 2H), 8.73 (d, *J* = 2.0 Hz, 2H).

^{13}C NMR (151 MHz, CD_2Cl_2): 147.24, 146.85, 140.17, 138.83, 137.48, 136.87, 132.28, 131.82, 131.70, 131.02, 130.80, 130.63, 130.07, 128.25, 128.13, 128.04, 127.39, 127.32, 126.75, 125.48, 124.22, 123.37, 122.58, 121.75, 114.46, 66.06.

IR ($CHCl_3$): 3088 w, 3059 w, 2927 w, 2855 vw, 1629 w, 1612 w, 1599 w, 1569 vw, 1518 w, 1493 m, 1448 w, 1423 w, 1119 vw, 1036 w, 1014 w, 990 w, 913 w, 827 m, 631 m, 567 w cm^{-1}.

MALDI MS: 989 ($[M\text{-}C_6H_5]^+$), 1067 ($[M+H]^+$), 1089 ($[M+Na]^+$).

HR MALDI MS: calcd. for $C_{84}H_{59}$ 1067.4611, found 1067.4589.

Macrocyclization of racemic 43 to macrocycles 31 and 32

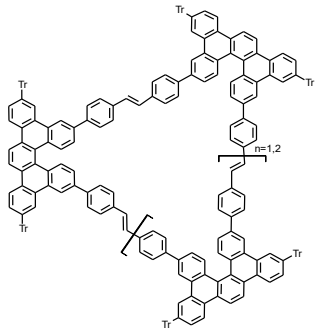

A pressure Schlenk flask was charged with **43** (25 mg, 23 µmol), Piers 2nd gen. catalyst (4.0 mg, 5.0 µmol, 20 mol%), and 1,2,4-trichlorobenzene (1.2 mL) was added. The mixture was stirred under vacuum (ca 1 mmHg) at 50 °C overnight until the solvent evaporated. Analytical gel permeation chromatography (dichloromethane) showed a mixture of oligomers with the trimer **31** as the main product. Quadrasil AP (ca 100 mg, Sigma Aldrich) was added to the mixture and the resulting suspension was left stirring at room temperature for 10 min after which time it was filtered off and the solvent was removed by vacuum distillation. The residue was then filtered through a short pad of silica gel (using alternately equal portions of toluene and chloroform, total of ca 150 mL), solvents were removed *in vacuo* and the residue submitted to three consecutive gel permeation chromatography separations on BioBeads SX1 polystyrene gel (dichloromethane). The separation provided trimer **31** (8 mg, 33%) and tetramer **32** (4 mg, 22%) as yellow highly fluorescent resins. Macrocyclization of racemic **43** and separation of products **31** and **32** were performed repeatedly with similar yields, *e.g.*, yielding up to 29 mg (27%) of **31** as a mixture of stereoisomers in a single run.

Trimer 31 as a mixture of stereoisomers

Detailed NMR assignment and discussion can be found in the NMR section (Chapters 3.6.2. and 5.14.).

IR ($CHCl_3$): 3087 w, 3060 m, 3032 w, 1611 w, 1599 w, 1580 vw, 1570 vw, 1558 vw, 1520 w, 1493 s, 1475 m, 1448 m, 1443 m, 1419 vw, sh, 1406 w, 1396 w, 1305 vw, 1261 vw, 1187 w, 1158 vw, 1112 vw, 1084 w, 1036 w, 1013 w, 1001 w, 966 w, 911 w, 844 vw, 824 m, 703 vs, 644 w, 631 m, 623 vw, 617 vw, 611 vw, 580 vw, sh, 483 w, 442 vw cm^{-1}.

MALDI MS: 2658 ($[M-C_{36}H_{24}]^+$), 2734 ($[M-C_{30}H_{20}]^+$), 2804 ($[M-C_{24}H_{23}]^+$), 2806 ($[M-C_{24}H_{21}]^+$), 2808 ($[M-C_{24}H_{19}]^+$), 2810 ($[M-C_{24}H_{17}]^+$), 2882 ($[M-C_{18}H_{19}]^+$), 2884 ($[M-C_{18}H_{17}]^+$), 2884 ($[M-C_{18}H_{15}]^+$), 2886 ($[M-C_{18}H_{13}]^+$), 2958 ($[M-C_{12}H_{13}]^+$), 2960 ($[M-C_{12}H_{11}]^+$), 2962 ($[M-C_{12}H_9]^+$), 3036 ($[M-C_6H_7]^+$), 3038 ($[M-C_6H_5]^+$), 3112 ($[M-3H]^+$), 3114 ($[M-H]^+$), 3116 ($[M+H]^+$).

HR MALDI MS: calcd. for $C_{246}H_{163}$ 3116.2749, found 3116.2704.

Tetramer 32 as a mixture of stereoisomers

Discussion regarding the NMR spectra can be found in the NMR section. Complete signal assignment was not performed.

IR ($CHCl_3$): 3087 w, 3060 m, 1612 m, 1599 m, 1558 w, 1515 w, 1493 s, 1475 m, 1443 m, 1396 w, 1305 w, 1084 w, 1036 m, 1013 w, 1001 w, 966 m, 824 m, 704 vs, 631 m, 484 w, 444 vw cm^{-1}.

MALDI MS: 3696 ($[M-C_{36}H_{19}]^+$), 3773 ($[M-C_{30}H_{16}]^+$), 3849 ($[M-C_{24}H_{13}]^+$), 3925 ($[M-C_{18}H_{10}]^+$), 4001 ($[M-C_{12}H_7]^+$), 4077 ($[M-C_6H_4]^+$), 4177 ($[M+Na]^+$), 4155 ($[M+H]^+$).

HR MALDI MS: calcd. for $C_{328}H_{216}$ 4154.6975, found 4154.6792.

Investigation of thermodynamic/kinetic control of metathesis leading to trimer 31

A pressure Schlenk flask was charged with **32** (40 mg, 39 µmol), Piers 2nd gen. catalyst (6.5 mg, 8.0 µmol, 20 mol%), and 1,2,4-trichlorobenzene (1.9 mL) was added. The mixture was stirred under vacuum (ca 1 mmHg) at 50 °C for 18 h until the solvent evaporated. Analytical GPC (dichloromethane) did not show formation of trimer **31**. 1,2,4-Trichlorobenzene (1.9 mL) was added, temperature was raised to 70 °C, and heating continued for additional 14 h after which the composition of the mixture was analyzed again by GPC. This time, a slight shouldering in the analytical peak of the starting material was observed indicating the formation of **31**. This result was also corroborated by MALDI MS spectrum of the mixture, showing the signal of trimer **31** along the majority signal of tetramer **32** (Figure 72). Moreover, a lot of precipitate formed which was attributed to undesired higher oligomers.

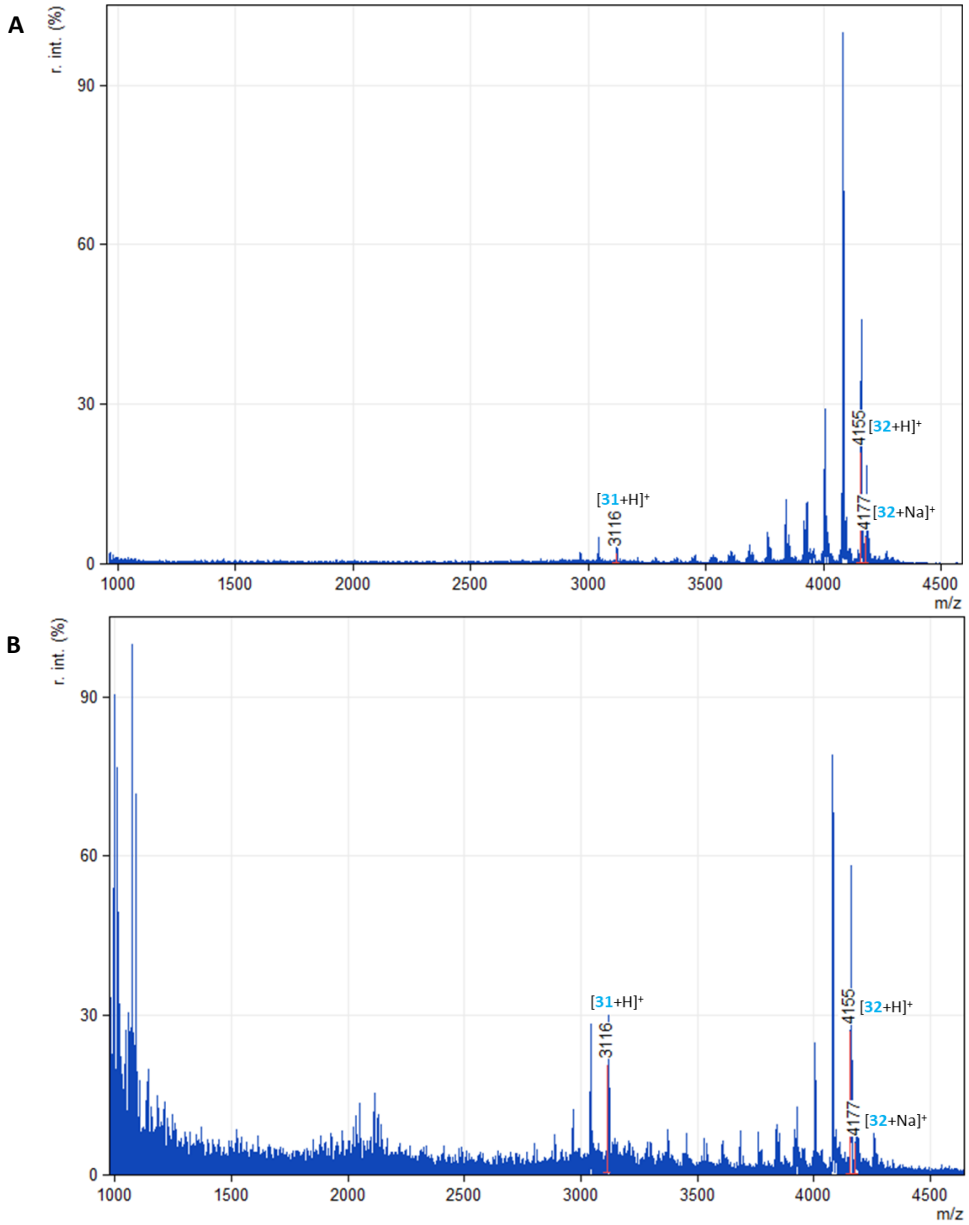

Figure 72. Normalized MALDI MS spectra of the reaction mixture before (A) and after the metathesis (B). The first spectrum shows the majority of tetramer **32** at 4155 m/z, while the second spectrum shows a noticeable increase in the signal of trimer **31** at 3116 m/z.

Stereoisomerically enriched trimer (+)-(*M,M,M*)-31

An Apollo-shaped 10 mL flask was charged with (-)-(*M*)-**43** (20 mg, 19 µmol, ca 95% *ee*), Piers 2nd gen. catalyst (3.2 mg, 4.0 µmol, 20 mol%), and 1,2,4-trichlorobenzene (1.2 mL) was added. The flask was connected *via* a 10 mm ID tubing to a hybrid vacuum oil pump equipped with a freeze trap and evacuated. The pressure in the flask was regulated with a Hoffmann tubing clamp to ca 0.15 mmHg. The reaction mixture was left stirring at room temperature until the solvent evaporated (2 d). The solid residue was dissolved in chloroform (3 mL), Quadrasil AP (ca 50 mg) was added, and the resulting suspension was stirred for 10 min. The mixture was then filtered through a short pad of silica gel (using alternately equal portions of toluene and chloroform, total of ca 100 mL), solvent was removed *in vacuo*, and the residue was submitted to gel permeation chromatography on BioBeads SX1 polystyrene gel (dichloromethane) furnishing the desired trimer **31** (5 mg, 26%) as a yellow solid. Analytical SFC chromatography confirmed the main product was (+)-(*M,M,M*)-**31** stereoisomer (Figure 73).

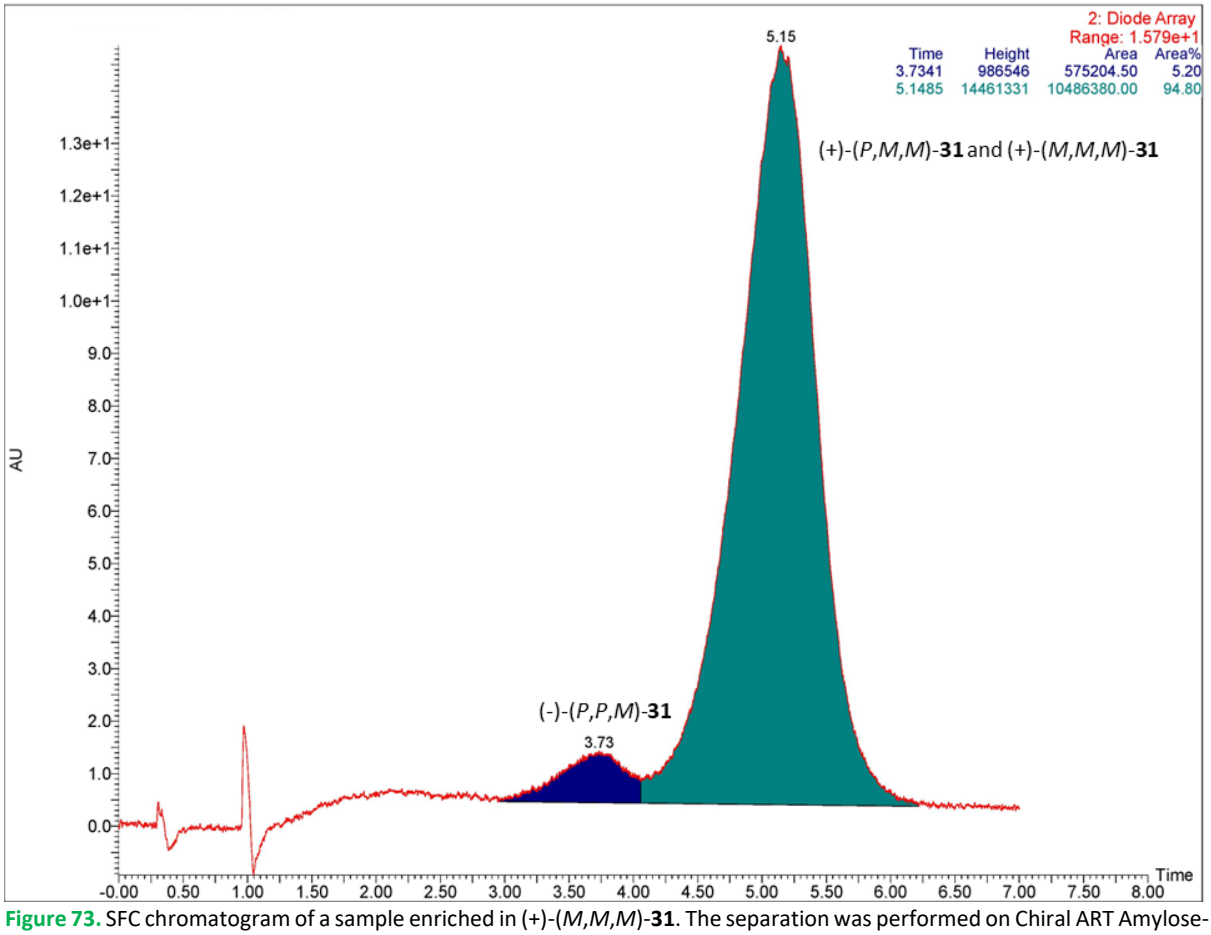

Figure 73. SFC chromatogram of a sample enriched in (+)-(*M,M,M*)-**31**. The separation was performed on Chiral ART Amylose-SA column (4.6 mm ID × 250 mm, 5 µm particle size) using CO_2 – chloroform (53:47) mixture as eluent, chloroform was modified by addition of 0.1% of *i*-PrOH (flow rate of 3 mL·min^{-1}, 35 °C column temperature, 1500 psi ABPR pressure).

Stereoisomerically enriched trimer (-)-(*P,P,P*)-31

The synthetic procedure was identical to that for (+)-(*M,M,M*)-**31** stereoisomer described above. (+)-(*P*)-**43** (10 mg, 10 µmol, ca 95% *ee*), Piers 2nd gen. catalyst (1.8 mg, 2.0 µmol, 20 mol%), 1,2,4-trichlorobenzene (0.6 mL). The product **31** (3 mg, 28%) was obtained as a yellow solid. Analytical SFC chromatography confirmed the main product was (-)-(*P,P,P*)-**31** stereoisomer (Figure 74).

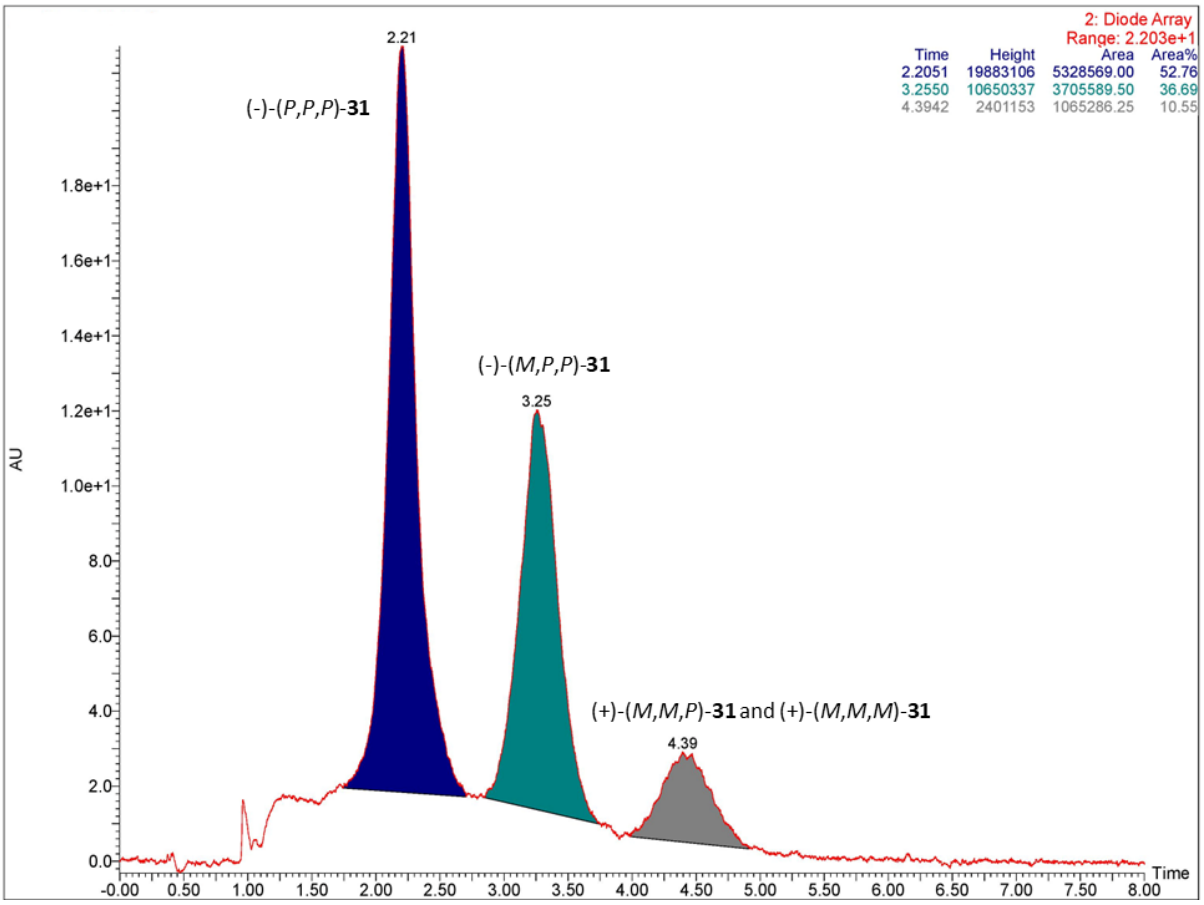

Figure 74. SFC chromatogram of a sample enriched in (-)-(*P,P,P*)-**31**. The separation was performed on Chiral ART Amylose-SA column (4.6 mm ID × 250 mm, 5 µm particle size) using CO_2 – chloroform (53:47) mixture as eluent, chloroform was modified by addition of 0.1% of *i*-PrOH (flow rate of 3 mL·min^{-1}, 35 °C column temperature, 1500 psi ABPR pressure).

5.3. Chiral Resolution of Stereoisomers of Trimer **31**

Separation of the individual stereoisomers at analytical scale was performed using SFC on a chiral column. Semipreparative scale separation was achieved by combination of repeated HPLC and/or SFC.

Supercritical fluid chromatography

Conditions: Analytical Chiral ART Amylose-SA column (4.6 mm ID × 250 mm, 5 µm particle size) using CO_2 – chloroform (53:47) mixture as eluent, chloroform was modified by addition of 0.1% of *i*-PrOH, (flow rate of 3 mL·min^{-1}, 35 °C column temperature, 1500 psi ABPR pressure). The column was thoroughly washed by chloroform between successive separations to ensure reproducibility and efficiency of the next separation.

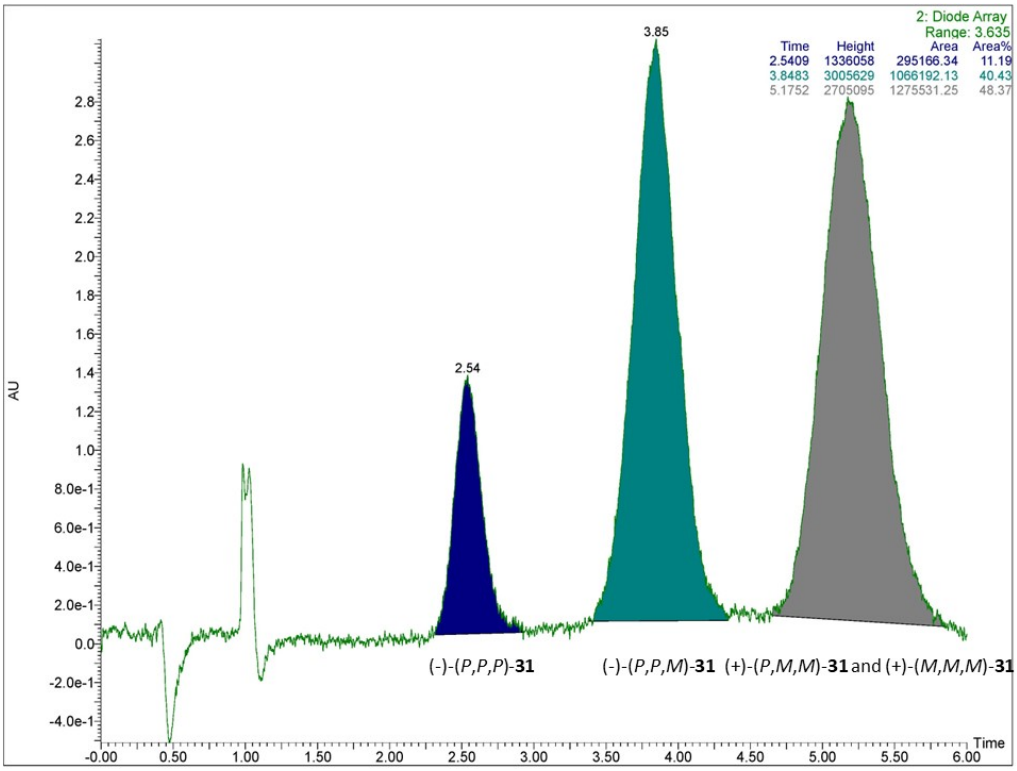

Figure 75. SFC chromatogram of **31**. The separation was performed on Chiral ART Amylose-SA column (4.6 mm ID × 250 mm, 5 µm particle size) using CO_2 – chloroform (53:47) mixture as eluent, chloroform was modified by addition of 0.1% of *i*-PrOH (flow rate of 3 mL·min^{-1}, 35 °C column temperature, 1500 psi ABPR pressure).

A range of different stationary phases was tested but Chiral ART Amylose-SA was the only stationary phase achieving satisfactory separation. The analytical SFC of trimer **31** produced a chromatogram with three peaks (Figure 75). Since both (*M**,*M**,*M**)-**31** and (*M**,*M**,*P**)-**31** stereoisomers are chiral, four stereoisomers should be possible to detect. As the peaks at 3.85 and 5.18 min have similar areas, one possible explanation was that these peaks correspond to mutual enantiomers, whereas the small peak at 2.54 min belongs to two unseparated enantiomers. The second possible explanation was that the first small peak was a single enantiomer, and the other complementary enantiomer was hidden in one of the large peaks. The first hypothesis was ruled out, as the first peak was optically active. The final evidence for

the second explanation came from the appearance of the calibration lines (Figures 29) and the isomerization kinetics (Figure 30).

Analytical HPLC

Conditions: Analytical Chiral ART Amylose-SA column (4.6 mm ID × 250 mm, 5 µm particle size) using *n*-heptane – toluene – tetrahydrofuran – *i*-PrOH (60:30:5:0.3) mixture as eluent (flow rate of 1 mL·min^{-1}, room temperature).

Separation of the stereoisomers of **31** on analytical HPLC equipped with both UV and polarimetric detectors gave generally poorer results compared to SCF but it allowed to measure the sign of optical rotation (Figure 26). However, the measurement was complicated by a small amount of injected sample leading to a very weak signal from the polarimetric detector. At higher sample concentrations, separation was not possible. The sign of optical rotation was also confirmed by a measurement on a standard polarimeter.

Preparative HPLC

Conditions: Semipreparative Chiral ART Amylose-SA column (20 mm ID × 250 mm, 5 µm particle size) using *n*-heptane – toluene – tetrahydrofuran – *i*-PrOH (60:30:5:0.3) mixture as eluent (flow rate of 20 mL·min^{-1}, room temperature).

Only (-)-(*P*,*P*,*P*)-**31** isomer could be separated in larger quantity (ca 0.2 mg) and purity of almost 100% by a repeated semipreparative scale HPLC. The other isomers were received in 67-75% purity. However, the obtained amount was insufficient for a useful NMR measurement. Moreover, the material was obtained in the form of a resin that could not be reliably weighed in such a small amount, thus only relative measurements could be performed (kinetic measurements, ECD spectra etc.).

5.4. Isomerization of Trimer **31**

Heating the original stereoisomeric mixture to 92 °C for 2 h did not alter its composition, suggesting that the compound **31** prepared from the racemic **43** was already an equilibrium product and the calibration lines were therefore measured on the equilibrated mixture.

It is worth mentioning that calibrations pertaining to the kinetic measurements were performed using a diode UV array detector with signal corresponding to a range of wavelengths. This allowed a simultaneous measurement of the internal standard and macrocycles **31**. The absolute values of extinction coefficients were estimated for the 350 nm wavelength.

Calibration curves

Experimental procedure: The equilibrated stereoisomeric mixture of **31** (ca 0.1 mg) was dissolved in chloroform (500 µL). From this solution, 75 µL, 50 µL, 25 µL, and 12.5 µL was transferred to separate vials and the volume was topped up to 100 µL, thereby creating solutions with relative concentrations c_r, $2c_r$, $4c_r$, $6c_r$, and $8c_r$, respectively. Each solution was then submitted to SFC analytical chromatography. Figures 75 and 76 show the chromatograms for each concentration c_r while Figures 29 and 78 show the corresponding calibration lines constructed from the measurements for each chromatogram peak. Sum of values for the peaks of (-)-(*P*,*P*,*P*)-**31** and (-)-(*M*,*P*,*P*)-**31** was compared to the peak corresponding to the mixture of (+)-(*M*,*M*,*P*)-**31** and (+)-(*M*,*M*,*M*)-**31**, showing that this peak was obviously an overlap of the opposite enantiomers of the first two peaks.

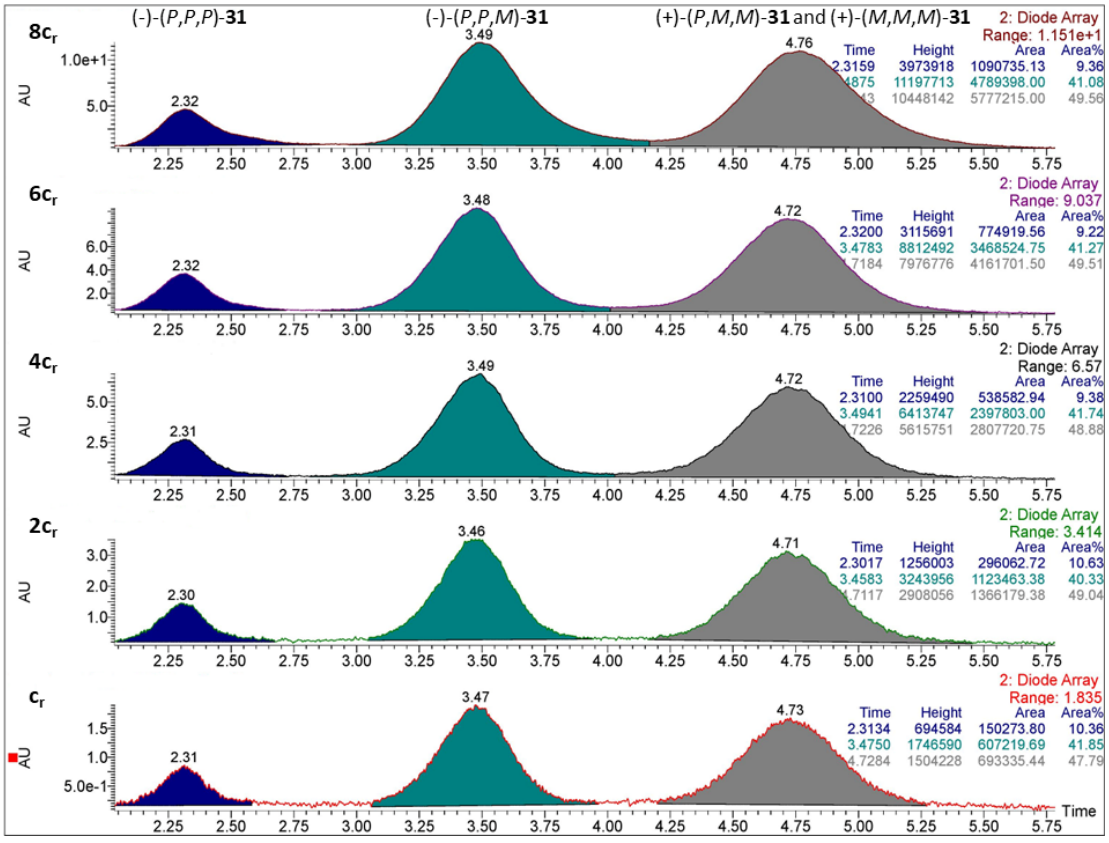

Figure 76. SFC chromatogram of stereoisomeric mixture of **31** at dimensionless concentrations ranging from c_r to $8c_r$.

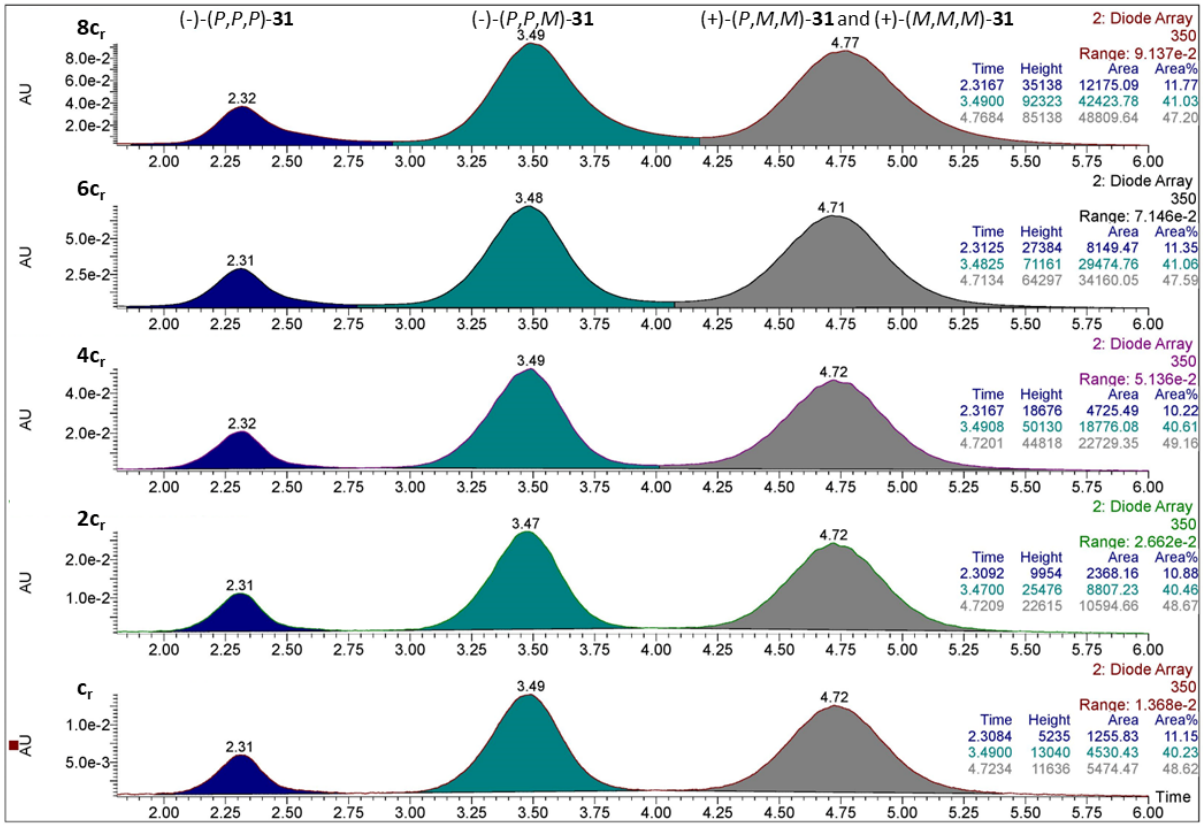

Figure 77. SFC chromatogram of stereoisomeric mixture of **31** at dimensionless concentrations ranging from c_r to $8c_r$. Signals at 350 nm wavelength are displayed.

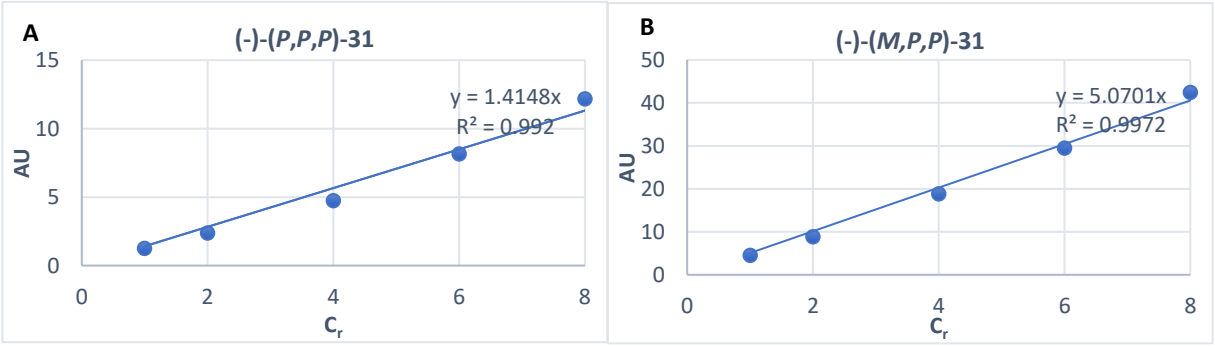

Figure 78. Calibration lines for individual chromatographic peaks of (-)-(*P*,*P*,*P*)-**31** (A) and (-)-(*M*,*P*,*P*)-**31** (B) from Figure 77 constructed as linear fit of absorbance at 350 nm wavelength *versus* concentration c_0.

Estimation of the equilibrium constant

Experimental procedure: A vial partially filled with polyethylene glycol (PEG) as a heat transfer medium was fitted with a glass insert charged with (-)-(*P*,*P*,*P*)-**31** (ca 0.2 mg) and a solution of triphenylmethanol (150 µL, 25 mg/mL in chloroform) as an internal standard. The solution was evaporated by a stream of nitrogen before the vial was closed with a crimp seal. The vial was evacuated and backfilled with nitrogen three times before adding chloroform (150 µL) and the mixture was purged with nitrogen for 5 min. The initial composition of the mixture was analyzed by SFC, followed by heating to 92 °C for 2 h, after which time the cooled mixture was analyzed by SFC again. The minute amount of other stereoisomers in the initial sample of **31** was neglected in further processing. After dividing

the peak areas corresponding to (-)-(*P*,*P*,*P*)-**31** by the triphenylmethanol areas, the ratio c_2/c_1 was obtained from equation (15) (Figure 79 and Table 9).

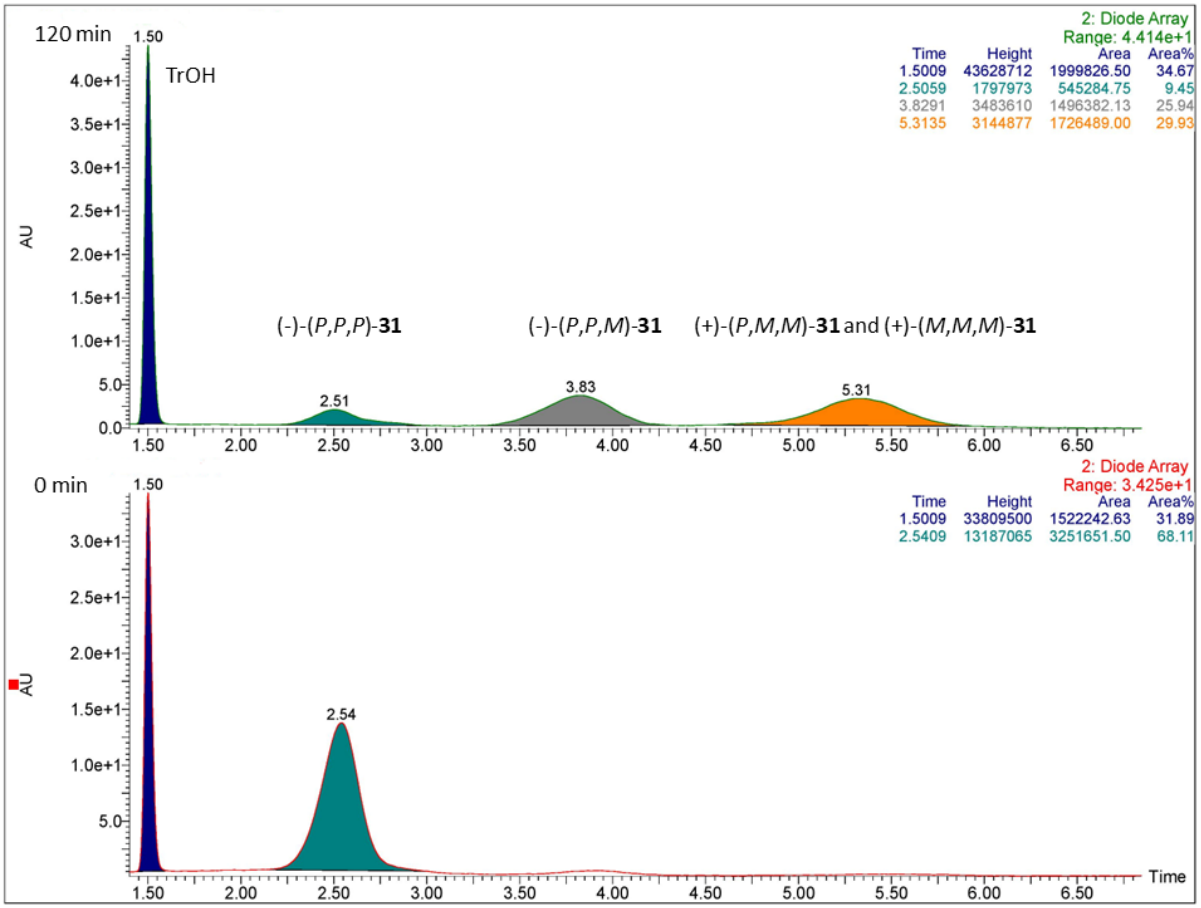

Figure 79. SFC chromatogram of (-)-(*P*,*P*,*P*)-**31** before (0 min) and after (120 min) thermal equilibration at 92 °C.

***T* = 92°C**	**Absolute peak areas**				**Relative to TrOH**			**Equilibrium constant**
***t* (min)**	**TrOH**	**PPP**	**PPM**	**PMM+MMM**	**PPP**	**PPM**	**PMM+MMM**	***K*=[*P**,*P**,*M**]/[(*M**,*M**,*M**)]**
0	1522243	3251652	negligible	negligible	**2.14**	-	-	**2.92**
120	1999827	545285	1496382	1726489	**0.27**	0.75	0.86	-

Table 9. Summary of data from thermal equilibration of (-)-(*P*,*P*,*P*)-**31**.

The final values of extinction coefficients for combined and 350 nm wavelengths are summarized in Tables 10 and 11, respectively. The obtained values were further used for the estimation of the molar concentrations of samples for UV and ECD spectra.

	Absolute peak areas – combined wavelength				**Ratio of extinction coeficients**
***c*₀**	**PPP**	**PPM**	**PMM+MMM**	**PPP+PPM**	**$\varepsilon = \varepsilon_1(P^*,P^*,M^*)/\varepsilon_2(P^*,P^*,P^*)$**
1	1.50	6.10	6.90	7.60	**1.51**
2	3.00	11.2	13.7	14.2	
4	5.40	24.0	28.1	29.4	
6	7.70	34.7	41.6	42.4	
8	10.9	47.9	57.8	58.8	
Slope	1.34	5.92	7.09	7.26	

Table 10. Summary of data from calibration plots and the resulting ratio of extinction coefficients at combined wavelength. The peak areas are divided by 100 000 for convenience.

	Absolute peak areas – 350 nm wavelength				Ratio of extinction coeficients
c_0	*PPP*	*PPM*	*PMM+MMM*	*PPP+PPM*	$\varepsilon = \varepsilon_1(M^*,M^*,P^*)/\varepsilon_2(M^*,M^*,M^*)$
1	1.26	4.53	5.47	5.79	**1.23**
2	2.37	8.81	10.6	11.2	
4	4.73	18.8	22.7	23.5	
6	8.15	29.5	34.2	37.6	
8	12.2	42.4	48.8	54.6	
Slope	1.41	5.07	6.15	6.93	

Table 11. Summary of data from calibration plots and the resulting ratio of extinction coefficients at 350 nm wavelength. The peak areas are divided by 1000 for convenience.

Kinetic measurement

Experimental procedure: A vial partially filled with liquid gallium as a heat transfer medium (heat transfer by PEG turned out to be too slow for the initial 5 min measurement) was fitted with a glass insert charged with (-)-(*P*,*P*,*P*)-**31** (ca 0.5 mg) and a solution of triphenylmethanol (200 µL, 25 mg/mL in chloroform) as an internal standard. The solution was evaporated by a stream of nitrogen before the vial was closed with a crimp seal. The vial was evacuated and backfilled with nitrogen three times before adding chloroform (200 µL). The resulting solution was then purged with nitrogen for 5 min. The initial composition of the mixture was analyzed by SFC at room temperature. The sample was then heated to 76 °C for a specified time after which it was quickly cooled in ice water and analyzed by SFC. The analysis was performed after 5, 15, 35, 75, and 155 minutes of heating. Figure 80 shows chromatograms for each specified heating time. The areas of the chromatogram peaks are summarized in Table 12 and were taken relative to the area of the triphenylmethanol internal standard.

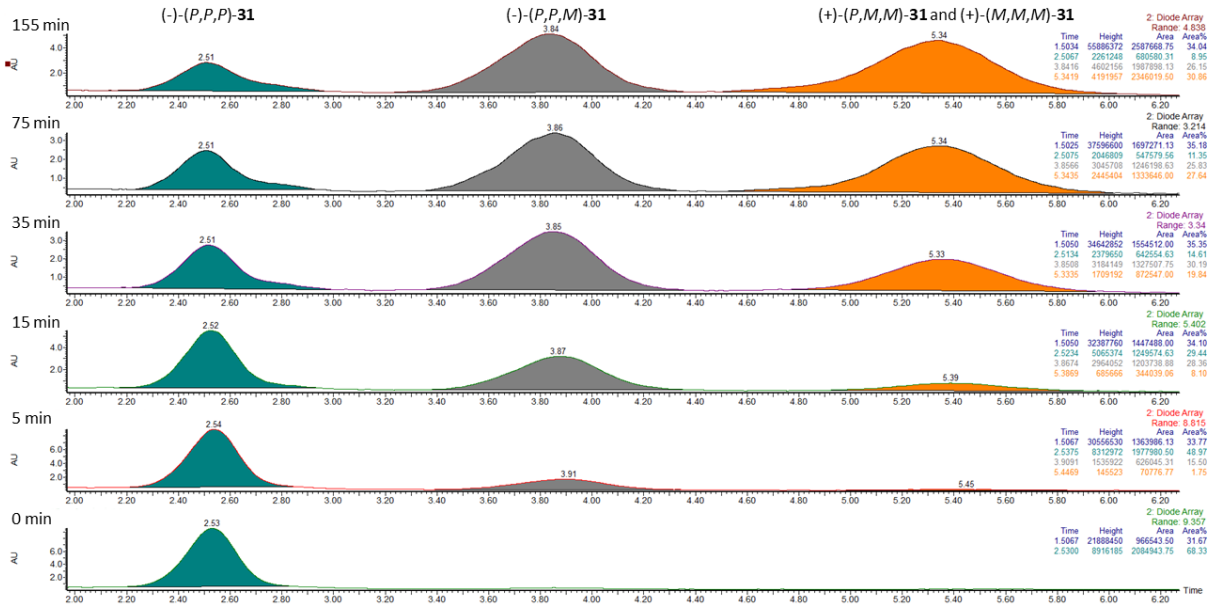

Figure 80. Measurement of isomerization kinetics of **31**. SFC chromatograms show composition of mixture after specified time of heating at 76 °C, starting from (-)-(*P*,*P*,*P*)-**31**.

	Absolute peak areas				Areas relative to TrOH			Relative absorbance (%)		
t (min)	**TrOH**	***PPP***	***PPM***	***PMM+MMM***	***PPP***	***PPM***	***PMM+MMM***	***MMM***	***MMP***	***MPP+PPP***
0	966544	208494	0	0	215.7	0.0	0.0	**100.0**	**0.0**	**0.0**
5	136398	197798	626045	70776	145.0	45.9	5.2	**73.9**	**23.4**	**2.6**
15	144748	124957	120373	344039	86.3	83.2	23.8	**44.7**	**43.0**	**12.3**
35	155451	642555	132750	872547	41.3	85.4	56.1	**22.6**	**46.7**	**30.7**
75	169727	547580	124619	1333646	32.3	73.4	78.6	**17.5**	**39.8**	**42.6**
155	258766	680580	198789	2346020	26.3	76.8	90.7	**13.6**	**39.6**	**46.8**

Table 12. Summary of data from isomerization kinetics of **31**.

5.5. Chiral Resolution and Estimation of Racemization Barrier of **45**

Analytical HPLC

Conditions: Analytical Chiral ART Amylose-SA column (4.6 mm ID × 250 mm, 5 µm particle size) using *n*-heptane – toluene (70:30) mixture as eluent (flow rate of 1 mL·min^{-1}, room temperature).

Preparative HPLC

Conditions: Semipreparative Chiral ART Amylose-SA column (20 mm ID × 250 mm, 5 µm particle size) using gradient *n*-heptane – toluene (80:20 to 60:40) as eluent (flow rate of 20 mL·min^{-1}, room temperature).

Supercritical fluid chromatography (SFC)

Conditions: Analytical Chiral ART Amylose-SA column (3 mm ID × 150 mm, 3 µm particle size) using CO_2 – dichloromethane (65:35) mixture as eluent (flow rate of 1.5 mL·min^{-1}, 35°C column temperature).

Experimental procedure: Enantiomers were separated using semi-preparative HPLC under conditions stated above. (+)-(*P*)-**45** (ca 0.5 mg) was placed in a glass vial and chloroform (0.5 mL) was added. The vial was closed by a crimp septum, and it was heated to 52 °C. The composition of the vial content was determined by SFC after specific time intervals. The values of the racemization rate constants and the corresponding free energy of the racemization barrier were calculated using the standard first order reversible kinetics.

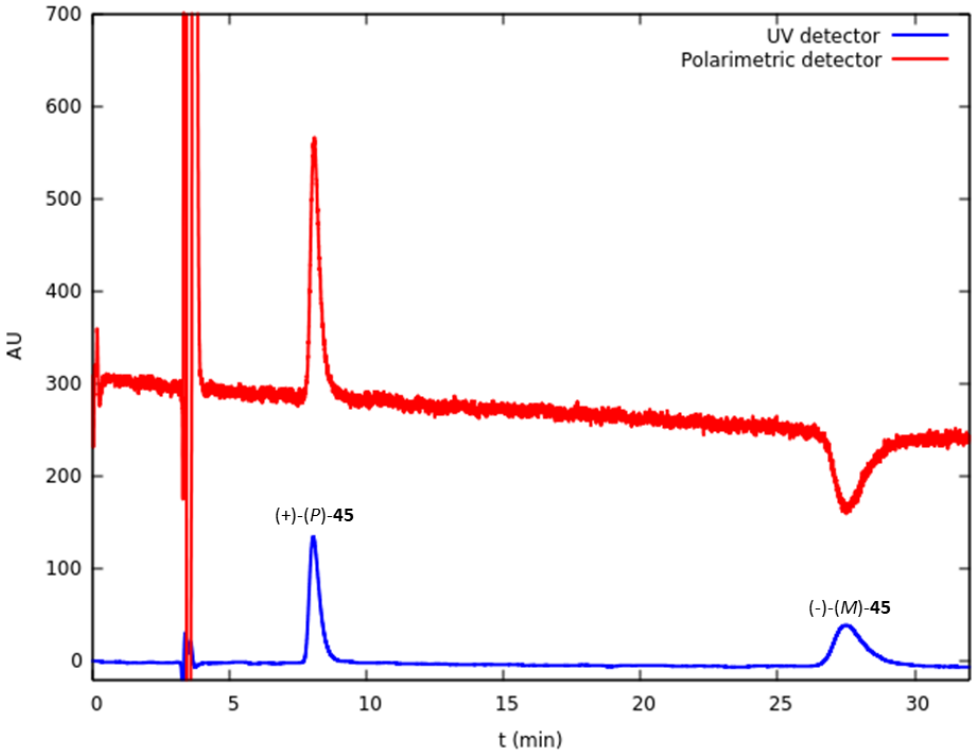

Figure 81. HPLC chromatogram of racemic **45**. Absorption signal is accompanied by signal from Chiralyser polarimetric detector for the assignment of the sense of optical rotation.

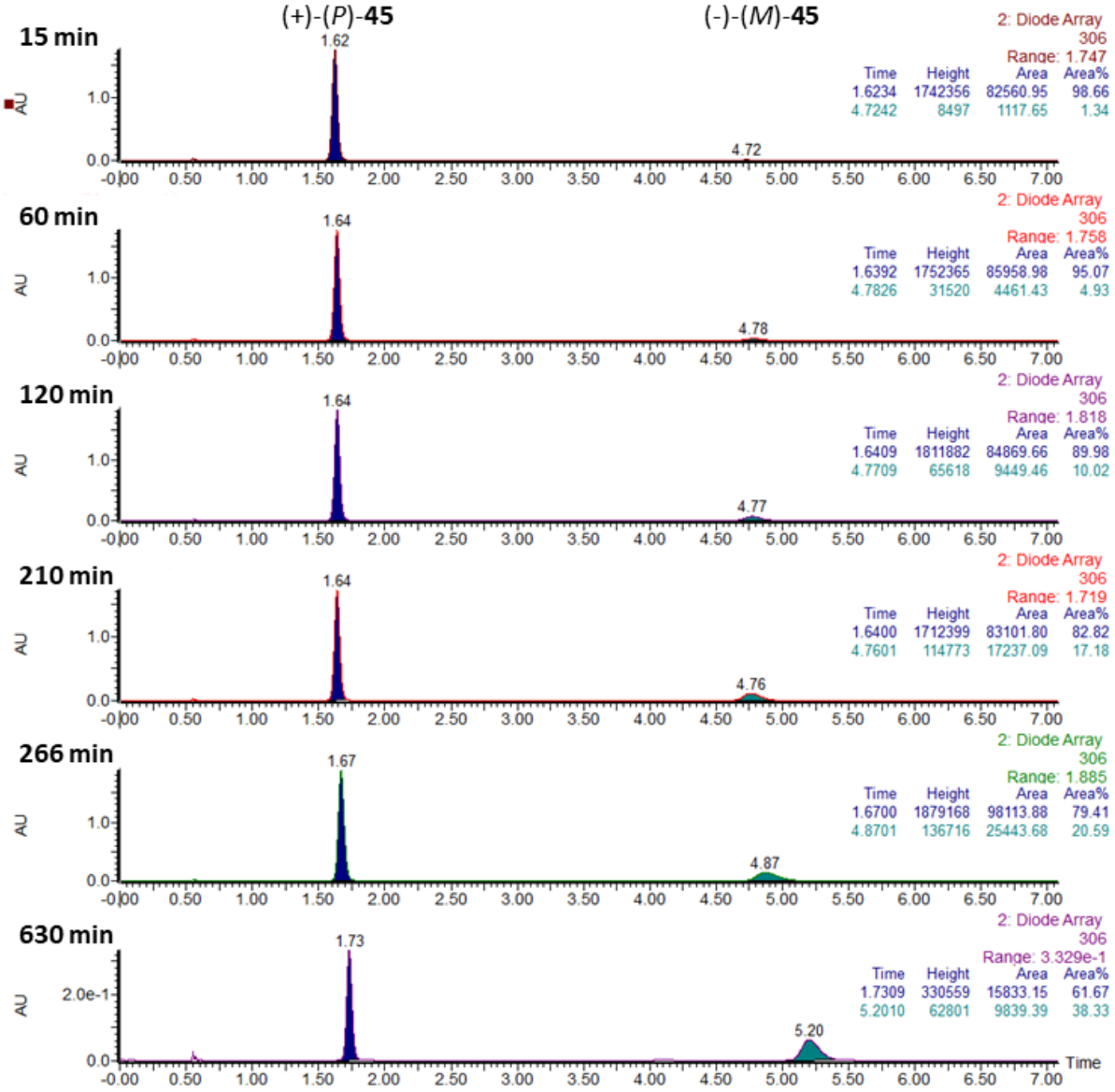

Figure 82. Measurement of racemization kinetics of **45**. SFC chromatograms show the composition of mixture after specified time of heating at 52 °C, starting from pure (+)-(*P*)-**45**.

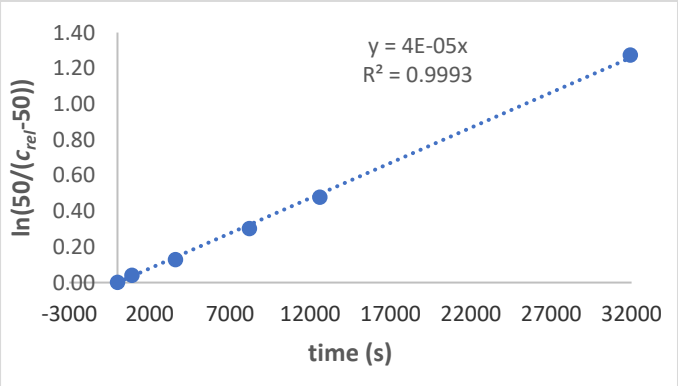

Figure 83. Racemization kinetics of **45** at 52 °C in $CHCl_3$.

t (s)	c_{rel}	ln(50/(c_{rel}-50))
0	100	0.00
900	99	0.02
3600	95	0.11
7200	90	0.22
12600	83	0.42
15960	79	0.54
37800	62	1.43
k **(s^{-1})**		**$3.7 \cdot 10^{-5}$**
ΔG_{exp} (kcal·mol^{-1})		**26.1**
ΔG_{DFT} (kcal·mol^{-1})		**26.3**

Table 13. Summary of data for racemization kinetics of **45** at 52 °C in $CHCl_3$. Inversion barrier calculated by DFT is also shown for comparison.

5.6. Chiral Resolution and Estimation of Racemization Barrier of **43**

Analytical HPLC

Conditions: Analytical Chiral ART Amylose-SA column (4.6 mm ID × 250 mm, 5 µm particle size) using *n*-heptane – toluene – *i*-PrOH (70:30:0.3) mixture as eluent (flow rate of 1 mL·min^{-1}, room temperature).

Preparative HPLC

Conditions: Semipreparative Chiral ART Amylose-SA column (20 mm ID × 250 mm, 5 µm particle size) using *n*-heptane – toluene – tetrahydrofuran – *i*-PrOH (70:30:5:0.3) mixture as eluent (flow rate of 20 mL·min^{-1}, room temperature).

Supercritical fluid chromatography (SFC)

Conditions: Analytical Chiral ART Amylose-SA column (3 mm ID × 150 mm, 3 µm particle size) using CO_2 – dichloromethane gradient (70:30 to 50:50) mixture as eluent (flow rate of 1.5 mL·min^{-1}, 35°C column temperature).

Experimental procedure: Enantiomers were obtained by repeated separations using analytical HPLC under conditions stated above. (+)-(*P*)-**43** (ca 0.5 mg) was placed in a glass vial and chloroform (0.5 mL) was added. The vial was closed by a crimp septum and heated to 52 °C. The composition of the vial content was determined after specific time intervals by SFC. The values of the rate constants of racemization and the corresponding free energy of the racemization barrier were calculated using the standard first order reversible kinetics.

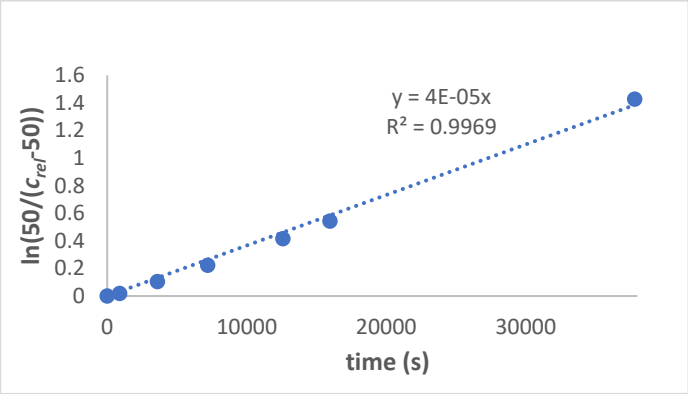

Figure 84. Racemization kinetics of **43** at 52 °C in $CHCl_3$.

t (s)	c_{rel}	ln(50/(c_{rel}-50))
0	100	0.00
900	98	0.04
3600	94	0.13
8220	87	0.30
12600	81	0.48
31920	64	1.27
k (s^{-1})		$3.9 \cdot 10^{-5}$
ΔG_{exp} (kcal·mol^{-1})		26.1
ΔG_{DFT} (kcal·mol^{-1})		26.8

Table 14. Summary of data for racemization kinetics of **43** at 52 °C in $CHCl_3$. Inversion barrier calculated by DFT is also shown for comparison.

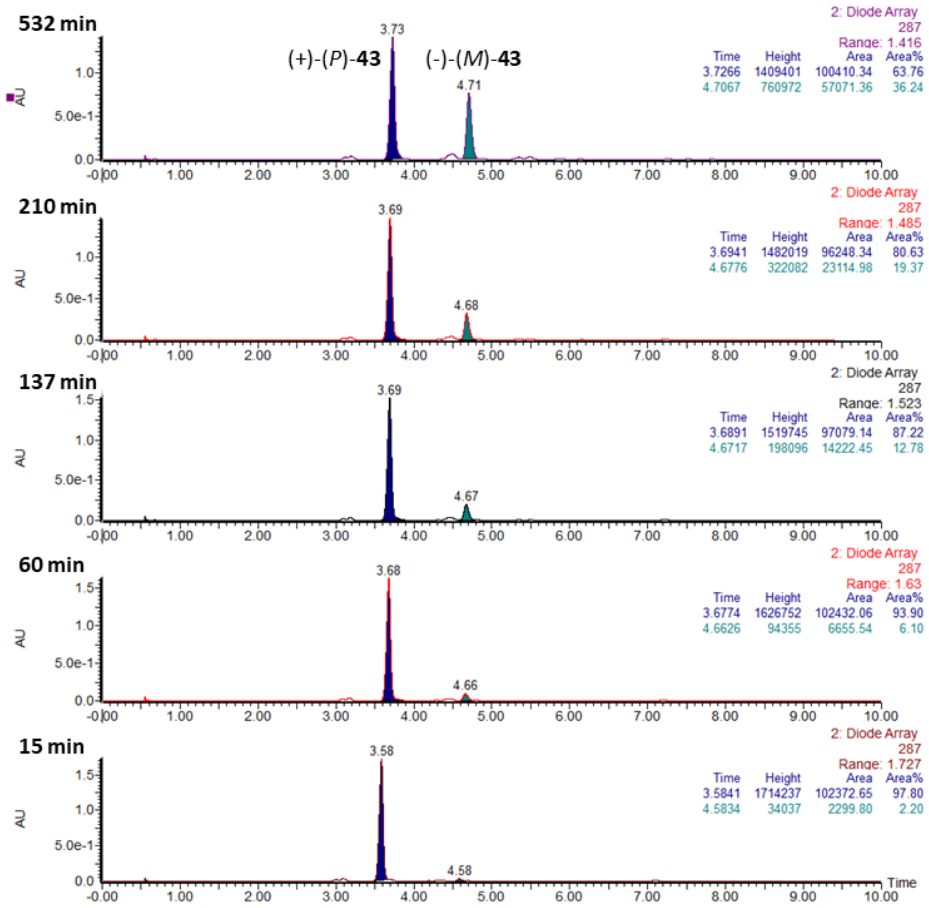

Figure 85. Measurement of racemization kinetics of **43**. SFC chromatograms show composition of mixture after specified time of heating at 52 °C, starting from pure (+)-(*P*)-**43**.

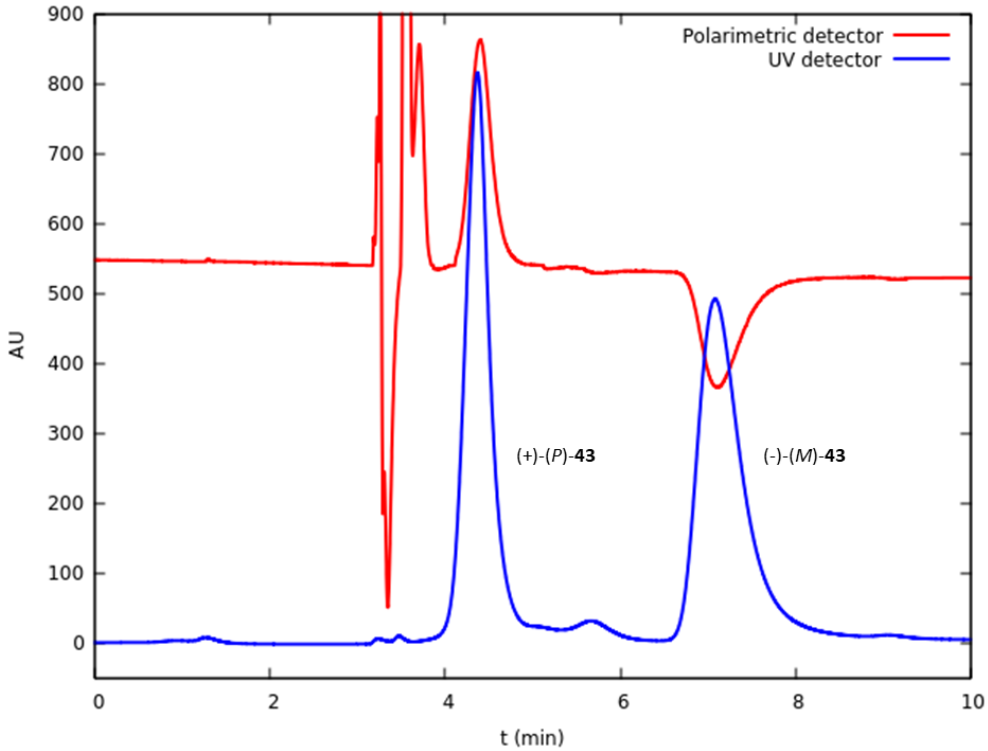

Figure 86. HPLC chromatogram of racemic **43**. Absorption signal is accompanied by signal from Chiralyser polarimetric detector for the assignment of the sense of optical rotation.

5.7. ECD Spectra of Stereoisomers of **45**, **43**, and **31** & Helicity Assignment

ECD spectra of **31** (Figure 45A) and **43** (Figure 45B) were expressed in differential molar extinction Δε. The concentration of **45** was 10^{-5} mol·L^{-1} and of **43** it was 10^{-4} mol·L^{-1}. Because **31** could not be accurately weighed, the concentration of the samples was assessed from its UV absorbance at 350 nm and previously calculated extinction coefficients. It can be noted from Figure 45A that the spectra of (*M**,*M**,*M**)-**31** and (*M**,*M**,*P**)-**31** are rather similar. This suggests a weak coupling between the individual helicene units and, as a result, the ECD spectra are dominated by a superposition of exciton couplets from these isolated units. The mirror-symmetric nature of the ECD spectra of (-)-(*P*,*P*,*P*)-**31** and (+)-(*M*,*M*,*M*)-**31**, or (-)-(*M,P,P*)-**31** and (+)-(*M*,*M*,*P*)-**31** is in line with their enantiomeric relationship.

To assign the chirality of the individual compounds, the measured ECD spectra were compared to their TD-DFT calculated equivalents. The details of the calculations are described in the DFT calculations section. There was a very convincing agreement between the calculated and measured spectra in the case of **45** and **43** (Figure 45). This, along with the kinetic and thermodynamic data, allowed the unequivocal chirality assignment to all stereoisomers of **31**. Macrocycles prepared from pure enantiomers of **43** must, in principle, give preferably the homochiral (+)-(*M,M,M*)-**31** or (-)-(*P*,*P*,*P*)-**31** products. Thus, by comparing SFC chromatograms of macrocycles prepared from either (-)-(*M*)-**43** or (+)-(*P*)-**43** (see Figures 73 and 74), the absolute configuration of the first and (part of) third peaks in the SFC chromatograms of **31** (such as in Figure 75) could be assigned. The assignment of the remaining peaks clearly followed from the isomerization kinetics and the corresponding kinetic model (see Figure 30 and Scheme 5).

5.8. AFM Measurements

A solution of macrocycle **31** or **32** (10 µL, c ≈ 10^{-7} g/mL) in dichloromethane (VWR, for HPLC 99.8%, filtered through a microfilter) was drop casted on a freshly exfoliated piece of 10 x 10 mm^2 highly oriented pyrolytic graphite (HOPG) substrate. Specific samples were then annealed in dichloromethane vapor at 30 °C for 10 min. The samples were scanned in ambient conditions in PeakForce mode using ultrasharp SNL-B (k = 0.12 $N \cdot m^{-1}$), SNL-A (0.35 $N \cdot m^{-1}$) cantilevers (Bruker) with nominal tip radius r = 2 nm, or CF_4 plasma treated Multi75Al (BudgetSensors) probe with nominal tip radius r = 10 nm, on the Dimension Icon AFM (Bruker). Where necessary, the obtained images were processed by 1D FFT filtering to remove clear periodical AFM noise and blurring to reduce the overall noise level, using Gwyddion software.

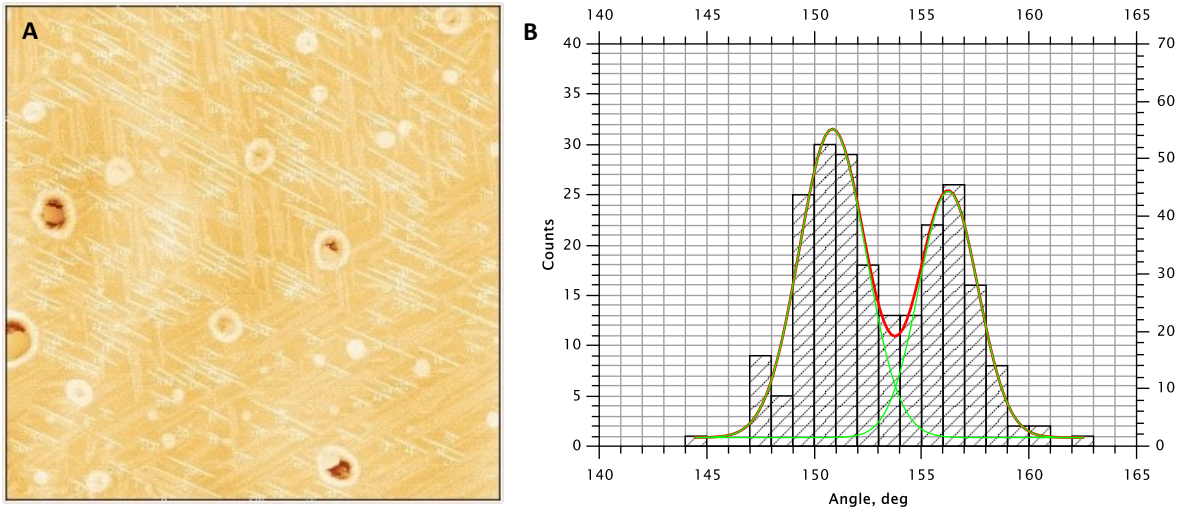

Figure 87. Region showing thin stripes of **31** on HOPG tagged for angle measurement. One of three observed main directions was selected and angle relative to horizontal direction was measured for each line in that main direction (A). Histogram of the measured angles showing non-random azimuthal tilt of the stripes (B).

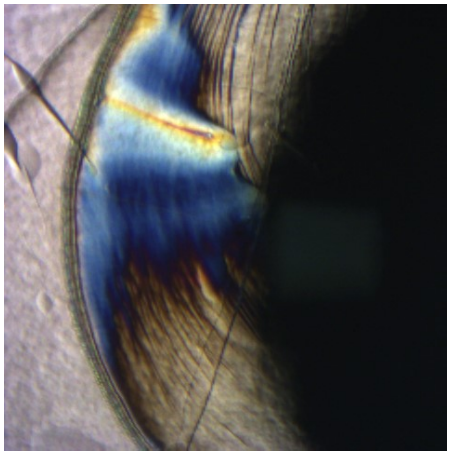

Figure 88. An optical camera image of deposits of **31** on HOPG from AFM experiment. Regions close to the visible deposits were used for AFM imaging. Scanning in the visible regions led to damage of the AFM tip (A).

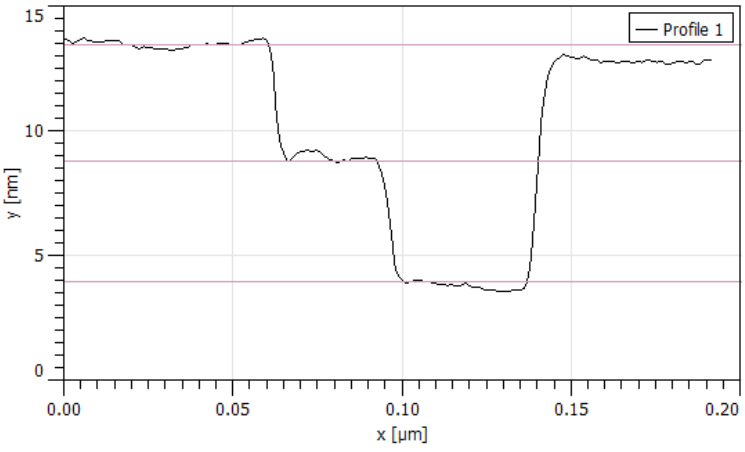

Figure 89. Height profile corresponding to line 1 in Figure 49 (B).

5.9.STM Measurements

Stereoisomeric macrocycles **31** deposited from a solution in *n*-octanoic acid on freshly cleaved HOPG were studied also in Ntegra STM using freshly cut $Pt_{90}Ir_{10}$ wire. STM measurements were performed in *n*-octanoic acid in ambient conditions. 50×50 nm^2 and 100×100 nm^2 images were obtained with 512×512 px^2 resolution at scanning speed 1 Hz with applied current 30 pA and applied voltage -1.2 V.

5.10. Voltammetry measurements

AC voltammetry measurement was performed using a solution of **31** in 1,2-dichloroethane (0.28 mg/mL) on polished platinum electrode with diameter of 0.5 mm. Ag|AgCl|1 M LiCl salt bridge system was used as a reference electrode. The frequency of the AC modulation wave was 16 Hz.

5.11. Single-Molecule DFT Calculations

Geometry optimizations, energies, and optical spectra

DFT calculations were performed using Gaussian16 software.[162] First, to account for a large rotational flexibility of the trityl groups and stilbene units in **43** and **31**, a conformational analysis was performed. The relevant conformers were obtained either from a 10 ns MD run at 400 K in vacuum using QuantumATK 2020 software,[163,164] where the most abundant conformers were chosen (4 conformers of **31** for each stereoisomer, see Chapter 5.13. for details on MD calculations), or from Open Babel[118] conformer search (8 conformers of **43** lowest in free energy). The energy barriers of the helicity inversion were evaluated as the Gibbs free energy difference between the most stable conformer and the transition state at the respective experimental temperature. The conformation analysis of the transition states was not performed but the starting conformation of the trityl groups was chosen to correspond to the most stable energy minima.

The selected conformers were then preoptimized at AM1 level,[165] followed by a sequential optimization at B3LYP[166,167]/6-31G[168,169]/GD3[170] and B3LYP/cc-pVDZ[171,172]/GD3 levels, respectively, before the final B3LYP/cc-pVDZ/GD3/PCM[173,174] optimization in chloroform. To reach geometry convergence, the Hessian matrix often had to be updated several times by calculating force constants. To successfully optimize the large structures of **31**, superfine integration grid and the smallest possible optimization step had to be used in the final stage. The frequencies and subsequent thermochemistry were calculated using RRHO approximation. The transition states were localized by the Berny algorithm.[175] The starting geometries for the transition states (*P*,*P*,*Saddle*)-**31**, *exo*-(*M*,*P*,*Saddle*)-**31**, *endo*-(*M*,*P*,*Saddle*)-**31** were obtained by replacing one helicene unit in the trimer **31** with a saddle transition state based on enantiomerization transition state of [5]helicene, calculated in a separate job. The transition state was subsequently optimized at AM1 level using analytical calculation of force constants in every step, before employing the optimization sequence described above. The nature of the optimized structures was checked by the number of imaginary frequencies. All minima had no imaginary frequencies, while the transition states had a single imaginary frequency. The Gibbs free energies during the isomerization (Table 2, Figure 31) were calculated at the experimental temperature of 349 K.

The Gibbs free energies for the Boltzmann averaging of ECD spectra were calculated at 298 K. The final ECD spectra were obtained by Boltzmann averaging of the individual ECD spectra of the most populated conformers. After geometry optimization of each conformer, a single point TD-DFT[176–182] calculation at CAM-B3LYP[183]/cc-pVDZ/GD3/PCM level was performed. The weighted ECD spectra of individual conformers were summed, and the final spectrum was shifted to match the highest wavelength exciton couplet. VMD software[184] was used to visualize the molecular geometry.

XYZ coordinates of all calculated structures and TD-DFT data can be found in Appendix 6.

Stereoisomers of trimer 31

Conformer	*ΔG* (kcal·mol^{-1})	Boltzmann proportions (%)
(-)-(*P*,*P*,*P*)-31-1	0	55.0
(-)-(*P*,*P*,*P*)-31-2	0.62	19.3
(-)-(*P*,*P*,*P*)-31-3	0.86	12.8
(-)-(*P*,*P*,*P*)-31-4	0.86	12.8
(-)-(*M*,*P*,*P*)-31-1	0	93.7
(-)-(*M*,*P*,*P*)-31-2	1.9	3.5
(-)-(*M*,*P*,*P*)-31-3	2.5	1.4
(-)-(*M*,*P*,*P*)-31-4	2.5	1.4

Table 15. Relative Gibbs free energies of individual conformers of **31** and the corresponding Boltzmann proportions calculated at 298 K.

Helicene derivative 43

Conformer	*ΔG* (kcal·mol^{-1})	Boltzmann proportions (%)
(-)-(*M*)-*43*-1	0	21.4
(-)-(*M*)-*43*-2	0.024	20.5
(-)-(*M*)-*43*-3	0.096	17.9
(-)-(*M*)-*43*-4	0.382	11.3
(-)-(*M*)-*43*-5	0.406	10.8
(-)-(*M*)-*43*-6	0.574	8.2
(-)-(*M*)-*43*-7	0.669	7.0
(-)-(*M*)-*43*-8	1.171	2.9

Table 16. Relative Gibbs free energies of individual conformers of **31** and the corresponding Boltzmann proportions calculated at 298 K.

NICS calculations

The calculations were performed on neutral and charged non-tritylated timers **31noTr**, namely, [(*P*,*P*,*P*)-**31noTr**]^{0}, [(*P*,*P*,*P*)-**31noTr**]$^{2+}$, [(*P*,*P*,*P*)-**31noTr**]$^{4+}$, and [(*M*,*P*,*P*)-**31noTr**]^{0}, [(*M*,*P*,*P*)-**31noTr**]$^{2+}$, [(*M*,*P*,*P*)-**31noTr**]$^{4+}$ in a singlet state. The geometry optimizations were performed by the standard procedure described above using either B3LYP functional or LC-ωhPBE functional (default ω = 0.11, without using Grimme dispersion which is not supported).[153] The NICS(0)$_{zz}$[49] was calculated using the GIAO method[185–189] in a grid of 251 × 251 points spaced by 0.2 Å placed in the macrocycle plane (Figure 90). The *ZZ* component of the chemical shielding tensor was used in the subsequent processing.[190,191] The color scale was kept identical for all species except for the boundary values which were chosen individually for each species.

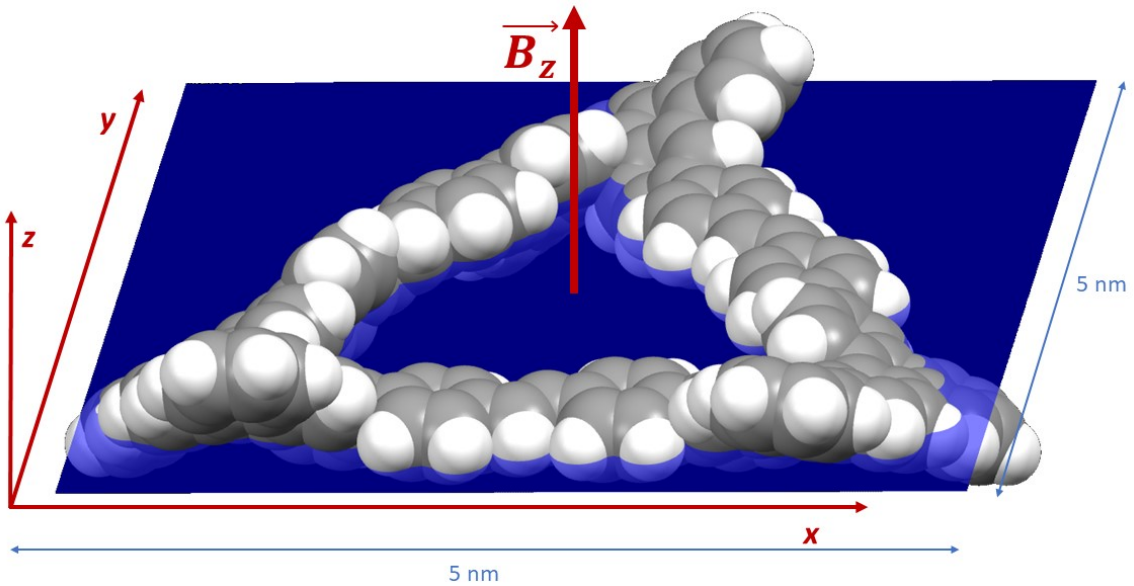

Figure 90. (-)-(*M*,*P*,*P*)-**31** dissected by the XY plane where an array of dummy atoms is placed for the NICS(0)$_{zz}$ calculations. The red arrow shows the direction of the applied magnetic field for the ACID calculation.

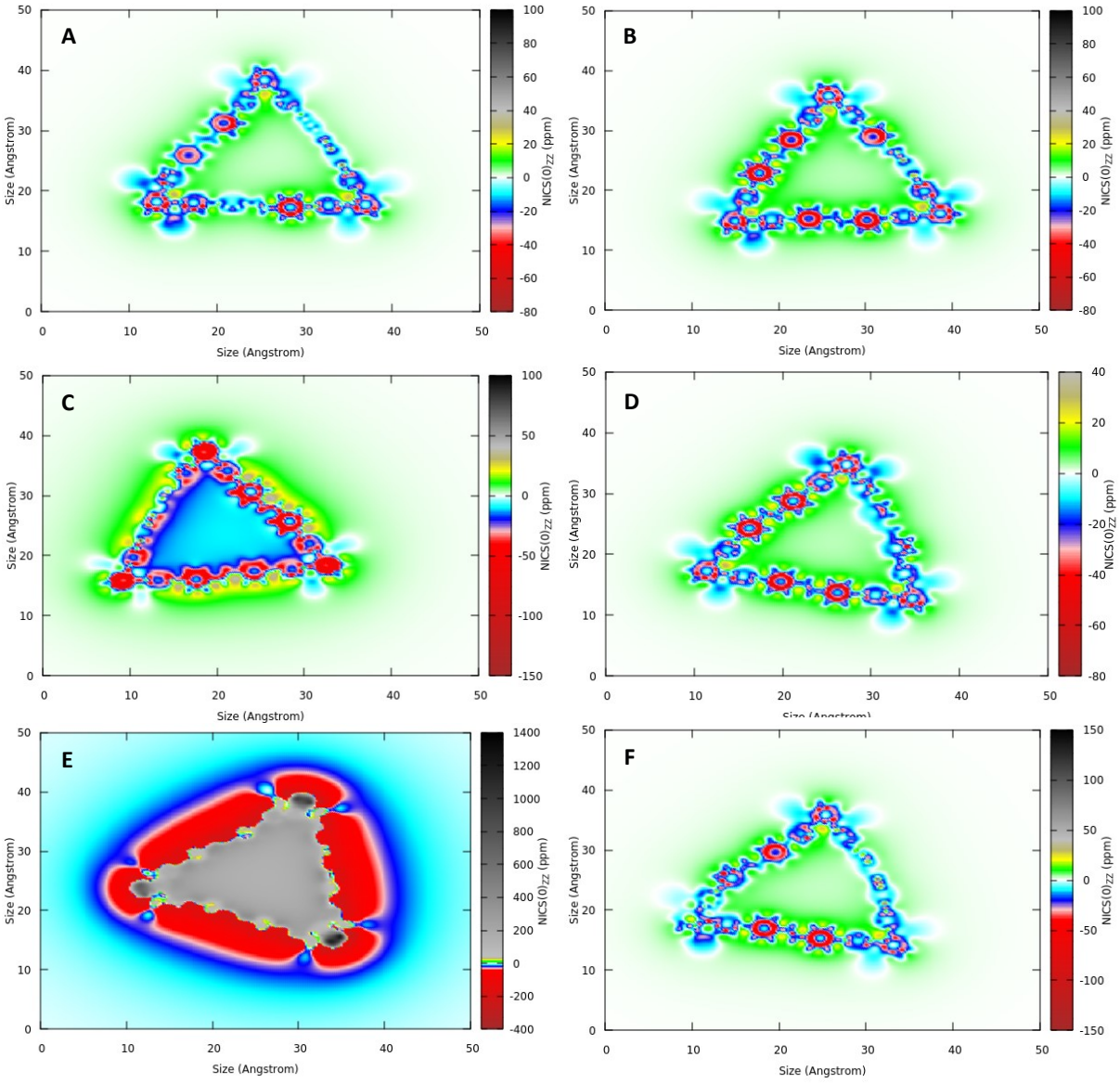

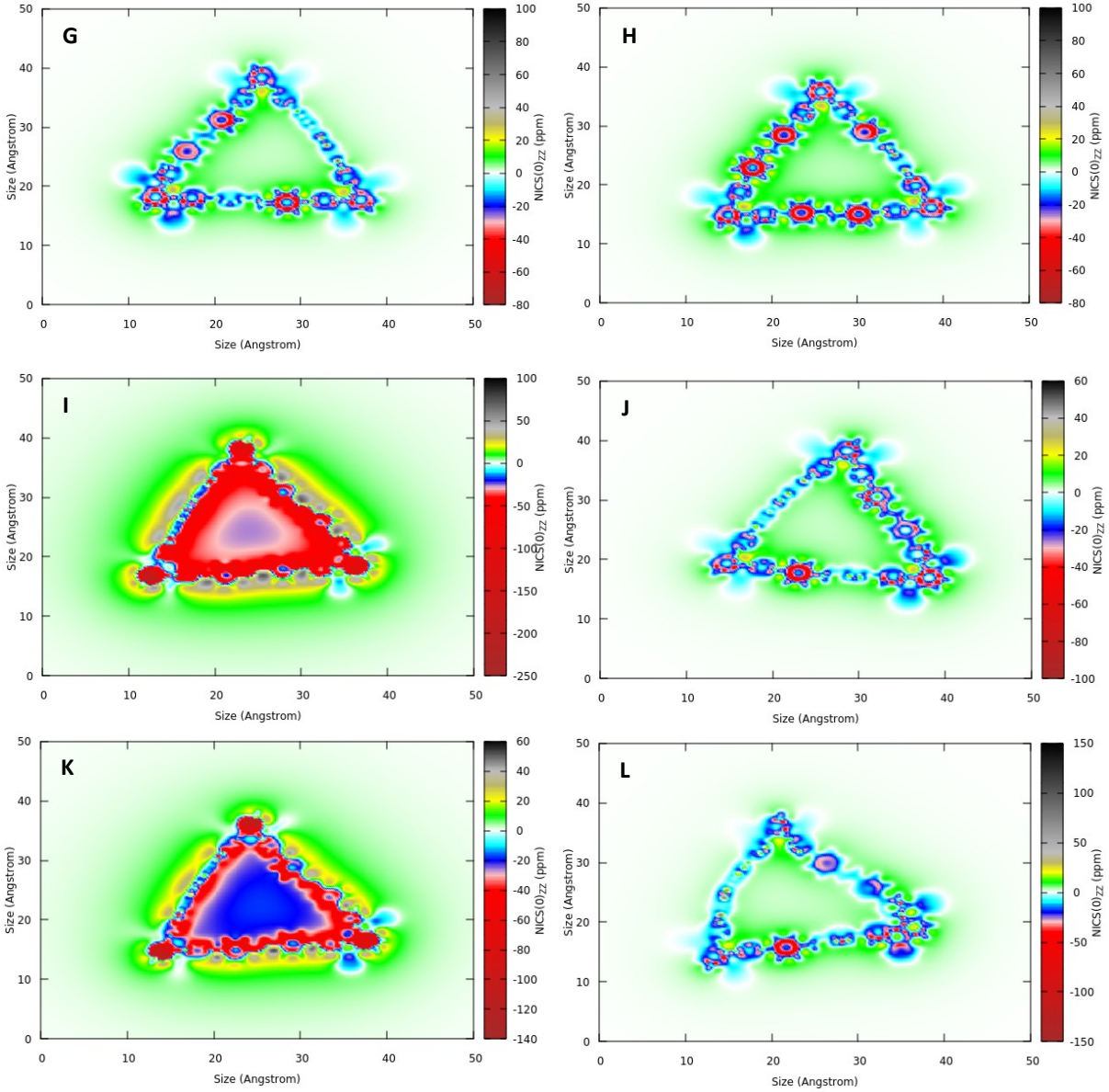

Figure 91. NICS(0)zz plots of different stereoisomers of **31noTr**. Calculations using B3LYP/cc-pVDZ/GD3/PCM($CHCl_3$)// B3LYP/cc-pVDZ/PCM($CHCl_3$): [(*M*,*P*,*P*)-**31noTr**]^0 (A), [(*M*,*P*,*P*)-**31noTr**]$^{2+}$ (C), [(*M*,*P*,*P*)-**31noTr**]$^{4+}$ (E), [(*P*,*P*,*P*)-**31noTr**]^0 (G), [(*P*,*P*,*P*)-**31noTr**]$^{2+}$ (I), [(*P*,*P*,*P*)-**31noTr**]$^{4+}$ (K). Calculations using LC-ωhPBE/cc-pVDZ/PCM($CHCl_3$)//LC-ωhPBE/cc-pVDZ/PCM($CHCl_3$): [(*M*,*P*,*P*)-**31noTr**]^0 (B), [(*M*,*P*,*P*)-**31noTr**]$^{2+}$ (D), [(*M*,*P*,*P*)-**31noTr**]$^{4+}$ (F), [(*P*,*P*,*P*)-**31noTr**]^0 (H), [(*P*,*P*,*P*)-**31noTr**]$^{2+}$ (J), [(*P*,*P*,*P*)-**31noTr**]$^{4+}$ (L).

ACID calculations

The structures used for the NICS calculations were used also for the ACID calculations. The magnetic anisotropy was calculated using CSGT method,[189,192,193] and tight SCF convergence criteria according to a method developed by Geuenich and Herges.[47,48] The orientation of the magnetic field in the induced current density calculation was perpendicular to the plane used in the $NICS(0)_{zz}$ calculations (Figure 90). The anisotropy of the current density was calculated using $5 \cdot 10^6$ gridpoints, symmetric part of the anisotropy was used for the image rendering. The software provided by the authors contains an error and the generated images show the opposite enantiomer. This mistake had not been discovered before as most systems

previously studied by this method were achiral. To compensate for the error, the rendered images were flipped horizontally. The size of the current density vectors was increased, compared to the original software, to improve their visibility on the large molecule of **31noTr**.

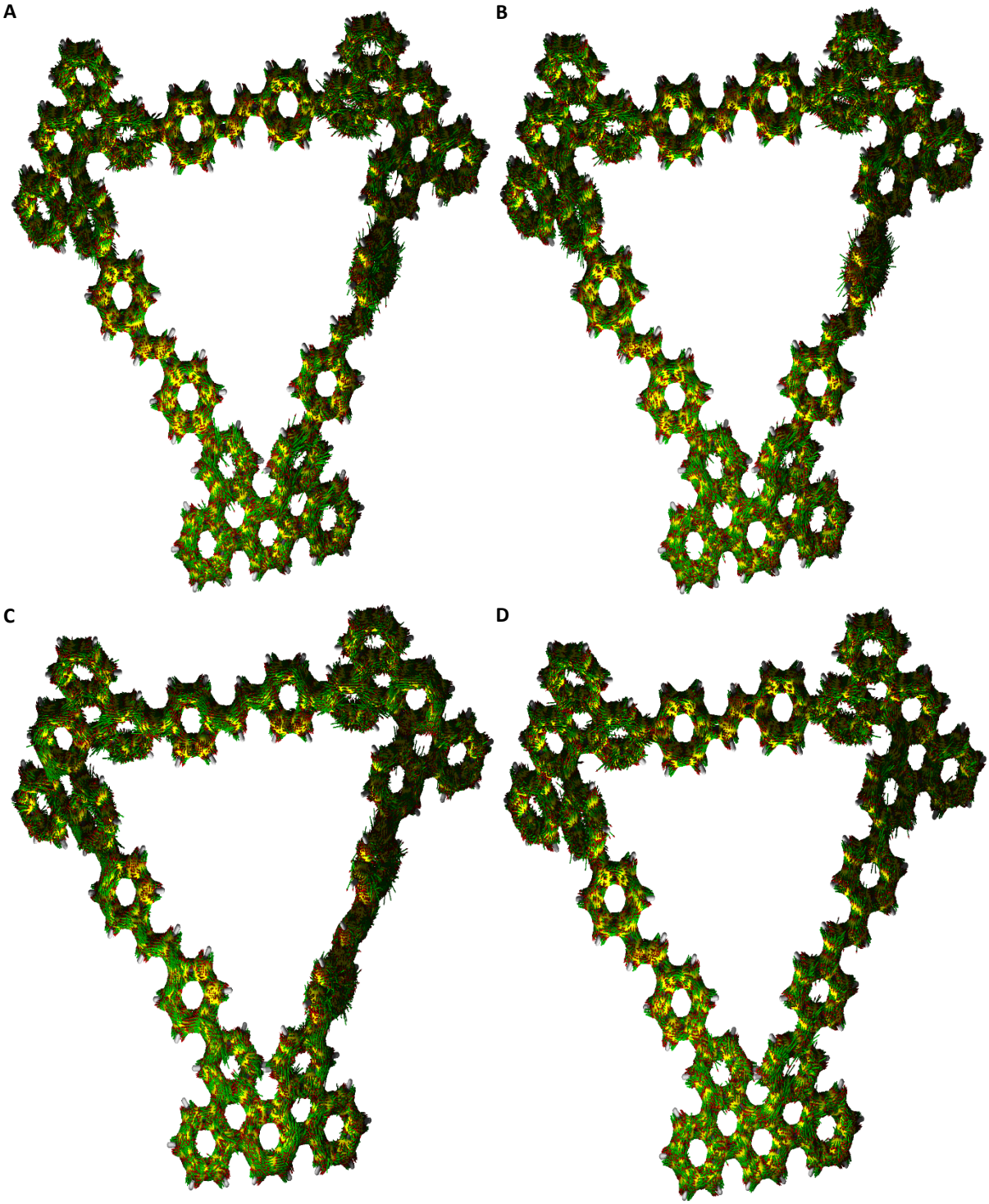

E

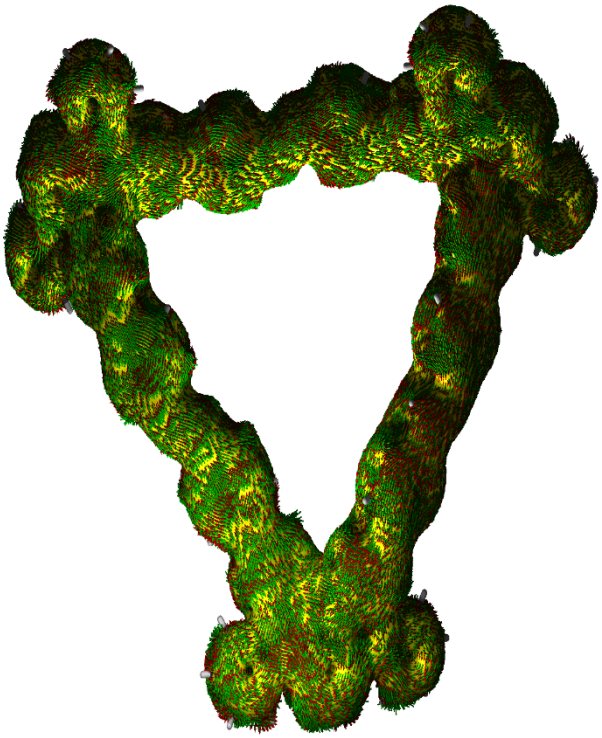

F

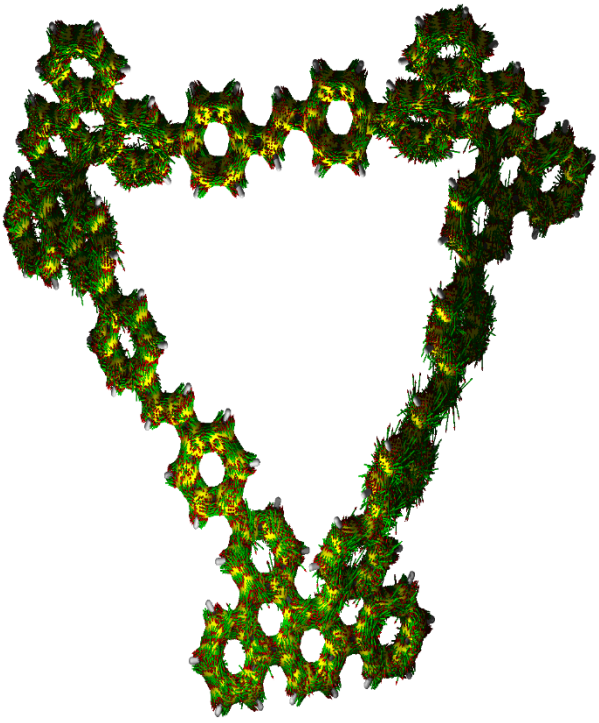

G

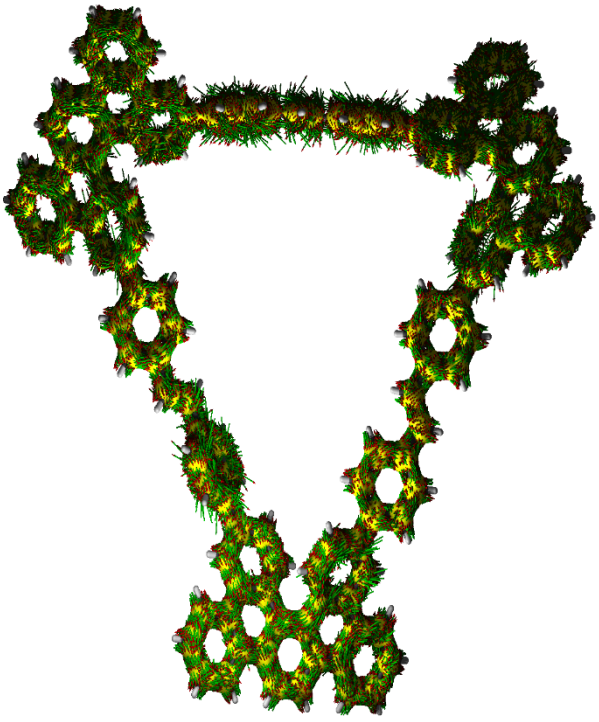

H

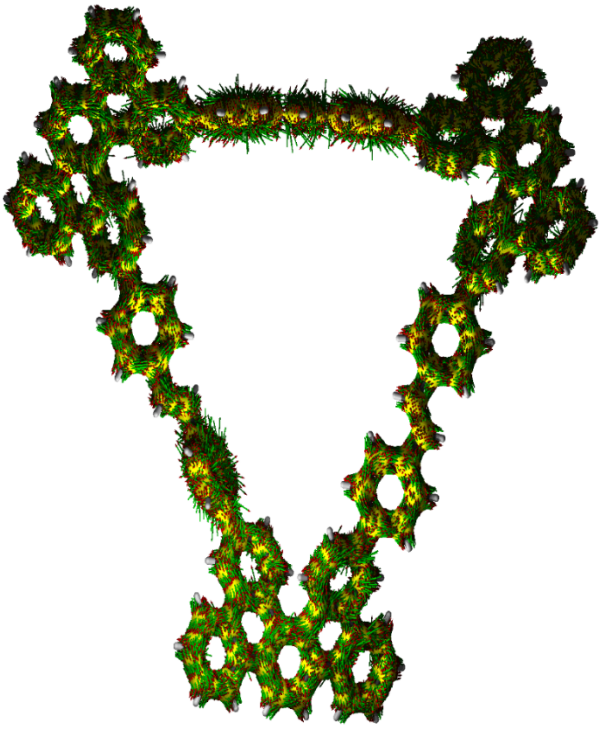

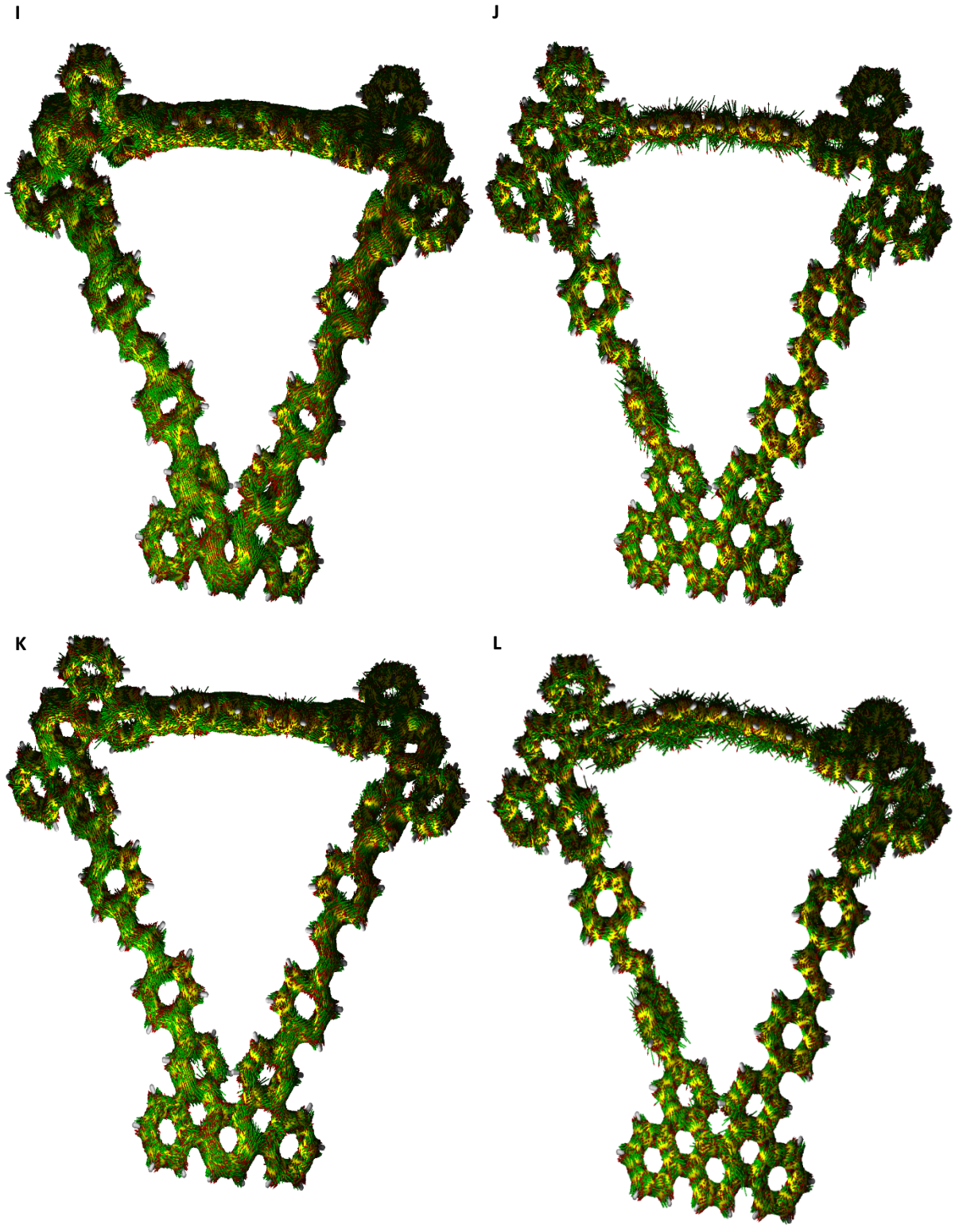

Figure 92. ACID plots of different stereoisomers of **31noTr**. Calculations using B3LYP/cc-pVDZ/GD3/PCM($CHCl_3$)//B3LYP/cc-pVDZ/PCM($CHCl_3$): [(*M*,*P*,*P*)-**31noTr**]^{0} (A), [(*M*,*P*,*P*)-**31noTr**]$^{2+}$ (C), [(*M*,*P*,*P*)-**31noTr**]$^{4+}$ (E), [(*P*,*P*,*P*)-**31noTr**]^{0} (G), [(*P*,*P*,*P*)-**31noTr**]$^{2+}$ (I), [(*P*,*P*,*P*)-**31noTr**]$^{4+}$ (K). Calculations using LC-ωhPBE/cc-pVDZ/PCM($CHCl_3$)//LC-ωhPBE/cc-pVDZ/PCM($CHCl_3$): [(*M*,*P*,*P*)-**31noTr**]^{0} (B), [(*M*,*P*,*P*)-**31noTr**]$^{2+}$ (D), [(*M*,*P*,*P*)-**31noTr**]$^{4+}$ (F), [(*P*,*P*,*P*)-**31noTr**]^{0} (H), [(*P*,*P*,*P*)-**31noTr**]$^{2+}$ (J), [(*P*,*P*,*P*)-**31noTr**]$^{4+}$ (L).

5.12. Periodic DFT Calculations

Charge transfer calculations

The charge transfer between molecule **31** and graphite was calculated in QuantumATK 2020 software using LCAO method and periodic boundary conditions, Perdew-Burke-Ernzerhof generalized gradient approximation,[194] and Grimme D3 Van der Waals correction with a 30 Å cutoff distance, without spin polarization. Numerical basis sets with PseudoDojo pseudopotential[195–200] as implemented in the software, at "medium" level for geometry optimizations, and at "ultra" level for the subsequent single point calculations, were used. Considering the large size of the simulation cell, a single k-point located in the Gamma point was used. Geometry optimizations were performed using L-BFGS method[201] (maximum force = 0.05 eV/Å, maximum stress = 0.1 GPa, maximum step length = 0.2 Å). One graphite atom was constrained to avoid migration of the graphite slab within the simulation cell. Other settings were kept default, unless stated otherwise.

A single molecule of (-)-(*M*,*P*,*P*)-**31** was placed on a slab of a double layer graphite (surface orientation: (001), size of the rectangular simulation cell in multiples of the graphite hexagonal unit cell: v_1 = [20, 0], v_2 = [12, 24], Figure 93). The input geometry of the system was taken from a simulated annealing protocol described in the previous chapter. A single point calculation at the "ultra" basis set level was performed for the charge transfer calculation.

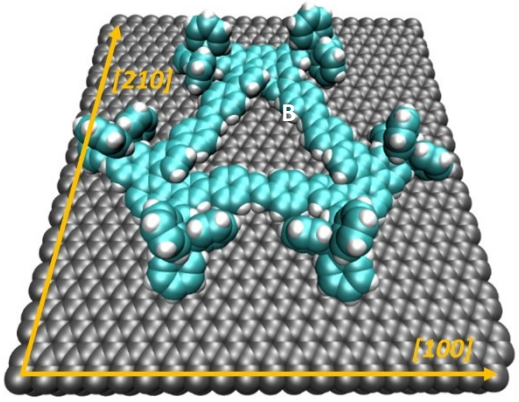

Figure 93. Simulation cell used for the calculation of the charge transfer between (-)-(*M*,*P*,*P*)-**31** and graphite.

The charge transfer was evaluated by summing the Mulliken charges on (-)-(*M*,*P*,*P*)-**31** and on graphite (see Appendix 3). Additionally, to calculate the electron density difference between the system and its individual components, single point calculations of the system with either only graphite or (-)-(*M*,*P*,*P*)-**31** were performed. The electron densities were then subtracted according to formula $\Delta\rho = \rho($(-)-(*M*,*P*,*P*)-**31**/Graphite$) - \rho($(-)-(*M*,*P*,*P*)-**31**$) - \rho($graphite$)$ to obtain the electron density difference after the adsorption of **31** (Figures 92 and 93, see also Appendix 2). The results were visualized using VMD software. XYZ coordinates of the calculated structures can be found in Appendix 6.

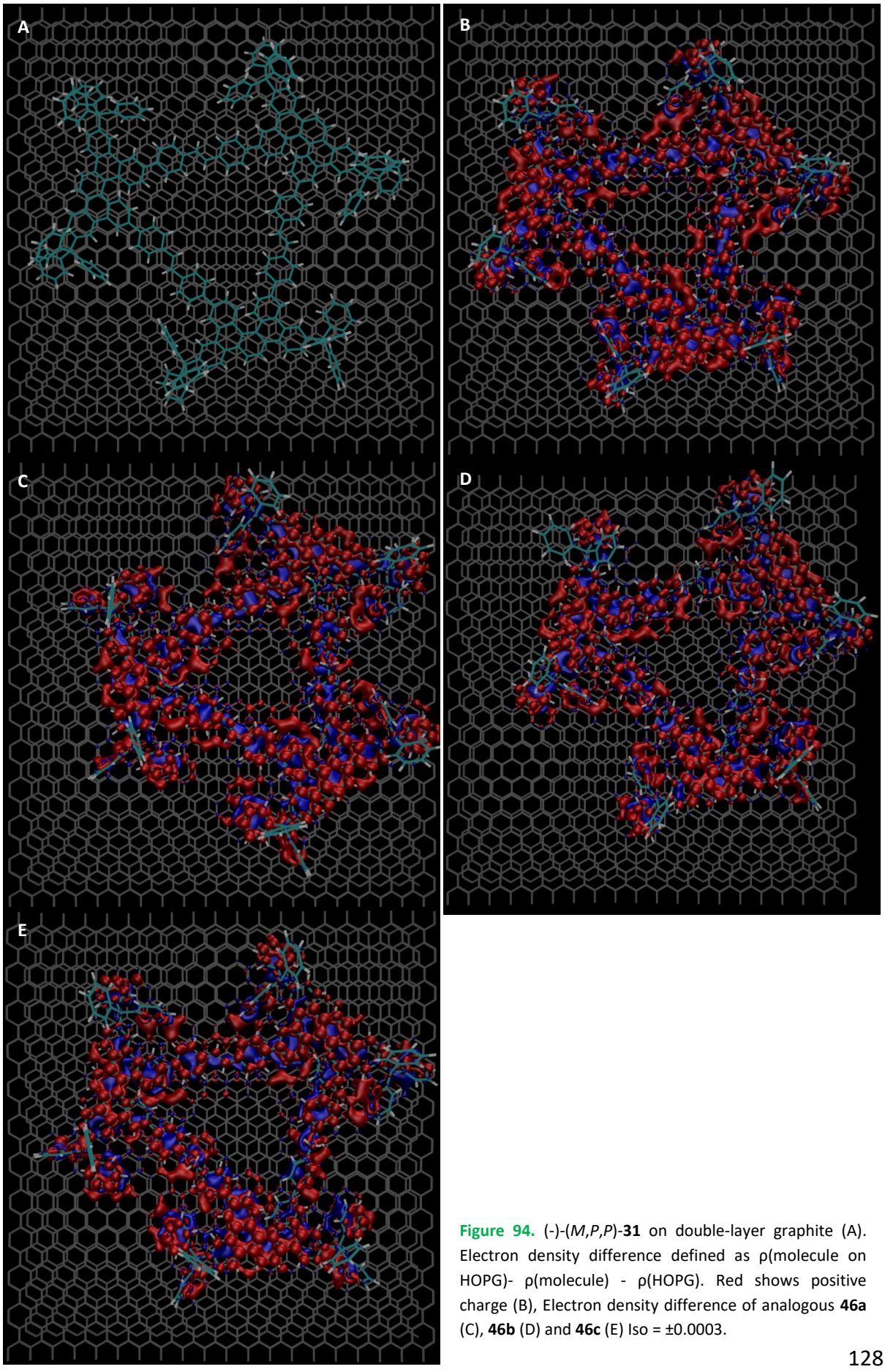

Figure 94. (-)-(*M*,*P*,*P*)-**31** on double-layer graphite (A). Electron density difference defined as ρ(molecule on HOPG)- ρ(molecule) - ρ(HOPG). Red shows positive charge (B), Electron density difference of analogous **46a** (C), **46b** (D) and **46c** (E) Iso = ±0.0003.

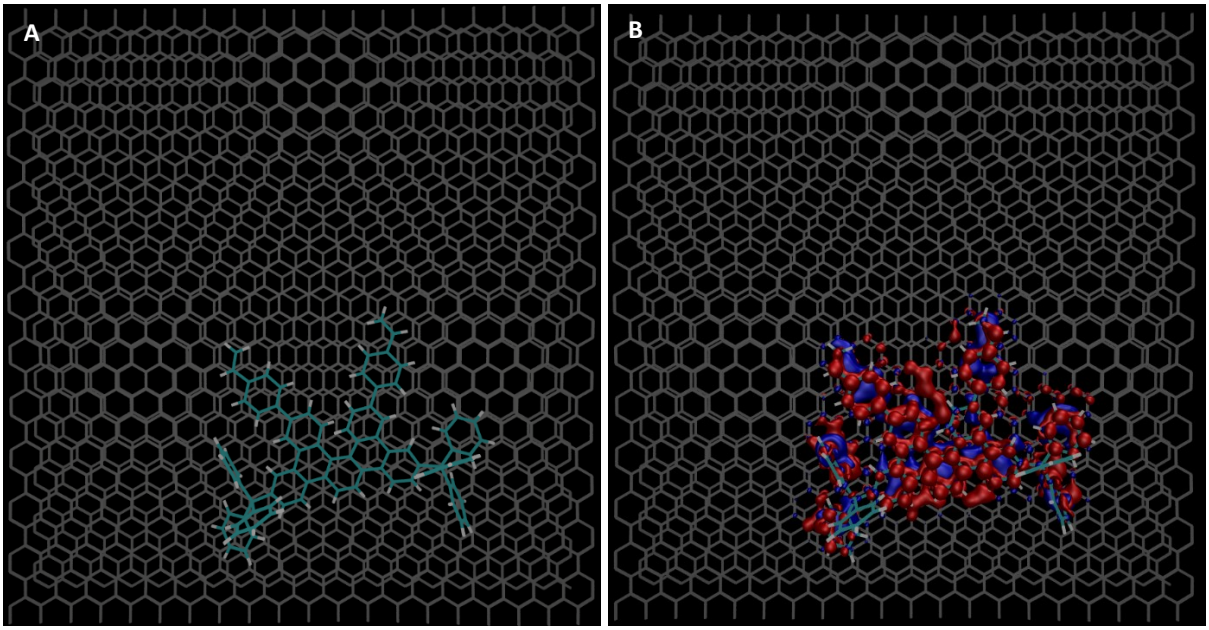

Figure 95. (*P*)-fragment of (-)-(*M*,*P*,*P*)-**31** on graphite surface. The disconnections of the fragment from the macrocycle were terminated by hydrogen atoms. Geometry (A), electron density difference (B). Iso = ±0.0003.

5.13. Molecular Dynamics Simulations

General

MD simulations were performed in QuantumATK 2020 software using ReaxFF force field[137] and Tremolo-X calculator.[202] Geometry optimizations were performed using L-BFGS method[201] (maximum force = 0.03 eV/Å, maximum stress = 0.1 GPa, maximum step length = 0.1 Å). Both optimizations and MD simulations were performed with a fixed center of mass of the system. All MD simulations were run as NVT ensemble with 1 fs time step. Nosé – Hoover thermostat was used to control the temperature. The initial velocities were taken from the Maxwell-Boltzmann distribution. Other settings were kept default, unless stated otherwise.

5.13.1. MD Simulation of Self-Assembly of **31** on Graphite Surface

Simulation protocol

Because the studied macrocycle **31** is an equilibrium mixture of 4 different stereoisomers (-)-(*P*,*P*,*P*)-**31**, (+)-(*M*,*M*,*M*)-**31**, (-)-(*M*,*P*,*P*)-**31**, and (+)-(*M*,*M*,*P*)-**31** (for simplicity in further text denoted as *PPP*, *MMM*, *MPP*, *MMP*, respectively), 6 different model systems were investigated to cover all relevant stereoisomer combinations, namely *MMM-PPP*, *MMP-MPP*, *MMM-MMP*, *MMM-MPP*, *MMM-MMM*. The first four systems naturally involve also contacts between the same kind of stereoisomers, but a system composed of only *MMM* molecules was also simulated to investigate how a purely monoisomeric system behaves on the global scale. Additionally, a system based on non-solubilized (*M,M,M)*-**31noTr** macrocycles *MMM*-noTr was simulated to elucidate the role of the peripheral trityl groups in the self-assembly process.

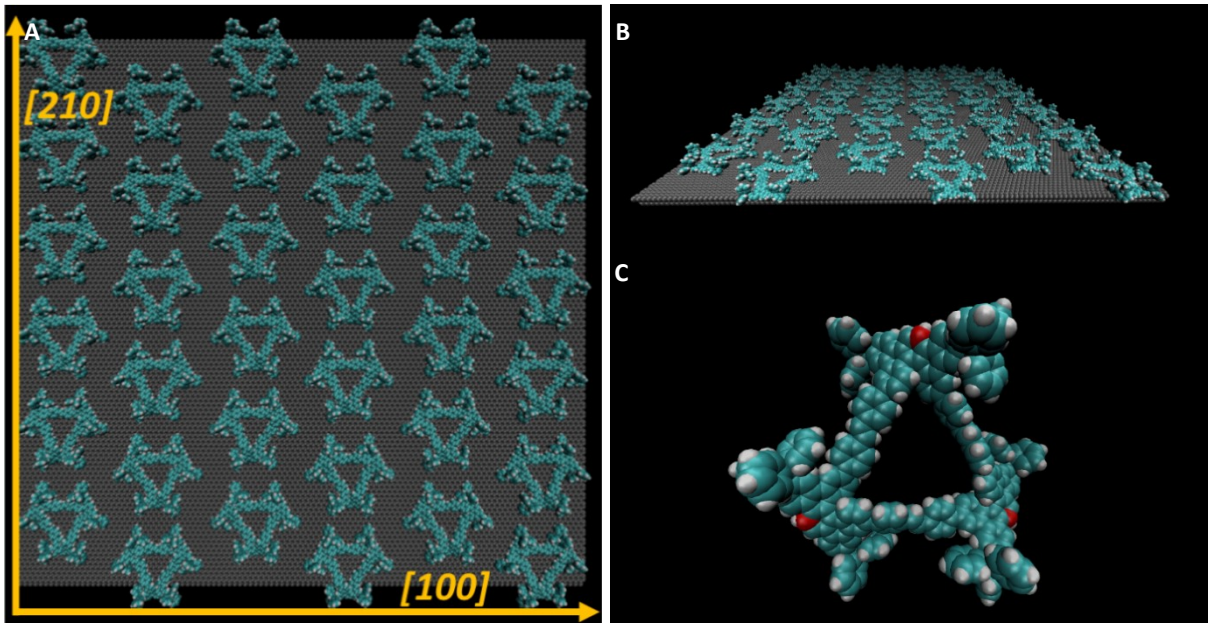

Figure 96. Initial geometry of the *MMM-PPP* system. Top view showing the layout of the molecules on the graphite surface (A) and a side view also showing both layers of the graphite slab (B). Orientation points shown in red on a single *PPP* molecule (C).

Each system was built from 18 molecules of one stereoisomer and 18 molecules of the other (or just 36 same molecules in the case of *MMM-MMM* and *MMM*noTr systems). A single molecule of each configuration was first preoptimized on a small graphite slab of appropriate size using a simulating annealing protocol. Such molecules were then placed on a surface of a double layer graphite slab within a periodic rectangular simulation cell (surface orientation: (001), size of the rectangular simulation cell in multiples of the graphite hexagonal unit cell: v_1 = [108, 0], v_2 = [60, 120], Figure 96A and B). The molecules were designated by unique tags, serving for the subsequent calculations of the intermolecular distances. Additionally, three specific atoms – orientation points – in each of the molecule's vertices were tagged to determine the molecular contact types (Figure 96C). Subsequently, simulated annealing protocol was applied consisting of a series of low temperature (1 – 100 K) MD runs and geometry optimizations to find an approximation to the global energy minimum. Once the system was sufficiently stable, it was left to evolve at 303 K (experimental temperature of the sample annealing, unless stated otherwise) for a specified time. In the case the system became unstable, the simulated annealing was repeated, and the MD was continued from that geometry. The MD trajectory obtained after the simulation was converted to *XYZ* format which served as the input for the statistical analysis of intermolecular contacts. The simulation cell was also converted to a 2 × 2 supercell for better visualization of the periodic contacts on the cell borders and the periodic images of atoms outside the simulation cell were imaged back to the original cell. The final visualization of the snapshots and MD trajectories was done in VMD software.[184]

Simulation parameters

The simulated annealing protocol consisted from a sequence of geometry optimizations and MD runs as schematically described by the following scheme: OPT1, 5 × (MD1, MD2, OPT2), 3 × (MD3, MD4, OPT1), where OPT1: N_{steps} = 200; OPT2: N_{steps} = 100; MD1: $T_{initial}$ = 3 K, $T_{reservoir}$ = 1 K, thermostat timescale = 25 fs, heating rate = 0.05 K/ps, chain length = 3, N_{steps} = 2000; MD2: $T_{initial}$ = 10K, $T_{reservoir}$ = 20 K, thermostat timescale = 100 fs, heating rate = 0.05 K/ps, chain length = 3, N_{steps} = 2000; MD3: $T_{initial}$ = 50 K, $T_{reservoir}$ = 10 K, thermostat timescale = 25 fs, heating rate = 0.05 K/ps, chain length = 3, N_{steps} = 2000; MD4: $T_{initial}$ = 50 K, $T_{reservoir}$ = 100 K, thermostat timescale = 100 fs, heating rate = 0.05 K/ps, chain length = 3, N_{steps} = 2000. The evolution MD runs were performed at constant temperature, unless stated otherwise, with the following parameters: $T_{initial}$ = 303 K, $T_{reservoir}$ = 303 K, thermostat timescale = 100 fs, heating rate = 0 K/ps, chain length = 3. First 1 ns of the evolution was taken as equilibration period and was not included in the statistical analyses of the MD trajectories.

Analysis of the MD trajectory

The full MD trajectories are available upon request from the author or, more conveniently, as YouTube videos.[138] Shortly after the MD simulation commenced, the molecules started to aggregate and gradually assembled into linear stripes (Figure 97A). A closer inspection of the trajectories clearly revealed three most common ways the molecules interacted with each other – contact types designated as *edge-to-edge*, *corner-to-corner*, and *corner-to-edge* (Figure 97B). To quantify this observation and thus obtain the rough comparison of their

thermodynamic stability, we used a custom-made Python script (see Appendix 4). The script detected the contact types in each frame of the trajectory and calculated their percentage among the total number of contacts. The time evolution of the contact type proportion was obtained as a rolling average over 500 frames. We also tried to analyze the chirality of the molecules within the found contacts, but the simulation length turned out to be insufficient to make reliable conclusions. For instance, the proportion of the *edge-to-edge* contacts in a frame *i* was calculated as

$$\%EE_i = 100 \cdot \frac{EE_i}{EE_i + CC_i + CE_i} \quad (25)$$

Where EE_i, CC_i, and EC_i are counts of the *edge-to-edge*, *corner-to-corner*, and *corner-to-edge* contacts, respectively, in the frame *i*.

The cumulative values over all *n* frames *i* were defined as:

$$\%EE_{tot} = 100 \cdot \frac{\sum_i^n EE_i}{\sum_i^n EE_i + CC_i + CE_i} \quad (26)$$

A more detailed description of the script routine is as follows: The underlying graphite was ignored, and only molecular coordinates were extracted. The coordinates were averaged along all atoms of each molecule to obtain the positions of the molecular geometric centers. To also include the periodic contacts on the borders of the 2 × 2 supercell, the positions of the molecular centers were copied and shifted along *X*, *Y*, and *XY* (diagonal) directions by the corresponding lattice parameter. From all the positions, a 144 × 144 matrix of mutual distances between every pair of molecules was calculated. Subsequently, an empty rectangular contact type matrix, having a contact type as each element, was created. The columns in the matrix corresponded to 36 real molecules (18 *MMM* and 18 *PPP*, for instance), while the rows also included the molecules in the periodic images (original 36 molecules and molecules shifted in each direction, 144 in total). To determine the contact type between each molecular pair, their mutual distance and orientation were evaluated. If their distance in the distance matrix was larger than a certain cutoff, the molecules were declared as noninteracting and were not considered in the statistical analysis. The contacts of the molecules with themselves (diagonal elements of the distance matrix) were, naturally, excluded either. The contact between two different molecules with smaller than cutoff distance was determined by comparing the distances between the orientation points of the two molecules. Empirical observation showed that each contact type had a characteristic range of distances between these points. Thus, for each molecular pair a 3 × 3 matrix of distances between orientation points was calculated. This matrix was then evaluated using distance criteria, characteristic for every contact type. The obtained contact type was then written to the corresponding element of the contact type matrix. The counts for each contact type were calculated, as well as their proportions among all contacts, as explained in the equation (25) above. The described procedure was looped over every frame to obtain the

total contact type counts, the proportion of each contact type from the total number of contacts and the corresponding time evolution of these values (eq. (26)).

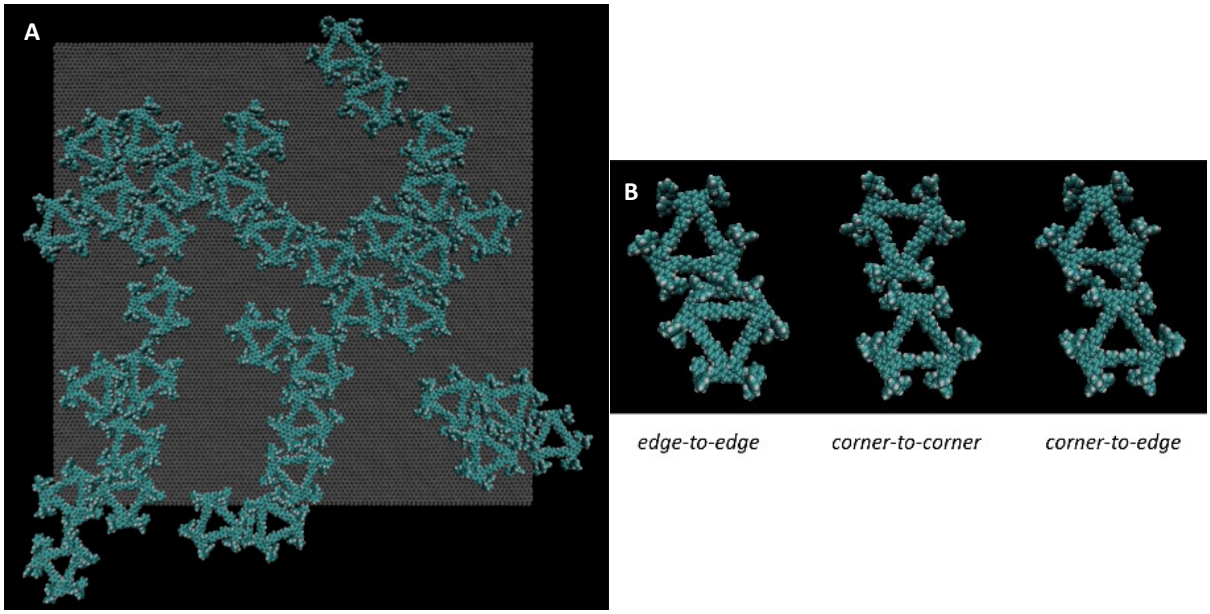

Figure 97. *MMP-MPP* system after 4.63 ns (A). Studied intermolecular contact types - *edge-to-edge*, *corner-to-corner*, and *corner-to-edge* as described in the text (B).

Figures 96A-F show the time evolutions of contact type proportion for the simulated systems. It is obvious from the time evolution plots that the *edge-to-edge* contacts are by far the most preferred while the *corner-to-corner* contacts are the least populated for the systems involving solubilized molecules **31**. This result is consistent with the observation of extensive interlocking of the trityl groups in the *edge-to-edge* contacts which is not very efficient in the other contact types. To elaborate further on this finding, we performed an analogous MD simulation with 36 non-solubilized macrocycles (*M,M,M)*-**31noTr**. Both the MD trajectory and its analysis revealed that the molecules have a very small tendency to aggregate. Only after cooling to 50 K, the molecules formed stable aggregates, vibrating about equilibrium positions. This was also evident from the significantly smaller number of contacts per trajectory frame when compared to the simulations involving the solubilized macrocycles. The contact lifetime was also significantly shorter. Table 17 summarizes the final statistical data and shows relative Helmholtz free energies (NVT ensemble) between every contact type or each system. The Helmholtz free energies were calculated from the statistical data shown in the table using the Boltzmann formula.

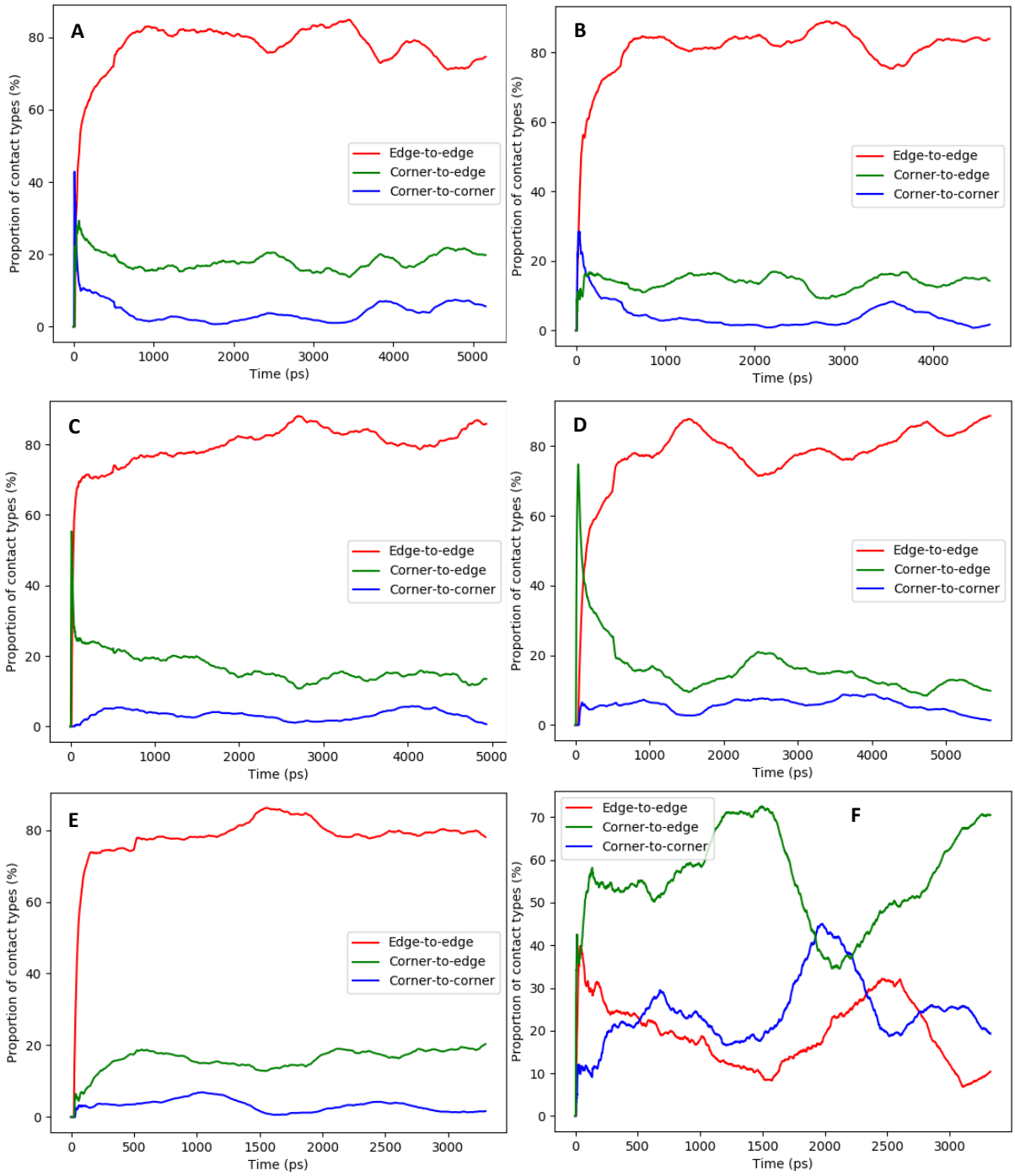

Figure 98. Time evolution of molecular contact types for individual simulated systems *MMM-PPP* (A), *MMP-MPP* (B), *MMM-MMP* (C), and *MMM-MPP* (D), *MMM-MMM* (E). Time evolution of the *MMM*noTr system. The system was gradually cooled to 50 K during the simulation (F).

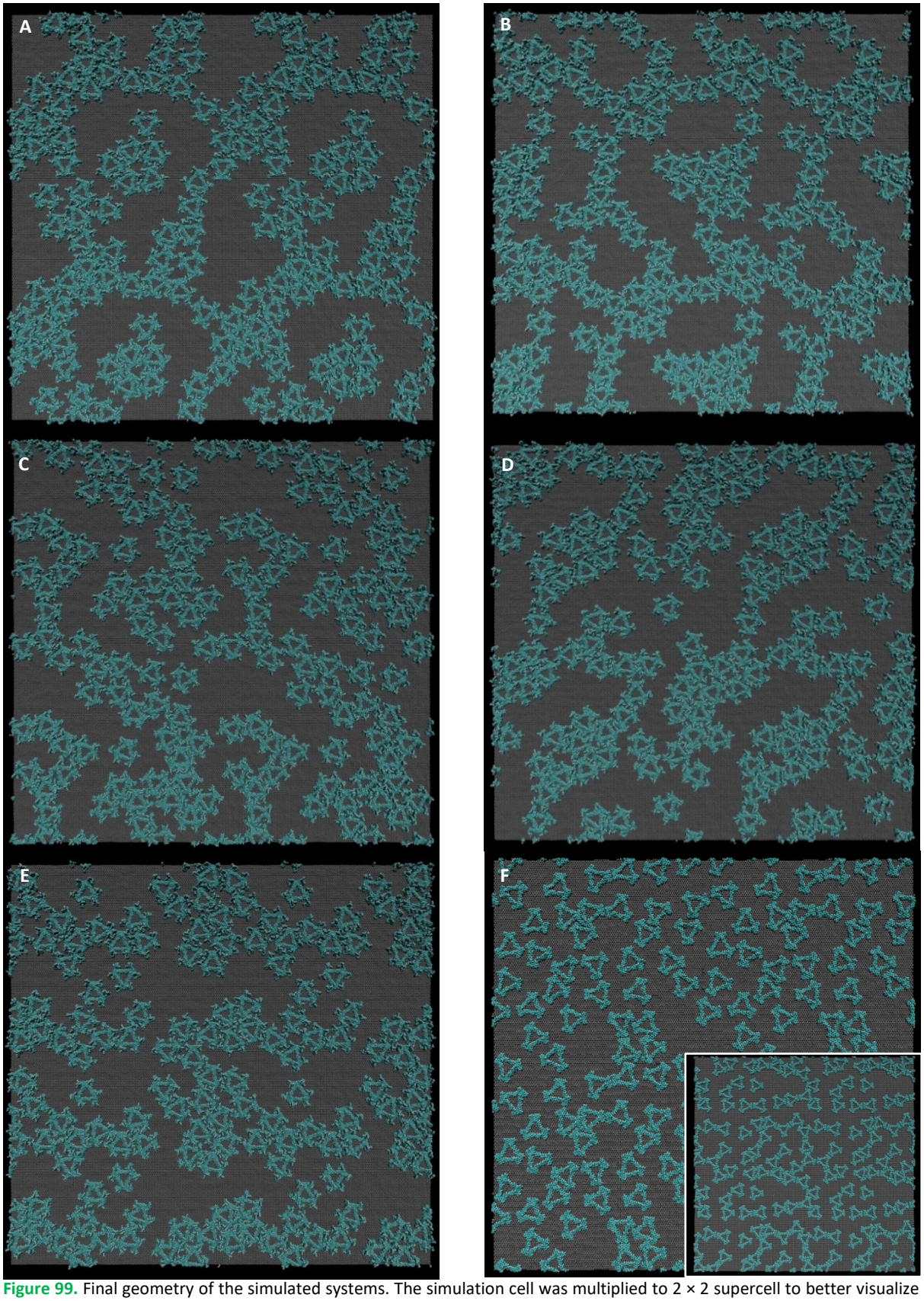

Figure 99. Final geometry of the simulated systems. The simulation cell was multiplied to 2 × 2 supercell to better visualize the boundary contacts. The atoms outside the simulation box were projected back to fit within the displayed box. *MMM-PPP* (A), *MMP-MPP* (B), *MMM-MMP* (C), *MMM-MPP* (D), and *MMM-MMM* (E). *MMM*noTr system after 0.8 ns (F) and

the same system after 3.3 ns and cooling to 50 K. Only at such a low temperature did the molecules formed stable aggregates (F-inset).

MMM-PPP			
Contact type	**Contacts per frame**	**Total proportion of contact types (%)**	***ΔF (kcal·mol^{-1})***
EE	39.0	78	0.0
CC	1.9	4	1.816
CE	9.1	18	0.884
Total	41.2	-	-
MMM-MPP			
Contact type	**Contacts per frame**	**Total proportion of contact types (%)**	***ΔF (kcal·mol^{-1})***
EE	44.1	81	0.0
CC	3.0	6	1.60
CE	7.4	13	1.08
Total	44.7	-	-
MMM-MMM			
Contact type	**Contacts per frame**	**Total proportion of contact types (%)**	***ΔF (kcal·mol^{-1})***
EE	19.6	80	0.0
CC	0.6	2	2.127
CE	4.2	17	0.932
Total	23.5	-	-
MMP-MPP			
Contact type	**Contacts per frame**	**Total proportion of contact types (%)**	***ΔF (kcal·mol^{-1})***
EE	35.8	83	0.0
CC	1.3	3	1.984
CE	6.1	14	1.052
Total	36.3	-	-
MMM-MMP			
Contact type	**Contacts per frame**	**Total proportion of contact types (%)**	***ΔF (kcal·mol^{-1})***
EE	37.2	82	0.0
CC	1.3	3	2.032
CE	6.7	15	1.028
Total	38.2	-	-
***MMM*noTr**			
Contact type	**Contacts per frame**	**Total proportion of contact types (%)**	***ΔF (kcal·mol^{-1})***
EE	0.8	17	-
CC	1.2	24	-
CE	2.8	59	-
Total	4.7	-	-

Table 17. Summary of the statistical and thermodynamic data from the MD simulations of systems in Figures 97. Helmholtz free energies are calculated from the total counts of individual contacts and are referenced to the most probable contact types. The analyses were performed after a 1 ns equilibration period. *MMM*noTr system was cooled to 50 K, thus *ΔF* is not well defined.

5.13.2. Orientation of Molecules **31** on Graphite Lattice

Simulation protocol

A single molecule of (-)-(*M*,*P*,*P*)-**31** was placed on a slab of a double layer graphite (surface orientation: (001), size of the hexagonal simulation cell in multiples of the graphite hexagonal unit cell: v_1 = [40, 0], v_2 = [0, 40], Figure 100). The molecule was first relaxed by the simulation annealing protocol described in the previous chapter before it was left to evolve for a specified time at a given temperature. The orientation of the molecule with respect to the underlying graphite lattice in every trajectory frame was then calculated.

Simulation parameters

The simulated annealing protocol consisted from a sequence of geometry optimizations and MD runs as schematically described by the following scheme: OPT1, 5 × (MD1, MD2, OPT2), 3 × (MD3, MD4, OPT1), where OPT1: N_{steps} = 200; OPT2: N_{steps} = 100; MD1: $T_{initial}$ = 3 K, $T_{reservoir}$ = 1 K, thermostat timescale = 25 fs, heating rate = 0.05 K/ps, chain length = 3, N_{steps} = 2000; MD2: $T_{initial}$ = 10K, $T_{reservoir}$ = 20 K, thermostat timescale = 100 fs, heating rate = 0.05 K/ps, chain length = 3, N_{steps} = 2000; MD3: $T_{initial}$ = 50 K, $T_{reservoir}$ = 10 K, thermostat timescale = 25 fs, heating rate = 0.05 K/ps, chain length = 3, N_{steps} = 2000; MD4: $T_{initial}$ = 50 K, $T_{reservoir}$ = 100 K, thermostat timescale = 100 fs, heating rate = 0.05 K/ps, chain length = 3, N_{steps} = 2000. The evolution MD runs were performed at constant temperature, with the following parameters: $T_{initial}$ = 298 K or 35 K, $T_{reservoir}$ = 298 K or 35 K, thermostat timescale = 100 fs, heating rate = 0 K/ps, chain length = 3. All other parameters were set as described in Chapter 5.13.1.

Analysis of the MD trajectory

A self-made Python script was used to assess the frequency of the molecular orientations (see Appendix 5). Two atoms coincident with one side of the triangular molecule of (-)-(*M*,*P*,*P*)-**31** (red C atoms, Figure 100) were chosen as an orientation reference. The rotation angle was calculated between the line defined by the reference atoms (thin yellow line in Figure 100) and the [100] lattice direction of the underling graphite. The orientation angle was calculated for each frame of the trajectory. The obtained angles were presented in a histogram showing the most probable orientations of the molecule on the surface.

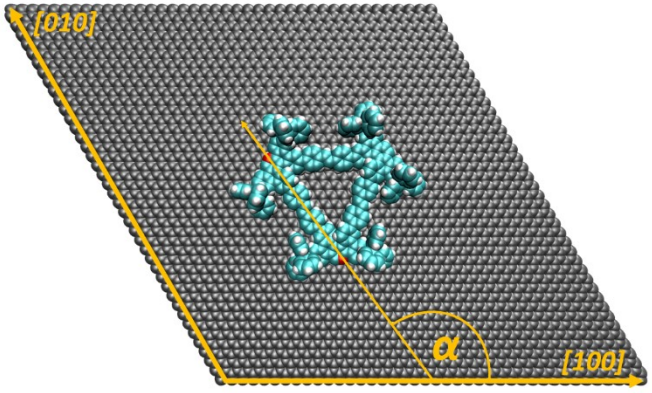

Figure 100. Simulation cell with double-layer graphite slab and (-)-(*M*,*P*,*P*)-**31**. The red color highlights the atoms used as a reference for the calculation of the orientation angle *α* between the *[100]* direction and the molecule.

5.14. NMR Structural Analysis of Trimer **31** and Tetramer **32**

NMR structural assignment of trimer 31

As **31** is a rather complex molecule, the most relevant aspects of its NMR structural assignment are discussed below.

Considering the C_2 symmetry of the (*M**,*M**,*P**)-**31** stereoisomer, it is expected to have signals from one half of the molecule. However, some signals are obviously indistinguishable resulting in that only signals from the (*M**,*P**) and (*P**,*P**) structural units can be observed. Numbers 1-25 were used to denote atoms in the (*M**,*P**) unit and daggered numbers 1†-25† to denote atoms in the (*P**,*P**) unit (atoms 1†-25†) (Figure 33A). On the contrary, the (*M**,*M**,*M**)-**31** isomer, possessing D_3 symmetry, should have only one set of signals which are denoted by numbers 1†-25† (Figure 33B). Alternative placement of the structural units was also considered but it did not reflect the experimental observations.

The common feature of the ^{1}H spectra of both stereoisomers is that the signals of the individual structural units are mostly independent of each other. Therefore, the spectra of (*M**,*M**,*M**)-**31** and (*M**,*M**,*P**)-**31** appear as a superposition of the signals from the individual structural units. It is also important to mention that the chemical shifts were significantly affected by the sample concentration, indicating a strong tendency of the macrocycles to aggregate.

Figure 101 shows a ^{1}H spectrum of the stereoisomeric mixture of (*M**,*M**,*P**)-**31** and (*M**,*M**,*M**)-**31** in ca 75 : 25 ratio. As discussed below, many signals of the individual stereoisomers overlap which renders the spectrum rather misleading. This is most pronounced in the case of signals 11 and 11† or 13 and 13† where the signals with dagger are in fact overlapping peaks from the (*P**,*P**) structural units of both (*M**,*M**,*P**)-**31** and (*M**,*M**,*M**)-**31**. If the mixture was pure (*M**,*M**,*M**)-**31**, the signal 11 (and other signals without dagger) would disappear. In the case of pure (*M**,*M**,*P**)-**31**, the ratio of the 11 and 11† would be exactly 2 : 1 (similarly for other signal pairs). Nevertheless, the intensity of these signals is practically equal in the equilibrium mixture. This becomes clear when we consider how the peak intensity varies with a molar ratio of the stereoisomers in the mixture. The stoichiometry of the molecules dictates that the signal intensity of 11 and 11† (and similarly for the other pairs) must be equal at a molar ratio between (*M**,*P**,*P**)-**31** and (*M**,*M**,*M**)-**31** of 75 : 25. This is the same ratio which was found by the equilibration experiment and slightly higher than the value from the kinetic measurement. Moreover, the same ratio is obtained when we consider a purely statistical formation of **31** which suggests that the free energy difference between (*M**,*P**,*P**)-**31** and (*M**,*M**,*M**)-**31** stems from the difference in their configurational entropies. Further, the only signals that clearly represent the distinct stereoisomers were that of the proton pairs 19, 19†; 16, 16†; or 8, 8†. On the other hand, the protons 13, 13†; 11, 11†; 15, 15†; 4, 4†; and 7, 7† show a marked chemical shift difference between the structural units, but the chemical shift differences originating from the different stereoisomers were practically absent.

The above observations were further reinforced by measuring the proton spectra of mixtures enriched in one stereoisomer. We were unable to obtain individual pure stereoisomers in an amount sufficient for NMR measurement, so only impure mixtures enriched in either (-)-(*P*,*P*,*P*)-**31** or (-)-(*M,P,P*)-**31** were measured. Thus, the spectrum enriched in homochiral (-)-(*P*,*P*,*P*)-**31** (Figures 106 and 109) shows less intense signals of protons 13, 11, 4, and 7, as compared to the spectrum of mixture enriched in heterochiral (-)-(*M,P,P*)-**31** (Figure 108 and 107), where the trend is reversed and the signals of protons 13, 11, 4, and 7, are more intense. It was the trend in the intensities of these signals in the compared spectra, which led us to the particular choice of the (*M**,*P**) and (*P**,*P**) structural units.

The ^{13}C APT spectra of the above mixtures also corroborated the results from their ^{1}H counterparts (Figures 108 and 110). Moreover, a comparison between the intensity of specific carbon signals and the abundance of a particular stereoisomer in the mixture further helped with the assignments of many carbon nuclei, complementing the information from HMBC spectra (see below). However, we were not able to assign all peaks in the spectra of these mixtures, as some signals might correspond to impurities or aggregation related phenomena. Moreover, the spectrum of (-)-(*P*,*P*,*P*)-**31** had a very low intensity and some signals could not be discerned from the background noise.

The atomic connectivity within **31** was inferred from the standard combination of COSY (Figure 103), HSQC (Figure 104), HMBC (Figure 105), and ROESY (Figure 106) spectra measured on the stereoisomeric mixture. COSY shows correlation within 4 spin systems. The protons 3, 3 and 4†, 4† of the stilbene moieties interact, but contrary to expectation, the ^{5}J coupling between protons 1, 1† and 3, 3† is not present, likely due to a large dihedral angle between the planes of the phenylene ring and the vinylene linker. However, the presence of protons 1, 1† is evident from HSQS and HMBC spectra. Both helicene spin systems consisting of protons 7, 7†; 8, 8†; 11, 11†; and 13, 13†; 15, 15†; and 16, 16†, have the expected coupling patterns of a 1,2,4-trisubstituted benzene ring. More complex is the coupling pattern of the trityl protons 23, 23†; 24, 24†; and 25, 25†, which reflects the superposition of signals from the helicene units of opposite chirality, either within one molecule or in the stereoisomeric mixture.

The HSQC spectrum was particularly useful for elucidation of the cluttered signals in the 7.27 – 7.49 ppm region of the ^{1}H domain. Apart from the obvious cross peaks of trityls, it revealed the ^{1}H and ^{13}C signals of 7, 7† and 1, 1† nuclei, which were not apparent from the ^{1}H spectrum alone. The cross-peak at (7.30, 128.30) ppm at first glance seems to correspond to nuclei 1, 1†. However, it can also be noted in other signals or other spectra that it is just a result of the broad second-order splitting of the trityl protons. In fact, all the trityl proton signals are very broad which can be seen in the cross peaks at (7.31, 126.78), (7.37, 128.27), and (7.43, 131.86) ppm. This creates many confusing cross peak patterns in all 2D spectra.

The HMBC spectrum was especially instrumental for assignment of nuclei 1, 1†; 2, 2†; 3, 3†; 4, 4†; 5, 5†; and 6, 6†, along with many quaternary carbons. Combining the information from HMBC and ROESY spectra, it was possible to assign many signals to the specific (*M**,*P**) or (*P**,*P**) structural units. For example, in the ROESY spectrum, protons 11 at 8.53 ppm

interact with protons 4 at 7.74 ppm, but not with 4† at 7.69 ppm. A similar interaction pattern can be observed between protons 7 and 4. Proton 8 at 8.20 ppm is then assigned by interaction with proton 7 at 7.48 ppm. Further, carbon 6 at 138.55 ppm interacts both with proton 8 at 8.20 ppm and with proton 4 at 7.74 ppm in the HMBC spectrum. An analogous reasoning was used to assign the nuclei on the (*P**,*P**) structural unit.

Regarding the crowded group of signals in the region of (7.67-7.75, 7.28-7.49) ppm in ROESY, its confusing nature results from the overlap of the proton signals of 3, 3† and 4†. Thus, the cross peaks at (7.73, 7.47) and (7.69, 7.42) ppm correspond to the 4-7 and 4†-7† interactions, respectively. The oblong cross peak at (7.69, 7.29) ppm seems to be the result of the 1-3 and 1†-3† interactions.

As the assignment of the carbon signals 2, 2†; 5, 5†; 6, 6†; 17, 17†; 23, 23†; 24, 24†; and 25, 25† solely from the spectra of the stereoisomeric mixture was challenging, we took advantage of the information from the APT ^{13}C spectra of the stereoisomerically enriched mixtures. Thus, by comparing the signal intensity of a particular nuclei among the three spectra, it became clear which signal corresponds to which structural unit (Figures 100, 108 and 110).

A variable temperature measurement of **31** in $CDCl_2CDCl_2$ measured at 500 MHz was also performed (Figure 107). Despite the considerably broader signals as compared to the spectrum in CD_2Cl_2, we could observe that the higher temperature had only minor effect on the intensity ratio of protons 11 and 11†, reflecting the dominant entropic contribution to the free energy difference between the stereoisomers of **31**.

^{1}H NMR (600.1 MHz, CD_2Cl_2): 7.28 (m, 3H, 1†), 7.29 (m, 3H, 1), 7.28 – 7.33 (m, 18H, 25, 25†), 7.34 – 7.40 (m, 36H, 24, 24†), 7.41 – 7.49 (m, 36H, 23, 23†), 7.42 (m, 3H, 7†), 7.48 (m, 3H, 7), 7.57 (m, 6H, 15, 15†), 7.69 (m, 12H, 3, 3†), 7.69 (m, 6H, 4†), 7.74 (m, 6H, 4), 8.19 (d, *J* = 8.2 Hz, 3H, 8†), 8.20 (d, *J* = 8.2 Hz, 3H, 8), 8.47 (d, *J* = 1.9 Hz, 3H, 11†), 8.53 (d, *J* = 1.9 Hz, 3H, 11), 8.55 (d, *J* = 8.8 Hz, 4.5H, 16, 16†, (*M**,*P**,*P**)-**31**), 8.56 (d, *J* = 8.8 Hz, 1.5H, 16, 16†, (*M**,*M**,*M**)-**31**), 8.647 (s, 4.5H, 19, 19†, (*M**,*P**,*P**)-**31**), 8.653 (s, 1.5H, 19, 19†, (*P**,*P**,*P**)-**31**), 8.77 (d, *J* = 1.8 Hz, 3H, 13†), 8.79 (d, *J* = 1.7 Hz, 3H, 13).

^{13}C NMR (150.9 MHz, CD_2Cl_2): 65.89 (21, 21†), 120.66 (11), 121.00 (11†), 122.53 (19, 19†), 123.40 (16, 16†), 123.97 (7), 124.40 (7†), 125.34 (13), 125.36 (13†), 126.77 (25†), 126.79 (25), 127.48 (4), 127.68 (3, 4†), 127.85 (3†), 128.06 (20, 20†), 128.16 (17†), 128.18 (17), 128.26 (24†), 128.28 (24), 128.63 (1), 128.94 (1†), 129.97 (12, 12†), 130.62 (9†, 18, 18†), 130. 67 (9), 130.95 (10†), 130.99 (10), 131.84 (23†), 131.88 (23), 132.10 (8, 8†), 132.30 (15†), 132.37 (15), 137.18 (2), 137.26 (2†), 138.55 (6), 139.24 (6†), 139.76 (5), 140.39 (5†), 146.86 (14, 14†), 147.25 (22, 22†).

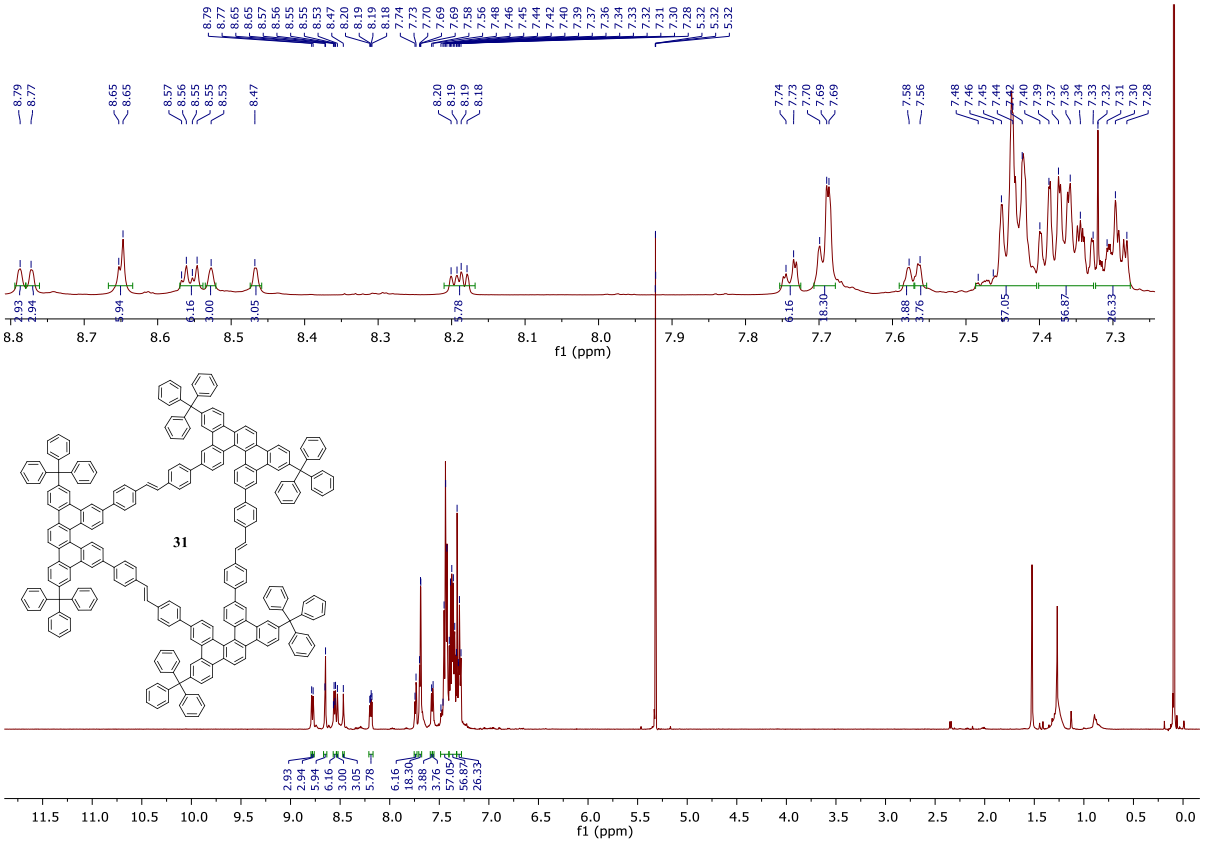

Figure 101. ^{1}H NMR spectrum of the stereoisomeric mixture of **31**.

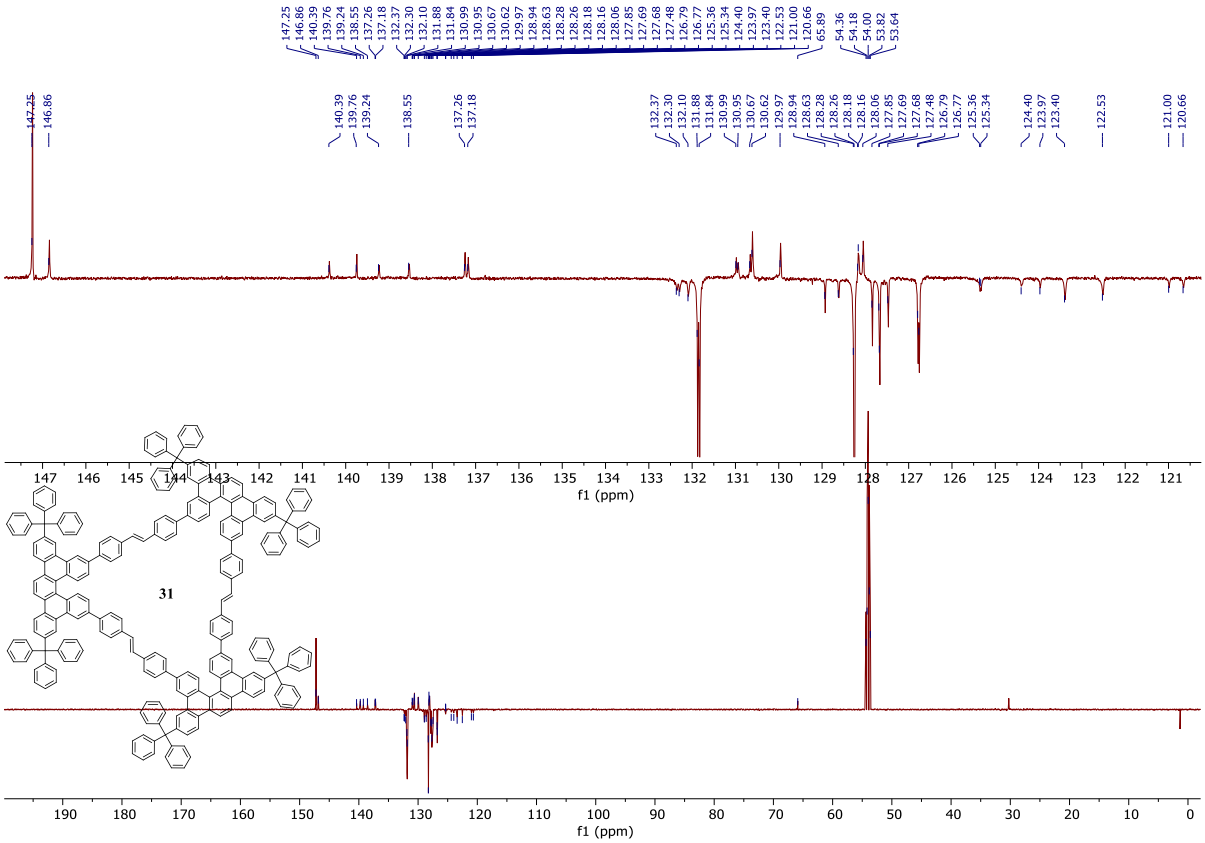

Figure 102. ^{13}C APT NMR spectrum of the stereoisomeric mixture of **31**.

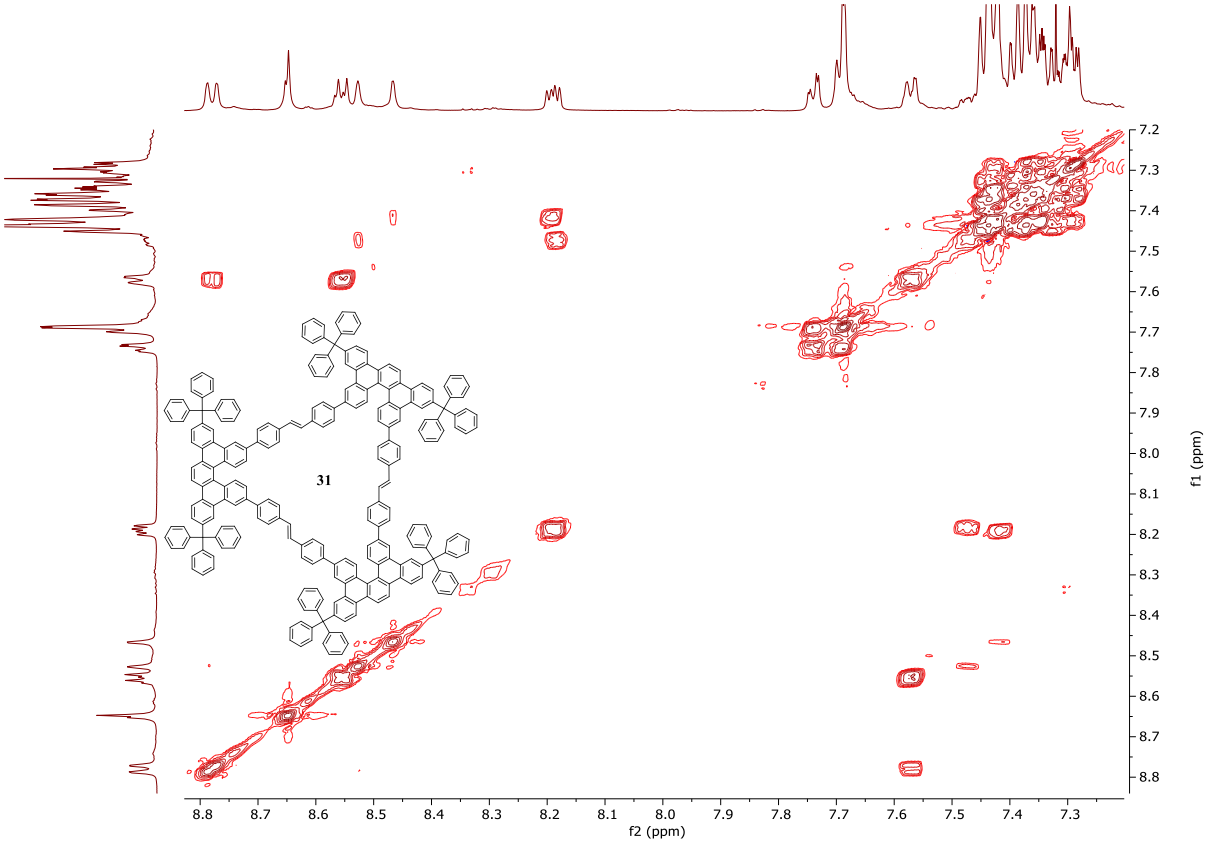

Figure 103. COSY NMR spectrum of the stereoisomeric mixture of **31**.

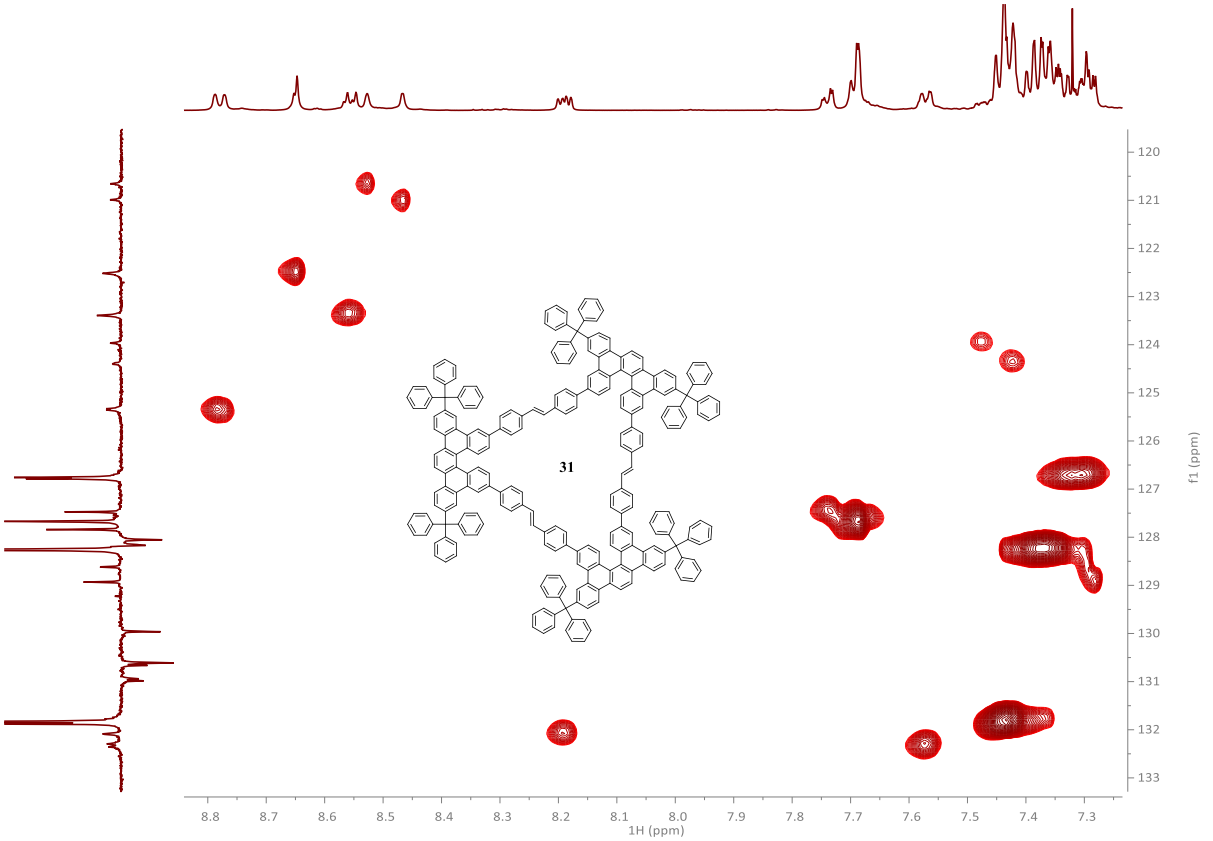

Figure 104. HSQC NMR spectrum of the stereoisomeric mixture of **31**.

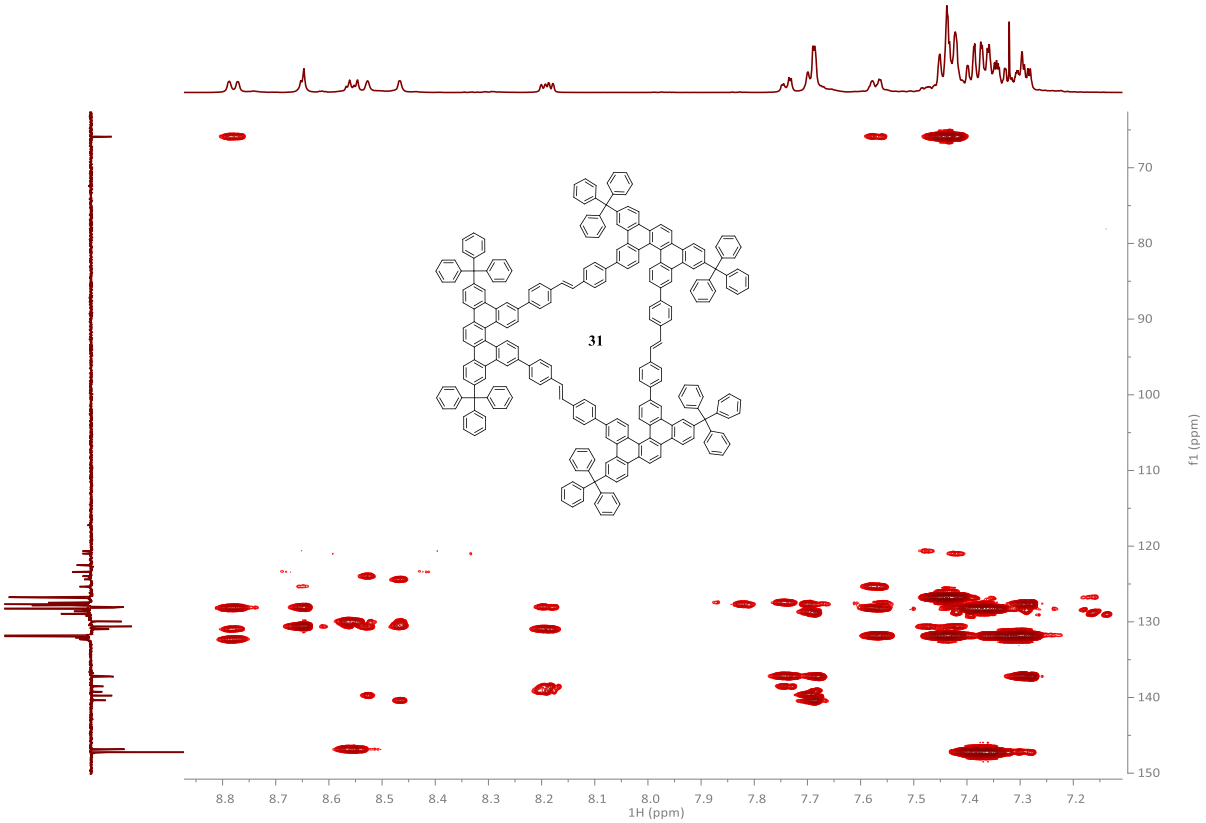

Figure 105. HMBC NMR spectrum of the stereoisomeric mixture of **31**.

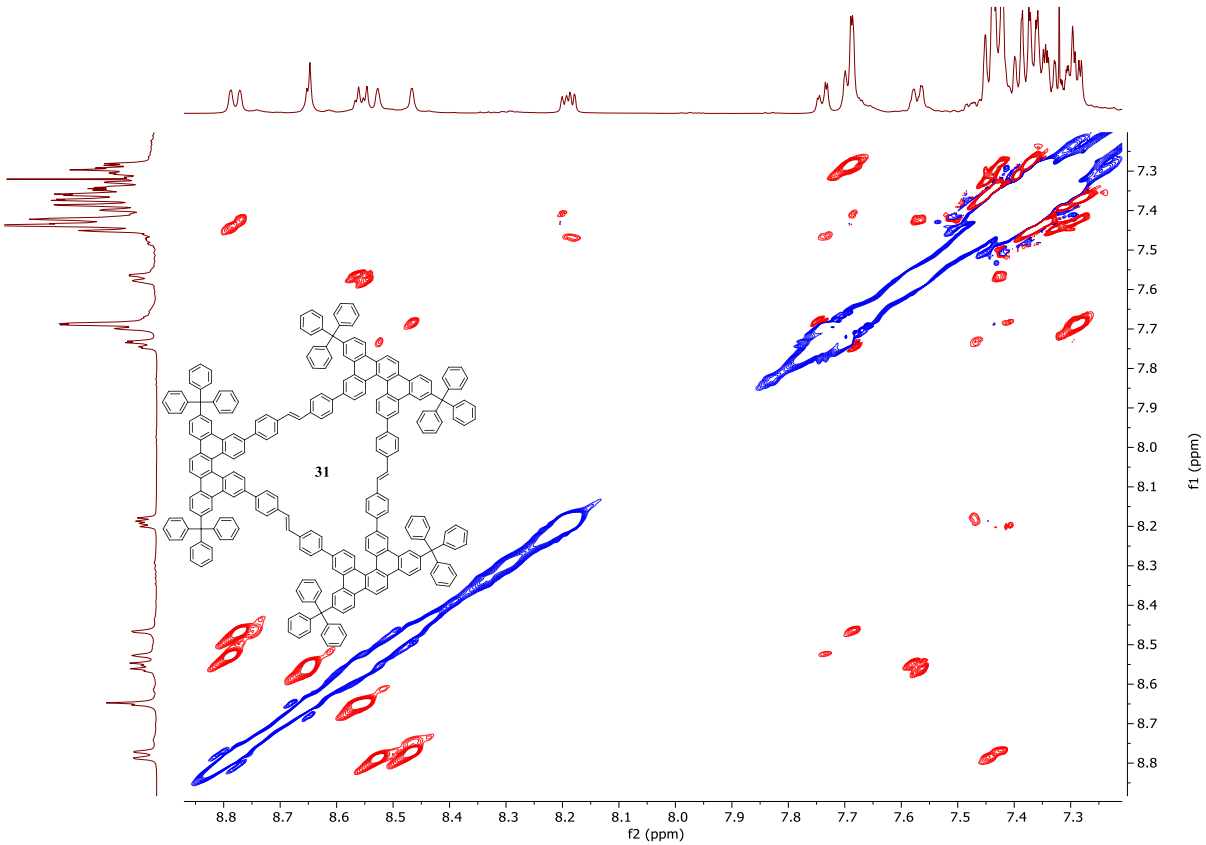

Figure 106. ROESY NMR spectrum of the stereoisomeric mixture of **31**.

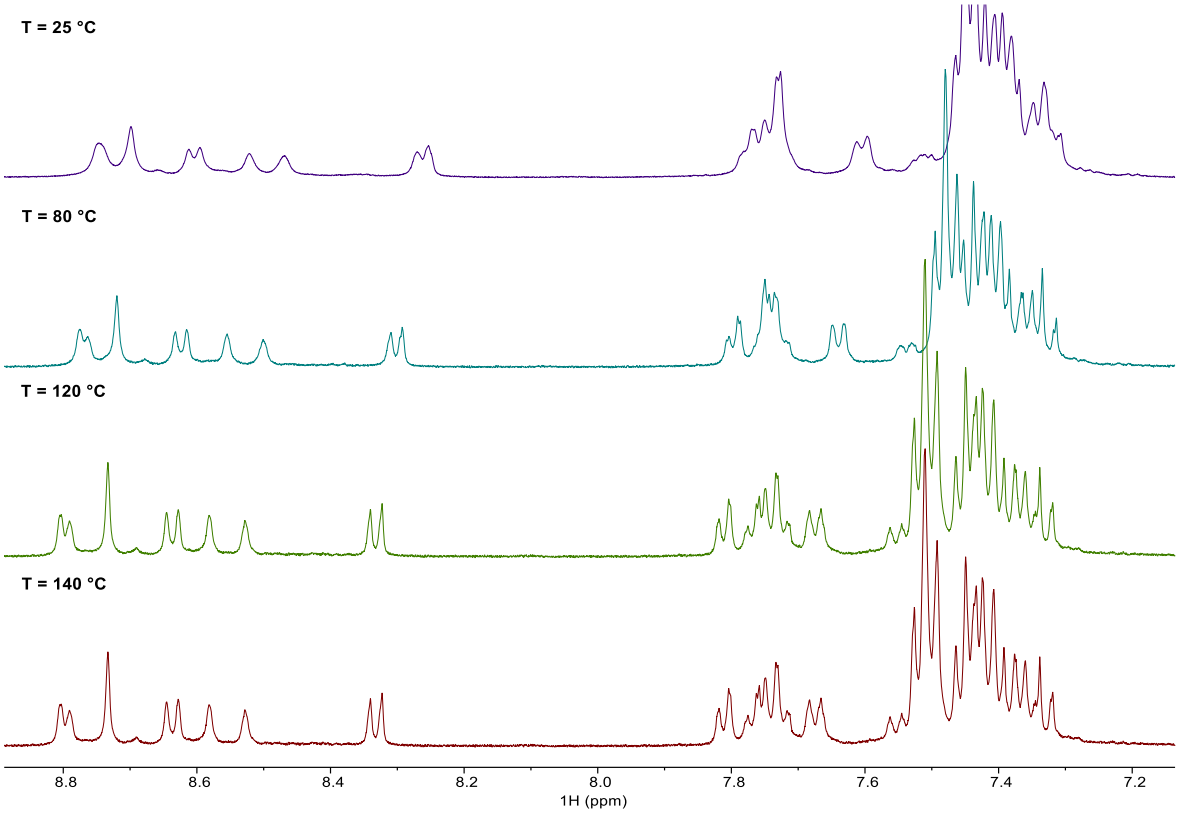

Figure 107. ^{1}H NMR spectra of the stereoisomeric mixture of **31** in $CDCl_2CDCl_2$ at various temperatures, measured at 500 MHz.

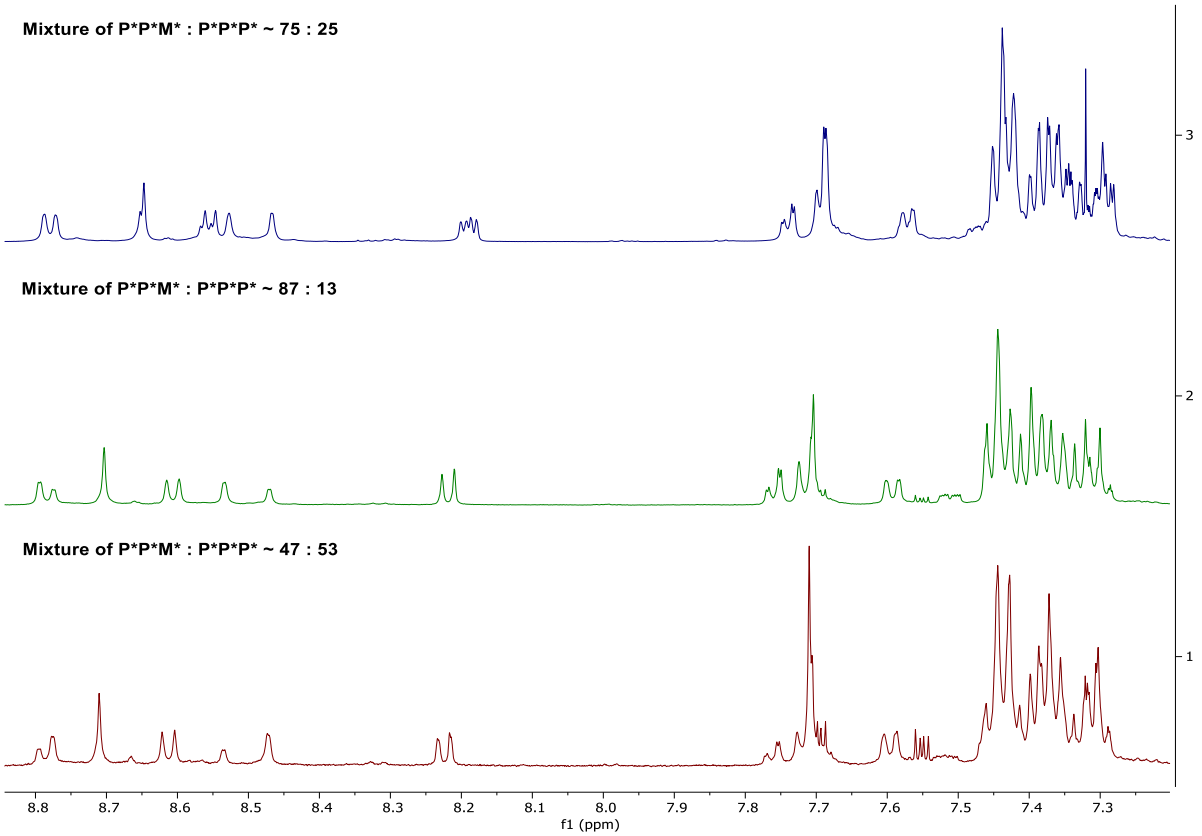

Figure 108. Comparison between the ^{1}H NMR spectra of the stereoisomeric mixture of **31** and the samples enriched in either (-)-(*M,P,P*)-**31** or (-)-(*P,P,P*)-**31** stereoisomers.

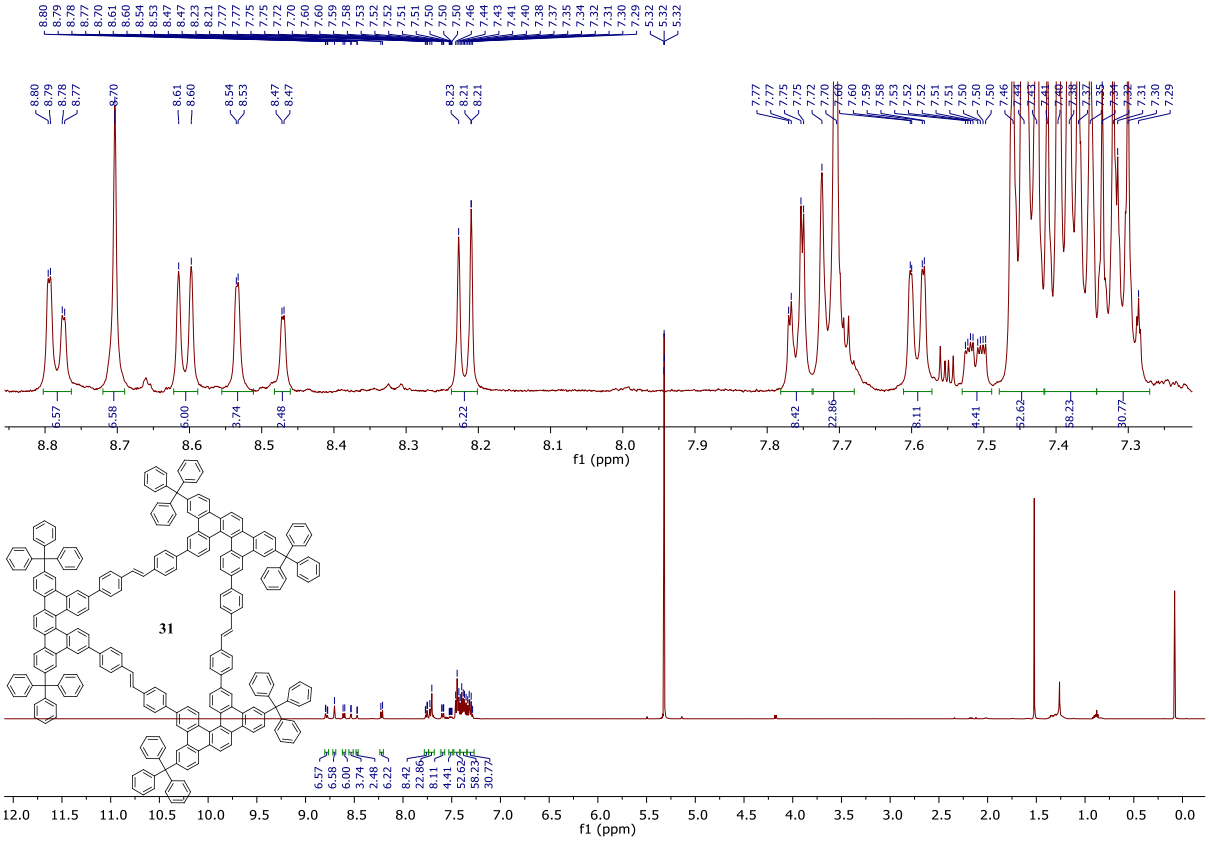

Figure 109. ^{1}H NMR spectrum of the stereoisomeric mixture enriched in (-)-(*M,P,P*)-**31**

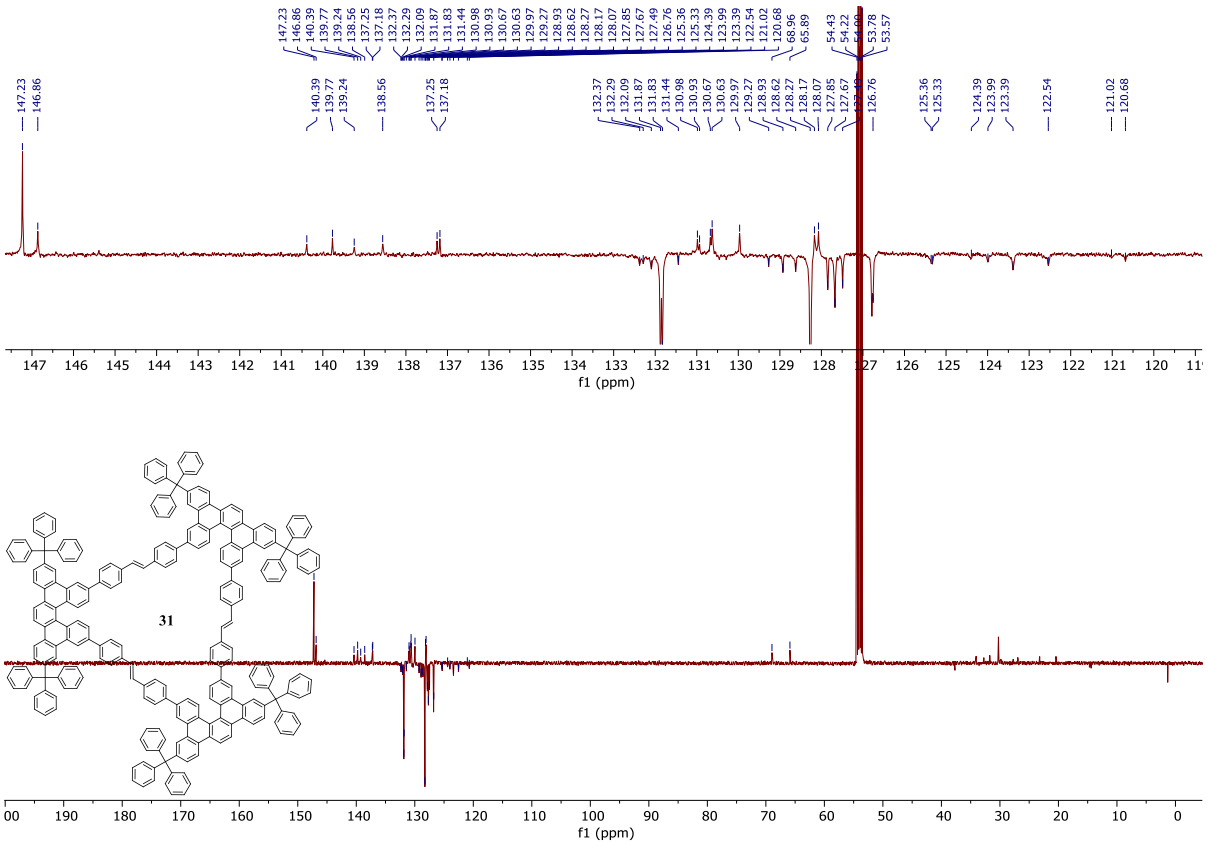

Figure 110. ^{13}C APT NMR spectrum of the stereoisomeric mixture enriched in (-)-(*M,P,P*)-**31**

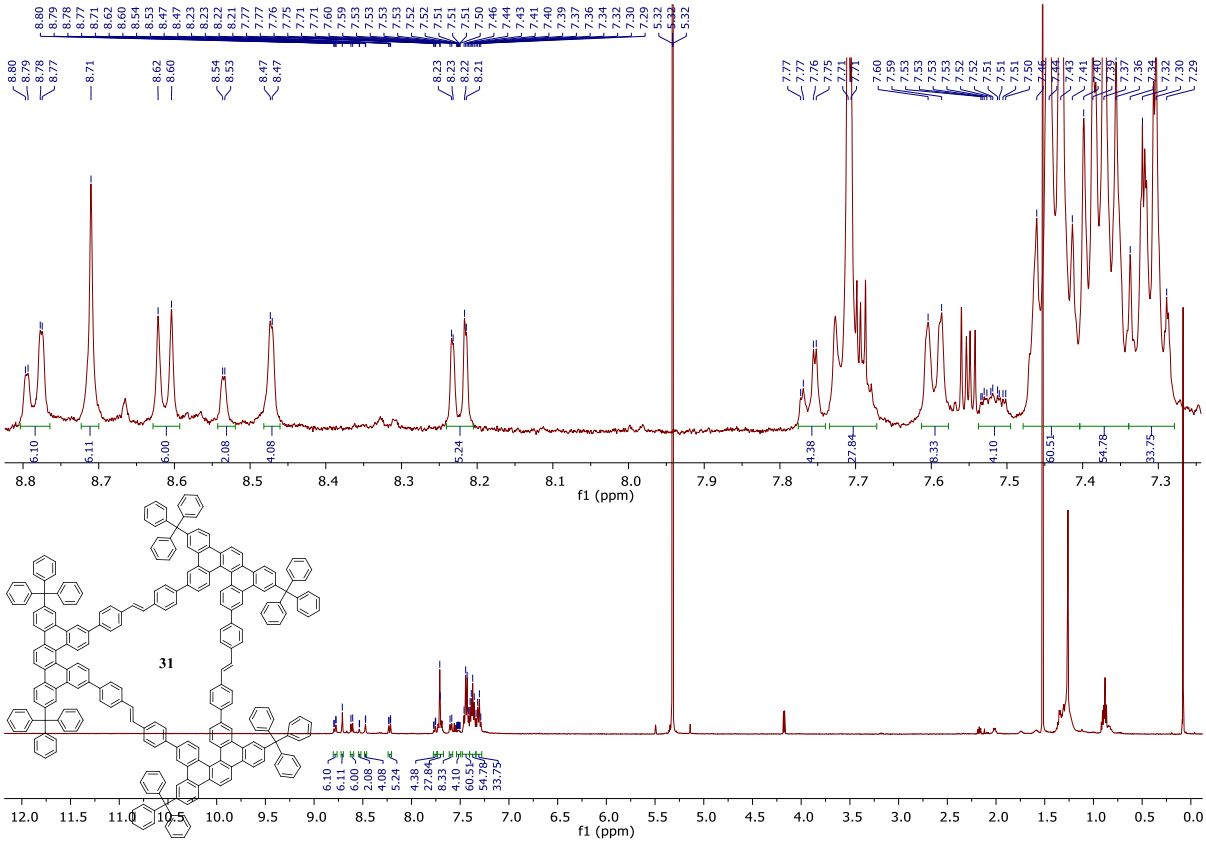

Figure 111. ^{1}H NMR spectrum of the stereoisomeric mixture enriched in (-)-(*P,P,P*)-**31**.

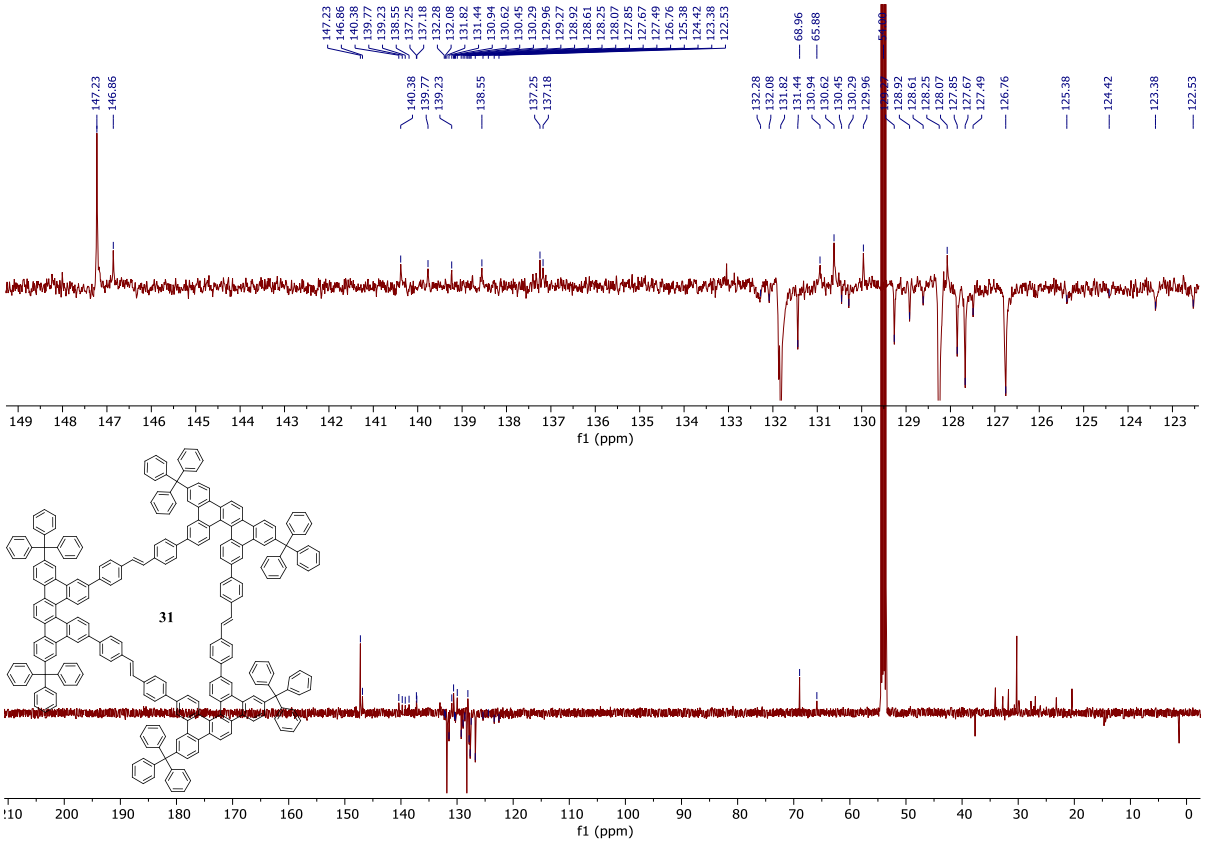

Figure 112. ^{13}C APT NMR spectrum of the stereoisomeric mixture enriched in (-)-(*P,P,P*)-**31**.

NMR structural assignment of tetramer 32

Tetramer **32** was obtained as a complex mixture of stereoisomers, so only basic structural information was obtained from NMR measurements. The compound was poorly soluble in CD_2Cl_2 which led to a strong aggregation and very broad spectral lines (Figures 113 and 114). A better solubility was achieved by using $CDCl_2CDCl_2$ as a solvent which provided spectra with an apparent helicene structural pattern, especially at high temperature (Figures 115, 116, and 117). Figure 116 shows a comparison between spectra of **31** and **32** at 140 °C. It can be noted that helicene, stilbene, and trityl peaks, common to both **31** and **32**, are present in the spectrum of **32**. Although the integration in the region 7.30-7.60 ppm is obviously inaccurate, the integrals in the rest of the spectrum are in accordance with the expected stoichiometry of **32**. It is interesting that the signals at 8.47 ppm and 8.53 ppm from the (*P**,*P**) and (*M**,*P**) structural units in the spectrum of **31** collapse to one broad peak at 8.53 ppm in the spectrum of **32**. This could suggest that a symmetrical or even (*P**,*P**,*P**,*P**)-**32** stereoisomer forms the bulk of the mixture.

To further show that the proton spectrum of **32** originates from molecules of a comparable size (and therefore similar diffusion coefficients), DOSY measurement of a mixture of **31** and **32** was performed. **31** was added to the sample as a reference. However, while the signals of the obvious impurities at 6.99 or 8.12 ppm are separated, the cross peaks of **31** and **32** seem to have practically identical diffusion coefficients, as shown by the spectrum in Figure 118. This could be a result of extensive aggregation of **31** and **32** into clusters which have similar diffusion behavior.

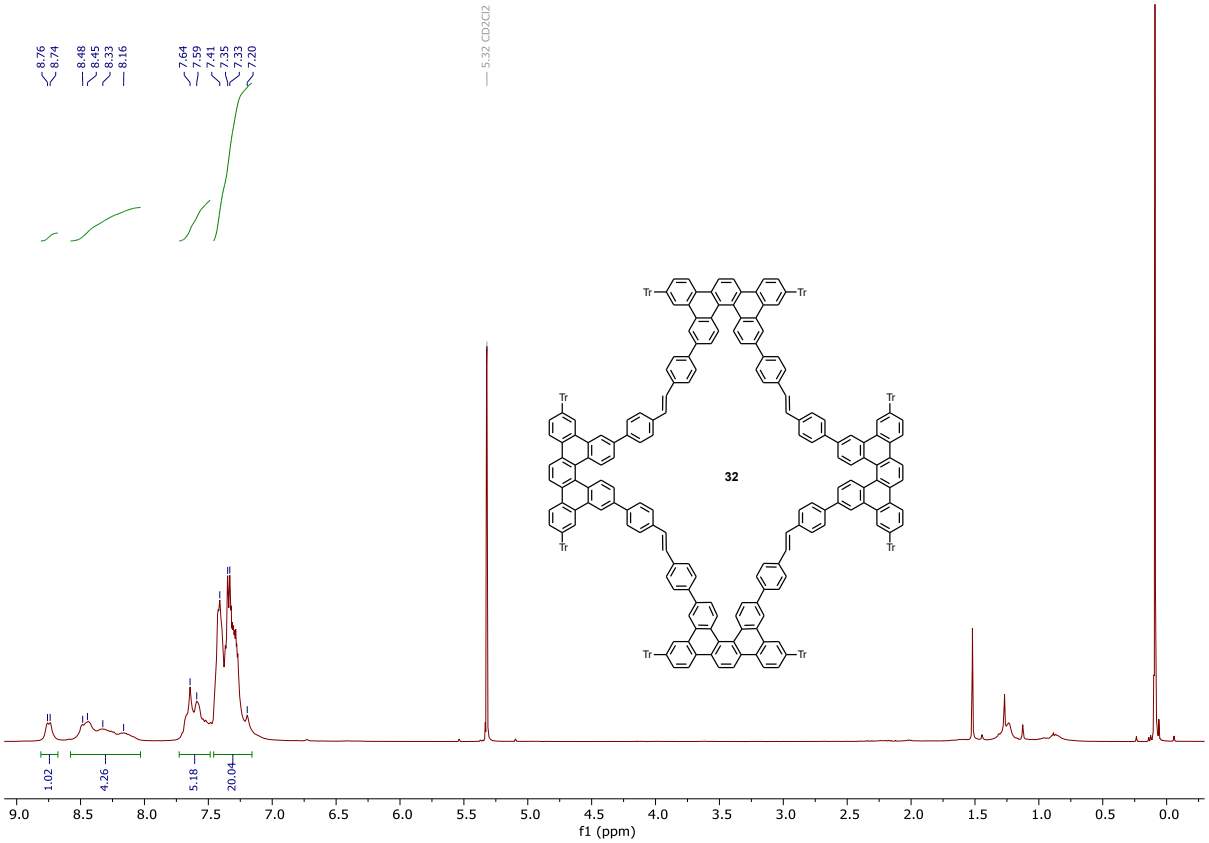

Figure 113. ^{1}H NMR spectrum of the stereoisomeric mixture of **32**, measured in CD_2Cl_2 at 400 MHz.

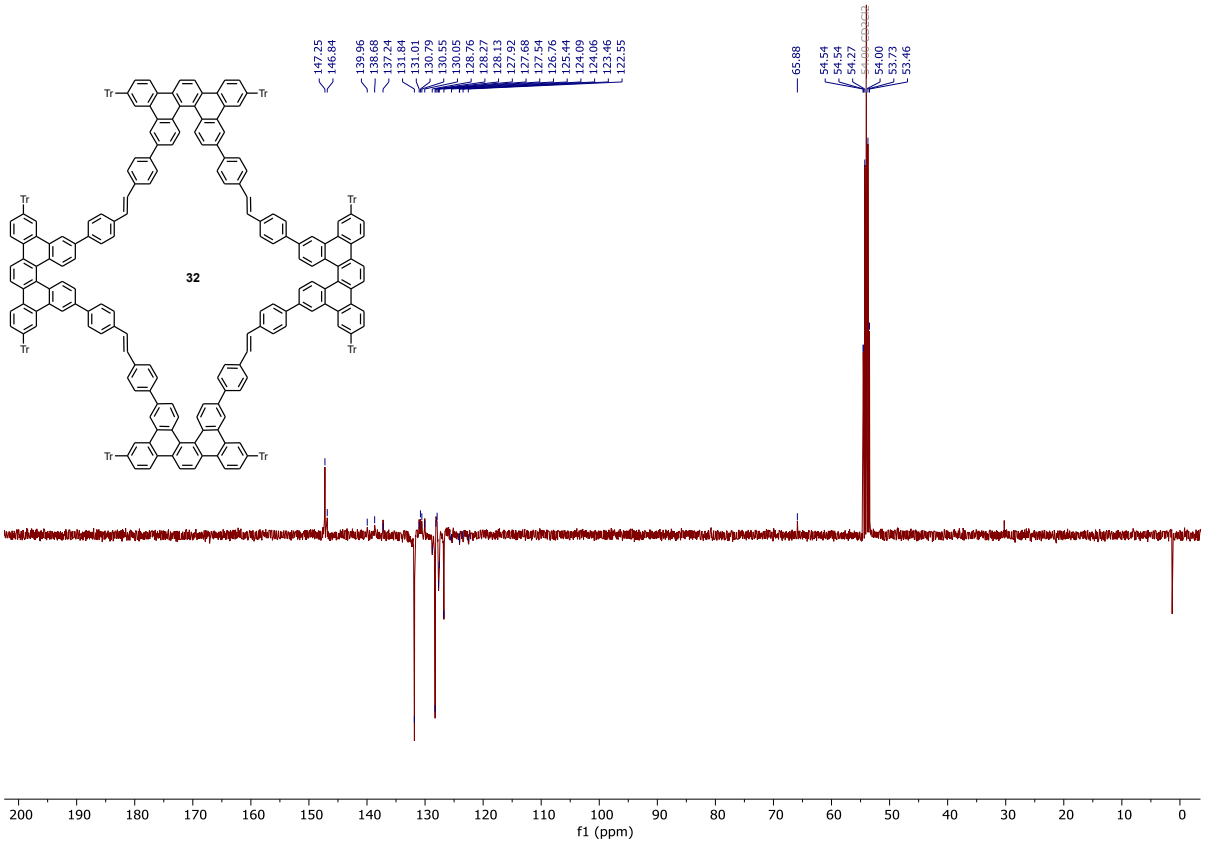

Figure 114. ^{13}C APT NMR spectrum of stereoisomeric mixture of **32**, measured in CD_2Cl_2 at 400 MHz.

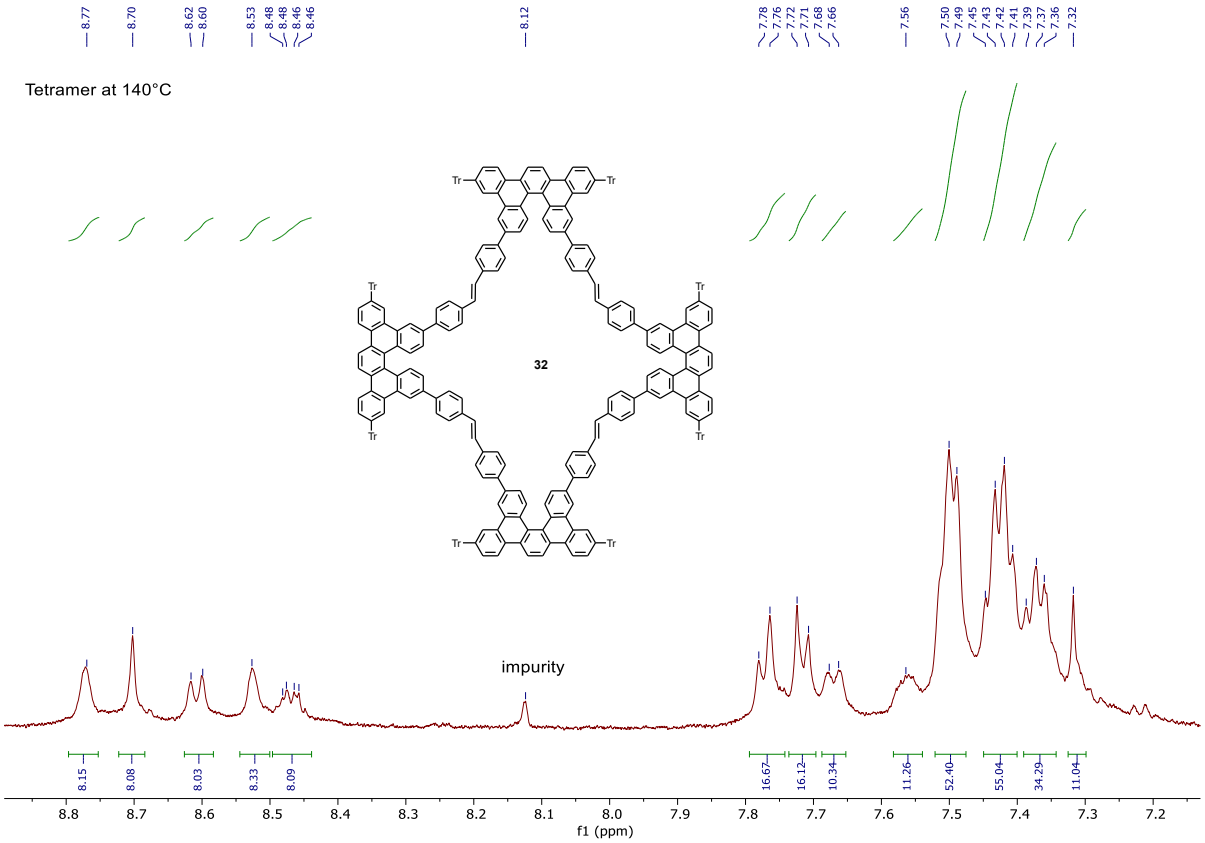

Figure 115. ^{1}H NMR spectrum of stereoisomeric mixture of **32**, measured in $CDCl_2CDCl_2$ at 140 °C and 500 MHz.

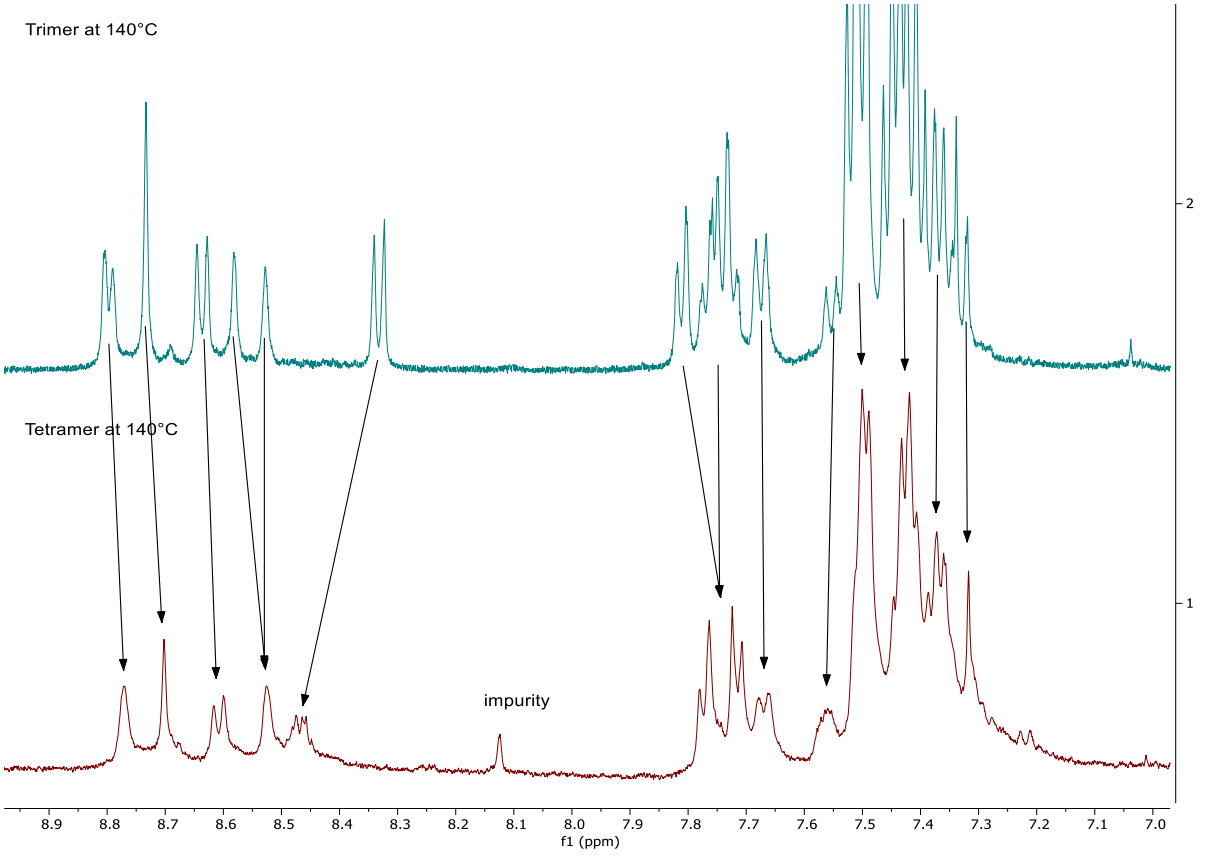

Figure 116. Comparison between ^{1}H NMR spectra of stereoisomeric mixtures of **31** and **32**, measured in $CDCl_2CDCl_2$ at 140 °C and 500 MHz.

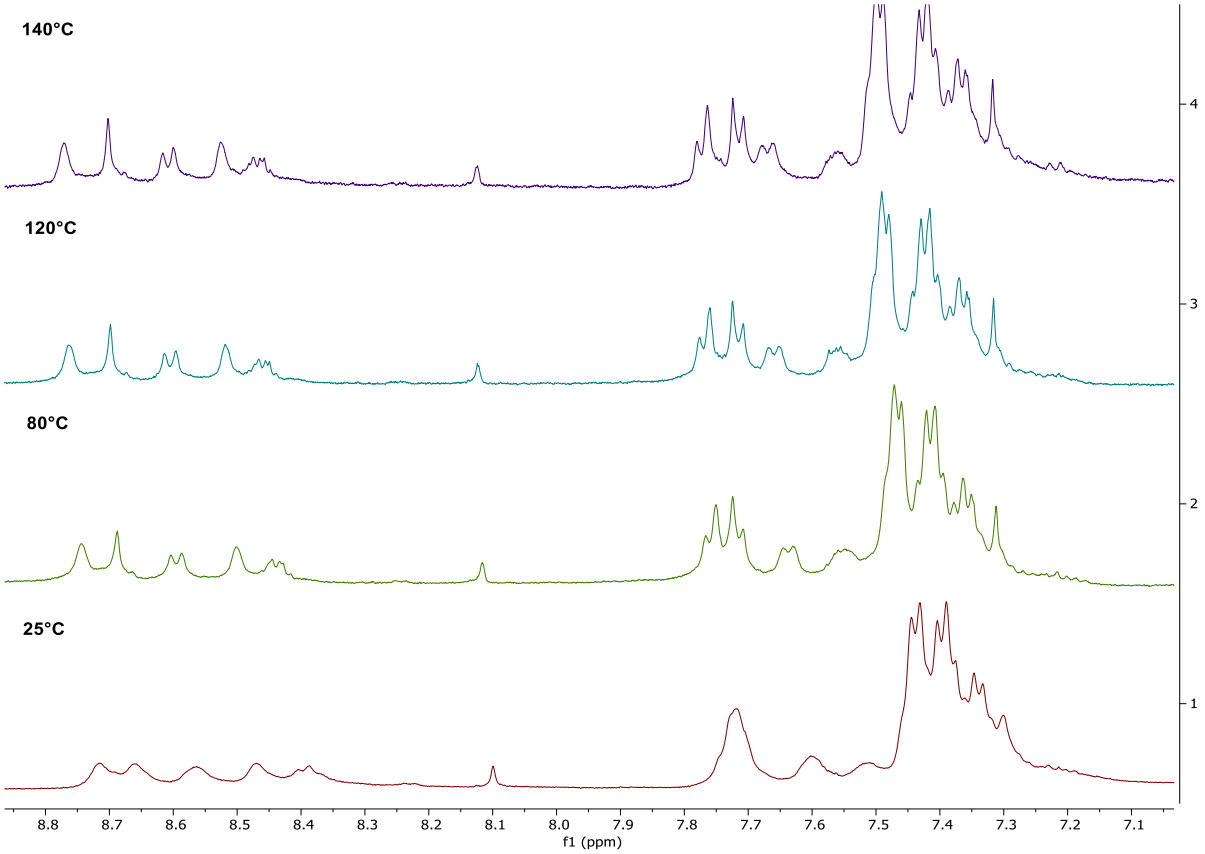

Figure 117. ^{1}H NMR spectra of the stereoisomeric mixture of **32** in $CDCl_2CDCl_2$ at various temperatures, measured at 500 MHz.

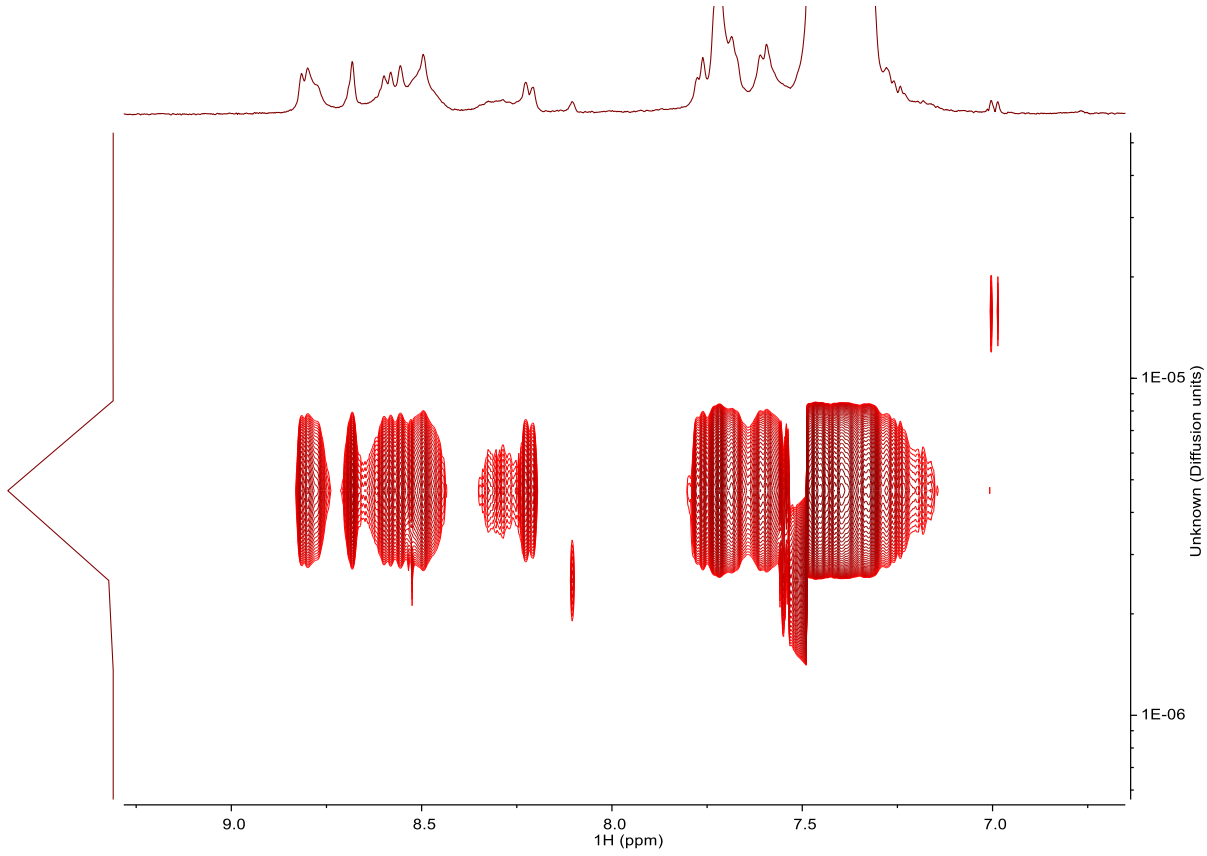

Figure 118. DOSY NMR spectrum of a combined mixture of **31** and **32**, measured in $CDCl_2CDCl_2$ at 500 MHz.

5.15. VT-NMR Investigation of (Anti)aromaticity

Procedure: A heat gun dried Schlenk flask was charged with CD_2Cl_2 (4 mL, dried over activated A3 molecular sieves) using a syringe equipped with a 200 nm PTFE syringe filter. The flask was briefly evacuated and backfilled with nitrogen five times to degas the solvent.

A vacuum dried NMR tube was installed into an apparatus ensuring its opening was under a stream of nitrogen. 1.5 mg of **31** was dissolved in 0.5 mL of degassed dry CD_2Cl_2 and the resulting solution was transferred to the NMR tube. The tube was then immersed in a dry ice bath.

$AgSbF_6$ (6.6 mg, 20 µmol) was weighed into a glass vial in a glovebox. The vial was closed, removed from the glovebox and its contents were quickly transferred into another heat gun dried Schlenk flask under a stream of nitrogen. Iodine (2.4 mg, 10 µmol) was weighed into a glass vial in air and subsequently transferred to the Schlenk flask already charged with $AgSbF_6$ under a stream of nitrogen. 0.5 mL of degassed CD_2Cl_2 was added to the solids which generated a pink solution and white precipitate which was allowed to settle.

Once the solution of **31** in the NMR tube cooled down, 50 µL (4 eq. of $AgSbF_6$ and 2 eq. of I_2) of the $AgSbF_6/I_2$ reagent was slowly added via syringe to the NMR tube under a stream of nitrogen, resulting in a dark purple homogeneous solution. The NMR tube was tightly closed and removed from the bath, briefly shaken to mix its contents, and quickly transferred to a 500 MHz NMR probe pre-cooled to -50 °C. The ^1H spectra were acquired at -50, -25, 0, and 25 °C (Figure 119).

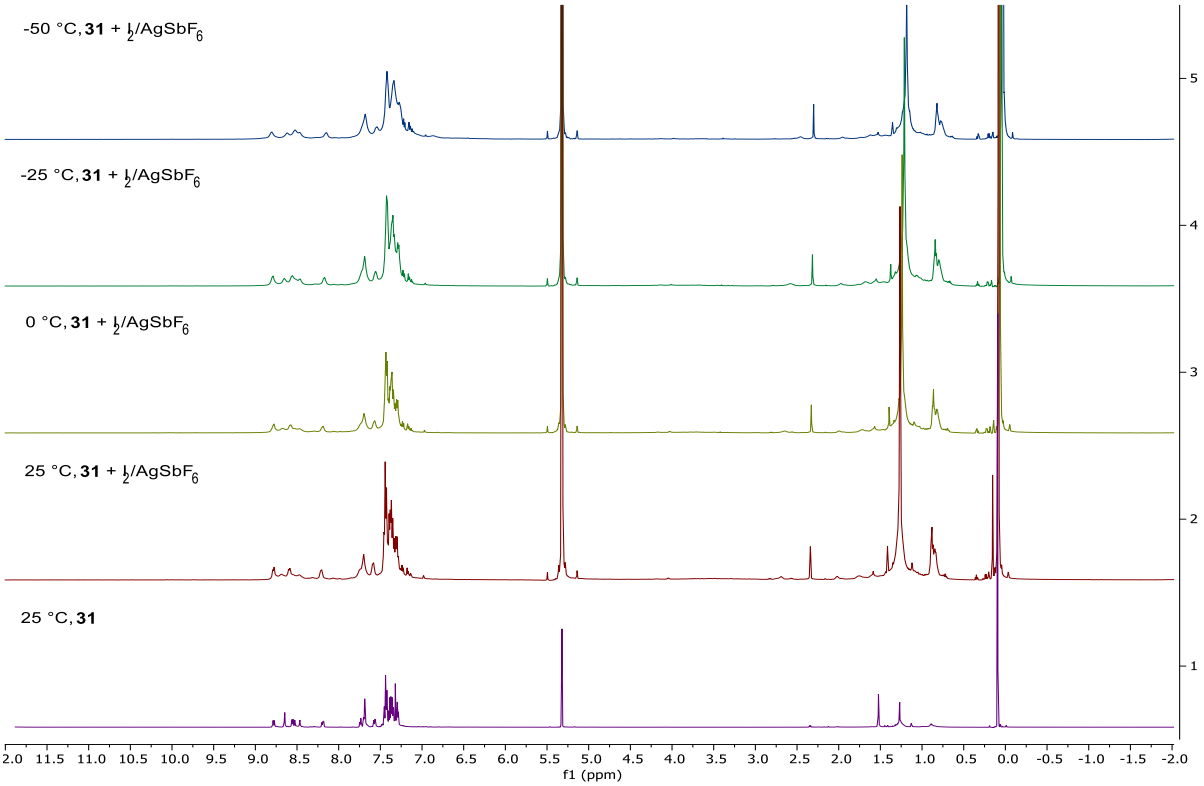

Figure 119. Full ^1H NMR spectra of mixture of **31** and $I_2/AgSbF_6$ reagent at various temperatures. The lowest spectrum shows pure stereoisomeric 31 for comparison. Spectra were measured in CD_2Cl_2 at 500 MHz, the lowest spectrum at 600 MHz.

5.16. ^{1}H and ^{13}C APT NMR spectra of the building blocks **42**, **43**, **35**, **36**, **37**, **38**, **40**, **41**

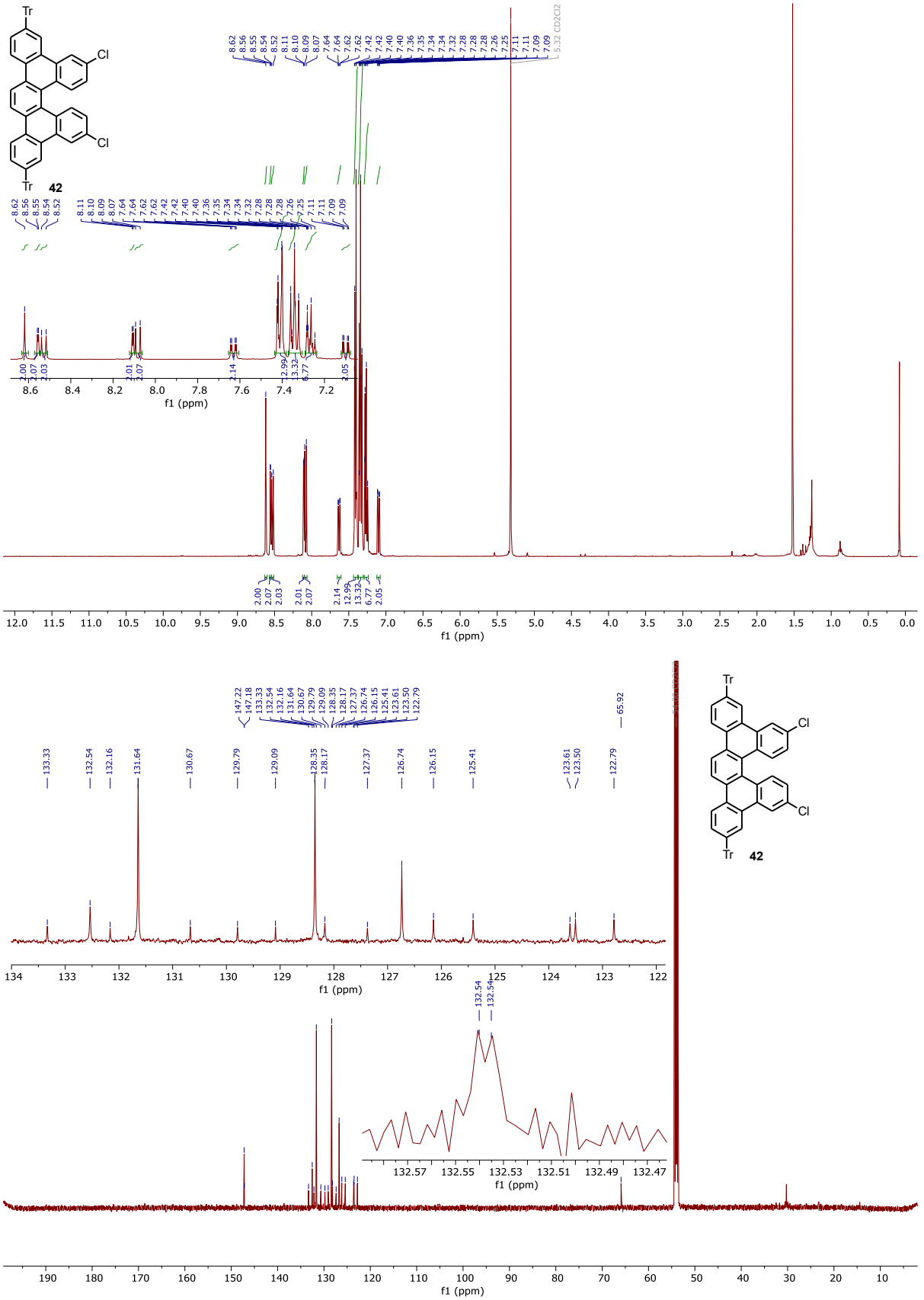

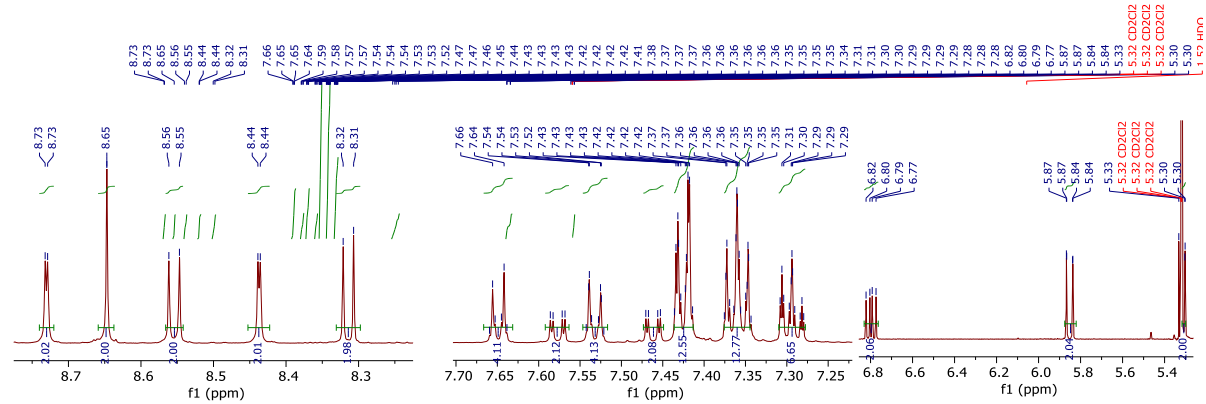
f1 (ppm)

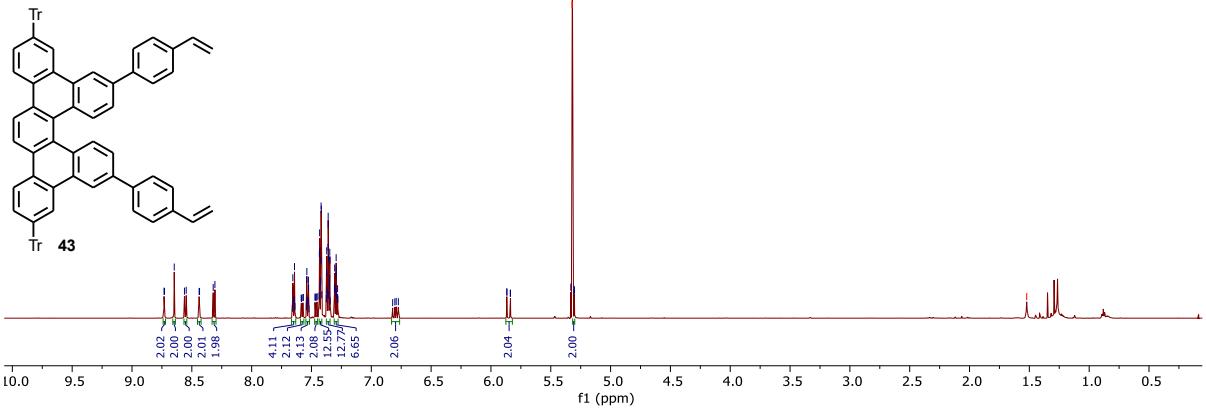
Tr
Tr
43
f1 (ppm)

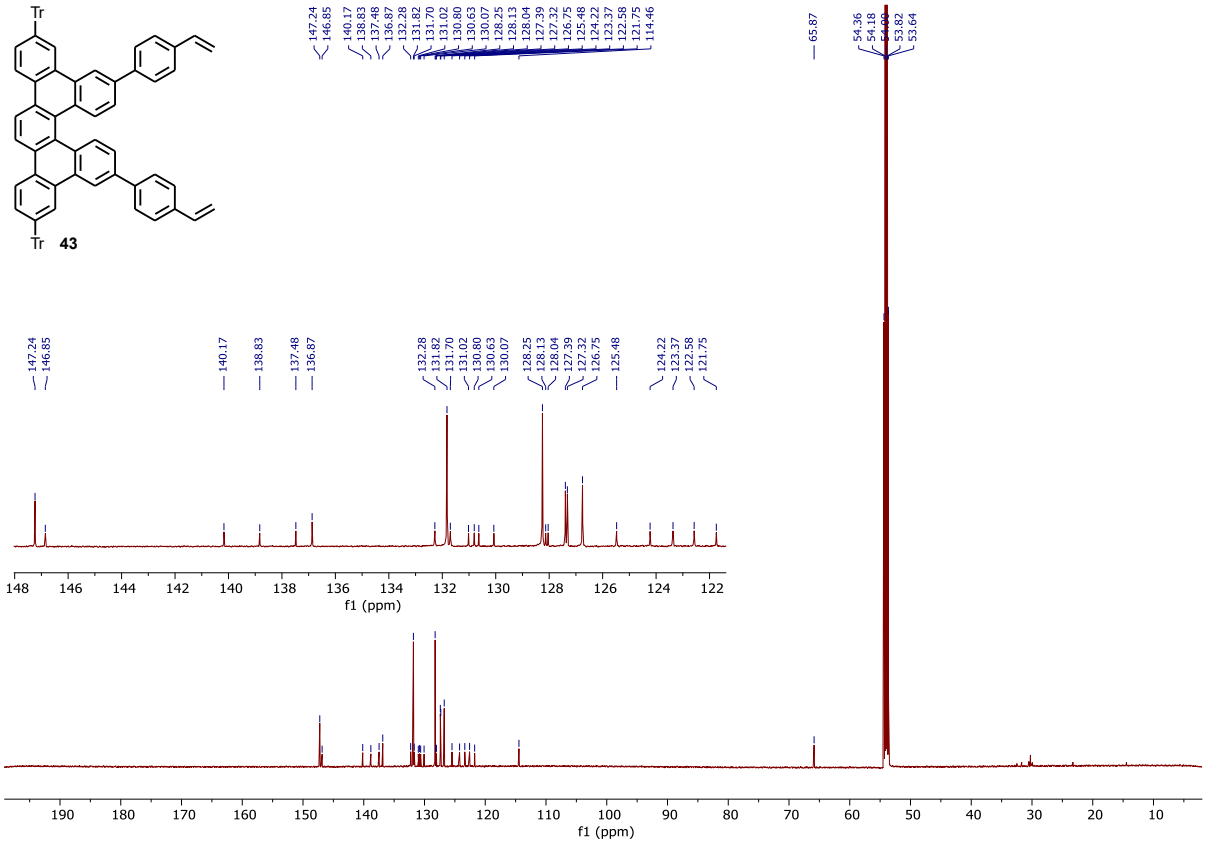
Tr
Tr
43
f1 (ppm)

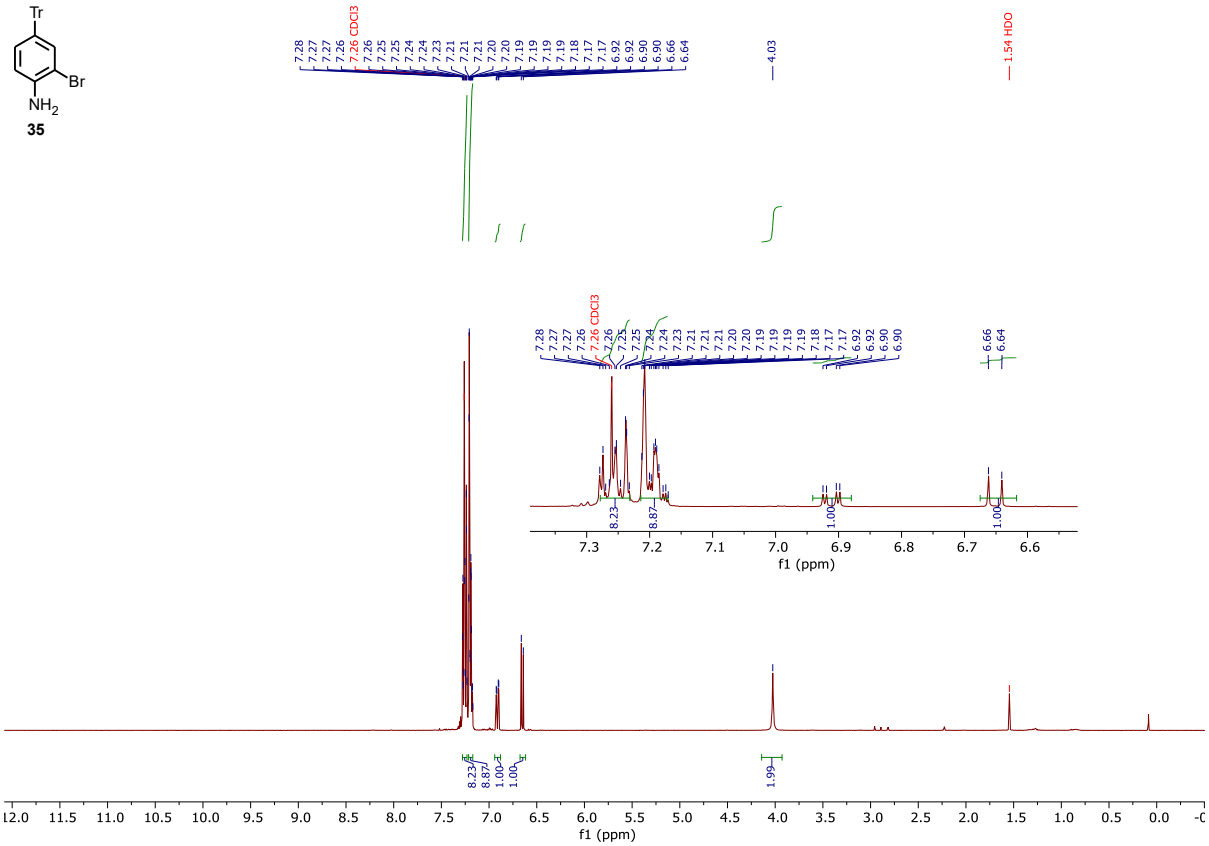
Tr
Br
NH2
35
7.28 7.27 7.27 7.26 7.26 CDCl3 7.26 7.25 7.25 7.24 7.24 7.23 7.21 7.21 7.21 7.20 7.20 7.19 7.19 7.19 7.19 7.18 7.17 7.17 6.92 6.92 6.90 6.90 6.66 6.64
4.03
1.54 HDO
8.23
8.87
1.00
1.00
1.99
f1 (ppm)

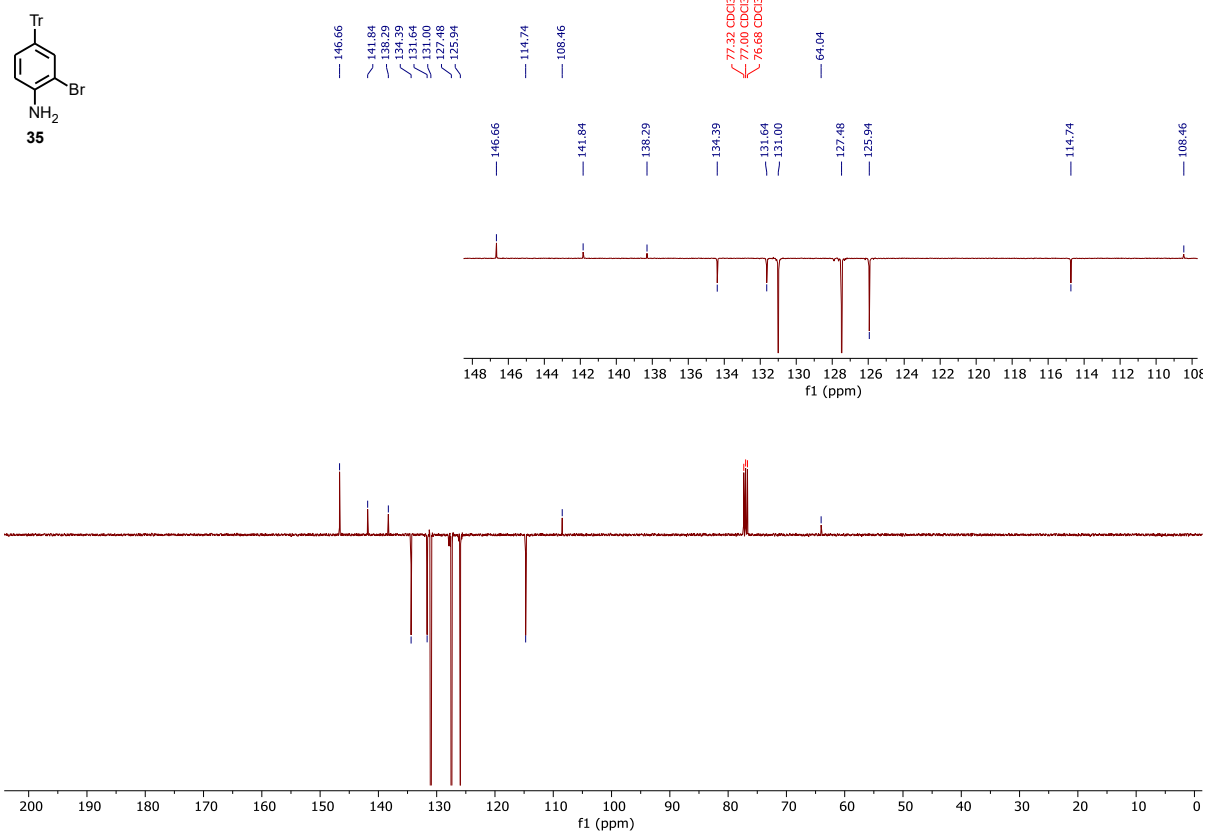
Tr
Br
NH2
35
146.66 141.84 138.29 134.39 131.64 131.00 127.48 125.94 114.74 108.46
77.32 CDCl3 77.00 CDCl3 76.68 CDCl3
64.04
f1 (ppm)

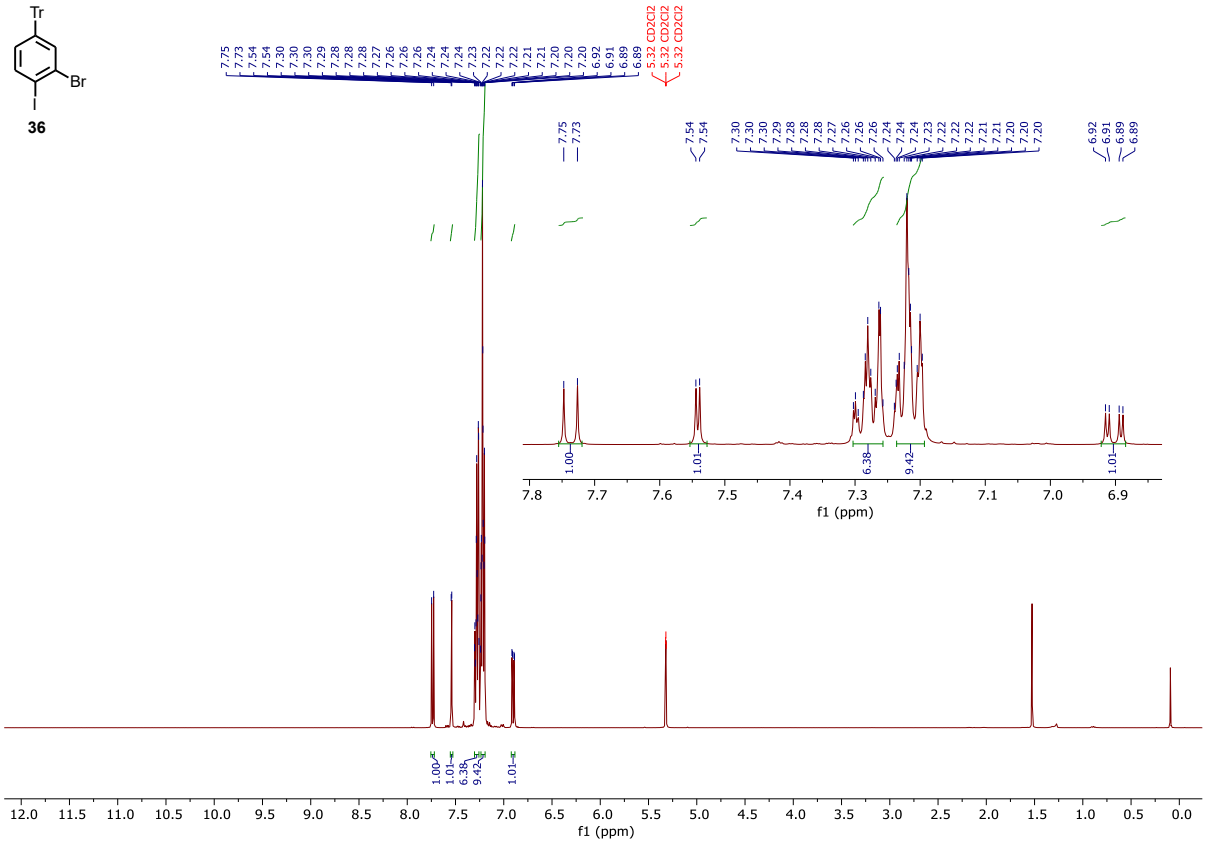
Tr
Br
I
36
f1 (ppm)

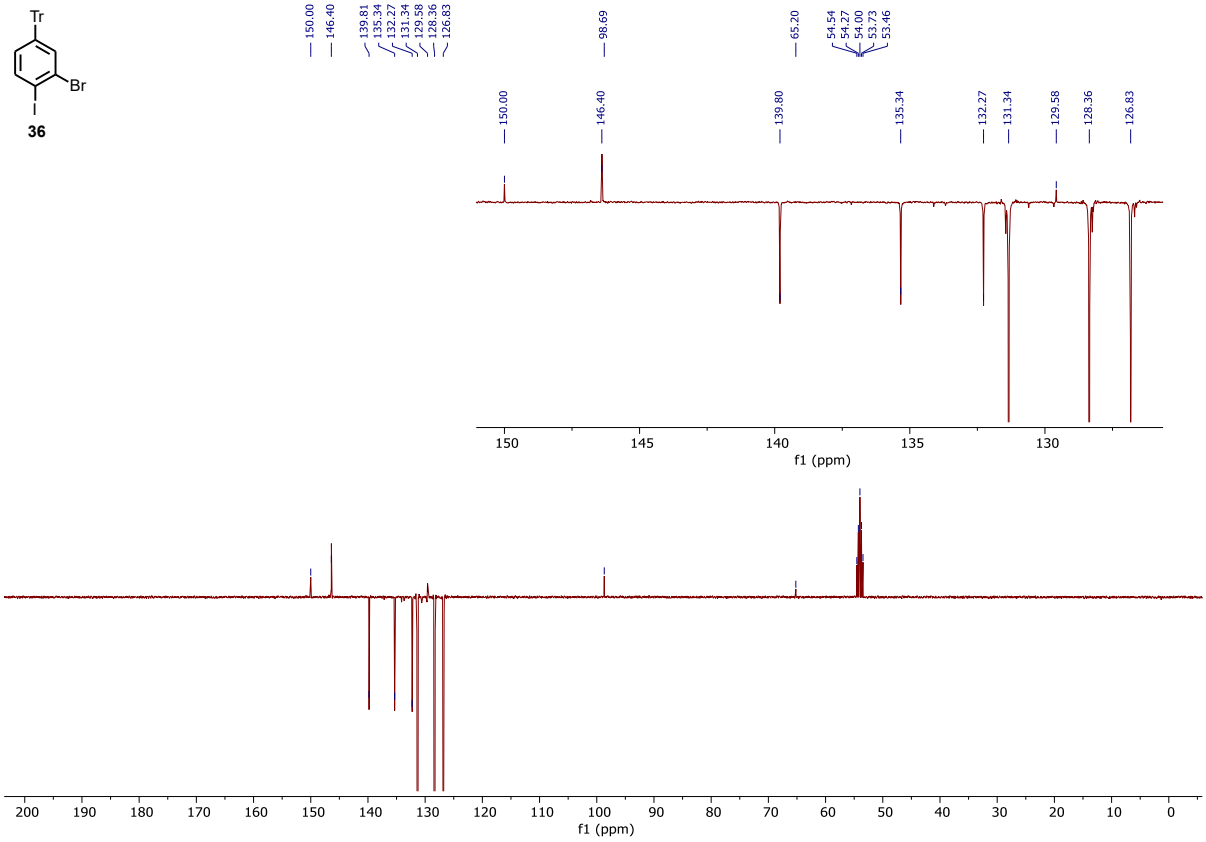
Tr
Br
I
36
f1 (ppm)

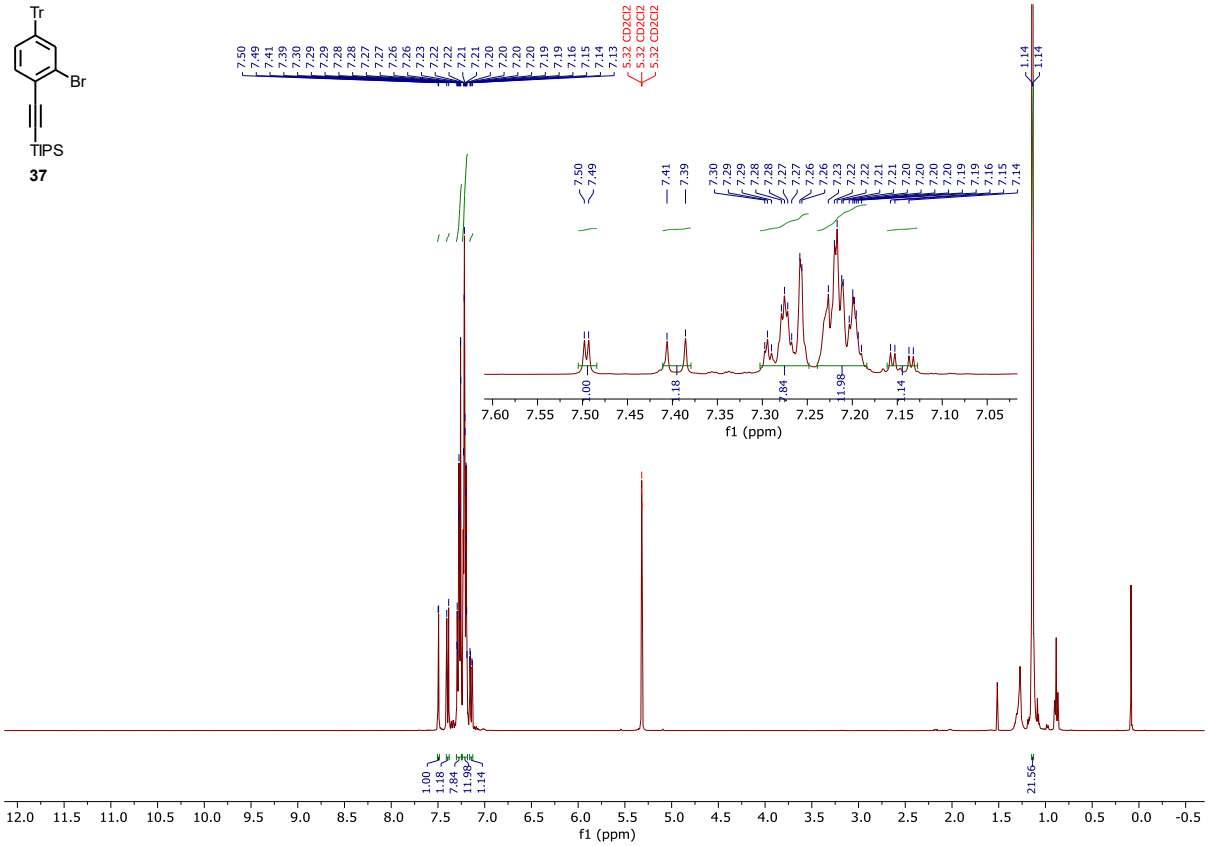
Tr
Br
TIPS
37
f1 (ppm)

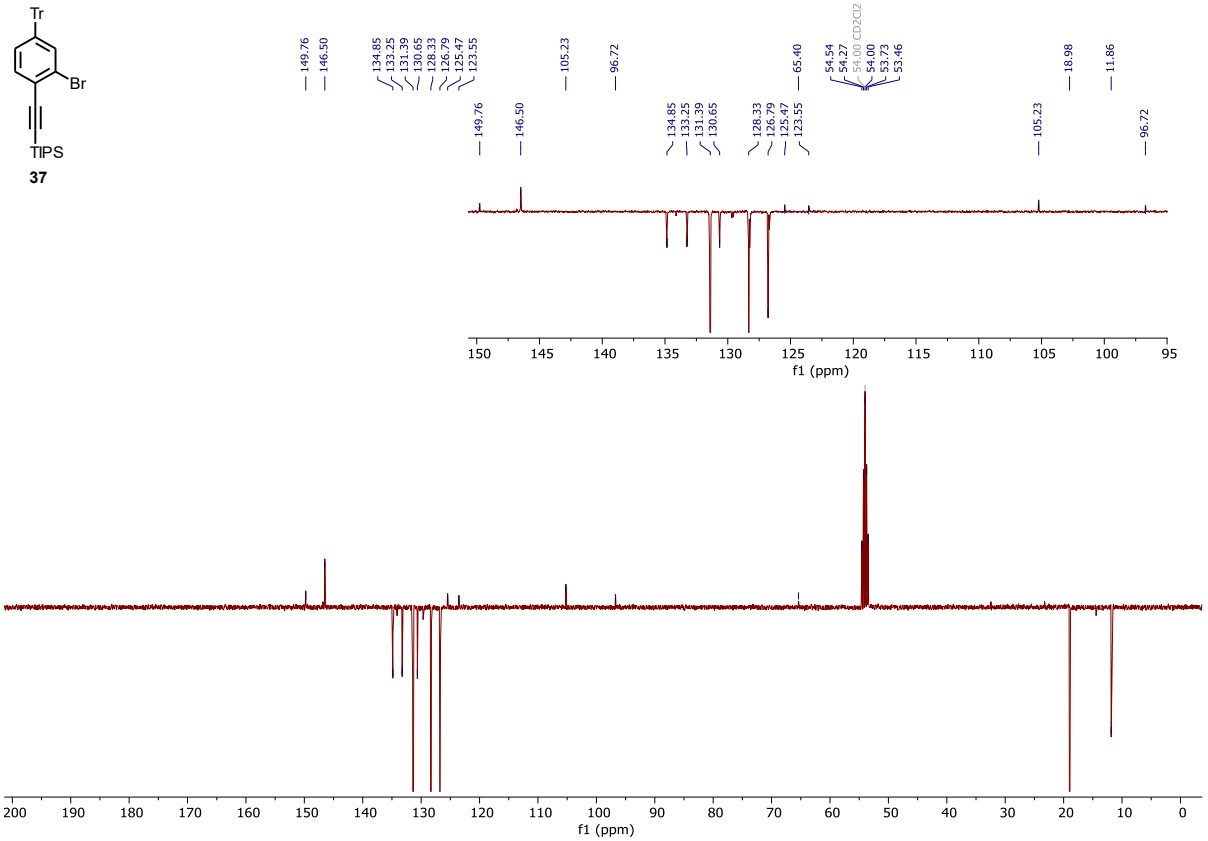
Tr
Br
TIPS
37
f1 (ppm)

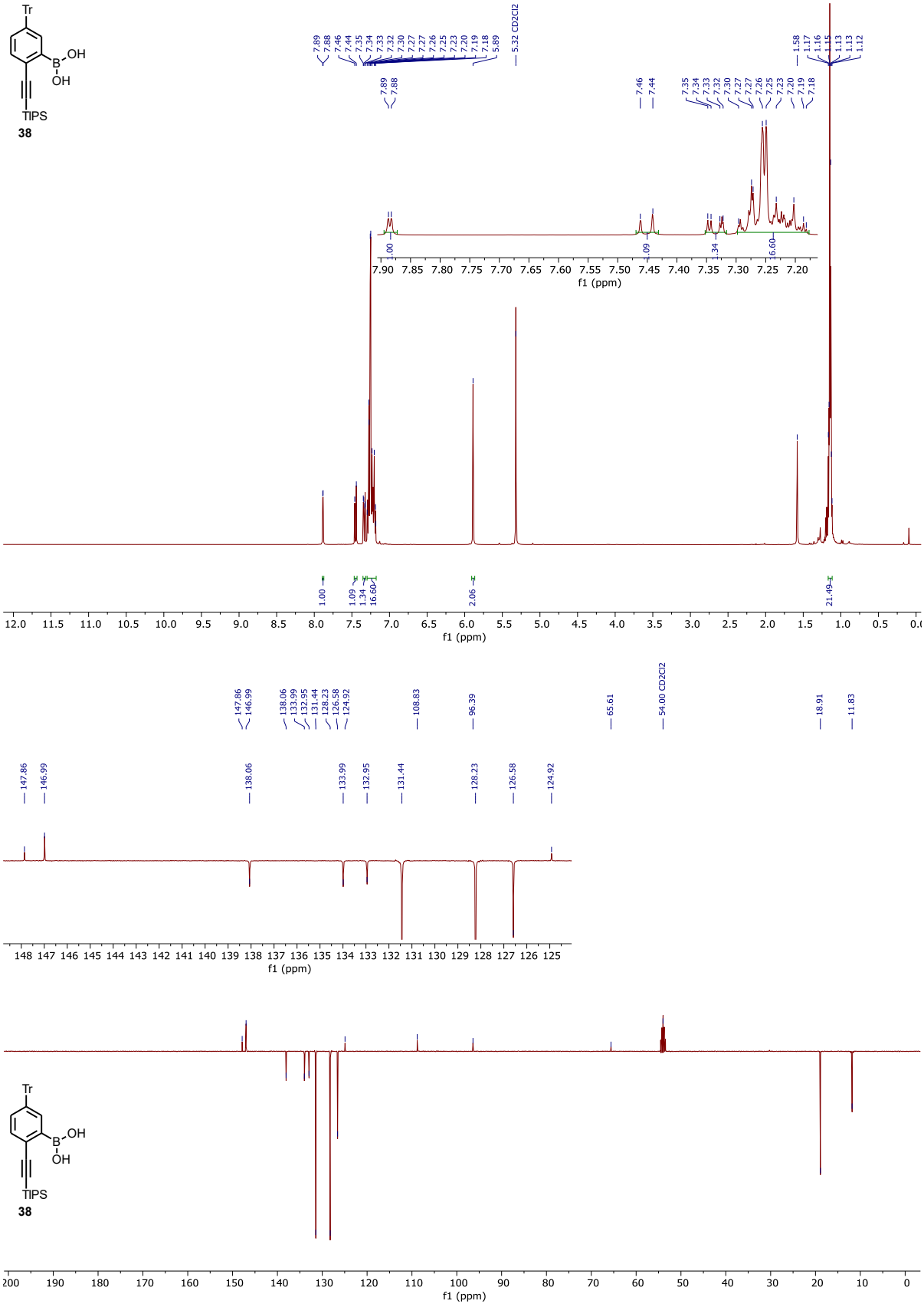
Tr
B
OH
OH
TIPS
38
f1 (ppm)
f1 (ppm)
f1 (ppm)

40

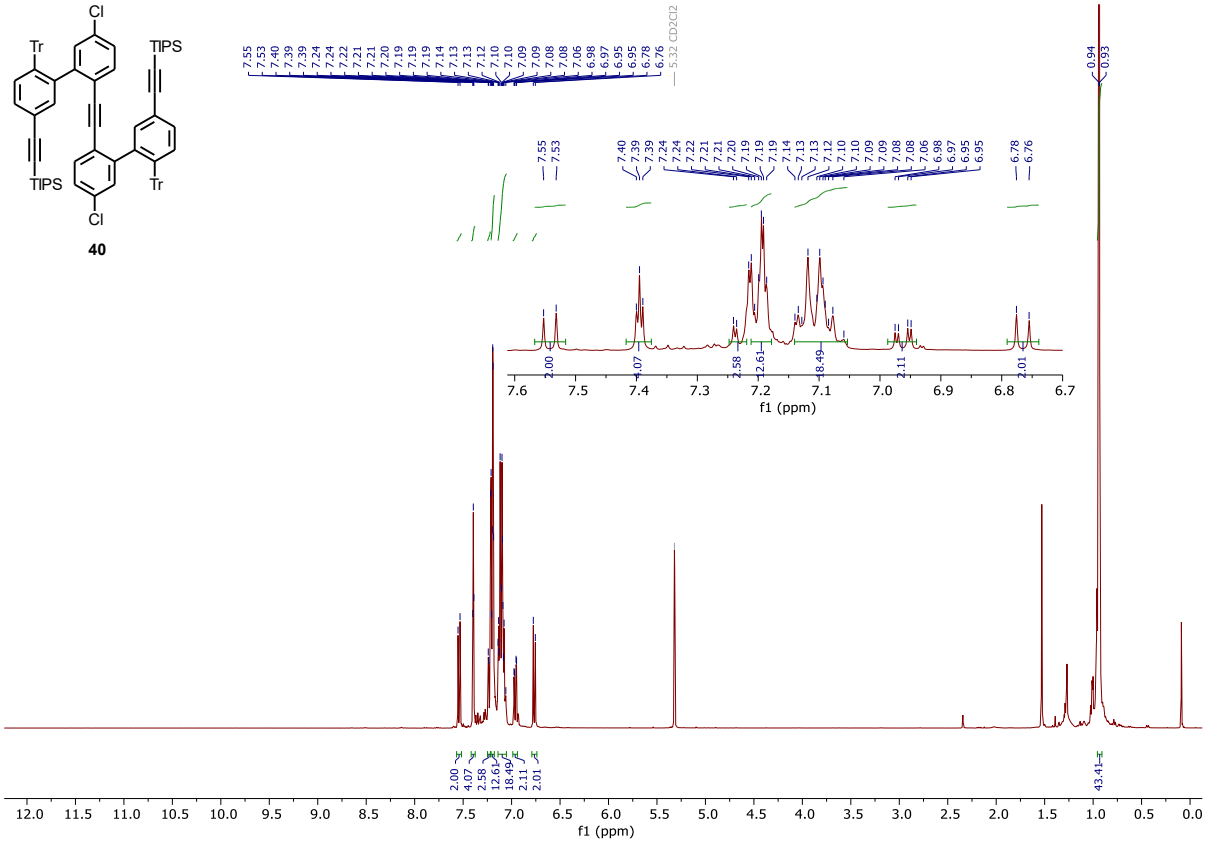

40

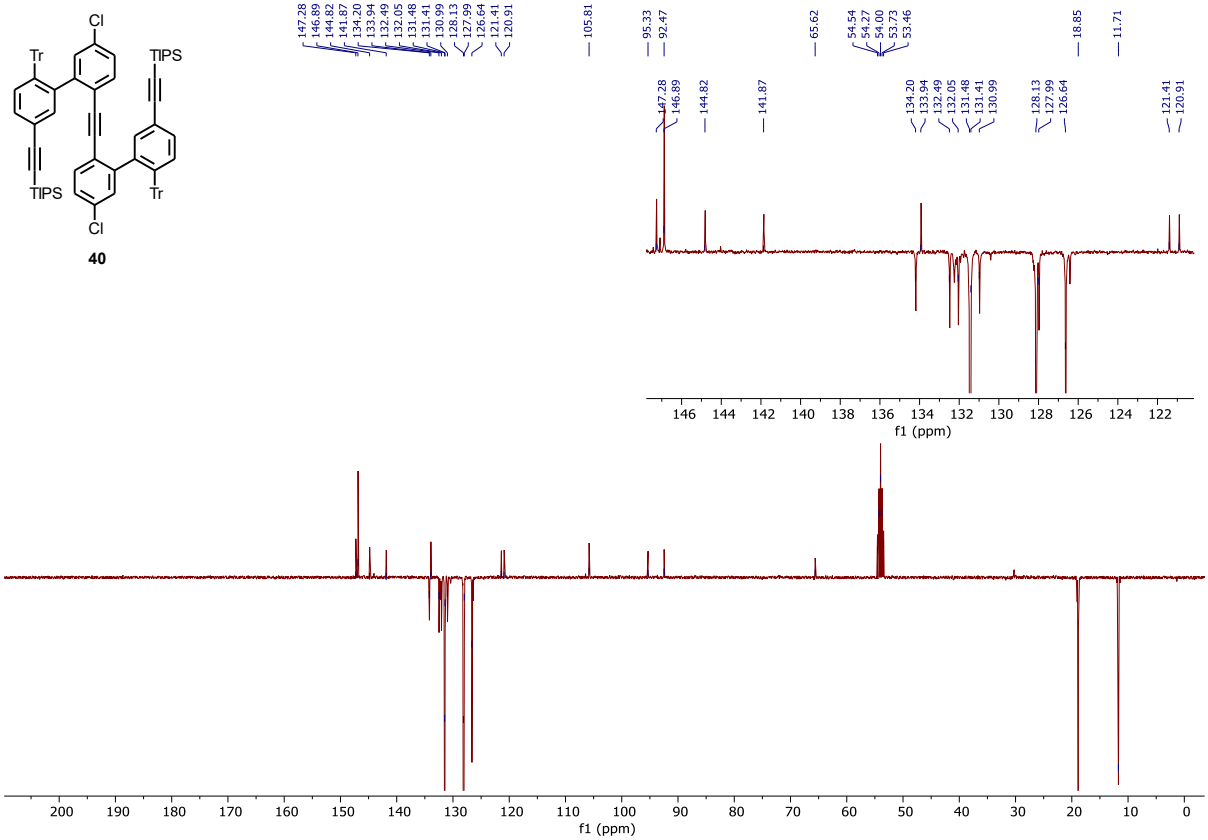

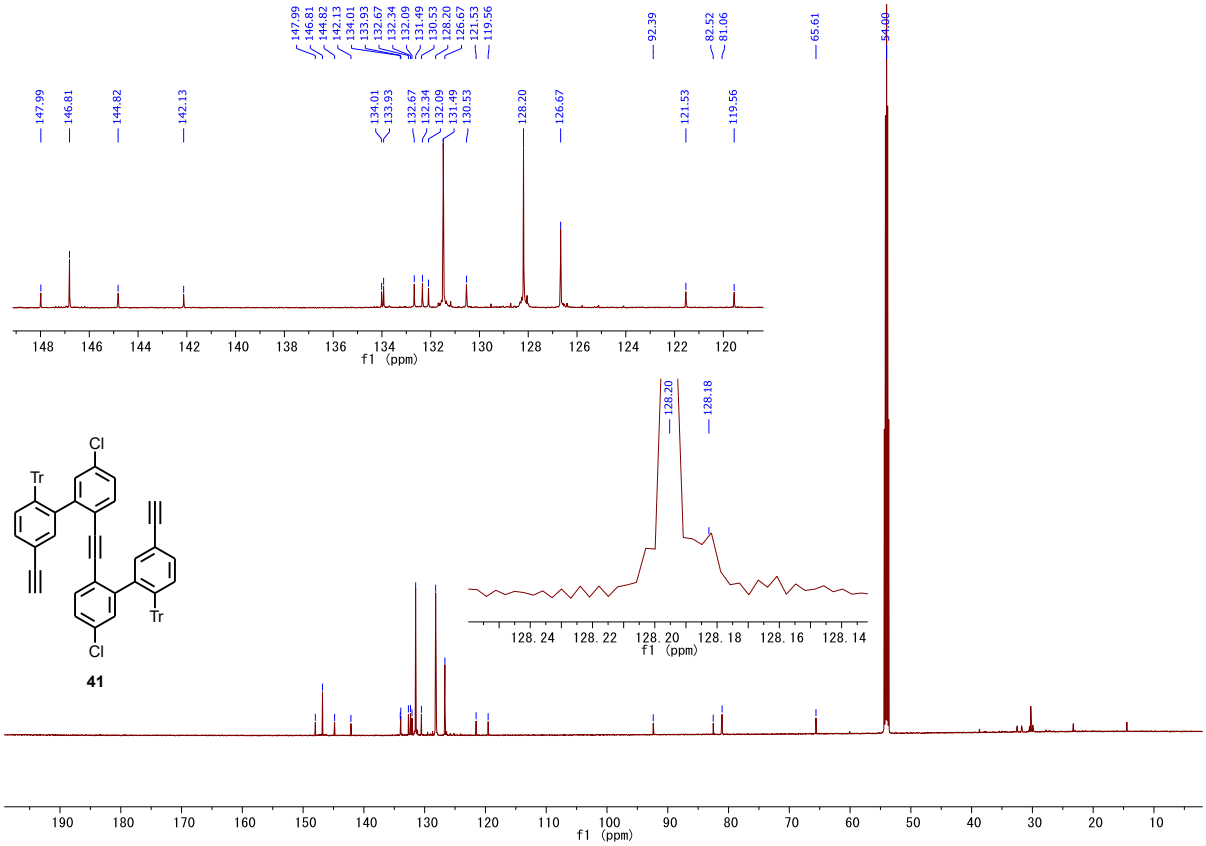
147.99
146.81
144.82
142.13
134.01
133.93
132.67
132.34
132.09
131.49
130.53
128.20
126.67
121.53
119.56
92.39
82.52
81.06
65.61
54.00
f1 (ppm)
128.20
128.18
Cl
Tr
Tr
Cl
41

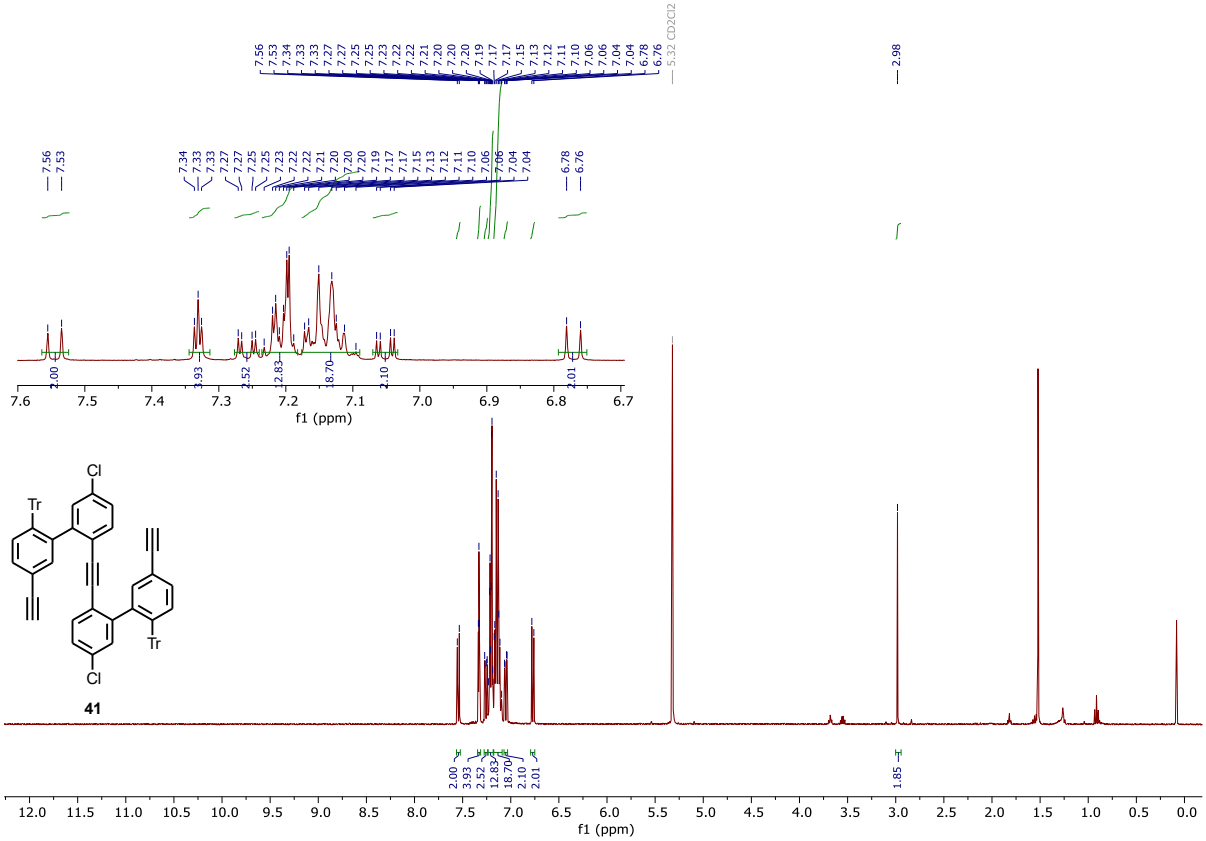
7.56
7.53
7.34
7.33
7.27
7.25
7.23
7.22
7.21
7.20
7.19
7.17
7.15
7.13
7.12
7.11
7.10
7.06
7.04
6.78
6.76
5.32 CD2Cl2
2.98
f1 (ppm)
2.00
3.93
2.52
2.83
18.70
2.10
2.01
1.85
Cl
Tr
Tr
Cl
41

5.17. References

(1) Houska, V.; Ukraintsev, E.; Vacek, J.; Rybáček, J.; Bednárová, L.; Pohl, R.; Stará, I. G.; Rezek, B.; Starý, I. Helicene-Based π-Conjugated Macrocycles: Their Synthesis, Properties, Chirality and Self-Assembly into Molecular Stripes on a Graphite Surface. *Nanoscale* **2023**, *15* (4), 1542–1553. https://doi.org/10.1039/D2NR04209F.

(2) Ukraintsev, E.; Houska, V.; Rezek, B. Small Angle Symmetry Splitting of Helicene-Based Molecular Wires on Pyrolytic Graphite. *Carbon* **2022**, *193*, 171–181. https://doi.org/10.1016/j.carbon.2022.03.013.

(3) Müller, T. J. J.; Bunz, U. H. F. *Functional Organic Materials: Syntheses, Strategies and Applications*; Wiley; Vol. 2007.

(4) Das, S.; Heasman, P.; Ben, T.; Qiu, S. Porous Organic Materials: Strategic Design and Structure–Function Correlation. *Chem. Rev.* **2017**, *117* (3), 1515–1563. https://doi.org/10.1021/acs.chemrev.6b00439.

(5) Höger, S. Shape-Persistent Macrocycles: From Molecules to Materials. *Chem. - Eur. J.* **2004**, *10* (6), 1320–1329. https://doi.org/10.1002/chem.200305496.

(6) Höger, S. Highly Efficient Methods for the Preparation of Shape-Persistent Macrocyclics. *J. Polym. Sci. Part Polym. Chem.* **1999**, *37* (15), 2685–2698. https://doi.org/10.1002/(SICI)1099-0518(19990801)37:15<2685::AID-POLA1>3.0.CO;2-S.

(7) Grave, C.; Schlüter, A. D. Shape-Persistent, Nano-Sized Macrocycles. *Eur. J. Org. Chem.* **2002**, *2002* (18), 3075–3098. https://doi.org/10.1002/1099-0690(200209)2002:18<3075::AID-EJOC3075>3.0.CO;2-3.

(8) Zhang, W.; Moore, J. S. Shape-Persistent Macrocycles: Structures and Synthetic Approaches from Arylene and Ethynylene Building Blocks. *Angew.Chem.Int.Ed.* **2006**, *2006* (45), 4416–4439. https://doi.org/10.1002/anie.200503988.

(9) Iyoda, M.; Yamakawa, J.; Rahman, M. J. Conjugated Macrocycles: Concepts and Applications. *Angew. Chem. Int. Ed.* **2011**, *50* (45), 10522–10553. https://doi.org/10.1002/anie.201006198.

(10) Summerfield, A.; Baldoni, M.; Kondratuk, D. V.; Anderson, H. L.; Whitelam, S.; Garrahan, J. P.; Besley, E.; Beton, P. H. Ordering, Flexibility and Frustration in Arrays of Porphyrin Nanorings. *Nat. Commun.* **2019**, *10* (1), 2932. https://doi.org/10.1038/s41467-019-11009-y.

(11) Meier, H.; Kretzschmann, H.; Kolshorn, H. [Abc]-Annelated [18]Annulenes. *J. Org. Chem.* **1992**, *57* (25), 6847–6852. https://doi.org/10.1021/jo00051a033.

(12) Jin, Y.; Zhang, A.; Huang, Y.; Zhang, W. Shape-Persistent Arylenevinylene Macrocycles (AVMs) Prepared via Acyclic Diene Metathesis Macrocyclization (ADMAC). *Chem. Commun.* **2010**, *46* (43), 8258. https://doi.org/10.1039/c0cc02941f.

(13) Meissner, U. E.; Gensler, A.; Staab, H. A. Benzo[14]Annulene. *Angew. Chem. Int. Ed. Engl.* **1976**, *15* (6), 365–366. https://doi.org/10.1002/anie.197603651.

(14) Meissner, U. E.; Gensler, A.; Staab, H. A. Benzo[18]Annulen. *Tetrahedron Lett.* **1977**, *1977* (1), 3–6. https://doi.org/10.1016/S0040-4039(01)92534-1.

(15) Meier, H.; Müller, K. Synthesis of Belt Cyclophanes. *Angew. Chem. Int. Ed. Engl.* **1995**, *34* (1314), 1437–1439. https://doi.org/10.1002/anie.199514371.

(16) Müller, K.; Meier, H.; Bouas-Laurent, H.; Desvergne, J. P. Belt-Shaped Cyclophanes via Photodimerization of Phenanthro-Condensed [18]Annulenes. *J. Org. Chem.* **1996**, *61* (16), 5474–5480. https://doi.org/10.1021/jo960572v.

(17) Meier, H.; Fetten, M.; Schnorpfeil, C.; Yakimansky, A. V.; Voigt-Martin, I. G. Synthesis and Photodimerisation of Tetrabenzo[Ab,f,Jk,o][18]Annulenes. *Tetrahedron Lett.* **1999**, *40* (26), 4791–4794. https://doi.org/10.1016/S0040-4039(99)00876-X.

(18) Yu, R.; Yakimansky, A.; Voigt-Martin, I. G.; Fetten, M.; Schnorpfeil, C.; Schollmeyer, D.; Meier, H. Tetrabenzo[Ab, f, Jk,o][18]Annulene: Synthesis, Crystal Structure Analysis, Ab Initio Quantum-Chemical Studies of Intermolecular Interactions in the Gas Phase and in Crystalline States, Photodimerization and Photopolymerization. *J. Chem. Soc. Perkin Trans. 2* **1999**, No. 9, 1881–1890. https://doi.org/10.1039/a903451j.

(19) Schnorpfeil, C.; Meier, H.; Irie, M. Aggregation and Photodimerization of Areno-Condensed Annulenes. *Helv. Chim. Acta 2001* (84), 2467–2475.

(20) Meier, H.; Fetten, M. A New Synthetic Route to Tribenzo[a,e,i][12]Annulenes. *Tetrahedron Lett. 2000* (41), 1535–1538. https://doi.org/10.1016/S0040-4039(99)02346-1.

(21) Liu, C.; Park, E.; Jin, Y.; Liu, J.; Yu, Y.; Zhang, W.; Lei, S.; Hu, W. Surface-Confined Dynamic Covalent System Driven by Olefin Metathesis. *Angew. Chem. Int. Ed.* **2018**, *57* (7), 1869–1873. https://doi.org/10.1002/anie.201711040.

(22) Liu, C.; Park, E.; Jin, Y.; Liu, J.; Yu, Y.; Zhang, W.; Lei, S.; Hu, W. Separation of Arylenevinylene Macrocycles with a Surface-Confined Two-Dimensional Covalent Organic Framework. *Angew.Chem.Int.Ed.* **2018**, *2018* (57), 8984–8988. https://doi.org/10.1002/anie.201803937.

(23) Lee, C. W.; Grubbs, R. H. Formation of Macrocycles *via* Ring-Closing Olefin Metathesis. *J. Org. Chem.* **2001**, *66* (21), 7155–7158. https://doi.org/10.1021/jo0158480.

(24) Zhang, C.; Yu, C.; Long, H.; Denman, R. J.; Jin, Y.; Zhang, W. Synthesis of Phenylene Vinylene Macrocycles through Acyclic Diene Metathesis Macrocyclization and Their Aggregation Behavior. *Chem. - Eur. J.* **2015**, *21* (47), 16935–16940. https://doi.org/10.1002/chem.201502848.

(25) Grimme, S. Do Special Noncovalent π–π Stacking Interactions Really Exist? *Angew. Chem. Int. Ed.* **2008**, *47* (18), 3430–3434. https://doi.org/10.1002/anie.200705157.

(26) Kuwatani, Y.; Igarashi, J.; Iyoda, M. All-Z-Hexabenzo[24]Annulene with a Triangular Benzene Cluster Substructure. *Tetrahedron Lett.* **2004**, *45* (2), 359–362. https://doi.org/10.1016/j.tetlet.2003.10.163.

(27) Sirinintasak, S.; Kuwatani, Y.; Hoshi, S.; Isomura, E.; Nishinaga, T.; Iyoda, M. Short-Step Syntheses and Complexation Properties of Z,Z-Tribenzodidehydro- and All-Z-Tribenzo[12]Annulenes. *Tetrahedron Lett.* **2007**, *48* (19), 3433–3436. https://doi.org/10.1016/j.tetlet.2007.03.044.

(28) Mohebbi, A. R.; Mucke, E.-K.; Schaller, G. R.; Köhler, F.; Sönnichsen, F. D.; Ernst, L.; Näther, C.; Herges, R. Singly and Doubly Twisted [36]Annulenes: Synthesis and Calculations. *Chem. - Eur. J.* **2010**, *16* (26), 7767–7772. https://doi.org/10.1002/chem.201000277.

(29) Kirinda, V. C.; Schrage, B. R.; Ziegler, C. J.; Hartley, C. S. *Ortho* -Phenylene-Based Macrocyclic Hydrocarbons Assembled Using Olefin Metathesis. *Eur. J. Org. Chem.* **2020**, *2020* (34), 5620–5625. https://doi.org/10.1002/ejoc.202000950.

(30) Kelvin, Lord. *Baltimore Lectures on Molecular Dynamics and the Wave Theory of Light.*; CJ Clay & Sons: London, 1904.

(31) Petitjean, M. Chirality and Symmetry Measures: A Transdisciplinary Review. *Entropy* **2003**, *5* (3), 271–312. https://doi.org/10.3390/e5030271.

(32) Weissbuch, I.; Lahav, M. Crystalline Architectures as Templates of Relevance to the Origins of Homochirality. *Chem. Rev.* **2011**, *111* (5), 3236–3267. https://doi.org/10.1021/cr1002479.

(33) TANEDO, F. *Helicity, Chirality, Mass, and the Higgs*. http://www.quantumdiaries.org/2011/06/19/helicity-chirality-mass-and-the-higgs/.

(34) Evers, F.; Aharony, A.; Bar-Gill, N.; Entin-Wohlman, O.; Hedegård, P.; Hod, O.; Jelinek, P.; Kamieniarz, G.; Lemeshko, M.; Michaeli, K.; Mujica, V.; Naaman, R.; Paltiel, Y.; Refaely-Abramson, S.; Tal, O.; Thijssen, J.; Thoss, M.; van Ruitenbeek, J. M.; Venkataraman, L.; Waldeck, D. H.; Yan, B.; Kronik, L. Theory of Chirality Induced Spin Selectivity: Progress and Challenges. *Adv. Mater.* **2022**, *34* (13), 2106629. https://doi.org/10.1002/adma.202106629.

(35) Shen, Y.; Chen, C.-F. Helicenes: Synthesis and Applications. *Chem. Rev.* **2012**, *112* (3), 1463–1535. https://doi.org/10.1021/cr200087r.

(36) Furche, F.; Ahlrichs, R.; Wachsmann, C.; Weber, E.; Sobanski, A.; Vögtle, F.; Grimme, S. Circular Dichroism of Helicenes Investigated by Time-Dependent Density Functional Theory. *J. Am. Chem. Soc.* **2000**, *122* (8), 1717–1724. https://doi.org/10.1021/ja991960s.

(37) Zhao, W.-L.; Li, M.; Lu, H.-Y.; Chen, C.-F. Advances in Helicene Derivatives with Circularly Polarized Luminescence. *Chem. Commun.* **2019**, *55* (92), 13793–13803. https://doi.org/10.1039/C9CC06861A.

(38) Arrico, L.; Di Bari, L.; Zinna, F. Quantifying the Overall Efficiency of Circularly Polarized Emitters. *Chem. – Eur. J.* **2021**, *27* (9), 2920–2934. https://doi.org/10.1002/chem.202002791.

(39) Kiran, V.; Mathew, S. P.; Cohen, S. R.; Hernández Delgado, I.; Lacour, J.; Naaman, R. Helicenes-A New Class of Organic Spin Filter. *Adv. Mater.* **2016**, *28* (10), 1957–1962. https://doi.org/10.1002/adma.201504725.

(40) Matxain, J. M.; Ugalde, J. M.; Mujica, V.; Allec, S. I.; Wong, B. M.; Casanova, D. Chirality Induced Spin Selectivity of Photoexcited Electrons in Carbon-Sulfur [*n*]Helicenes. *ChemPhotoChem* **2019**, *3* (9), 770–777. https://doi.org/10.1002/cptc.201900128.

(41) Aillard, P.; Voituriez, A.; Marinetti, A. Helicene-like Chiral Auxiliaries in Asymmetric Catalysis. *Dalton Trans.* **2014**, *43* (41), 15263–15278. https://doi.org/10.1039/C4DT01935K.

(42) Gingras, M. One Hundred Years of Helicene Chemistry. Part 3: Applications and Properties of Carbohelicenes. *Chem Soc Rev* **2013**, *42* (3), 1051–1095. https://doi.org/10.1039/C2CS35134J.

(43) Nakamura, K.; Okubo, H.; Yamaguchi, M. Synthesis and Self-Aggregation of Cyclic Alkynes Containing Helicene. *Org. Lett.* **2001**, *3* (8), 1097–1099. https://doi.org/10.1021/ol015550w.

(44) Takahira, Y.; Sugiura, H.; Yamaguchi, M. Synthesis and Ring Size Effect of Macrocyclic Ethynylhelicene Oligomers. *J. Org. Chem.* **2006**, *71* (2), 763–767. https://doi.org/10.1021/jo0521549.

(45) Robert, A.; Dechambenoit, P.; Hillard, E. A.; Bock, H.; Durola, F. Non-Planar Oligoarylene Macrocycles from Biphenyl. *Chem Commun* **2017**, *53* (84), 11540–11543. https://doi.org/10.1039/C7CC06798D.

(46) Naulet, G.; Sturm, L.; Robert, A.; Dechambenoit, P.; Röhricht, F.; Herges, R.; Bock, H.; Durola, F. Cyclic Tris-[5]Helicenes with Single and Triple Twisted Möbius Topologies and Möbius Aromaticity. *Chem. Sci.* **2018**, *9* (48), 8930–8936. https://doi.org/10.1039/C8SC02877J.

(47) Herges, R.; Geuenich, D. Delocalization of Electrons in Molecules †. *J. Phys. Chem. A* **2001**, *105* (13), 3214–3220. https://doi.org/10.1021/jp0034426.

(48) Geuenich, D.; Hess, K.; Köhler, F.; Herges, R. Anisotropy of the Induced Current Density (ACID), a General Method To Quantify and Visualize Electronic Delocalization. *Chem. Rev.* **2005**, *105* (10), 3758–3772. https://doi.org/10.1021/cr0300901.

(49) Schleyer, P. von R.; Maerker, C.; Dransfeld, A.; Jiao, H.; van Eikema Hommes, N. J. R. Nucleus-Independent Chemical Shifts: A Simple and Efficient Aromaticity Probe. *J. Am. Chem. Soc.* **1996**, *118* (26), 6317–6318. https://doi.org/10.1021/ja960582d.

(50) Chen, Z.; Wannere, C. S.; Corminboeuf, C.; Puchta, R. Nucleus-Independent Chemical Shifts (NICS) as an Aromaticity Criterion. 47.

(51) Kruszewski, J.; Krygowski, T. M. Definition of Aromaticity Basing on the Harmonic Oscillator Model. *Tetrahedron Lett.* **1972**, *13* (36), 3839–3842. https://doi.org/10.1016/S0040-4039(01)94175-9.

(52) Krygowski, T. M.; Szatylowicz, H.; Stasyuk, O. A.; Dominikowska, J.; Palusiak, M. Aromaticity from the Viewpoint of Molecular Geometry: Application to Planar Systems. *Chem. Rev.* **2014**, *114* (12), 6383–6422. https://doi.org/10.1021/cr400252h.

(53) Jiang, X.; Laffoon, S. D.; Chen, D.; Pérez-Estrada, S.; Danis, A. S.; Rodríguez-López, J.; Garcia-Garibay, M. A.; Zhu, J.; Moore, J. S. Kinetic Control in the Synthesis of a Möbius Tris((Ethynyl)[5]Helicene) Macrocycle Using Alkyne Metathesis. *J. Am. Chem. Soc.* **2020**, *142* (14), 6493–6498. https://doi.org/10.1021/jacs.0c01430.

(54) Fan, W.; Matsuno, T.; Han, Y.; Wang, X.; Zhou, Q.; Isobe, H.; Wu, J. Synthesis and Chiral Resolution of Twisted Carbon Nanobelts. *J. Am. Chem. Soc.* **2021**, *143* (39), 15924–15929. https://doi.org/10.1021/jacs.1c08468.

(55) Malinčík, J.; Gaikwad, S.; Mora-Fuentes, J. P.; Boillat, M.-A.; Prescimone, A.; Häussinger, D.; Campaña, A. G.; Šolomek, T. Circularly Polarized Luminescence in a Möbius Helicene Carbon Nanohoop**. *Angew. Chem. Int. Ed.* **2022**, *61* (37), e202208591. https://doi.org/10.1002/anie.202208591.

(56) Jasti, R.; Bhattacharjee, J.; Neaton, J. B.; Bertozzi, C. R. Synthesis, Characterization, and Theory of [9]-, [12]-, and [18]Cycloparaphenylene: Carbon Nanohoop Structures. *J. Am. Chem. Soc.* **2008**, *130* (52), 17646–17647. https://doi.org/10.1021/ja807126u.

(57) Kiel, G. R.; Bay, K. L.; Samkian, A. E.; Schuster, N. J.; Lin, J. B.; Handford, R. C.; Nuckolls, C.; Houk, K. N.; Tilley, T. D. Expanded Helicenes as Synthons for Chiral Macrocyclic Nanocarbons. *J. Am. Chem. Soc.* **2020**, *142* (25), 11084–11091. https://doi.org/10.1021/jacs.0c03177.

(58) Binnig, G.; Rohrer, H.; Gerber, Ch.; Weibel, E. Surface Studies by Scanning Tunneling Microscopy. *Phys. Rev. Lett.* **1982**, *49* (1), 57–61. https://doi.org/10.1103/PhysRevLett.49.57.

(59) Binnig, G.; Quate, C. F.; Gerber, Ch. Atomic Force Microscope. *Phys. Rev. Lett.* **1986**, *56* (9), 930–933. https://doi.org/10.1103/PhysRevLett.56.930.

(60) Emmrich, M.; Huber, F.; Pielmeier, F.; Welker, J.; Hofmann, T.; Schneiderbauer, M.; Meuer, D.; Polesya, S.; Mankovsky, S.; Ködderitzsch, D.; Ebert, H.; Giessibl, F. J. Subatomic Resolution Force Microscopy Reveals Internal Structure and Adsorption Sites of Small Iron Clusters. *Science* **2015**, *348* (6232), 308–311. https://doi.org/10.1126/science.aaa5329.

(61) Chaika, A. N.; Nazin, S. S.; Semenov, V. N.; Bozhko, S. I.; Lübben, O.; Krasnikov, S. A.; Radican, K.; Shvets, I. V. Selecting the Tip Electron Orbital for Scanning Tunneling Microscopy Imaging with Sub-Ångström Lateral Resolution. *Europhys. Lett.* **2010**, *92* (4), 46003. https://doi.org/10.1209/0295-5075/92/46003.

(62) Jelínek, P. High Resolution SPM Imaging of Organic Molecules with Functionalized Tips. *J. Phys. Condens. Matter* **2017**, *29* (34), 343002. https://doi.org/10.1088/1361-648X/aa76c7.

(63) Palma, C.-A.; Bjork, J.; Bonini, M.; Dyer, M. S.; Llanes-Pallas, A.; Bonifazi, D.; Persson, M.; Samorì, P. Tailoring Bicomponent Supramolecular Nanoporous Networks: Phase Segregation, Polymorphism, and Glasses at the Solid−Liquid Interface. *J. Am. Chem. Soc.* **2009**, *131* (36), 13062–13071. https://doi.org/10.1021/ja9032428.

(64) Lei, S.; Tahara, K.; De Schryver, F. C.; Van der Auweraer, M.; Tobe, Y.; De Feyter, S. One Building Block, Two Different Supramolecular Surface-Confined Patterns: Concentration in Control at the Solid–Liquid Interface. *Angew. Chem.* **2008**, *120* (16), 3006–3010. https://doi.org/10.1002/ange.200705322.

(65) Bellec, A.; Arrigoni, C.; Schull, G.; Douillard, L.; Fiorini-Debuisschert, C.; Mathevet, F.; Kreher, D.; Attias, A.-J.; Charra, F. Solution-Growth Kinetics and Thermodynamics of Nanoporous Self-Assembled Molecular Monolayers. *J. Chem. Phys.* **2011**, *134* (12), 124702. https://doi.org/10.1063/1.3569132.

(66) Gutzler, R.; Sirtl, T.; Dienstmaier, J. F.; Mahata, K.; Heckl, W. M.; Schmittel, M.; Lackinger, M. Reversible Phase Transitions in Self-Assembled Monolayers at the Liquid−Solid Interface: Temperature-Controlled Opening and Closing of Nanopores. *J. Am. Chem. Soc.* **2010**, *132* (14), 5084–5090. https://doi.org/10.1021/ja908919r.

(67) Piot, L.; Marchenko, A.; Wu, J.; Müllen, K.; Fichou, D. Structural Evolution of Hexa- *p Eri* -Hexabenzocoronene Adlayers in Heteroepitaxy on *n* -Pentacontane Template Monolayers. *J. Am. Chem. Soc.* **2005**, *127* (46), 16245–16250. https://doi.org/10.1021/ja0548844.

(68) Marie, C.; Silly, F.; Tortech, L.; Müllen, K.; Fichou, D. Tuning the Packing Density of 2D Supramolecular Self-Assemblies at the Solid−Liquid Interface Using Variable Temperature. *ACS Nano* **2010**, *4* (3), 1288–1292. https://doi.org/10.1021/nn901717k.

(69) Ahn, S.; Matzger, A. J. Six Different Assemblies from One Building Block: Two-Dimensional Crystallization of an Amide Amphiphile. *J. Am. Chem. Soc.* **2010**, *132* (32), 11364–11371. https://doi.org/10.1021/ja105039s.

(70) Nath, K. G.; Ivasenko, O.; Miwa, J. A.; Dang, H.; Wuest, J. D.; Nanci, A.; Perepichka, D. F.; Rosei, F. Rational Modulation of the Periodicity in Linear Hydrogen-Bonded Assemblies of Trimesic Acid on Surfaces. *J. Am. Chem. Soc.* **2006**, *128* (13), 4212–4213. https://doi.org/10.1021/ja0602896.

(71) Baker, R. T.; Mougous, J. D.; Brackley, A.; Patrick, D. L. Competitive Adsorption, Phase Segregation, and Molecular Motion at a Solid−Liquid Interface Studied by Scanning Tunneling Microscopy. *Langmuir* **1999**, *15* (14), 4884–4891. https://doi.org/10.1021/la981658h.

(72) Florio, G. M.; Klare, J. E.; Pasamba, M. O.; Werblowsky, T. L.; Hyers, M.; Berne, B. J.; Hybertsen, M. S.; Nuckolls, C.; Flynn, G. W. Frustrated Ostwald Ripening in Self-Assembled Monolayers of Cruciform π-Systems. *Langmuir* **2006**, *22* (24), 10003–10008. https://doi.org/10.1021/la0617199.

(73) Samorí, P.; Müllen, K.; Rabe, J. P. Molecular-Scale Tracking of the Self-Healing of Polycrystalline Monolayers at the Solid–Liquid Interface. *Adv. Mater.* **2004**, *16* (19), 1761–1765. https://doi.org/10.1002/adma.200400132.

(74) Hooks, D. E.; Fritz, T.; Ward, M. D. Epitaxy and Molecular Organization on Solid Substrates. *Adv. Mater.* **2001**, *13* (4), 227–241. https://doi.org/10.1002/1521-4095(200102)13:4<227::AID-ADMA227>3.0.CO;2-P.

(75) Bai, C. *Scanning Tunneling Microscopy and Its Application*, 2nd rev. ed.; Springer series in surface sciences; Springer: Berlin ; New York, 2000.

(76) Libioulle, L.; Houbion, Y.; Gilles, J. -M. Very Sharp Platinum Tips for Scanning Tunneling Microscopy. *Rev. Sci. Instrum.* **1995**, *66* (1), 97–100. https://doi.org/10.1063/1.1146153.

(77) So/rensen, A. H.; Hvid, U.; Mortensen, M. W.; Mo/rch, K. A. Preparation of Platinum/Iridium Scanning Probe Microscopy Tips. *Rev. Sci. Instrum.* **1999**, *70* (7), 3059–3067. https://doi.org/10.1063/1.1149891.

(78) Tahara, K.; Balandina, T.; Furukawa, S.; Feyter, D. S.; Tobe, Y. Molecular Pentagonal Tiling- Self-Assemblies of Pentagonal-Shaped Macrocycles at Liquid-Solid Interfaces. *CrystEngComm* **2011**, *13* (18), 5551–5558. https://doi.org/10.1039/c1ce05336a.

(79) Vollmeyer, J.; Eberhagen, F.; Höger, S.; Jester, S.-S. Self-Assembled Monolayers of Shape-Persistent Macrocycles on Graphite: Interior Design and Conformational Polymorphism. *Beilstein J. Org. Chem.* **2014**, *10*, 2774–2782. https://doi.org/10.3762/bjoc.10.294.

(80) Girard, C.; Joachim, C.; Chavy, C.; Sautet, P. The Electric Field under a STM Tip Apex: Implications for Adsorbate Manipulation. *Surf. Sci.* **1993**, *282* (3), 400–410. https://doi.org/10.1016/0039-6028(93)90944-F.

(81) Idelson, A.; Sterzenbach, C.; Jester, S.-S.; Tschierske, C.; Baumeister, U.; Höger, S. A Liquid-Crystalline Phenylene-Based Shape-Persistent Molecular Spoked Wheel. *J. Am. Chem. Soc.* **2017**, *139* (12), 4429–4434. https://doi.org/10.1021/jacs.6b13020.

(82) MacLeod, J. M.; Lipton-Duffin, J. A.; Cui, D.; De Feyter, S.; Rosei, F. Substrate Effects in the Supramolecular Assembly of 1,3,5-Benzene Tricarboxylic Acid on Graphite and Graphene. *Langmuir* **2015**, *31* (25), 7016–7024. https://doi.org/10.1021/la5048886.

(83) Miao, X.; Xu, L.; Li, Z.; Deng, W. Solvent-Induced Structural Transitions of a 1,3,5-Tris(10-Ethoxycarbonyldecyloxy)Benzene Assembly Revealed by Scanning Tunneling Microscopy. *J. Phys. Chem. C* **2011**, *115* (8), 3358–3367. https://doi.org/10.1021/jp109686n.

(84) De Feyter, S.; De Schryver, F. C. Self-Assembly at the Liquid/Solid Interface: STM Reveals. *J. Phys. Chem. B* **2005**, *109* (10), 4290–4302. https://doi.org/10.1021/jp045298k.

(85) Li, B.; Tahara, K.; Adisoejoso, J.; Vanderlinden, W.; Mali, K. S.; De Gendt, S.; Tobe, Y.; De Feyter, S. Self-Assembled Air-Stable Supramolecular Porous Networks on Graphene. *ACS Nano* **2013**, *7* (12), 10764–10772. https://doi.org/10.1021/nn4039047.

(86) Das, S.; Nascimbeni, G.; de la Morena, R. O.; Ishiwari, F.; Shoji, Y.; Fukushima, T.; Buck, M.; Zojer, E.; Zharnikov, M. Porous Honeycomb Self-Assembled Monolayers: Tripodal Adsorption and Hidden Chirality of Carboxylate Anchored Triptycenes on Ag. *ACS Nano* **2021**, *15* (7), 11168–11179. https://doi.org/10.1021/acsnano.1c03626.

(87) Bucher, J.-P.; Santesson, L.; Kern, K. Thermal Healing of Self-Assembled Organic Monolayers: Hexane- and Octadecanethiol on Au(111) and Ag(111). *Langmuir* **1994**, *10* (4), 979–983. https://doi.org/10.1021/la00016a001.

(88) Schmaltz, B.; Rouhanipour, A.; Räder, H. J.; Pisula, W.; Müllen, K. Filling the Cavity of Conjugated Carbazole Macrocycles with Graphene Molecules: Monolayers Formed by Physisorption Serve as a Surface for Pulsed Laser Deposition. *Angew. Chem. Int. Ed.* **2009**, *48* (4), 720–724. https://doi.org/10.1002/anie.200803156.

(89) Xu, L.; Yang, L.; Cao, L.; Li, T.; Chen, S.; Zhao, D.; Lei, S.; Ma, J. Effect of Bulky Substituents on the Self-Assembly and Mixing Behavior of Arylene Ethynylene Macrocycles at the Solid/Liquid Interface. *Phys. Chem. Chem. Phys.* **2013**, *15* (28), 11748. https://doi.org/10.1039/c3cp51413g.

(90) Meng, T.; Lu, Y.; Lei, P.; Li, S.; Deng, K.; Xiao, X.; Ogino, K.; Zeng, Q. Self-Assembly of Triphenylamine Macrocycles and Co-Assembly with Guest Molecules at the Liquid–Solid Interface Studied by STM: Influence of Different Side Chains on Host–Guest Interaction. *Langmuir* **2022**, *38* (11), 3568–3574. https://doi.org/10.1021/acs.langmuir.2c00188.

(91) Shen, Y.-T.; Guan, L.; Zhu, X.-Y.; Zeng, Q.-D.; Wang, C. Submolecular Observation of Photosensitive Macrocycles and Their Isomerization Effects on Host−Guest Network. *J. Am. Chem. Soc.* **2009**, *131* (17), 6174–6180. https://doi.org/10.1021/ja808434n.

(92) May, R.; Jester, S.-S.; Höger, S. A Giant Molecular Spoked Wheel. *J. Am. Chem. Soc.* **2014**, *136* (48), 16732–16735. https://doi.org/10.1021/ja5096705.

(93) Yu, Y.; Lin, J.; Wang, Y.; Zeng, Q.; Lei, S. Room Temperature On-Surface Synthesis of Two-Dimensional Imine Polymers at the Solid/Liquid Interface: Concentration Takes Control. *Chem. Commun.* **2016**, *52* (39), 6609–6612. https://doi.org/10.1039/C6CC02005D.

(94) Yu, Y.; Lin, J.; Lei, S. Dynamic Covalent Chemistry of Imine Polymers at the Liquid/Solid Interface Investigated by Scanning Tunneling Microscopy. *RSC Adv.* **2017**, *7* (19), 11496–11502. https://doi.org/10.1039/C6RA27395E.

(95) Elings, V. B.; Gurley, J. A. Tapping Atomic Force Microscope. US5412980A, May 9, 1995. https://patents.google.com/patent/US5412980A/en (accessed 2023-03-29).

(96) Shi, J.; Hu, Y.; Hu, S.; Ma, J.; Su, C. (54) METHOD AND APPARATUS OF USING PEAK FORCETAPPING MODE TO MEASURE PHYSICAL PROPERTIES OF A SAMPLE.

(97) Martin, Y.; Abraham, D. W.; Wickramasinghe, H. K. High-resolution Capacitance Measurement and Potentiometry by Force Microscopy. *Appl. Phys. Lett.* **1988**, *52* (13), 1103–1105. https://doi.org/10.1063/1.99224.

(98) Houzé, F.; Meyer, R.; Schneegans, O.; Boyer, L. Imaging the Local Electrical Properties of Metal Surfaces by Atomic Force Microscopy with Conducting Probes. *Appl. Phys. Lett.* **1996**, *69* (13), 1975–1977. https://doi.org/10.1063/1.117179.

(99) Martin, Y.; Rugar, D.; Wickramasinghe, H. K. High-resolution Magnetic Imaging of Domains in TbFe by Force Microscopy. *Appl. Phys. Lett.* **1988**, *52* (3), 244–246. https://doi.org/10.1063/1.99482.

(100) Klinov, D.; Magonov, S. True Molecular Resolution in Tapping-Mode Atomic Force Microscopy with High-Resolution Probes. *Appl. Phys. Lett.* **2004**, *84* (14), 2697–2699. https://doi.org/10.1063/1.1697629.

(101) Korolkov, V. V.; Summerfield, A.; Murphy, A.; Amabilino, D. B.; Watanabe, K.; Taniguchi, T.; Beton, P. H. Ultra-High Resolution Imaging of Thin Films and Single Strands of Polythiophene Using Atomic Force Microscopy. *Nat. Commun.* **2019**, *10* (1), 1537. https://doi.org/10.1038/s41467-019-09571-6.

(102) Houska, V. Synthesis and Properties of Complex π-Electron Systems with Helical Chirality. Bachelor thesis, Charles University in Prague Faculty of Science, Prague, 2012.

(103) Houska, V. Π-Conjugated Oligomers Comprising Helically Chiral Units, Charles University in Prague Faculty of Science, Prague, 2015.

(104) Kessler, H.; Moosmayer, A.; Rieker, A. Das ausmass sterischer hinderung in substituierten triarylmethanen und triarylmethyl-radikalen. *Tetrahedron* **1969**, *25* (2), 287–293. https://doi.org/10.1016/S0040-4020(01)82623-5.

(105) Jančařík, A.; Rybáček, J.; Cocq, K.; Vacek Chocholoušová, J.; Vacek, J.; Pohl, R.; Bednárová, L.; Fiedler, P.; Císařová, I.; Stará, I. G.; Starý, I. Rapid Access to Dibenzohelicenes and Their Functionalized Derivatives. *Angew. Chem. Int. Ed.* **2013**, *52* (38), 9970–9975. https://doi.org/10.1002/anie.201301739.

(106) Nejedlý, J.; Šámal, M.; Rybáček, J.; Sánchez, I. G.; Houska, V.; Warzecha, T.; Vacek, J.; Sieger, L.; Buděšínský, M.; Bednárová, L.; Fiedler, P.; Císařová, I.; Starý, I.; Stará, I. G. Synthesis of Racemic, Diastereopure, and Enantiopure Carba- or Oxa[5]-, [6]-, [7]-, and -[19]Helicene (Di)Thiol Derivatives. *J. Org. Chem.* **2020**, *85* (1), 248–276. https://doi.org/10.1021/acs.joc.9b02965.

(107) Collins, S. K. Preparation of Cyclic Molecules Bearing “Strained” Olefins Using Olefin Metathesis. *J. Organomet. Chem.* **2006**, *691* (24–25), 5122–5128. https://doi.org/10.1016/j.jorganchem.2006.08.010.

(108) Zhang, W.; Moore, J. S. Arylene Ethynylene Macrocycles Prepared by Precipitation-Driven Alkyne Metathesis. *J. Am. Chem. Soc.* **2004**, *126* (40), 12796–12796. https://doi.org/10.1021/ja046531v.

(109) Zhang, W.; Brombosz, S. M.; Mendoza, J. L.; Moore, J. S. A High-Yield, One-Step Synthesis of *o* -Phenylene Ethynylene Cyclic Trimer via Precipitation-Driven Alkyne Metathesis. *J. Org. Chem.* **2005**, *70* (24), 10198–10201. https://doi.org/10.1021/jo0517803.

(110) Zhang, W.; Moore, J. S. Reaction Pathways Leading to Arylene Ethynylene Macrocycles via Alkyne Metathesis. *J. Am. Chem. Soc.* **2005**, *127* (33), 11863–11870. https://doi.org/10.1021/ja053466w.

(111) Romero, P. E.; Piers, W. E.; McDonald, R. Rapidly Initiating Ruthenium Olefin-Metathesis Catalysts. *Angew. Chem. Int. Ed.* **2004**, *43* (45), 6161–6165. https://doi.org/10.1002/anie.200461374.

(112) Romero, P. E.; Piers, W. E. Direct Observation of a 14-Electron Ruthenacyclobutane Relevant to Olefin Metathesis. *J. Am. Chem. Soc.* **2005**, *127* (14), 5032–5033. https://doi.org/10.1021/ja042259d.

(113) Martin, R. H.; Marchant, M. J. Thermal Racemisation of Hepta-, Octa-, and Nonahelicene. *Tetrahedron* **1974**, *30* (2), 347–349. https://doi.org/10.1016/S0040-4020(01)91469-3.

(114) Janke, R. H.; Haufe, G.; Würthwein, E.-U.; Borkent, J. H. Racemization Barriers of Helicenes: A Computational Study [1]. *J. Am. Chem. Soc.* **1996**, *118* (25), 6031–6035. https://doi.org/10.1021/ja950774t.

(115) Grimme, S.; Peyerimhoff, S. D. Theoretical Study of the Structures and Racemization Barriers of [n]Helicenes (n = 3–6, 8). *Chem. Phys.* **1996**, *204* (2–3), 411–417. https://doi.org/10.1016/0301-0104(95)00275-8.

(116) Barroso, J.; Cabellos, J. L.; Pan, S.; Murillo, F.; Zarate, X.; Fernandez-Herrera, M. A.; Merino, G. Revisiting the Racemization Mechanism of Helicenes. *Chem. Commun.* **2018**, *54* (2), 188–191. https://doi.org/10.1039/C7CC08191J.

(117) Bauschlicher, C. W. A Comparison of the Accuracy of Different Functionals. *Chem. Phys. Lett.* **1995**, *246* (1–2), 40–44. https://doi.org/10.1016/0009-2614(95)01089-R.

(118) O’Boyle, N. M.; Banck, M.; James, C. A.; Morley, C.; Vandermeersch, T.; Hutchison, G. R. Open Babel: An Open Chemical Toolbox. *J. Cheminformatics* **2011**, *3* (1), 33. https://doi.org/10.1186/1758-2946-3-33.

(119) Voigt, J.; Roy, M.; Baljozović, M.; Wäckerlin, C.; Coquerel, Y.; Gingras, M.; Ernst, K. Unbalanced 2D Chiral Crystallization of Pentahelicene Propellers and Their Planarization into Nanographenes. *Chem. – Eur. J.* **2021**, *27* (40), 10251–10254. https://doi.org/10.1002/chem.202101223.

(120) Xue, X.; Scott, L. T. Thermal Cyclodehydrogenations To Form 6-Membered Rings: Cyclizations of [5]Helicenes. *Org. Lett.* **2007**, *9* (20), 3937–3940. https://doi.org/10.1021/ol7015516.

(121) Swarbrick, J. C.; Taylor, J. B.; O'Shea, J. N. Electrospray Deposition in Vacuum. *Appl. Surf. Sci.* **2006**, *252* (15), 5622–5626. https://doi.org/10.1016/j.apsusc.2005.12.025.

(122) Satterley, C. J.; Perdigão, L. M. A.; Saywell, A.; Magnano, G.; Rienzo, A.; Mayor, L. C.; Dhanak, V. R.; Beton, P. H.; O'Shea, J. N. Electrospray Deposition of Fullerenes in Ultra-High Vacuum: *In Situ* Scanning Tunneling Microscopy and Photoemission Spectroscopy. *Nanotechnology* **2007**, *18* (45), 455304. https://doi.org/10.1088/0957-4484/18/45/455304.

(123) Saywell, A.; Sprafke, J. K.; Esdaile, L. J.; Britton, A. J.; Rienzo, A.; Anderson, H. L.; O'Shea, J. N.; Beton, P. H. Conformation and Packing of Porphyrin Polymer Chains Deposited Using Electrospray on a Gold Surface. *Angew. Chem. Int. Ed.* **2010**, *49* (48), 9136–9139. https://doi.org/10.1002/anie.201004896.

(124) Hinaut, A.; Pawlak, R.; Meyer, E.; Glatzel, T. Electrospray Deposition of Organic Molecules on Bulk Insulator Surfaces. *Beilstein J. Nanotechnol.* **2015**, *6*, 1927–1934. https://doi.org/10.3762/bjnano.6.195.

(125) Hinaut, A.; Meier, T.; Pawlak, R.; Feund, S.; Jöhr, R.; Kawai, S.; Glatzel, T.; Decurtins, S.; Müllen, K.; Narita, A.; Liu, S.-X.; Meyer, E. Electrospray Deposition of Structurally Complex Molecules Revealed by Atomic Force Microscopy. *Nanoscale* **2018**, *10* (3), 1337–1344. https://doi.org/10.1039/C7NR06261C.

(126) Rauschenbach, S.; Stadler, F. L.; Lunedei, E.; Malinowski, N.; Koltsov, S.; Costantini, G.; Kern, K. Electrospray Ion Beam Deposition of Clusters and Biomolecules. *Small* **2006**, *2* (4), 540–547. https://doi.org/10.1002/smll.200500479.

(127) Kahle, S.; Deng, Z.; Malinowski, N.; Tonnoir, C.; Forment-Aliaga, A.; Thontasen, N.; Rinke, G.; Le, D.; Turkowski, V.; Rahman, T. S.; Rauschenbach, S.; Ternes, M.; Kern, K. The Quantum Magnetism of Individual Manganese-12-Acetate Molecular Magnets Anchored at Surfaces. *Nano Lett.* **2012**, *12* (1), 518–521. https://doi.org/10.1021/nl204141z.

(128) Walz, A.; Stoiber, K.; Huettig, A.; Schlichting, H.; Barth, J. V. Navigate Flying Molecular Elephants Safely to the Ground: Mass-Selective Soft Landing up to the Mega-Dalton Range by Electrospray Controlled Ion-Beam Deposition. *Anal. Chem.* **2022**, *94* (22), 7767–7778. https://doi.org/10.1021/acs.analchem.1c04495.

(129) De Feyter, S.; De Schryver, F. C. Two-Dimensional Supramolecular Self-Assembly Probed by Scanning Tunneling Microscopy. *Chem. Soc. Rev.* **2003**, *32* (3), 139–150. https://doi.org/10.1039/b206566p.

(130) Cyr, D. M.; Venkataraman, B.; Flynn, G. W. STM Investigations of Organic Molecules Physisorbed at the Liquid−Solid Interface. *Chem. Mater.* **1996**, *8* (8), 1600–1615. https://doi.org/10.1021/cm960113a.

(131) Hu, Y.; Miao, K.; Xu, L.; Zha, B.; Miao, X.; Deng, W. Effects of Alkyl Chain Number and Position on 2D Self-Assemblies. *RSC Adv.* **2017**, *7* (51), 32391–32398. https://doi.org/10.1039/C7RA05811J.

(132) Ye, Y.; Sun, W.; Wang, Y.; Shao, X.; Xu, X.; Cheng, F.; Li, J.; Wu, K. A Unified Model: Self-Assembly of Trimesic Acid on Gold. *J. Phys. Chem. C* **2007**, *111* (28), 10138–10141. https://doi.org/10.1021/jp072726o.

(133) Payer, D.; Comisso, A.; Dmitriev, A.; Strunskus, T.; Lin, N.; Wöll, C.; DeVita, A.; Barth, J. V.; Kern, K. Ionic Hydrogen Bonds Controlling Two-Dimensional Supramolecular Systems at a Metal Surface. *Chem. - Eur. J.* **2007**, *13* (14), 3900–3906. https://doi.org/10.1002/chem.200601325.

(134) Lackinger, M.; Griessl, S.; Markert, T.; Jamitzky, F.; Heckl, W. M. Self-Assembly of Benzene−Dicarboxylic Acid Isomers at the Liquid Solid Interface: Steric Aspects of Hydrogen Bonding. *J. Phys. Chem. B* **2004**, *108* (36), 13652–13655. https://doi.org/10.1021/jp048248o.

(135) Rezek, B.; Ukraintsev, E.; Krátká, M.; Taylor, A.; Fendrych, F.; Mandys, V. Epithelial Cell Morphology and Adhesion on Diamond Films Deposited and Chemically Modified by Plasma Processes. *Biointerphases* **2014**, *9* (3), 031012. https://doi.org/10.1116/1.4890471.

(136) Fasel, R.; Parschau, M.; Ernst, K.-H. Amplification of Chirality in Two-Dimensional Enantiomorphous Lattices. *Nature* **2006**, *439* (7075), 449–452. https://doi.org/10.1038/nature04419.

(137) Tavazza, F.; Senftle, T. P.; Zou, C.; Becker, C. A.; van Duin, A. C. T. Molecular Dynamics Investigation of the Effects of Tip–Substrate Interactions during Nanoindentation. *J. Phys. Chem. C* **2015**, *119* (24), 13580–13589. https://doi.org/10.1021/acs.jpcc.5b01275.

(138) *Václav Houska et al. - YouTube*. https://www.youtube.com/playlist?list=PLFJNDHHAxyMsANSckWZQmh_3w1TRtPQDX (accessed 2022-11-29).

(139) Xu, J.; Li, T.; Geng, Y.; Zhao, D.; Deng, K.; Zeng, Q.; Wang, C. Two-Dimensional Self-Assembly of a Pair of Triangular Macrocycles Studied by STM. *J. Phys. Chem. C* **2015**, *119* (17), 9227–9233. https://doi.org/10.1021/jp512079z.

(140) Nishio, M. The CH/π Hydrogen Bond in Chemistry. Conformation, Supramolecules, Optical Resolution and Interactions Involving Carbohydrates. *Phys. Chem. Chem. Phys.* **2011**, *13* (31), 13873. https://doi.org/10.1039/c1cp20404a.

(141) Morse, P. M. Diatomic Molecules According to the Wave Mechanics. II. Vibrational Levels. *Phys. Rev.* **1929**, *34* (1), 57–64. https://doi.org/10.1103/PhysRev.34.57.

(142) Jones, J. E.; Chapman, S. On the Determination of Molecular Fields.—I. From the Variation of the Viscosity of a Gas with Temperature. *Proc. R. Soc. Lond. Ser. Contain. Pap. Math. Phys. Character* **1924**, *106* (738), 441–462. https://doi.org/10.1098/rspa.1924.0081.

(143) Jones, J. E.; Chapman, S. On the Determination of Molecular Fields. —II. From the Equation of State of a Gas. *Proc. R. Soc. Lond. Ser. Contain. Pap. Math. Phys. Character* **1924**, *106* (738), 463–477. https://doi.org/10.1098/rspa.1924.0082.

(144) Forrest, S. R.; Zhang, Y. Ultrahigh-Vacuum Quasiepitaxial Growth of Model van Der Waals Thin Films. I. Theory. *Phys. Rev. B* **1994**, *49* (16), 11297–11308. https://doi.org/10.1103/PhysRevB.49.11297.

(145) Gershoni-Poranne, R.; Stanger, A. Magnetic Criteria of Aromaticity. *Chem Soc Rev* **2015**, *44* (18), 6597–6615. https://doi.org/10.1039/C5CS00114E.

(146) Schaller, G. R.; Herges, R. Möbius Molecules with Twists and Writhes. *Chem Commun* **2013**, *49* (13), 1254–1260. https://doi.org/10.1039/C2CC34763F.

(147) Eder, S.; Yoo, D.; Nogala, W.; Pletzer, M.; Santana Bonilla, A.; White, A. J. P.; Jelfs, K. E.; Heeney, M.; Choi, J. W.; Glöcklhofer, F. Switching between Local and Global Aromaticity in a Conjugated Macrocycle for High-Performance Organic Sodium-Ion Battery Anodes. *Angew. Chem. Int. Ed.* **2020**, *59* (31), 12958–12964. https://doi.org/10.1002/anie.202003386.

(148) Rickhaus, M.; Jirasek, M.; Tejerina, L.; Gotfredsen, H.; Peeks, M. D.; Haver, R.; Jiang, H.-W.; Claridge, T. D. W.; Anderson, H. L. Global Aromaticity at the Nanoscale. *Nat. Chem.* **2020**, *12* (3), 236–241. https://doi.org/10.1038/s41557-019-0398-3.

(149) Hückel, E. Quantentheoretische Beiträge zum Benzolproblem. *Z. Für Phys.* **1931**, *70* (3), 204–286. https://doi.org/10.1007/BF01339530.

(150) Hückel, E. Quanstentheoretische Beiträge zum Benzolproblem. *Z. Für Phys.* **1931**, *72* (5), 310–337. https://doi.org/10.1007/BF01341953.

(151) Hückel, E. Quantentheoretische Beiträge zum Problem der aromatischen und ungesättigten Verbindungen. III. *Z. Für Phys.* **1932**, *76* (9), 628–648. https://doi.org/10.1007/BF01341936.

(152) *Emerging applications of curved aromatic compounds | Elsevier Enhanced Reader*. https://doi.org/10.1016/j.trechm.2022.04.005.

(153) Henderson, T. M.; Izmaylov, A. F.; Scalmani, G.; Scuseria, G. E. Can Short-Range Hybrids Describe Long-Range-Dependent Properties? *J. Chem. Phys.* **2009**, *131* (4), 044108. https://doi.org/10.1063/1.3185673.

(154) Ehrlich, S.; Moellmann, J.; Grimme, S. Dispersion-Corrected Density Functional Theory for Aromatic Interactions in Complex Systems. *Acc. Chem. Res.* **2013**, *46* (4), 916–926. https://doi.org/10.1021/ar3000844.

(155) Palata, O.; Andronova, A.; Šámal, M.; Nejedlý, J.; Rybáček, J.; Buděšínský, M.; Bednárová, L.; Pospíšil, L.; Císařová, I.; Starý, I.; Stará, I. G. Synthesis of (Di)Thiahelicenes and Dithiophenohelicenes by [2+2+2] Cycloisomerization of Alkynes. *Helv. Chim. Acta* **2022**, *105* (3), e202100225. https://doi.org/10.1002/hlca.202100225.

(156) Peeks, M. D.; Claridge, T. D. W.; Anderson, H. L. Aromatic and Antiaromatic Ring Currents in a Molecular Nanoring. *Nature* **2017**, *541* (7636), 200–203. https://doi.org/10.1038/nature20798.

(157) Koel, B. E.; Blank, D. A.; Carter, E. A. Thermochemistry of the Selective Dehydrogenation of Cyclohexane to Benzene on Pt Surfaces. *J. Mol. Catal. Chem.* **1998**, *131* (1–3), 39–53. https://doi.org/10.1016/S1381-1169(97)00255-0.

(158) Duhm, S.; Gerlach, A.; Salzmann, I.; Bröker, B.; Johnson, R. L.; Schreiber, F.; Koch, N. PTCDA on Au(111), Ag(111) and Cu(111): Correlation of Interface Charge Transfer to Bonding Distance. *Org. Electron.* **2008**, *9* (1), 111–118. https://doi.org/10.1016/j.orgel.2007.10.004.

(159) Järvinen, P.; Hämäläinen, S. K.; Banerjee, K.; Häkkinen, P.; Ijäs, M.; Harju, A.; Liljeroth, P. Molecular Self-Assembly on Graphene on SiO_2 and h-BN Substrates. *Nano Lett.* **2013**, *13* (7), 3199–3204. https://doi.org/10.1021/nl401265f.

(160) Witte, G.; Lukas, S.; Bagus, P. S.; Wöll, C. Vacuum Level Alignment at Organic/Metal Junctions: "Cushion" Effect and the Interface Dipole. *Appl. Phys. Lett.* **2005**, *87* (26), 263502. https://doi.org/10.1063/1.2151253.

(161) Zugermeier, M.; Herritsch, J.; Luy, J.-N.; Chen, M.; Klein, B. P.; Niefind, F.; Schweyen, P.; Bröring, M.; Schmid, M.; Tonner, R.; Gottfried, J. M. On-Surface Formation of a Transient Corrole Radical and Aromaticity-Driven Interfacial Electron Transfer. *J. Phys. Chem. C* **2020**, *124* (25), 13825–13836. https://doi.org/10.1021/acs.jpcc.0c04451.

(162) Gaussian 16, Revision A.03, M. J. Frisch, G. W. Trucks, H. B. Schlegel, G. E. Scuseria, M. A. Robb, J. R. Cheeseman, G. Scalmani, V. Barone, G. A. Petersson, H. Nakatsuji, X. Li, M. Caricato, A. V. Marenich, J. Bloino, B. G. Janesko, R. Gomperts, B. Mennucci, H. P. Hratchian, J. V. Ortiz, A. F. Izmaylov, J. L. Sonnenberg, D. Williams-Young, F. Ding, F. Lipparini, F. Egidi, J. Goings, B. Peng, A. Petrone, T. Henderson, D. Ranasinghe, V. G. Zakrzewski, J. Gao, N. Rega, G. Zheng, W. Liang, M. Hada, M. Ehara, K. Toyota, R. Fukuda, J. Hasegawa, M. Ishida, T. Nakajima, Y. Honda, O. Kitao, H. Nakai, T. Vreven, K. Throssell, J. A. Montgomery, Jr., J. E. Peralta, F. Ogliaro, M. J. Bearpark, J. J. Heyd, E. N. Brothers, K. N. Kudin, V. N. Staroverov, T. A. Keith, R. Kobayashi, J. Normand, K. Raghavachari, A. P. Rendell, J. C. Burant, S. S. Iyengar, J. Tomasi, M. Cossi, J. M. Millam, M. Klene, C. Adamo, R. Cammi, J. W. Ochterski, R. L. Martin, K. Morokuma, O. Farkas, J. B. Foresman, and D. J. Fox, Gaussian, Inc., Wallingford CT, 2016.

(163) Schneider, J.; Hamaekers, J.; Chill, S. T.; Smidstrup, S.; Bulin, J.; Thesen, R.; Blom, A.; Stokbro, K. ATK-ForceField: A New Generation Molecular Dynamics Software Package. *Model. Simul. Mater. Sci. Eng.* **2017**, *25* (8), 085007. https://doi.org/10.1088/1361-651X/aa8ff0.

(164) Smidstrup, S.; Markussen, T.; Vancraeyveld, P.; Wellendorff, J.; Schneider, J.; Gunst, T.; Verstichel, B.; Stradi, D.; Khomyakov, P. A.; Vej-Hansen, U. G.; Lee, M.-E.; Chill, S. T.; Rasmussen, F.; Penazzi, G.; Corsetti, F.; Ojanperä, A.; Jensen, K.; Palsgaard, M. L. N.; Martinez, U.; Blom, A.; Brandbyge, M.; Stokbro, K. QuantumATK: An Integrated Platform of Electronic and Atomic-Scale Modelling Tools. *J. Phys. Condens. Matter* **2020**, *32* (1), 015901. https://doi.org/10.1088/1361-648X/ab4007.

(165) Dewar, M. J. S.; Zoebisch, E. G.; Healy, E. F.; Stewart, J. J. P. Development and Use of Quantum Mechanical Molecular Models. 76. AM1: A New General Purpose Quantum Mechanical Molecular Model. *J. Am. Chem. Soc.* **1985**, *107* (13), 3902–3909. https://doi.org/10.1021/ja00299a024.

(166) Becke, A. D. A New Mixing of Hartree–Fock and Local Density-functional Theories. *J. Chem. Phys.* **1993**, *98* (2), 1372–1377. https://doi.org/10.1063/1.464304.

(167) Lee, C.; Yang, W.; Parr, R. G. Development of the Colle-Salvetti Correlation-Energy Formula into a Functional of the Electron Density. *Phys. Rev. B* **1988**, *37* (2), 785–789. https://doi.org/10.1103/PhysRevB.37.785.

(168) Ditchfield, R.; Hehre, W. J.; Pople, J. A. Self-Consistent Molecular-Orbital Methods. IX. An Extended Gaussian-Type Basis for Molecular-Orbital Studies of Organic Molecules. *J. Chem. Phys.* **1971**, *54* (2), 724–728. https://doi.org/10.1063/1.1674902.

(169) Hehre, W. J.; Ditchfield, R.; Pople, J. A. Self—Consistent Molecular Orbital Methods. XII. Further Extensions of Gaussian—Type Basis Sets for Use in Molecular Orbital Studies of Organic Molecules. *J. Chem. Phys.* **1972**, *56* (5), 2257–2261. https://doi.org/10.1063/1.1677527.

(170) Grimme, S.; Antony, J.; Ehrlich, S.; Krieg, H. A Consistent and Accurate *Ab Initio* Parametrization of Density Functional Dispersion Correction (DFT-D) for the 94 Elements H-Pu. *J. Chem. Phys.* **2010**, *132* (15), 154104. https://doi.org/10.1063/1.3382344.

(171) Dunning, T. H. Gaussian Basis Sets for Use in Correlated Molecular Calculations. I. The Atoms Boron through Neon and Hydrogen. *J. Chem. Phys.* **1989**, *90* (2), 1007–1023. https://doi.org/10.1063/1.456153.

(172) Kendall, R. A.; Dunning, T. H.; Harrison, R. J. Electron Affinities of the First-row Atoms Revisited. Systematic Basis Sets and Wave Functions. *J. Chem. Phys.* **1992**, *96* (9), 6796–6806. https://doi.org/10.1063/1.462569.

(173) Miertus, S.; Tomasi, J. Approximate Evaluations of the Electrostatic Free Energy and Internal Energy Changes in Solution Processes. *Chemical Physics* **1982**, *65*, 239–245.

(174) Miertus, S.; Scrocco, E.; Tomasi, J. Electrostatic Interaction of a Solute with a Continuum. A Direct Utilization of Ab Initio Molecular Potentials for the Prevision of Solvent Effects. *Chemical Physics* **1981**, *55*, 117–129.

(175) Schlegel, H. B. Optimization of Equilibrium Geometries and Transition Structures. *J. Comput. Chem.* **1982**, *3* (2), 214–218. https://doi.org/10.1002/jcc.540030212.

(176) Bauernschmitt, R.; Ahlrichs, R. Treatment of Electronic Excitations within the Adiabatic Approximation of Time Dependent Density Functional Theory. *Chem. Phys. Lett.* **1996**, *256* (4–5), 454–464. https://doi.org/10.1016/0009-2614(96)00440-X.

(177) Casida, M. E.; Jamorski, C.; Casida, K. C.; Salahub, D. R. Molecular Excitation Energies to High-Lying Bound States from Time-Dependent Density-Functional Response Theory: Characterization and Correction of the Time-Dependent Local Density Approximation Ionization Threshold. *J. Chem. Phys.* **1998**, *108* (11), 4439–4449. https://doi.org/10.1063/1.475855.

(178) Stratmann, R. E.; Scuseria, G. E.; Frisch, M. J. An Efficient Implementation of Time-Dependent Density-Functional Theory for the Calculation of Excitation Energies of Large Molecules. *J. Chem. Phys.* **1998**, *109* (19), 8218–8224. https://doi.org/10.1063/1.477483.

(179) Furche, F.; Ahlrichs, R. Adiabatic Time-Dependent Density Functional Methods for Excited State Properties. *J. Chem. Phys.* **2002**, *117* (16), 7433–7447. https://doi.org/10.1063/1.1508368.

(180) Scalmani, G.; Frisch, M. J.; Mennucci, B.; Tomasi, J.; Cammi, R.; Barone, V. Geometries and Properties of Excited States in the Gas Phase and in Solution: Theory and Application of a Time-Dependent Density Functional Theory Polarizable Continuum Model. *J. Chem. Phys.* **2006**, *124* (9), 094107. https://doi.org/10.1063/1.2173258.

(181) Van Caillie, C.; Amos, R. D. Geometric Derivatives of Excitation Energies Using SCF and DFT. *Chem. Phys. Lett.* **1999**, *308* (3–4), 249–255. https://doi.org/10.1016/S0009-2614(99)00646-6.

(182) Van Caillie, C.; Amos, R. D. Geometric Derivatives of Density Functional Theory Excitation Energies Using Gradient-Corrected Functionals. *Chem. Phys. Lett.* **2000**, *317* (1–2), 159–164. https://doi.org/10.1016/S0009-2614(99)01346-9.

(183) Yanai, T.; Tew, D. P.; Handy, N. C. A New Hybrid Exchange–Correlation Functional Using the Coulomb-Attenuating Method (CAM-B3LYP). *Chem. Phys. Lett.* **2004**, *393* (1–3), 51–57. https://doi.org/10.1016/j.cplett.2004.06.011.

(184) Humphrey, W.; Dalke, A.; Schulten, K. VMD: Visual Molecular Dynamics. *J Mol Graph.* **1996**, *14* (1), 33.

(185) London, F. Théorie quantique des courants interatomiques dans les combinaisons aromatiques. *J. Phys. Radium* **1937**, *8* (10), 397–409. https://doi.org/10.1051/jphysrad:01937008010039700.

(186) McWeeny, R. Perturbation Theory for the Fock-Dirac Density Matrix. *Phys. Rev.* **1962**, *126* (3), 1028–1034. https://doi.org/10.1103/PhysRev.126.1028.

(187) Ditchfield, R. Self-Consistent Perturbation Theory of Diamagnetism. *Mol. Phys.* **1974**, *27* (4), 789–807. https://doi.org/10.1080/00268977400100711.

(188) Wolinski, K.; Hinton, J. F.; Pulay, P. Efficient Implementation of the Gauge-Independent Atomic Orbital Method for NMR Chemical Shift Calculations. *J. Am. Chem. Soc.* **1990**, *112* (23), 8251–8260. https://doi.org/10.1021/ja00179a005.

(189) Cheeseman, J. R.; Trucks, G. W.; Keith, T. A.; Frisch, M. J. A Comparison of Models for Calculating Nuclear Magnetic Resonance Shielding Tensors. *J. Chem. Phys.* **1998**, *104* (14), 5497. https://doi.org/10.1063/1.471789.

(190) FOWLER, P. W.; STEINER, E.; ZANASI, R.; CADIOLI, B. Electric and Magnetic Properties of Hexaethynylbenzene. *Mol. Phys.* **1999**, *96* (7), 1099–1108. https://doi.org/10.1080/00268979909483052.

(191) Steiner, E.; Fowler, P. W.; Jenneskens, L. W. Counter-Rotating Ring Currents in Coronene and Corannulene. *Angew. Chem. Int. Ed.* **2001**, *40* (2), 362–366. https://doi.org/10.1002/1521-3773(20010119)40:2<362::AID-ANIE362>3.0.CO;2-Z.

(192) Keith, T. A.; Bader, R. F. W. Calculation of Magnetic Response Properties Using Atoms in Molecules. *Chem. Phys. Lett.* **1992**, *194* (1–2), 1–8. https://doi.org/10.1016/0009-2614(92)85733-Q.

(193) Keith, T. A.; Bader, R. F. W. Calculation of Magnetic Response Properties Using a Continuous Set of Gauge Transformations. *Chem. Phys. Lett.* **1993**, *210* (1–3), 223–231. https://doi.org/10.1016/0009-2614(93)89127-4.

(194) Perdew, J. P.; Burke, K.; Ernzerhof, M. Generalized Gradient Approximation Made Simple. *Phys. Rev. Lett.* **1996**, *77* (18), 3865–3868. https://doi.org/10.1103/PhysRevLett.77.3865.

(195) van Setten, M. J.; Giantomassi, M.; Bousquet, E.; Verstraete, M. J.; Hamann, D. R.; Gonze, X.; Rignanese, G.-M. The PseudoDojo: Training and Grading a 85 Element Optimized Norm-Conserving Pseudopotential Table. *Comput. Phys. Commun.* **2018**, *226*, 39–54. https://doi.org/10.1016/j.cpc.2018.01.012.

(196) Lejaeghere, K.; Bihlmayer, G.; Björkman, T.; Blaha, P.; Blügel, S.; Blum, V.; Caliste, D.; Castelli, I. E.; Clark, S. J.; Dal Corso, A.; de Gironcoli, S.; Deutsch, T.; Dewhurst, J. K.; Di Marco, I.; Draxl, C.; Dułak, M.; Eriksson, O.; Flores-Livas, J. A.; Garrity, K. F.; Genovese, L.; Giannozzi, P.; Giantomassi, M.; Goedecker, S.; Gonze, X.; Grånäs, O.; Gross, E. K. U.; Gulans, A.; Gygi, F.; Hamann, D. R.; Hasnip, P. J.; Holzwarth, N. A. W.; Iuşan, D.; Jochym, D. B.; Jollet, F.; Jones, D.; Kresse, G.; Koepernik, K.; Küçükbenli, E.; Kvashnin, Y. O.; Locht, I. L. M.; Lubeck, S.; Marsman, M.; Marzari, N.; Nitzsche, U.; Nordström, L.; Ozaki, T.; Paulatto, L.; Pickard, C. J.; Poelmans, W.; Probert, M. I. J.; Refson, K.; Richter, M.; Rignanese, G.-M.; Saha, S.; Scheffler, M.; Schlipf, M.; Schwarz, K.; Sharma, S.; Tavazza, F.; Thunström, P.; Tkatchenko, A.; Torrent, M.; Vanderbilt, D.; van Setten, M. J.; Van Speybroeck, V.; Wills, J. M.; Yates, J. R.; Zhang, G.-X.; Cottenier, S.

Reproducibility in Density Functional Theory Calculations of Solids. *Science* **2016**, *351* (6280), aad3000. https://doi.org/10.1126/science.aad3000.

(197) Garrity, K. F.; Bennett, J. W.; Rabe, K. M.; Vanderbilt, D. Pseudopotentials for High-Throughput DFT Calculations. *Comput. Mater. Sci.* **2014**, *81*, 446–452. https://doi.org/10.1016/j.commatsci.2013.08.053.

(198) Hamann, D. R. Optimized Norm-Conserving Vanderbilt Pseudopotentials. *Phys. Rev. B* **2013**, *88* (8), 085117. https://doi.org/10.1103/PhysRevB.88.085117.

(199) García, A.; Verstraete, M. J.; Pouillon, Y.; Junquera, J. The Psml Format and Library for Norm-Conserving Pseudopotential Data Curation and Interoperability. *Comput. Phys. Commun.* **2018**, *227*, 51–71. https://doi.org/10.1016/j.cpc.2018.02.011.

(200) Jollet, F.; Torrent, M.; Holzwarth, N. Generation of Projector Augmented-Wave Atomic Data: A 71 Element Validated Table in the XML Format. *Comput. Phys. Commun.* **2014**, *185* (4), 1246–1254. https://doi.org/10.1016/j.cpc.2013.12.023.

(201) Liu, D. C.; Nocedal, J. On the Limited Memory BFGS Method for Large Scale Optimization. *Math. Program.* **1989**, *45* (1–3), 503–528. https://doi.org/10.1007/BF01589116.

(202) Hamaekers J., Bollerhey G., Bulin J., Neuen C., Thesen R. Griebel M. Tremolo-X, 2017. www.tremolo-x.com.

5.18. Appendix 1 – 6

Appendices 1 – 6 are provided in separate documents.